Design of High Performance Indium Phosphide (InP) - based Quantum Dot Light Emitting Diodes (QLEDs)

vorgelegt von
M.Eng.
Yohan Kim
Geb. in Chungcheongbuk-do, Südkorea

von der Fakultät IV- Elektrotechnik und Informatik
der Technischen Universität Berlin
zur Erlangung des akademischen Grades

Doktor der Ingenieurwissenschaften
- Dr.-Ing. -

genehmigte Dissertation

Promotionsausschuss:

Vorsitzender: Prof. Dr. Bernd Szyszka
Gutachter: Prof. Dr.-Ing. Klaus-Dieter Lang
Gutachter: Prof. Dr. Alexander Böker
Gutachter: Prof. Dr. Andreas Taubert
Gutachter: Dr. Armin Wedel

Tag der wissenschaftlichen Aussprache: 02. Mai 2018

Berlin 2018

Abstract

This dissertation is dedicated to the development and understanding of fundamental device mechanism and engineering of the device architecture of quantum dot light-emitting diodes (QLEDs) based on indium phosphide (InP) quantum dots. QLEDs have emerged as a next-generation flat panel display (FPD) technology with promising properties. Their device performance and fabrication methods are developed extensively through the assistance of the highly developed organic light-emitting diode (OLED) technology. However, the operation mechanism and the optimized device architecture, which both control the device performance, remain unclear especially for devices with cadmium (Cd)-free materials. Moreover specifically, the device efficiency and luminance are relatively low compared to the Cd-based QLEDs. The important QD material design aspects such as outer shell thickness of the InP/ZnSe/ZnS, core/multishell structure and the ligand chain length of the QDs are investigated with conventional QLEDs to improve device performance. Through the QD design, maximum external quantum efficiency (EQE) and luminance of the conventional QLEDs reach 2.5% and 3164 cd/m^2, respectively. Since an inverted device structure is more favorable for commercialization of QLED displays due to recent advances in the well-developed active matrix (AM) OLED technology, this architecture is more thoroughly investigated considering a charge carrier balance in the multilayered QLEDs. In addition, the inverted architecture offers other advantages such as an improved device stability and enhanced efficiency. The maximum EQE of the inverted QLEDs of 3.1% was achieved by controlling electron transport with an adopted multi-spin-coated zinc oxide (ZnO) nanoparticle electron transport layer (ETL); however, the maximum luminance was less than 3000 cd/m^2. Further enhancement of device performance (i.e. maximum EQE and luminance of 3.3% and 8449 cd/m^2, respectively) and stability was accomplished through well-balanced charge carriers and a charge neutralization effect in the QD emission layer. Moreover, a recombination-zone (RZ) shift model which depends on the different thicknesses of QD film, and a charge neutralization model consisted of electric field-assisted Auger electron injection via the mid-gap states of ZnO nanoparticles were developed based on the experimental results and theoretical hypotheses. These two theoretical models provide a broad scope to understand the optimization process of InP QD-based QLEDs, not only for this dissertation but also the further investigations. Consequently, the developments in this dissertation can provide the experimental guidelines and theoretical insights for designing efficient and stable Cd-free QLEDs.

Zusammenfassung

Diese Arbeit beschäftigt sich mit der Entwicklung von Quantenpunkt (QD)-basierten LEDs (QLED) auf der Basis von Indiumphosphid und dem Verständnis fundamentaler Mechanismen in diesen QLEDs. QLEDs werden aufgrund ihrer vielversprechenden Eigenschaften als Technik der nächsten Generation im Bereich der Flachdisplays (Flat Panel Display, FPD) angesehen. Auf Grundlage der bereits weit entwickelten organischen Leuchtdioden (OLED) wird die Entwicklung im Bereich des Bauteil-Aufbaus und der Effizienzoptimierung der QLEDs momentan intensiv bearbeitet. Nichtsdestotrotz sind bis jetzt, insbesondere für Cadmium-freie Systeme, die grundlegenden Mechanismen und die optimale Bauteil-Architektur, welche beide enorm wichtig für die Effizienz der LED sind, nicht umfassend untersucht und verstanden. Insbesondere die Effizienz und Helligkeit sind im Vergleich zu den Cadmium-basierten Gegenstücken deutlich geringer. Wichtige Aspekte des Quantenpunkt-Designs, wie z.B. Hüllendicke der äußeren Hülle der InP/ZnSe/ZnS-Kern-Multischalen-Struktur und die Länge der Liganden auf der Oberfläche des Quantenpunkts wurden an konventionellen QLED-Aufbauten hinsichtlich ihres Einflusses auf die Effizienz untersucht. So konnten externe Quanteneffizienzen (EQE) von bis zu 2.5% im konventionellen Aufbau bei Helligkeiten von 3164 cd/m² erreicht werden. Für eine Kommerzialisierung der QLED-Technik wird jedoch nicht die konventionelle, sondern, aufgrund der kürzlichen Weiterentwicklungen der Aktive-Matrix OLED (AMOLED) Technologie, eine invertierte Bauteil-Architektur bevorzugt. Die invertierte Architektur hat mehrere Vorteile, z.B. eine bessere Stabilität und verbesserte Effizienz und ist hinsichtlich der Ladungsbalance deutlich umfangreicher untersucht. In dieser Arbeit wurden EQE von 3.1% durch gezielte Kontrolle des Elektronentransports mittels einer mehrfach spingecoateten Zinkoxidnanopartikel (ZnO) Elektron-Transport-Schicht (ETL). Dabei betrug die maximal erreichte Helligkeit jedoch geringer als 3000 cd/m². Weitere Anpassungen durch gut balancierte Ladungsträger und einem Ladungsneutralisationseffekt in der Quantenpunkt-Emissionschicht führten zu deutlich verbesserter Effizienz (EQE = 3.3%, Helligkeit 8449 cd/m²) und Stabilität. Zusätzlich wurden zwei Modelle etabliert basierend auf experimentell ermittelten Daten und theoretisch entwickelten Hypothesen. Zum einen die Verschiebung der Rekombinationszone in Abhängigkeit von den verschiedenen QD-Schichtdicken. Zum anderen die Ladungsneutralisation auf Basis der vom elektrischen Feld unterstützten Injektion der Auger Elektronen durch die mittleren Energieniveaus der Bandlücke von

ZnO Nanopartikeln. Diese beiden theoretischen Modelle erlauben ein generelles umfangreiches Verständnis des Optimierungsprozesses von InP-QLEDs über den Horizont dieser Arbeit hinaus. Entsprechend erlauben die Entwicklungen auf praktischer sowie theoretischer Ebene im Rahmen dieser Arbeit das Design von effizienten und stabilen Cadmium-freien QLEDs.

Fraunhofer IAP
Geiselbergstr. 69
14476 Potsdam-Golm

This dissertation originated in a cooperation with the Fraunhofer Institute for Applied Polymer Research (IAP) and the Technical University of Berlin.

Acknowledgements

For the first, I give thanks to the Lord for his guidance of my journey including this humble but noble Ph.D. work.

I am deeply grateful to my supervisor Dr. Armin Wedel for the opportunity to pursue my Ph.D. work in Fraunhofer IAP, and for his unwavering support to not only my work but also to my family in Berlin.

I would like to thank my advisor Prof. Dr. Klaus-Dieter Lang from TU Berlin for his collegial guidance and support to continue and finalize my Ph.D. work.

I would like to express infinitely thanks to my dissertation committee members, Prof. Dr. Andreas Taubert, Prof. Dr. Alexander Böker and of course again Dr. Armin Wedel.

My thankfulness is also to all the current or former group members at Fraunhofer IAP. Dr. Christian Ippen, Dr. Tonino Greco, and Christopher Pries helped with QD synthesis and, provided personal assistance for my family to adapt in Berlin. Stefanie Krießel, Bert Fischer, Stefan Kröpker, Björn Gruber, Katrin Fink, Franziska Ebert also provided great support in the lab works. I would like to also thank Benjamin Heyne for his supports in the lots of chemical syntheses, his kind care, and of course his friendship. Dr. Christin Böffel, Dr. Andre Geßner, Dr. Andreas Holländer also provided helpful insight into my work with fruitful and critical discussions. I would like to also thank Dr. Alexader Langer, Edgar Nandayapa, and Xeupu Wang for the help with papers and dissertation correction, and for the interesting discussions always.

Financial support was received from the “Deutsche Forschungsgemeinschaft (DFG)” SPP 1708 through ILPIN project. I would like to extend my thankfulness to this project partner in Potsdam University, especially Prof. Dr. Andreas Taubert again, and Ahed Abouserie for broadening my knowledge through very interesting and adventurous topics.

I would like to also remain special thanks to my former colleagues in KETI in Korea, Dr. Chuljong Han, Dr. Min-Suk Oh, Dr. Bunguk Yoo, Prof. Dr. Jiwan Kim, and Prof. Dr.

Young-Hoon Kim. I could move forward to the future every time with their strong support and wonderful cares.

Last but not least, this dissertation is dedicated to my lovely family, especially my wife, artist Kee-Rim Kwon, and my litter princess Giyu Kim who was born during this journey. My wife has thrown herself in Germany without any plan, any preparation, and any friends because of me. Without her support and great and infinite love, I could not have accomplished any of this work and survived in Germany. I would like to give thanks also to my lovely parents, Dong-Chan Kim, Geum-Sun Jeong, for their supports with endless love.

Berlin, 02nd May 2018

Yohan Kim

Contents

List of Figures

List of Table

List of Acronyms

AFM	atomic force microscope
ALD	atomic layer deposition
AM	active matrix
A1	a mixture of IPA, ethanol, and H_2O
BLU	backlight unit
BP	boiling point
CBM	conduction band minimum
CIE	Commission Internationale de l'Eclairage
CTL	charge transport layers
C-V	capacitance-voltage
DTG	derivative thermogravimetric
EL	electroluminescence
EML	emitting layer
EOD	electron only device
EQE	external quantum efficiency
ETL	electron transport layer
FPD	flat panel display
FRET	Förster resonance energy transfer
FWHM	full-width half-maximum
HDTV	high-definition-television
HIL	hole injection layer
HOD	hole only device
HOMO	highest occupied molecular orbital
HTL	hole transport layer
IE	ionization energy
IPA	isopropanol
IR	infrared
ITO	indium tin oxide
IZO	indium zinc oxide
J-V-L	current density-voltage-luminance
LCD	liquid crystal display
LED	light-emitting diode

LUMO	lowest unoccupied molecular orbital
OLED	organic light-emitting diode
PAA	poly-allylamine
PEDOT:PSS	poly(3,4-ethylenedioxythiophene)-poly(styrenesulfonate)
PEI	polyethyleneimine
PESA	photoelectron spectroscopy in air
PFO	polyethylene oxide
PL	photoluminescence
poly-TPD	poly-(N,N'-bis(4-butylphenyl)-N,N'-bis(phenyl)benzidine)
PPV	Poly(p-phenylene vinylene)
QCSE	quantum confined Stark effect
QD	quantum dot
QLED	quantum dot light-emitting diode
QY	quantum yield
RoHS	Restriction of Hazardous Substances
RZ	recombination zone
R_{pv}	peak to valley roughness
R_q	root mean square roughness
SCLC	space-charge-limited conduction
SEC	spectro-electrochemistry
SUHD	super-ultra-high-definition
STM	scanning probe microscopy
STS	scanning probe spectroscopy
TAPC	1,1-bis((di-4-tolylamino)phenyl)cyclohexane
TCTA	4,4',4"-Tris(carbazol-9-yl)triphenylamine
TEM	transmission electron microscopic
TFT	thin-film transistor
TGA	thermogravimetric analysis
TPBi	2,2′,2"-(1,3,5-benzinetriyl)-tris(1-phenyl-1-H-benzimidazole)
UV	ultraviolet
UHD	ultra-high-definition
VBM	valence band maximum
WF	work function
2ME	2-methoxyethanol

Chapter 1

1 Introduction

1.1 Quantum dot light-emitting diodes

The flat panel display (FPD) market has developed dramatically since the innovation of liquid crystal display (LCD) technology in the 1970's. Now, the FPD is the workhorse of the information display market and it is included in most of the electronic devices such as smartphones, tablet PCs, laptops, monitors, televisions, microdisplays, medical equipment, military gadgets, digital cameras and other portable devices. Moreover, organic light-emitting diodes (OLEDs), which have been heavily researched and optimized since the pioneering research at Kodak in 1987 [1], are in stronger demand for future FPD applications (***Figure 1.1.1ab***) such as flexible and transparent displays. Advantages of OLEDs include their self-emitting property, wide viewing angle, high contrast ratio, low power consumption and their light weight [2]. In addition, high resolution and large area display shown in ***Figure 1.1.1cd*** are additional future trends in FPD market, which can be potentially realized with OLEDs fabricated with solution processing (i.e. gravure printing, screen printing, inkjet printing) that provides a cost-effective and high flow-rates manufacturing process. However, the manufacture of multilayer OLEDs with solution deposition methods is challenging because of the low solubility of the OLED materials used in high-performance devices [3]. Colloidal quantum dots (QDs)-based light-emitting diodes (LEDs), where the electric current is used to generate the exciton in the QD emitter and produce electroluminescence (EL), are considered as another potential technology to fulfill the future needs in FPD market because of their solution processability, and excellent optical and electrical properties which are competitive to the OLED technology. The superior properties of

quantum dot light-emitting diodes (QLEDs) are mainly originated from QD emitters. Colloidal QDs exhibit unique characteristics such as size-controlled tunable emission that reduces production cost, narrow full-width half-maximum (FWHM) of photoluminescence (PL) spectrum which leads to the wide color gamut of display, low-cost solution-based processing and good material stability originated from inorganic emitters. These advantages make QDs an important class of material for next-generation optoelectronic devices including lasers, photodetectors, solar cells, QD backlight units (BLUs) and especially QLEDs [4–7].

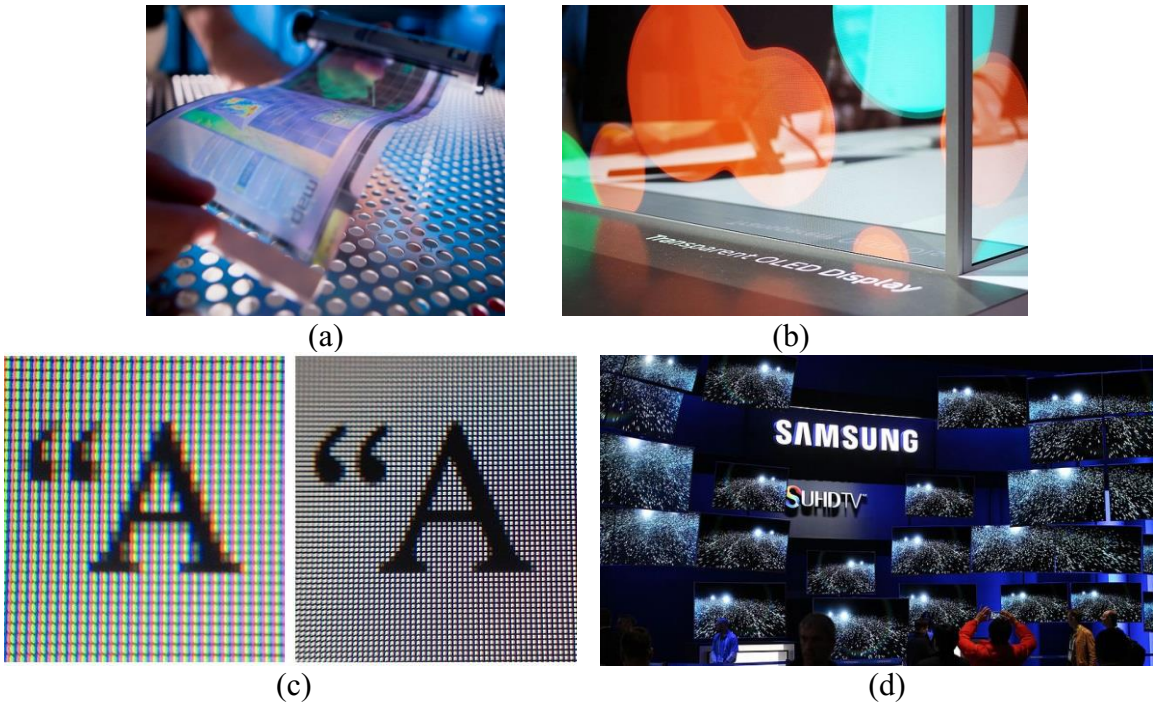

(a) (b) (c) (d)

Figure 1.1.1 The future main display trends: (a) flexible [8], (b) transparent [9], (c) (d) high resolution and large area display (e.g. retina display and large SUHD TV) [10,11].

Particularly, B.H Kim et al. have already demonstrated high resolution (i.e. 30 × 30 μm^2 of pixel size) patterns printed by E-jet printing using cadmium selenide (CdSe)-based QD inks, shown in ***Figure 1.1.2a***. In addition, the green indium phosphide (InP)-based QD inks were successfully printed on a common printer paper in our previous work, shown in ***Figure 1.1.2b***. Both examples mentioned above utilize the properties of QLEDs which allow QDs to be inkjet-printed for display applications that require large area or high resolution.

Electrically driven QLEDs were first invented in 1994 by V. Colvin et al. where II-VI semiconductor CdSe QDs were embedded in a poly(p-phenylene vinylene) (PPV) layer [12]. The device external quantum efficiency (EQE), which is defined by the ratio between the number of photons emitted into free space to the number of injected charge

carriers, was only 0.001-0.01% because of the charge carrier imbalance in the QD emitter layer and the low internal quantum yield (QY) of the QD material itself. However, the performance of the QLEDs using CdSe QDs was improved dramatically by applying different QD structure designs which enhance the QY and stability, and by using organic-inorganic hybrid device structure which provides efficient charge carrier injection and balance in the QD layer [13–17].

(a) (b)

Figure 1.1.2 (a) E-jet printed homogeneous QD array with a pixel size of 30 × 30 μm^2 using CdSe-based QD inks [18] and (a) an inkjet-printed picture on paper with InP-based QD inks.

Therefore, the EQE of QLEDs is currently comparable to that of phosphorescent OLEDs (c.a. 20%), shown in ***Figure 1.1.4a***. Recently, the extraordinary potential of QLEDs as the future display technology was demonstrated in the various researches, shown in ***Figure 1.1.3***. T. Kim et al. from Samsung Electronics demonstrated the potential of QLEDs as a full-color display by preparing a 4-inch active-matrix display panel with a resolution of 320 × 240 pixels. This panel was fabricated by transfer printing of red, green and blue (RGB) QDs in 2011, shown in ***Figure 1.1.3a*** [14]. Y. Yang et al. also reported a more efficient and stable a 4.3-inch monochrome display panel fabricated by a spin-coating with a resolution of 480 × 800 pixels in 2015, shown in ***Figure 1.1.3b*** [15]. M.K. Choi et al. successfully fabricated ultra-thin wearable (i.e. flexible) QLEDs by using an intaglio transfer printing technique on the flexible substrate which consisted of a parylene-C and epoxy double layer, shown in ***Figure 1.1.3c*** [19]. In addition, H. Y. Kim et al. realized transparent Cd-free InP-based QLEDs which utilized an indium zinc oxide (IZO) top electrode, shown in ***Figure 1.1.3d*** [20].

Despite the well-developed performance of QLEDs with Cd-based QDs, a crucial future task is the substitution of Cd-containing QDs by less toxic materials. Current regulations prohibit the use of toxic materials such as Pb, Cd, and Hg because of their

threats to human health and the environment [21]. In the European Union, for example, the Restriction of Hazardous Substances (RoHS) directive prohibits the use of toxic materials in consumer electronics when they contain more than certain amounts [22]. To avoid potential limitations, more and more studies on QLEDs using Cd-free QDs including InP [23], Si [24], carbon/graphene [25], ZnSe [26], CuInS [27], CuInGaS [28] and CuZnInS [29] have been reported. ***Figure 1.1.4*** summarizes the progress of Cd-free QLEDs regarding maximum current efficiency, and EQE and luminance. While significant development of Cd-free QLEDs has taken place over the last five years, InP III-V semiconductor nanocrystals are considered as the most promising materials for Cd-free QLEDs. InP-based QDs have a less ionic lattice, reduced toxicity, a wide emission spectrum tunability covering the range of visible light, and a relatively narrow FWHM around 45~50 nm when compared to other Cd-based QDs (i.e. 80~130 nm) [30–33].

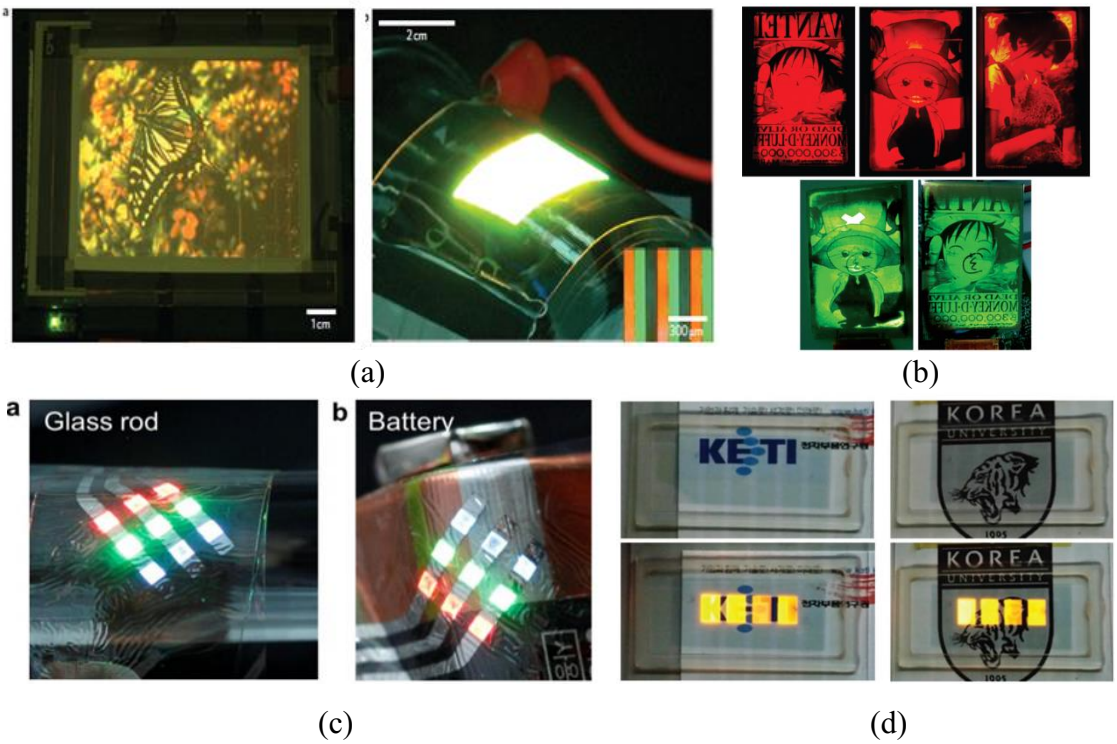

Figure 1.1.3 (a) 4 inch full-color QLEDs from Samsung Electronics (hafnium indium zinc oxide (HIZO) thin-film transistor (TFT) backplane, 320×240 pixel array) [14], (b) 4.3 inch red and green monochrome display (low temperature poly silicon (LTPS) TFT backplane, 480 × 800 pixel array) [15], (c) ultra-thin and wearable QLEDs [19] and (d) transparent Cd-free QLEDs with indium zinc oxide (IZO) top electrode [20].

Most of the early result with InP QD-based QLEDs that consist of organic charge transport layers (CTLs) in a conventional structure had poor device performance (i.e. EQE of 0.008 %, 16 cd/m^2) a color purity with the parasitic emission from hole transport layer (HTL) [34]. However, later J. Lim et al. demonstrated high efficient green QLEDs

fabricated with InP/ZnSeS QDs in the organic/inorganic hybrid inverted structure adopting ZnO nanoparticle electron transport layer (ETL) instead of using the organic materials [35]. As the results of confined exciton recombination in the QD layer attributed to the well-balanced charge carriers, their green QLEDs reached the maximum EQE and luminance up to 3.46% (max. 10.9 cd/A) and 3900 cd/m^2, respectively. Most recently, J. Jo et al. also demonstrated saturated red-emitting QLEDs using InP/ZnSeS/ZnS QDs in the organic/inorganic hybrid conventional structure where ZnO nanoparticles used as ETL, which shows 2.5% (max. 4.2 cd/A) and 2849 cd/m^2 of maximum EQE and luminance, respectively [36].

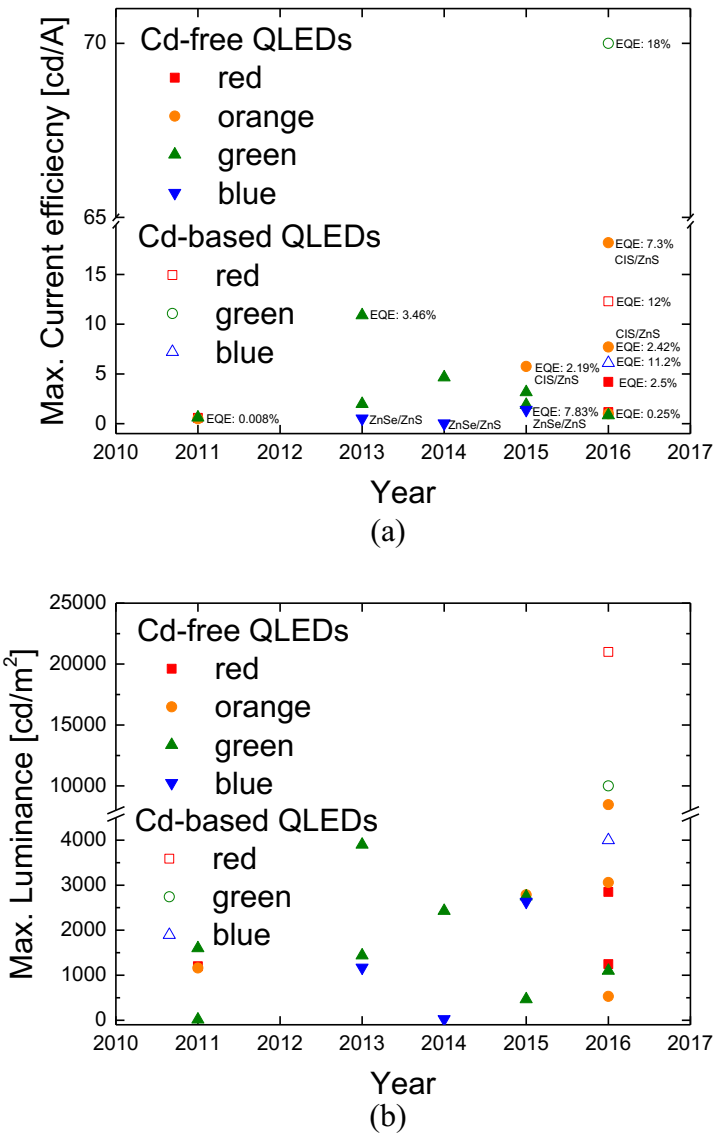

Figure 1.1.4 Development of red/orange/green/blue-emitting QLED performance based on Cd-free QDs (without Si and graphene QDs) over time regarding (a) maximum current efficiency (maximum EQE from some of the results is labeled) and (b) luminance. (including recent development of Cd-based QLEDs, open shapes [17]) [20,26–29,34–44]

Our previous development shown in ***Figure 1.1.5*** also indicates the potential of InP-based QD as the promising emitter material in QLEDs. The achieved color saturation with InP/ZnSe/ZnS QDs is visualized in a Commission Internationale de l'Eclairage (CIE) 1931 chromaticity diagram with a high-definition-television (HDTV) standard color triangle (i.e. sRGB standard).

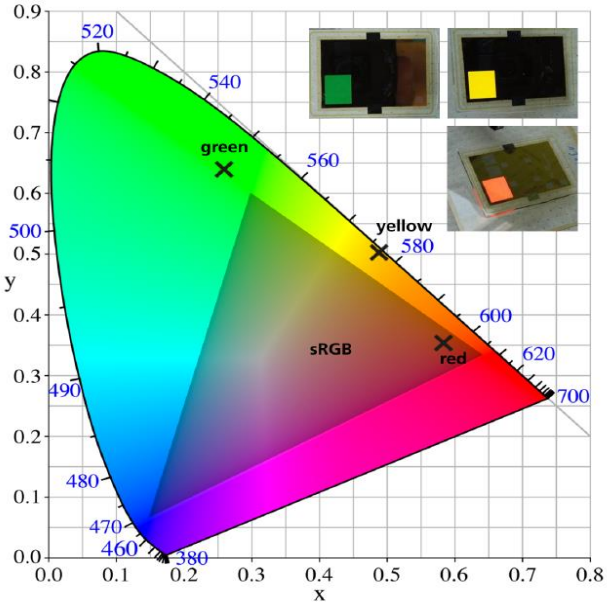

Figure 1.1.5 The CIE (Commission Internationale de l'Eclairage) 1931 chromaticity diagram showing the coordinates of green, yellow and red QLEDs using InP/ZnSe/ZnS QDs.

The coordinates of yellow QLEDs indicate the excellent color purity. For green, the coordinates extend the color gamut broader than the sRGB standard (i.e. HDTV standard). For red, the coordinates are located inside of the sRGB triangle because of the parasitic emission of QLEDs, originated from organic CTL. The blue emitting InP/ZnSe/ZnS QD was also demonstrated, however, their performance in QLEDs was quite low due to the relatively smaller particle size with more surface states compared to the red and green QDs [45]. Even though the intensive investigation on Cd-free QLEDs, the reported electroluminescence (EL) performance of InP QD-based QLEDs is insufficient compared to the Cd-based devices, which especially have lower maximum luminance below 4000 cd/m^2. Moreover, there are remained challenges such as efficiency roll-off, attributed to the EL quenching through Auger recombination and strong electric field, and device degradation, which limits the commercialization of QLEDs [34–36,42].

1.2 Design aspects for efficient and stable QLEDs

QLEDs have become a future dilly trend with their potential properties, and the optoelectronic device performance has been dramatically enhanced with in-depth of investigation regarding chemistry and device mechanism based on the Cd-based QDs. However, the investigation on Cd-free QLEDs during last five years especially with InP-based QDs is left far behind compared to the highly developed Cd-based technology, and there are remained critical challenges.

First of all, the high and stable QY of Cd-free QDs should be accomplished even under the electric field and the charged condition in the device in order to have high device EQE concerning the confinement of electron and hole wave function. D. Bozyigit and V. Wood suggested that alloyed core/multishell system design to be favorable for EL device applications. The alloyed core can especially provide the smoothed confinement which minimizes Auger recombination quenching. In addition, proper multishell design (i.e. thickness and materials) confining electron and hole wave functions in the core can minimize the exciton polarization under the applied electric field and also provide the effective passivation of the particles [46]. Our InP/ZnSe/ZnS QDs have been designed upon the consideration of alloyed core/multishell system from the previous work, which has the delocalization of the excitons by the ZnSe shell while an outer ZnS shell confines the excitons again effectively [47].

Since QLEDs with inorganic QD emitter are often considered to be more resistant than OLED to device degradation caused by oxygen and humidity, replacing organic charge transport material with inorganic charge transport materials such as metal oxide nanoparticles is the more rational strategy for the material choice in order to develop even air-stable all-inorganic QLEDs [48–51]. In terms of QLED device system design, two type of main luminance quenching mechanisms, field-induced quenching with high driving voltage [52] and Auger recombination quenching with device charging [53], should be sophisticatedly considered since drastic efficiency roll-off and device instability are mainly originated from the both quenching process. Therefore, efficient electron and hole injection (i.e. by direct charge injection or Förster resonance energy transfer (FRET)), charge carriers balance at the QD active layer, and the minimization of the applied electric field and the carrier charging in the QD layer are the critical device design points [22,46].

1.3 Objectives of research

The main focus of this dissertation revolves three main current issues of QLED research including the development of Cd-free QLEDs, the enhancement of low performance and instability of Cd-free devices, and the better fundamental understanding of device mechanisms that governs the device optimization process.

InP/ZnSe/ZnS multishell QDs were chosen for the "Cd-free" material. Both conventional and inverted QLED test-beds were developed to understand interactions between InP-based QDs and the physical property of the multilayered device that consist of organic and inorganic semiconductor layers, via the assistance of current highly developed OLED technologies.

Moreover, since the charge carrier balance control is the most critical process for device performance and stability but it remains unclear for the InP-based QLEDs, the developing theoretical models with the perspectives of the device optimization process considering charge injection, transport and exciton recombination in the multilayered device is one of the most important focus of this dissertation.

1.4 Structure of dissertation

The dissertation is divided into seven chapters. Chapter 1 introduces the research needs and the history of current QLED technologies, Chapter 2 discusses the fundamentals of QD and QLEDs, and Chapter 3 details the experimental methods used in QLED fabrication and characterization. As shown in ***Figure 1.4.1***, the main results and discussion parts are separated into Chapter 4, Chapter 5 and Chapter 6.

Chapter 4 discusses the most promising QD design aspects by embedding the QDs in the well optimized conventional QLED structure which consists of mainly organic CTLs. Even though the optimized QD design and the device architecture, however, the conventional device still shows serious drawback against device luminance and stability because the carrier charging in the multilayered QLEDs during the operation occurs the strong efficiency roll-off and the fast degradation of the device due to the thermal energy loss in organic CTL or QD/organic interface defects.

Therefore, inverted QLEDs are developed in Chapter 5 with an in-depth of investigation to improve device performance and stability considering the charge carrier balance and process conditions in different device architectures, as the inverted structure with inorganic CTLs provides not only the better stability of device but also the

capability to integrate current well-developed backplane technology from OLEDs [54,55]. In this chapter, the electron injection properties from cathode (i.e. indium tin oxide (ITO)) to conduction band minimum (CBM) of QD are investigated by applying thin buffer layers such as an aluminum oxide (Al_2O_3) layer deposited an atomic layer deposition (ALD) or a polyethyleneimine (PEI) layer deposited by solution process. Moreover, commercially available or synthesized ZnO nanoparticles as ETL and different HTLs are applied in the device and their influence on the QLED performance was investigated.

Chapter 6, the culmination of this dissertation, is dedicated to developing theoretical models by the investigation on strong dependence between QD emissive layer thicknesses and device performance considering charge carrier balance. The possible physical models are suggested to understand optimization process considering the mid-gap states of ZnO nanoparticle and the thickness of the QD layer, which is the critical point to achieve high-performance InP/ZnSe/ZnS-based QLEDs. The suggested models are also discussed throughout the manuscript to explain the experimental results and they show the broad range of agreements.

Finally, Chapter 7 summarizes the contribution of this dissertation and discusses the considerations for the future works.

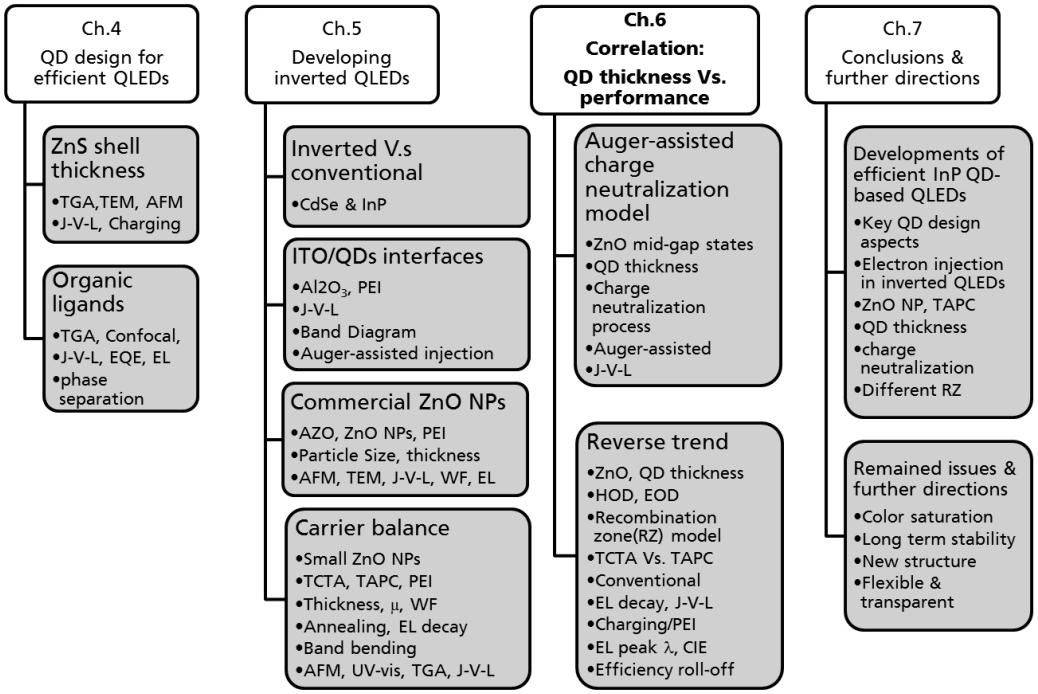

Figure 1.4.1 Structure of dissertations. Each chapter consists of several sub chapters including the techniques to evaluate the experimental results.

Chapter 2

2 Fundamentals

2.1 Colloidal quantum dots

2.1.1 Quantum confinement effect

Quantum confinement effect, so-called quantum size effect, occurs when the nanoparticle radius (R) is smaller than the exciton Bohr radius of bulk material (***Figure 2.1.1***), accompanying the change of electrical and optical properties of nanoparticles. The exciton Bohr radius (a_B) can be described by following equation with the effective mass approximation:

$$a_B = \frac{\varepsilon \hbar^2}{\mu_{eh} e^2} \quad (where\ \hbar = \frac{h}{2\pi}, \mu_{eh} = \frac{m_e m_h}{m_e + m_h})$$

where ε is the dielectric constant of the specific material, h is the Planck constant, e is the elementary charge, and m_e and m_h are the effective electron and hole mass [56]. When the size of nanoparticle is close to the exciton Bohr radius, the electron and hole wave function is physically confined within the particles size. Therefore, the smaller particle (i.e. $R << a_B$) undergoes the stronger confinement. The band gap (E_g) and the particle diameter (R) have a correlation based on the following equation:

$$E_g = E_{g,bulk} + \frac{h^2}{8R^2}\left(\frac{1}{m_e} + \frac{1}{m_h}\right) - \frac{1.786e^2}{4\pi\varepsilon R^2} - 0.248\ {E_{Ry}}^*$$

where $E_{g,bulk}$ is the bulk band gap and ${E_{Ry}}^*$ is the exciton Rydberg energy (i.e. the binding energy of exciton, ${E_{Ry}}^* = \mu_{eh} e^4 / 2\hbar^2 \varepsilon^2$). This equation is based on the Brus's effective mass approximation, which considers an effective mass of electron and hole to be confined in a spherical potential well of the crystallite [57–60].

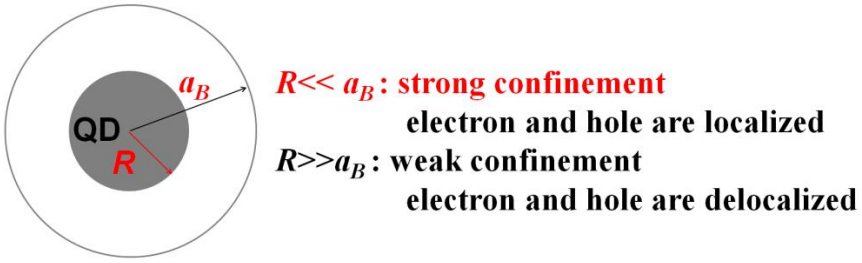

Figure 2.1.1 Exciton Bohr radius and quantum confinement effect.

As the size of particle become smaller (i.e. top-down process), the quantization of continuous conduction or valence band from bulk semiconductor becomes present (i.e. from right to left in ***Figure 2.1.2***). The electronic structure of QD is considered as an intermediate state between single molecules which have the band gap between highest occupied and the lowest unoccupied molecular orbital (HOMO and LUMO) and bulk semiconductors which have continuous energy band [61,62]. Therefore, the energy states in QD are composed of discrete levels like those in an atom. The number of atoms in QD (typically 1,000 to 100,000 atoms) is much smaller than that of bulk material, quantum well, or quantum wire, but larger than an atom, molecule, and cluster [63].

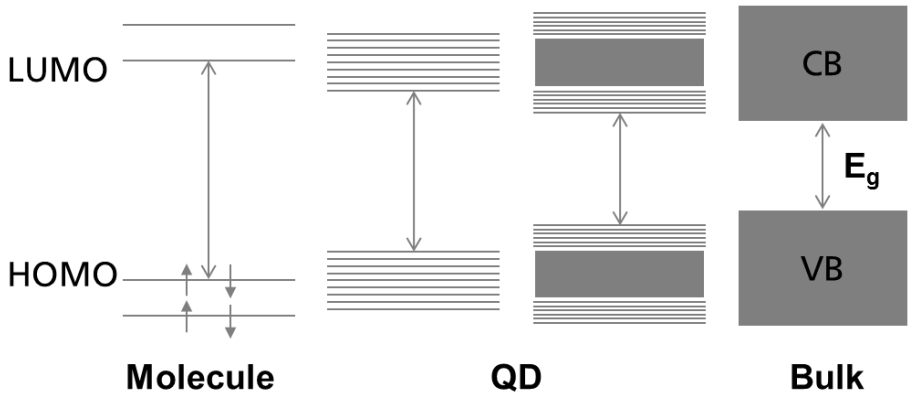

Figure 2.1.2 Schematics of energy band diagram in bulk, QD, and molecule with quantum confinement effect

This quantization process can be explained in reverse direction as well (i.e. bottom-up process from left to right in ***Figure 2.1.2***). When the molecule becomes larger, the number of atomic orbitals which can form molecular orbitals increases and it leads to an increased number of energy states, and the decrease of the energy gap [64]. Therefore, the QD semiconductor which has quantized energy band structure causes different physicochemical properties compared to the bulk such as broad absorption spectrum,

narrow and symmetric photoluminance spectrum, and slow exciton decay rates. The color of QD emission depends on the particle size and chemical composition, which can realize the wide spectrum range from the ultraviolet (UV) to the infrared (IR) wavelength [62].

2.1.2 Synthesis of quantum dots

Nucleation and particle growth are the critical stages for the formation of nanocrystals from homogeneous solution. ***Figure 2.1.3*** shows the LaMer plot for the synthesis of monodispersed nanocrystals [33,65–67]. The nanocrystal synthesis starts from the precursors to monomers, followed by the mutual reaction between the monomers and nanocrystals (Precursors → Monomers ⇌ Nanocrystals). If the concentration of monomer is over the critical threshold point (C^*), nucleation takes place. A minimum critical radius (r_c) of generated nuclei with thermodynamically stable condition is given by:

$$r_c = \frac{2\gamma V_m}{RT \ln S}$$

where γ is the surface free energy per unit area, V_m is the molar volume of the particle, R is the universal gas constant, T is the absolute temperature, and S is the degree of supersaturation ($S = C^*/Cs$). When the nuclei are smaller than the critical radius ($r < r_c$), the nuclei dissolve because of the high surface free energy, however, the nuclei grow in size when $r > r_c$. The monomer concentration decreases fast due to the nucleation process. For the nucleation process, it ends after the monomer concentration becomes lower than C^*. The further growth of the nuclei takes place by use of remaining monomers with the size-dependent process explained as follows [33]. The distribution focusing (i.e. narrow size distribution) can be observed because of smaller particles grow faster than larger particles during this process [45]. The separation of stages B and C (i.e. separation of nucleation and growth) is critical aspects for the obtaining monodispersity of the nanoparticles. Subsequently, the process called Ostwald ripening or Lifshit-Slyozov-Wagner growth leads to a further increase of the particle diameter with time [33]. The smallest particles with the highest surface free energy are partially dissolved, which helps the growth of the mean size of other particles while the number of particles decreases. The particles growth becomes saturated while the monomer concentration is also saturated to the supersaturation point (C_s, saturation concentration). The red curves shown in ***Figure 2.1.3*** explains that a high precursor-to-monomer conversion rate brings a

larger number of particles during the nucleation periods, which leads to smaller final nanoparticles compared to the blue curves. To get the high precursor-to-monomer conversion, the hot-injection method is commonly adopted, while the heating-up methods have relatively lower conversion ratio with even slower synthesis [33].

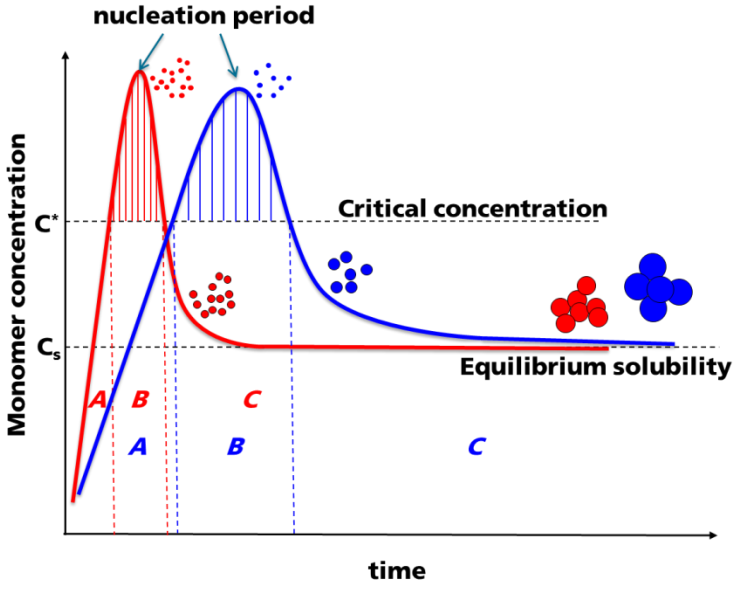

Figure 2.1.3 LaMer plot for the monodisperse nanocrystals. (A) Precursor conversion to the monomer and the monomer concentration increase above the critical concentration C*; (B) nucleation period; and (C) the growth of the particles from solution ($C_s < C < C^*$) [33].

2.1.3 Structure of quantum dots

The properties of nanocrystal strongly depend on the surface condition due to the large surface-to-volume ratio (c.a. 20%) that leads to the high percentage of atoms on the QD surface [63]. While the optical absorption properties of QDs do not strongly depend on the surface condition, the luminescence of QDs is quite relying on the surface properties. The luminescence easily quenches by the non-radiative recombination with the surface defects of QD such as a dangling bond even though the organic ligands capping of QDs, which leads to the low internal QY. An important strategy to enhance the surface condition of QD is the overcoating of the core with larger bandgap shell materials, resulting in a core/shell system with much higher QY and stability (***Figure 2.1.4a***). The higher QY is attributed to not only the reduced surface defects but also the increased confinement effect of electron and hole wave function within core/shell structure (Type I in ***Figure 2.1.4b***). The different type of core/shell structure can be designed for another purpose by choosing different shell materials. Type II structure

shown in ***Figure 2.1.4b*** make the electron localized in the shell, which leads to a smaller effective band gap than that of the core. Therefore, shell growth in Type II structure causes a significant red-shift of the emission peak wavelength compared to that of the core, which is favorable for developing the IR emission of QDs.

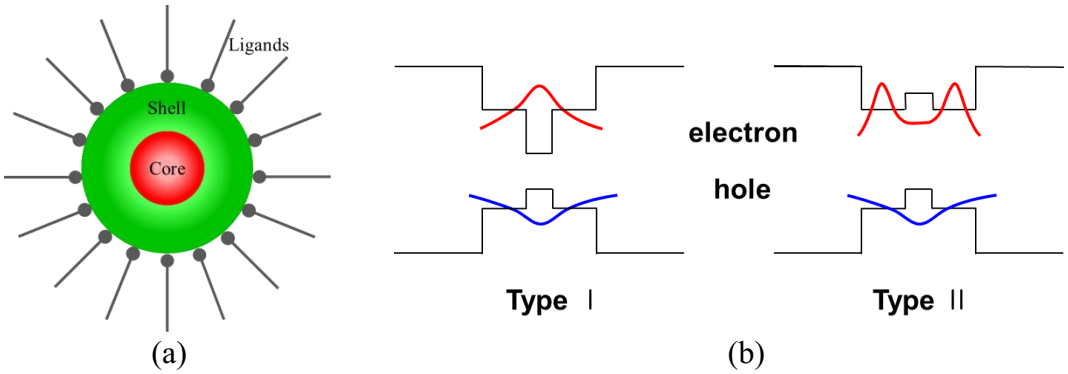

Figure 2.1.4 Schematics of (a) the typical QD structure (core/shell/ligands) and (b) the energy-level alignment in different core/shell type.

The organic ligands on the surface of QD provide not only the surface passivation but also the mono-dispersion of nanoparticle in the polar or non-polar solvent. However, the insulating nature of organic ligands commonly used in QD synthesis results in very weak interparticle coupling (i.e. low carrier injection efficiency in QD film). Therefore, there are many types of researches on the ligand exchange with short-chain length or even conductive ligands [68–72]. Moreover, there is a broad range of feasibility to utilize the functional group of organic ligands, and make the nanocomposite in the polymer matrix for both electroluminescent (EL) [73,74] and photoluminescent (PL) [7,75] device applications.

2.2 QLED mechanisms

2.2.1 External quantum efficiency (EQE)

In general, the EQE of QLEDs is defined as the ratio between the number of photons emitted by the QLED into free space and the number of injected charge carriers (i.e. EQE= $N_{\text{emitted photons}}$ / $N_{\text{injected electrons}}$). For a better physical understanding of the device mechanisms, EQE can be described with several parameters;

$$\eta_{eqe} = \eta_{int} \cdot \eta_{oc} = \gamma \cdot \varphi_{QY} \cdot \chi \cdot \eta_{oc}$$

where η_{eqe} is the external quaum efficiency, η_{int} is the internal quaum efficiency, η_{oc} is the light out-coupling efficiency, γ is the charge carrier balance factor which includes the carrier injection and transport efficiceny, φ_{QY} is the internal luminescent QY and χ is the

spin-allowed optical transition rate [22]. χ is assumed to be 100% for QDs due to the heavy atom mediated spin-orbit coupling in the heavy metal center [76], or the efficient crossing of excitons from 'dark' states to higher energy 'bright' states [77]. η_{oc} is typically found to be c.a. 20% for planar devices [78]. Therefore, the important parameters to enhance the device efficiency are the charge carrier balance factor (γ) and the internal luminescent QY (φ_{QY}). Especially, φ_{QY} is described by following equation;

$$\varphi_{\mathrm{QY}} = \frac{k_r}{(k_{nr} + k_r)}$$

where k_r is the radiative recombination rate which depends on the applied electric field, and k_{nr} ($k_{nr} = k_t + k_a$) is the non-radiative recombination rate which depends on the charging of QDs [46]. The electronic trap states which increase the trap-assisted recombination rate (k_t), and the free-charge carriers which increase the Auger recombination quenching rate (k_a) are the two major problems for the non-radiative recombination rate. Since k_a is not affected by the electric field but strongly depending on the charge carrier balance, and k_r can be reduced under the high electric, k_a and k_r can be described as follows;

$$\gamma \propto \frac{1}{k_a} \quad , \quad \vec{E} \propto \frac{1}{k_r}$$

where $\vec{\boldsymbol{E}}$ is the electric field.

As it is mentioned in the introduction, to obtain high φ_{QY}, a multilayered alloyed QD structure would be favorable for the particle design, which provides the smoothed confinement of the core, the confined electron and hole wave functions in the core, and the passivated QD by the multishell structure [46]. To increase the carrier balance factor (γ), the appropriate CTL with low injection barrier to QD should be carefully chosen, considering carrier mobility and material stability. Moreover, the ligand design with shorter chain length or conductive materials on the QD surface could increase the carrier balance.

2.2.2 Operation principle of QLEDs

The basic operation principle of QLEDs is like that of OLEDs. ***Figure 2.2.1*** shows typical QLED energy band diagram. The QD emitter is embedded between anode and cathode for hole and electron injection into the valence band maximum (VBM) and conduction band minimum (CBM) of QDs, respectively. In order to facilitate the charge injection from both electrodes into the QDs via large energy offsets, various organic or inorganic charge transport materials should be applied to the QLEDs considering the mobility, band alignment and electron and hole block property of the materials.

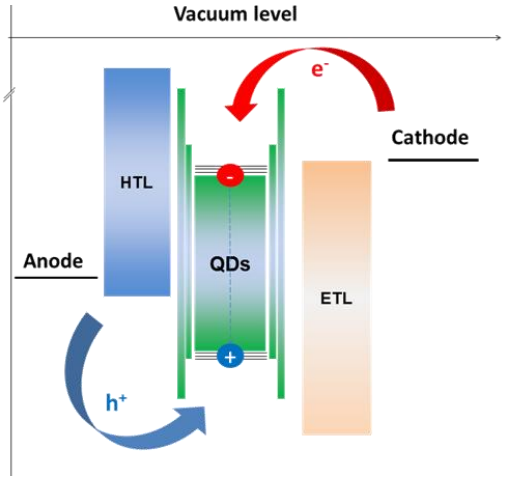

Figure 2.2.1 Energy band diagram of a typical conventional QLED

The main operation mechanisms, considering the processes contributing exciton generation, and the processes quenching luminescence, are summarized in ***Figure 2.2.2*** [22,79–81]. The excitons that recombine to emit a photon can be directly formed from the direct electron and hole injection by the adjacent CTL as shown in ***Figure 2.2.2a***. Förster resonance energy transfer (FRET) shown in ***Figure 2.2.2b*** is also a possible mechanism to generate exciton in the QDs. The generated exciton energy on the luminescent species such as emissive organic or inorganic semiconductor is non-radiatively transferred to the QD by the dipole-dipole coupling. The FRET occurs when the emission spectrum of the donor (i.e. organic) overlaps with the excitation spectrum of the acceptor (i.e. QDs), and the donor and acceptor are in close proximity within Förster radius [82].

The FRET process is dominant on the device with organic CTL. However, the exciton losses by the inefficient donor or incomplete energy transfer accompanying the parasitic emission from the CTL will limit the device efficiency [83]. Therefore, the direct charge injection developed through the precise charge balance control with the low carrier

injection barrier could have the more potential to develop the high efficient QLED device. However, the distinction between the direct charge injection and FRET in the QLED operation remains unclear.

There are also the processes which limit the QLED performances. ***Figure 2.2.2c*** shows the non-radiative Auger recombination quenching process attributed to the charge carrier unbalance in QLEDs [53]. This process is originated from the charged excitons, or the negative (***Figure 2.2.2c***) and positive triones (i.e. X^- and X^+, respectively). When the charged exciton recombines, the recombination energy transfers to the other charged electrons or holes in the QD film and subsequently relaxes to the ground state through the interactions with the phonons. This process is extremely efficient due to the relaxation of linear momentum conservation in the QDs, which is originated from the discrete energy levels of the nanoparticles [84]. Since this non-radiative Auger process is much faster (c.a. 10 - 100 ps) than the radiative recombination process (c.a. 5 ns) [82], the charge carrier balance should be controlled delicately for the efficient and stable device.

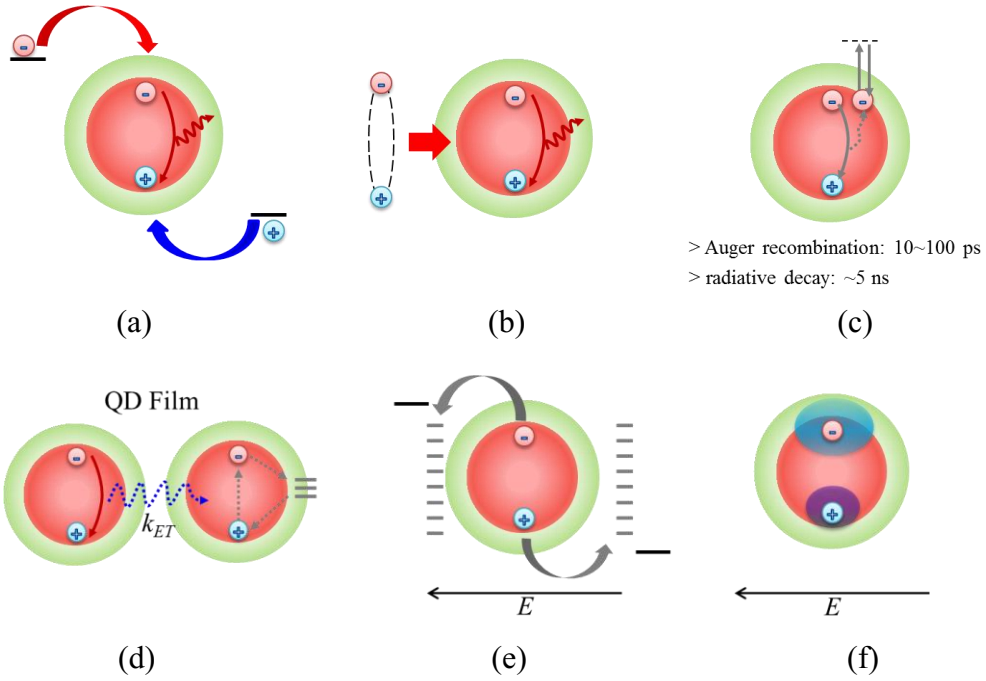

Figure 2.2.2 Schematic diagram illustrates the QLED mechanisms. Contributing processes to the QD EL: (a) charge injection, (b) energy transfer. Quenching processes to the QD EL: (c) Auger recombination exciton quenching, (d) dot-to-dot energy transfer and field induced (e) exciton dissociation and (f) exciton polarization.

For the closely packed QDs in the thin film, the exciton recombination energy (k_{ET}) transfers to the adjacent QDs due to the overlap of absorption and PL spectra of QDs. This energy transfer time is c.a. 100 ps which are faster than the radiative lifetime (c.a. 20 ns). Therefore, it can reduce PL QY of QD film compared to that of the solution by

the transfer energy loss (***Figure 2.2.2d***) [81]. Moreover, this process causes the red-shift of PL peak wavelength of the QD film compared to that of the solution. ***Figure 2.2.2e,f*** show the electric field-induced exciton dissociation and exciton polarization process. The excitons in the QD are dissociated to the surface defects states of QD or to both electrodes of the device by the high electric field during the device operation [85]. Moreover, the strong electric field also delocalizes the electron and hole wave function (i.e. reduced overlap of wave functions by the polarized exciton) [80]. These two processes finally decrease the radiative recombination rate as well. In addition, the efficiency roll-off of QLEDs, the severe problem of QLEDs, is known to the results of the field-induced quenching during the device operation [80]. However, the device charging, accompanying the Auger recombination quenching, during the high voltage operating condition is another origin of the efficiency roll-off.

Chapter 3

3 Experimental methods

3.1 Device layout

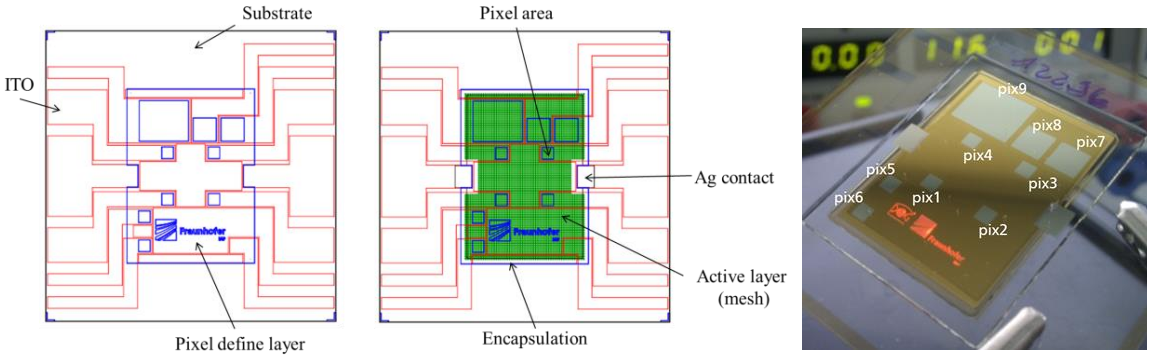

(a) (b)

Figure 3.1.1 (a) Diagrams of the device layout (top view) and (b) a photograph of fabricated QLEDs with pixel number (pix 1–6: 2 mm × 2 mm, pix 7–8: 4 mm × 4 mm and pix 9: 7 mm × 8.5 mm).

The device layout design is shown in ***Figure 3.1.1***. A square glass substrate of 5 cm × 5 cm is used with a patterned transparent ITO and passivation layer (i.e. photoresist) which is used to define the pixel area. The CTL and QD layer were deposited by the solution process (i.e. spin-coating) on the ITO substrate followed by the patterning of the materials to reveal the top electrode contact area. The small molecule CTLs were deposited by thermal evaporation process with a metal shadow mask. The top metal electrodes were also deposited as a common electrode with another metal shadow mask. After the fabrication process, the active area of the device was encapsulated with a cover glass using UV-curable sealant in a N_2 glove box

.

3.2 Device fabrication

A Standard fabrication process of the conventional device

The conventional devices were fabricated with the patterned ITO on the glass substrates. First, the ITO substrates were cleaned by sequential ultra-sonication with acetone, methanol, and isopropanol and dried in an oven, followed by the oxygen plasma treatment. Then, the substrates were transferred into a N_2 glove box for following steps. Poly(3,4-ethylenedioxythiophene)-poly(styrenesulfonate) (PEDOT:PSS, Heraeus CH8000) was spin-coated on the ITO substrates at a spin rate of 3000 rpm for 30 seconds and dried on a hot plate at 180 °C for 30 minutes as hole injection layer (HIL). Then, poly-(N,N'-bis(4-butylphenyl)-N,N'-bis(phenyl)benzidine) (poly-TPD, Solaris Chem Inc. SOL2420H) dissolved in chlorobenzene (3 mg/mL) was also spin-coated at a spin rate of 4000 rpm for 60 sec on the PEDOT:PSS layer and dried on the hot plate at 130 °C for 30 seconds as HTL. In order to deposit the emission layer, the colloidal QDs were spin-coated on the poly-TPD layer at a spin rate of 3000 rpm for 20 seconds. After the solution processes, 2,2′,2"-(1,3,5-benzinetriyl)-tris(1-phenyl-1-H-benzimidazole) (TPBi, Lumtec LT-E302, 65 nm) and calcium/silver (Ca/Ag, Balzers Lot # 93-4295 / Umicore, Lot # C000291487, 0.5 nm/150 nm) were deposited on the QD layer by the thermal evaporation as ETL and metallic cathode, respectively. This is shown in ***Figure 3.2.1***.

A standard fabrication process of the inverted device

The completed inverted QLEDs consisted of an ITO layer as cathode, ZnO nanoparticles as ETL, InP/ZnSe/ZnS multishell QDs as light emission layer, 4,4',4"-Tris(carbazol-9-yl)triphenylamine (TCTA, Lumtec LT-E207) or 1,1-bis((di-4-tolylamino)phenyl)cyclohexane (TAPC, Lumtec LT-N137) as the HTL, molybdenum oxide (MoO_3, Aldrich, 99.99%) as HIL, and Ag as metallic anode (ITO/Al:ZnO/PEI/QDs/TCTA/MoO_3/Ag). First, the ZnO NPs were spin-coated on the cleaned ITO substrates at 2000 rpm for 20 seconds, followed by drying at 180 °C for 30 minutes. Then, the dispersed QDs in nonane with a specific concentration (i.e. 3, 5 and 10 mg/mL) were spin-coated on the ZnO layer at 3000 rpm for 20 seconds without the further thermal annealing. After the solution processes which were conducted in the N_2 atmosphere, TCTA (40 nm) and MoO_3/Ag (5 nm/150 nm) were deposited by the thermal

evaporation on the QD layer in a high vacuum chamber, respectively. This is shown in ***Figure 3.2.1***.

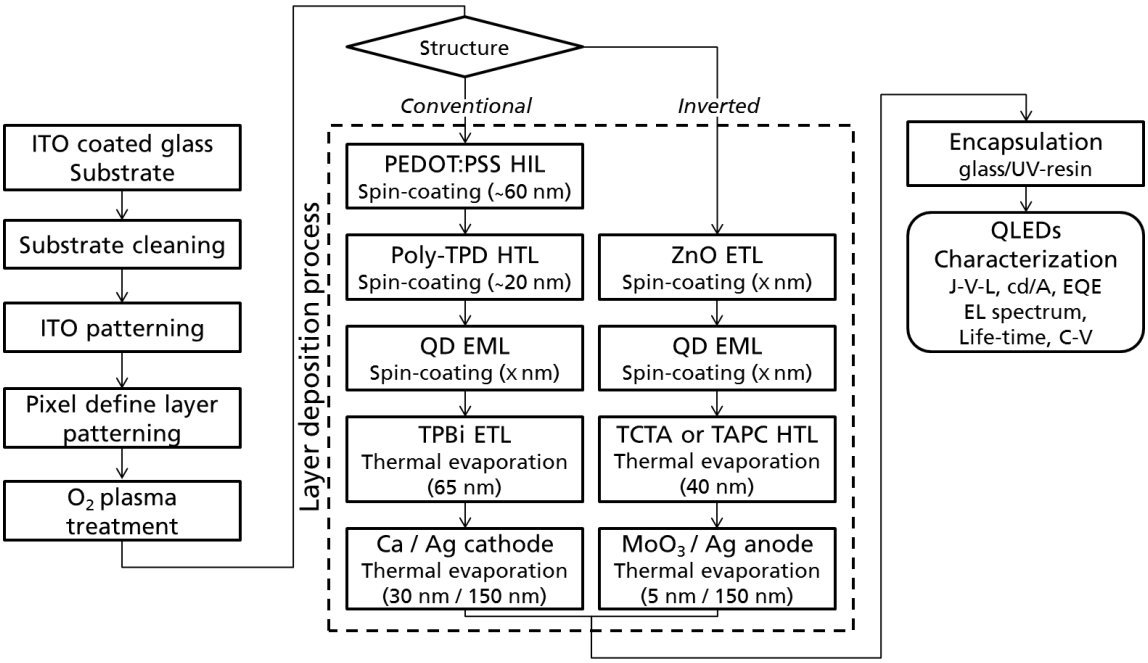

Figure 3.2.1 The flowchart for the QLED fabrication process. (Detailed device structure and performance investigated in this dissertation are summarized in ***Appendix B.2***. Device numbers are written in the figure caption over the manuscript)

3.3 Characterization

3.3.1 Material and thin film characterization

Photoluminescence (PL) spectra and **QY** were measured by a Hamamatsu C9920-02 (wavelength measurement rage: 200 nm to 950 nm, resolution: < 2 nm / PL QY precision: ±5%) with an excitation wavelength of 350 nm (Xenon light source).

Ultraviolet–visible–near infrared (UV–vis–NIR) absorption spectroscopy data were acquired with a PerkinElmer Lambda 19 spectrometer (measurement range: 220 nm to 2000 nm, accuracy: ±0.2 nm) with a scan step of 1 nm between 300 and 800 nm.

UV-Photoelectron spectroscopy (PESA, Riken Keiki AC-2, excitation energy: 3.4 – 6.2 eV, accuracy: ±0.02 eV) to measure ionization energy (IE), which corresponds to the valence band maximum (VBM), were done with QD thin films deposited on a glass

substrate. UV intensity was 300 nW and energy step was 0.1 eV. Measurements were done in air.

Thermogravimetric analysis (TGA) of the QD and ZnO NPs was carried out by a Netzsch TG 209 F1 Iris thermo-microbalance (temperature range: 20 to 1000°C, resolution: 0.1 μg) at a heating rate of 10 K/min under N_2 flow in aluminum oxide crucibles.

Transmission electron microscopy (TEM) images were acquired on a Philips CM 200 instrument with a LaB6 cathode operated at 200 kV. TEM samples were prepared by drop-casting the solution on a carbon-coated Cu grid. The diameter of the QD was determined from the TEM images using the software ImageJ.

Atomic force microscopy (AFM) was done on a Nanosurf Easyscan-2 (cantilever ACLA-20, n-type silicon, spring constant 36–90 N/m, scan size of 5 × 5 μm). Roughness values in the article are averages obtained from three randomly selected scan regions per sample.

Contact profilometry to determine the film thicknesses was done by a Veeco Dektak 150 (vertical resolution of 1 Å, a stylus radius of 12.5 μm).

Bandgap estimation through Tauc plot

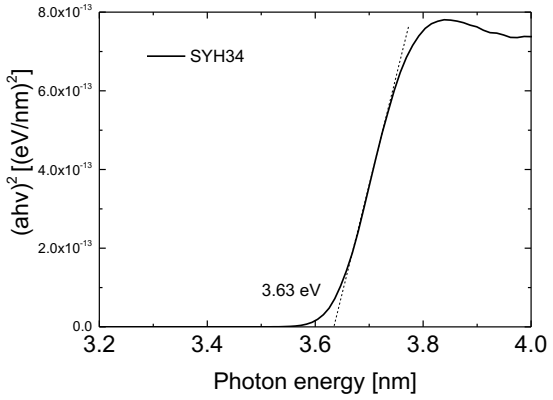

Figure 3.3.1 Tauc plot: a plot of $(\alpha hv)^2$ as a function of photon energy (hv).

According to Tauc, the dependence of the absorption coefficient α on the photon energy hv for near-edge optical absorption in semiconductors takes from the following expression [86,87],

$$(\alpha hv)^{1/m} = k(hv - E_g)$$

where E_g is the optical band gap, k is the constant, and m is the number which relates the mechanism of the transmission process (m = 1/2 or 3/2 for direct allowed or direct forbidden, while m = 2 or 3 for indirect allowed or indirect forbidden transitions, respectively). Since ZnO nanoparticles and InP-based QDs have the directly allowed transition, $(\alpha hv)^2$ was plotted versus hv. The direct band gap of the nanoparticles was obtained by extrapolating the linear part to the zero of the ordinate.

3.3.2 Device characterization

Current density-voltage-luminance (J-V-L) characteristic

Source meter: Keithley SMU 236**,** voltage source range: ±11.000 V, step size: 1 mV, accuracy: ± (0.033% + 2.4 mV) / current measure resolution: 100 nA, accuracy: ±(0.038 % + 600 nA)

Spectroradiometer: Konica-Minolta CS-2000, wavelength range: 380 nm to 780 nm, resolution: 0.9 nm/pixel, precision: ±0.3 nm / luminance range: 0.075 to 125000 cd/m^2 (measuring angle: 0.2°), accuracy: ±2% / chromaticity accuracy (over 1.25 cd/m^2): x = ±0.0015 y = ±0.001)

Current density-voltage-luminance (J-V-L) characteristic measured with an experimental setup consisting of a source meter and spectroradiometer at ambient condition. The spectroradiometer was also used to measure EL spectrum and xy chromaticity coordinate.

Current density-voltage characteristics are the most important part of QLED characterization in terms of turn-on voltage, device resistance, and different conduction mechanisms. The log-log scale J-V curves visualize a power law dependence on current and voltage [79];

$$J \sim V^n \rightarrow \log J \sim n \log V,$$

where n is the slope of double-logarithmic J-V curves which indicates the characteristic of a specific type of conduction. This slope n can be used to describe the different distribution of trap levels as well. As shown in ***Figure 3.3.2***, the J-V can be separated into four regions: an ohmic conduction region A, a space-charge-limited current (SCLC) region B, a trap-controlled (or trap-filling) conduction region C, and a trap-free SCLC region D [88]. In the ohmic conduction, the current is proportional to the applied voltage ($J \sim V$) because thermally generated free carrier density has dominant effect on this region [89], which is described by

$$J = \frac{q\mu n_T V}{d},$$

where q is the electronic charge, μ is the carrier mobility, n_T is the thermally generated free charge density and d is the layer thickness. This ohmic conduction region also suggests the leakage current range of the device. With increasing voltage, the SCLC regime arises because an equilibrium charge concentration becomes trivial compared to an injected charge concentration (i.e. injection level is below the trap level) [90]. The current in the SCLC region B and region D is proportional to the square of applied voltage ($J \sim V^2$), which is described by

$$J = \frac{9\mu\varepsilon_r\varepsilon_0 V^2}{8d^3},$$

where ε_r is the relative dielectric constant and ε_0 is the permittivity free space.

In the region C with further bias increase, the slope becomes extremely steep because of the filling of trap levels. When this trapped energy levels are exponentially distributed in the band gap, the density of traps per unit energy is given by [91],

$$N_t(E) = \left(\frac{N_t}{kT_t}\right) exp\left(\frac{E - E_c}{kT_t}\right),$$

where N_t is the total rap density, k is Boltzmann's constant, and T_t is the characteristic trap temperature defining the exponentially distributed trap energy $E_t = kT_t$. Therefore, under the trap-controlled SCLC condition, the current increases with a finite slope ($J \sim V^n, n > 2$), which is described by

$$J = N_c\mu q^{(1-n)}\left[\frac{\varepsilon_r\varepsilon_0 n}{N_t(n+1)}\right]^n\left[\frac{2n+1}{n+1}\right]^{(n+1)}\left[\frac{V^{n+1}}{d^{(2n+1)}}\right],$$

where $n = T/T_t$ (commonly $T_t > T$), T is the absolute temperature, and N_c is the effective density of states in the transport level. Here, a low slope usually indicates the gradual distribution of traps or shallow level of traps, while a high slope indicates an abrupt distribution or deep level of traps [92–96].

In the region D, after the trap levels are filled, the trap-free SCLC occurs ($J \sim V^2$). However, region D also shows a pseudo-SCLC ($J \sim V^n, n \geq 2$) if there still remains unfilled traps or if the device has deep trap levels [95,96].

The above models are based on the Schottky diode structure with single-carrier (i.e. electron) device. In the Schottky diode structure with an ultrathin layer thickness, drift-controlled transport is dominant without a diffusion mechanism. Therefore, the SCLC

model governed by only a drift mechanism provides a useful platform for the extracting parameters such as the carrier concentration, drift mobility, and trap density [97].

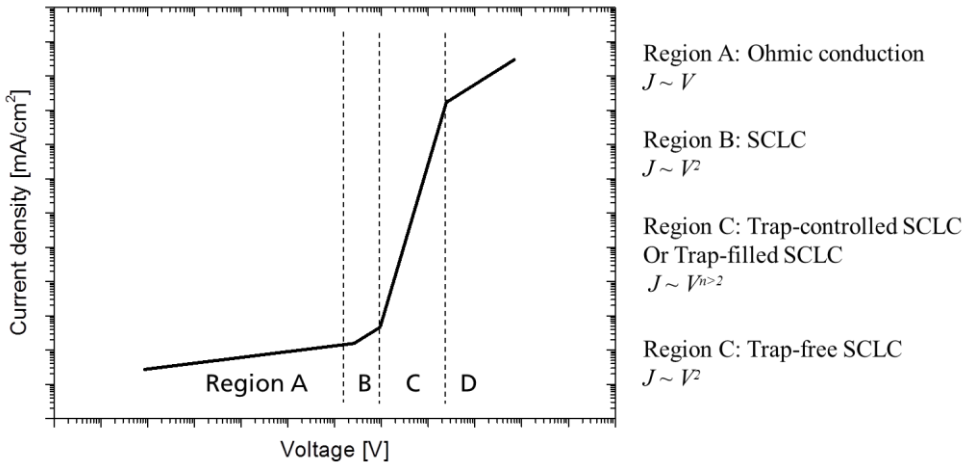

Figure 3.3.2 Typical double-logarithmic J-V curves with the different conduction regions [90].

External quantum efficiency (EQE) characteristic

The EQE of QLEDs measured with an integrating sphere system of Hamamatsu C9920-02 and also calculated with the data obtained from J-V-L and the EL spectrum measurement via the following steps based on the literature [98]. The EQE is the ratio between the number of photons emitted externally from QLED (P_{ext}) and the number of injected electrons (n_e), which can be written as

$$EQE = \frac{P_{ext}}{n_e}, \qquad n_e = \frac{J \times A}{q},$$

$$P_{ext} = \int_{380}^{780} \frac{\pi \times L(\lambda) \times \lambda}{683 \times \bar{y}(\lambda) \times h \times c} d\lambda,$$

where $L(\lambda)$ is the luminous intensity (candela, cd) of the device, $\bar{y}(\lambda)$ is the CIE standard photopic efficiency function (i.e. the luminosity function shown in ***Figure 3.3.3a***), h is Plank's constant, c is speed of light, A is device area, J is measured current density, q is elementary charge, and λ is wavelength.

The total luminous intensity (L_t) of the device can be given as

$$L_t\,(cd) = \int_{380}^{780} L(\lambda)\, d\lambda = \beta \int_{380}^{780} \bar{y}(\lambda) \times I(\lambda)\, d\lambda,$$

where β is a constant, $I(\lambda)$ is the normalized EL spectrum of device. L_t and $I(\lambda)$ can be obtained expermimentally using a Spectroradiometer (i.e. CS-2000). Therefore, β can be calculated. Now P_{ext} can be written again with following equation;

$$P_{ext} = \pi \times \beta \int_{380}^{780} \frac{I(\lambda) \times \lambda}{683 \times h \times c} d\lambda.$$

The EQE calculated with the explained equation is well matched with the measured value from the integrating sphere system (i.e. Hamamatsu C9920-02), shown in ***Figure 3.3.3b***.

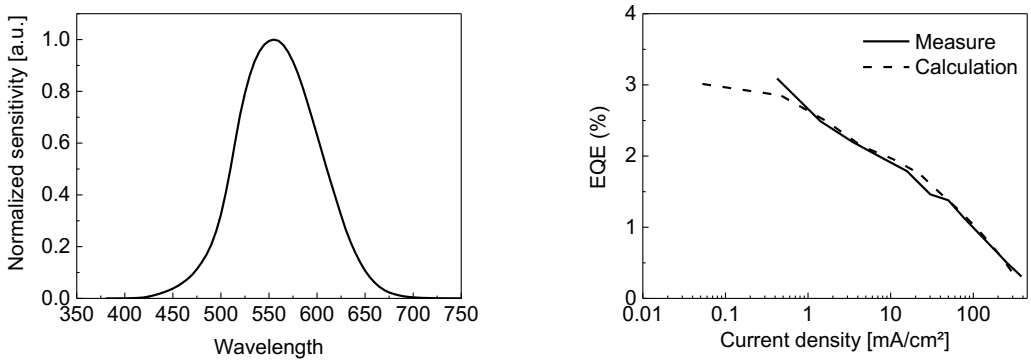

(a) (b)

Figure 3.3.3 (a) CIE 1931 standard luminosity function $\bar{y}(\lambda)$ and (b) compared EQE data between calculated and measured results.

Besides EQE, current efficiency (CE, cd/A) is also a quite important and useful parameter for the device characterization because it contains the sensitivity of a human eye to a specific wavelength. ***Figure 3.3.3a*** shows the human eye sensitivity curve spectrum which is known as standard luminosity function $\bar{y}(\lambda)$ [99].

The current efficiency in cd/A is simply calculated by

$$CE\ (cd/A) = \frac{Luminance\ (cd/m^2)}{Current\ density\ J\ (mA/cm^2)}$$

The power efficiency (PE or luminous efficiency) is the ratio of the lumen output to the input electrical power described by the following equation,

$$PE\ (lm/W) = \frac{luminous\ flux\ (lm)}{electrical\ input\ power\ (W)} = \frac{\pi \times cd}{IV} = \frac{\pi \times CE}{V}$$

where V is the applied voltage and J is the current density (mA/cm^2). Lumen and candela are related by *1 cd = 1 lm/sr*, therefore for a Lambertian source emitting into the half plane, *1 lm* = $\pi \times$ (*1 cd*) [100].

The EQE provides a more physical meaning of how efficiently a device transforms the injected charges into the photons regardless of the human eye sensitivity, while the current efficiency (cd/A) provides device efficiency depending on the color (i.e. spectrum). Accordingly, the current efficiency is a more important parameter for material evaluation on the development of QLED. Moreover, power efficiency is more considered

for developing display system considering the power consumption of the QLED at a certain brightness.

Practical device characteristic curves

Figure 3.3.4 shows the practical device characteristic curves and their correlations. In the figure, quadrant I shows J-V curve, quadrant II shows cd/A-J curve, quadrant III shows cd/A-cd/$m^{2,}$ and quadrant III shows cd/m^2 -V curve. Quadrant I, II and IV show the most common way to show the device characteristics, which provides electrical and optical properties of the device. However, quadrant III also effectively shows the important device performance parameters concerning maximum luminance and current efficiency. Moreover, it also presents the efficiency roll-off behavior as the increase in luminance (i.e. increase of driving voltage). An example of the device characteristic for the inverted device is shown in ***Figure 3.3.4***, and the result shows the efficiency roll-off beginning at 4 V, 27 mA/cm^2, and 1100 cd/m^2.

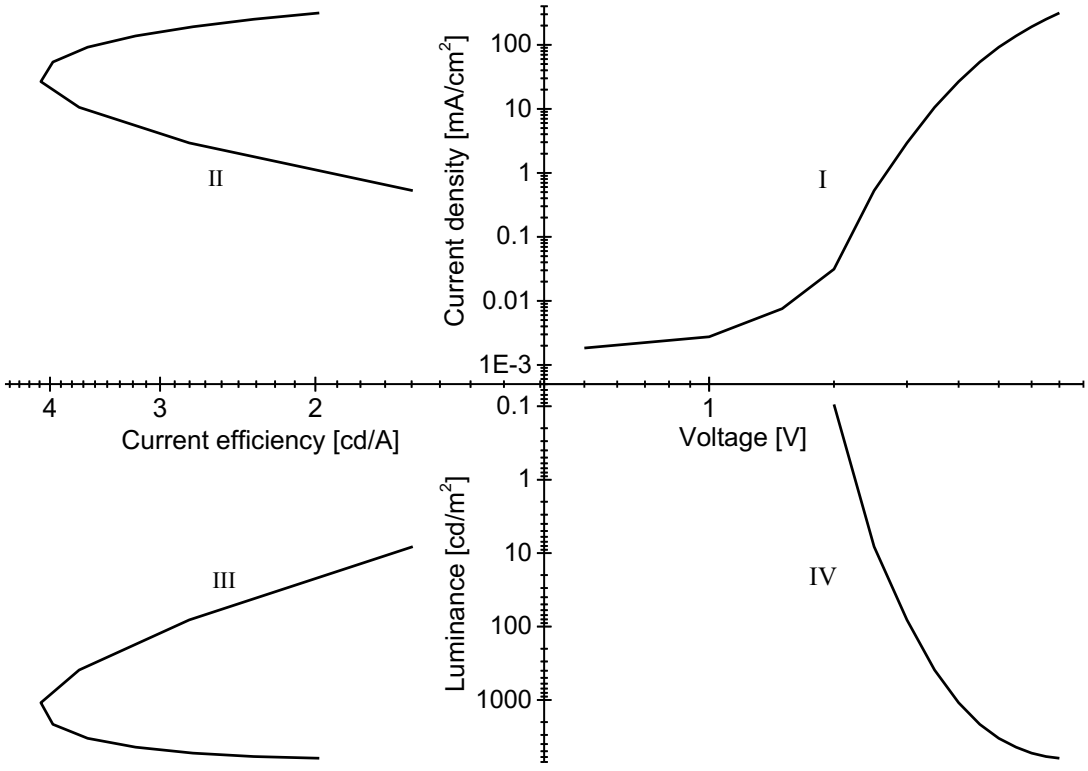

Figure 3.3.4 Correlation between the device characteristic curves. *(YH362, ITO/ZnO/QD/TCTA/MoO_3/Ag)*

Measurement and error tolerance

In order to shows more reliable experiments results, multiple measurements are necessary. However, the QLEDs developed in this work have a degradation issue over time. The initial luminance decreases rapidly within few seconds during constant current driving by device charging or degradation, shown in ***Figure 3.3.5a***. This instability of device provokes huge performance difference within the sequential device measurements in both conventional and inverted devices, shown in ***Figure 3.3.5b,c***. Therefore, providing the average and standard deviation of repeated measurements was not suitable. Instead, the measurement results in this dissertation were compared within the range of device tolerance and equipment resolution.

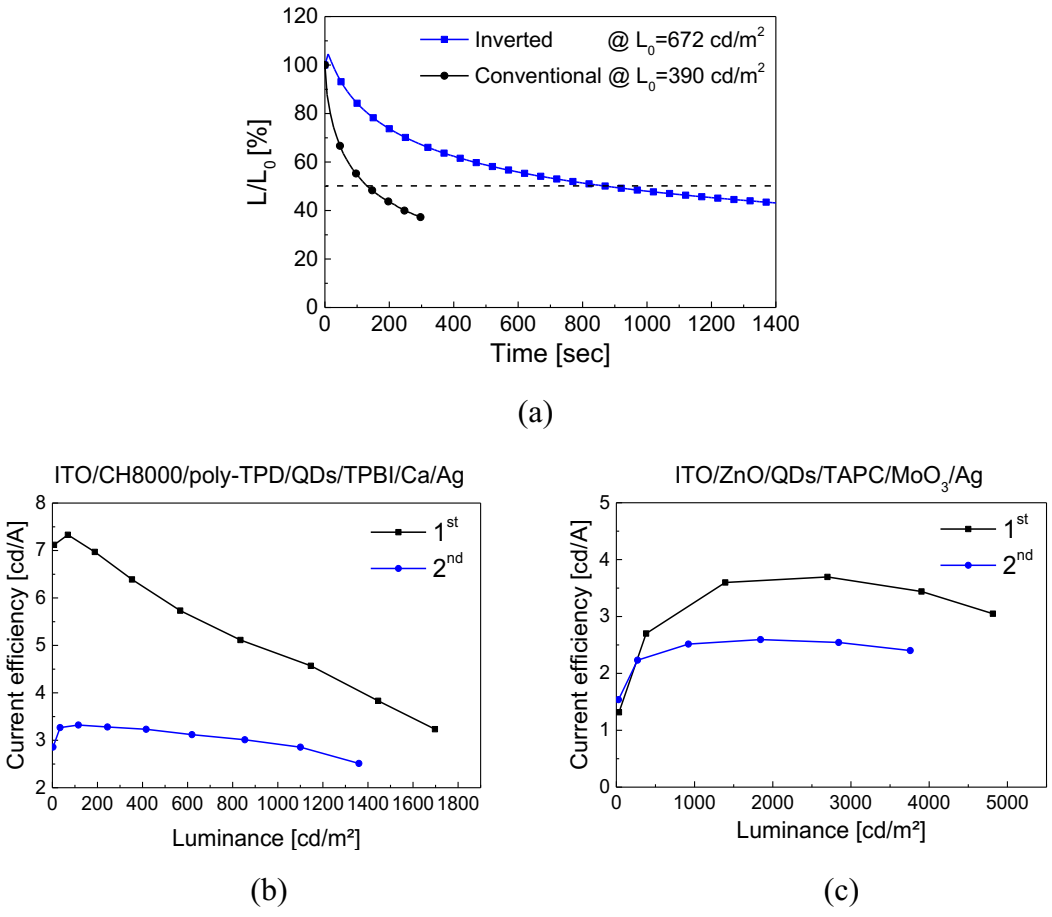

Figure 3.3.5 (a) Luminance decay curves under continuous device operation. The variation of device performance according to several measurement sequences in both (b) conventional and (c) inverted devices.

Figure 3.3.6 shows the batch to batch and pixel variation of current efficiency and luminance with the error bars which reflect the standard deviations (SD) of 8 pixels from two different batches. The measured current efficiency and luminance show relative SD (RSD) of 5.9% and 9.6% at the maximum current efficiency and luminance, respectively. In this dissertation, most of the parameter variation was investigated within the same batch. However, the RSD given here were considered for the comparison of parameters in the different batches. The performance curves in this dissertation were chosen for a specific pixel after the considering all the tolerance explained here.

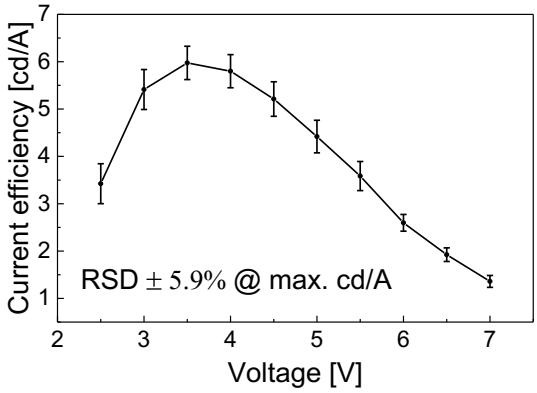

(a)

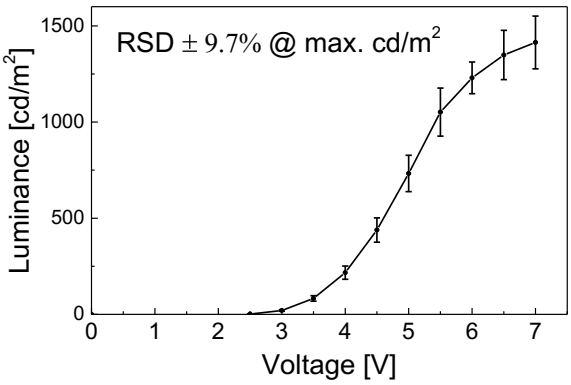

(b)

Figure 3.3.6 The batch to batch and pixel variation of (s) current efficiency and (b) luminance measurement result. The error bars reflect the average and SD of 8 pixels from two devices (4 pixels for each inverted devices). The RSD of one device with 4 pixels is 5.8% and 8.9% for cd/A and cd/m^2, respectively) *(YH193, YH200)*

Chapter 4

4 InP-based QD design for efficient QLEDs

Colloidal QDs have a high feasibility to develop high performance LEDs by the tuning of QD structure including the ligands and core/shell structure. In principle, high and stable QY is the most important parameter, but the high efficiency of QLED is not only promised by that. The origin of QD structure could limit the developing highly efficient device. For example, insulating ligands surrounding the surface of the QDs will disturb the charge injection and transport. In addition, weak or strong confinement of exciton in the quantum-well structure of core/shell also could decrease the efficiency by the luminance quenching under the charge accumulation condition or electric field induced condition, respectively (see the ***Chapter 2.2***). Therefore, optimizing the QD material for the QLEDs is not a superficial work. From the learning of enormous research on the Cd-based QLEDs, there are some strategies developing QD emitter for high-efficiency QLEDs [46]. An alloyed core provides a smooth condiment potential by suppressing the Auger recombination quenching. A multi-shell structure confines the excitons in the core against the polarization of electron and hole wave functions in the applied electric field. Moreover, the optimized ligand length considering the carrier mobility and exciton diffusion length [68,69,72] could provide effect charge injection and radiative exciton recombination in the QD film. Our InP/ZnSe/ZnS QD is designed with a multilayered alloyed structure to realize the above strategies. In this chapter, the most promising InP/ZnSe/ZnS QD design effects on the performance of conventional QLEDs (i.e. ITO/PEDOT:PSS/poly-TPD/QDs/TPBi/CaAg) were introduced.

4.1 Shell thickness of QD structure

The effects of ZnS outer shell thickness

This section is based on the modification of a publication in Optical Materials Express first-authored by the candidate [39].

The thicker ZnS shell of multishell QDs was adopted to improve the device efficiency, and the optoelectronic characteristics of QLEDs were investigated. Moreover, a severe QD charging problem was found in EL stability measurement. However, it was also suppressed by the QD system of thicker zinc sulfide (ZnS) shell to some extent. InP/ZnSe/ZnS QDs which have different ZnS shell thickness were synthesized via the heating-up method (see details in ***Appendix A.1***). The heating-up synthesis is more simple and reproducible compared to the hot-injection method because the manual injection process can be avoided. Through the synthesis, PL QY of InP/ZnSe/ZnS QDs can be significantly improved compared to the conventional InP/ZnS single shell QDs due to the better match of lattice constants between InP and ZnSe [47]. Two different QD samples, which have identical InP core but different ZnS outer shell thickness (referred as InP/ZnSe/ZnS-t1 for thinner shell and InP/ZnSe/ZnS-t2 for thicker shell), were used for the fabrication of QLEDs. They were obtained by several following shell coating steps in the same InP core batch. Since PL characteristics of QDs are determined by core structure, both QDs have almost same PL peak wavelength (539-540 nm) and FWHM (52-54 nm) as shown in ***Figure 4.1.1a***, as well as 40 % of PL QY. There is only a slight change in PL wavelength with ZnS growth, which indicates that core properties are not affected by the shell growth. A substantial red-shift from 523 to 535 nm is observed only after depositing the ZnSe shell. It has been reported in the literature that increasing ZnSe shell thickness results in increasing red-shift because the energy level confinement of the ZnSe shell is weaker than that of the ZnS shell [47]. Therefore, here only a thin ZnSe shell was used to obtain the desired smooth interface between core and shell, and then increase the outer ZnS shell thickness to achieve a strong exciton confinement. The TGA data reveals the amount of inorganic content in the QDs (i.e. core and shells) by removing the ligands through heating to 600 °C. The TGA curves show the slightly increased residual mass with the thicker shell, which is an indication of the particle growth with shell coating, as shown in ***Figure 4.1.1b***. Further, the high inorganic content proves the exceptional purity of the samples regarding excess ligands or reaction

side products, which is essential for efficient device operation. Moreover, inset of ***Figure 4.1.1a*** which shows that InP/ZnSe/ZnS-t2 has more absorption from shell than InP/ZnSe/ZnS-t1 under the range of 350 nm which matches the ZnS band gap of 3.54 eV. Therefore, this is additional agreement of increased shell thickness [101]. Based on the TEM images in ***Figure 4.1.1c,d***, the particle size is estimated to 2.5±0.3 nm and 2.9±0.3 nm for the thinner shell and thicker shell QDs, respectively, which corresponds to a difference of approximately one monolayer of ZnS between the two types of QDs.

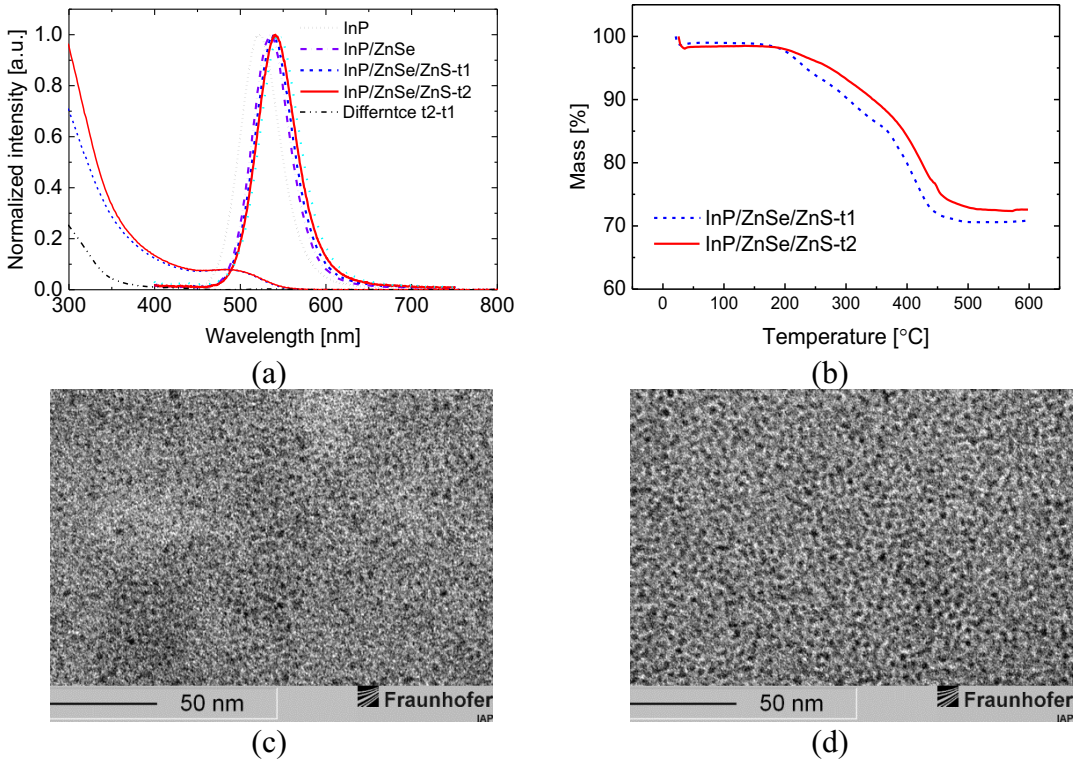

Figure 4.1.1 (a) Normalized PL spectra (inset: absorption spectra and difference of intensity caused by thicker ZnS shell) and (b) TGA curves of synthesized colloidal InP/ZnSe/ZnS QDs with different core/shell structures. TEM images of (c) InP/ZnSe/ZnS-t1 and (d) InP/ZnSe/ZnS-t2. *(YHK 10, YHK 11)*

Figure 4.1.2 presents the schematic of the InP-based QLEDs and the corresponding energy diagram. The QLED structure was sophisticatedly designed to achieve efficient carrier injection and balance in the QD layer and to minimize parasitic luminescence of neighboring organic layers. The choice of organic CTL surrounding the QD emitting layer is critical for the efficient QLEDs considering energy band alignment and material properties. The device structure presented in this study consists of organic materials having high mobility, the low potential barrier for carrier injection into the QDs, and spectral overlap between the emission of organic materials and QD absorption, based on

the previous work [38]. PEDOT:PSS is used as the HIL on ITO anode mainly to increase the anode work function and to compensate the surface roughness of the anode to obtain a stable organic/inorganic interface. Poly-TPD is used as the HTL to reduce the energy barrier of 0.3 eV between the work function of PEDOT:PSS and VBM of the InP/ZnSe/ZnS QDs. The thin film of poly-TPD is chemically and physically stable to nonpolar alkane solvents such as hexane and nonane so that the QDs can simply be spin-coated on top of the poly-TPD layer from these solvents. TPBi is adopted as the ETL because it exhibits a suitable LUMO energy and works as well as a good hole blocking layer. As shown in the energy band diagram of ***Figure 4.1.2b***, electrons are easily transported from the cathode via TPBi to the emitting layer. The hole injection is facilitated by the low energy barrier of 0.1 eV between the HOMO energy level of HTL and the VBM of QDs. The InP-based QLEDs generally have a great potential to compete with Cd-based devices because of a lower energy barrier between the HTL and the InP-based QDs.

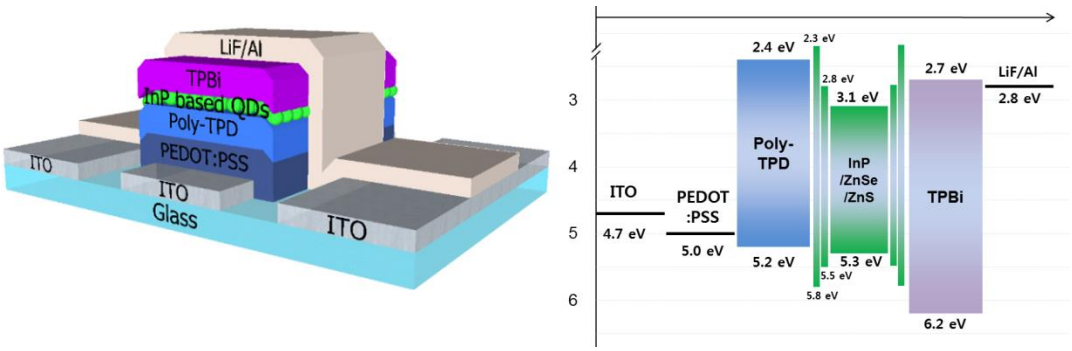

(a) (b)

Figure 4.1.2. (a) A cross-section schematic and band structure of InP/ZnSe/ZnS QLEDs and (b) the corresponding energy levels.

Table 4.1 Different parameters according to the shell thickness

QDs	PL λ_{max} (nm)	EL λ_{max} (nm)	FWHM (nm)	PS (nm)	QY (%)	TGA (%)	V_{th} (V)	Max. cd/m^2, cd/A
t1: ZnS shell	540	555	52	2.5±0.3	40	70.8	2.7	1960, 3.32
t2: thicker ZnS shell	540	555	54	2.9±0.3	42	72.5	2.7	2430, 4.65

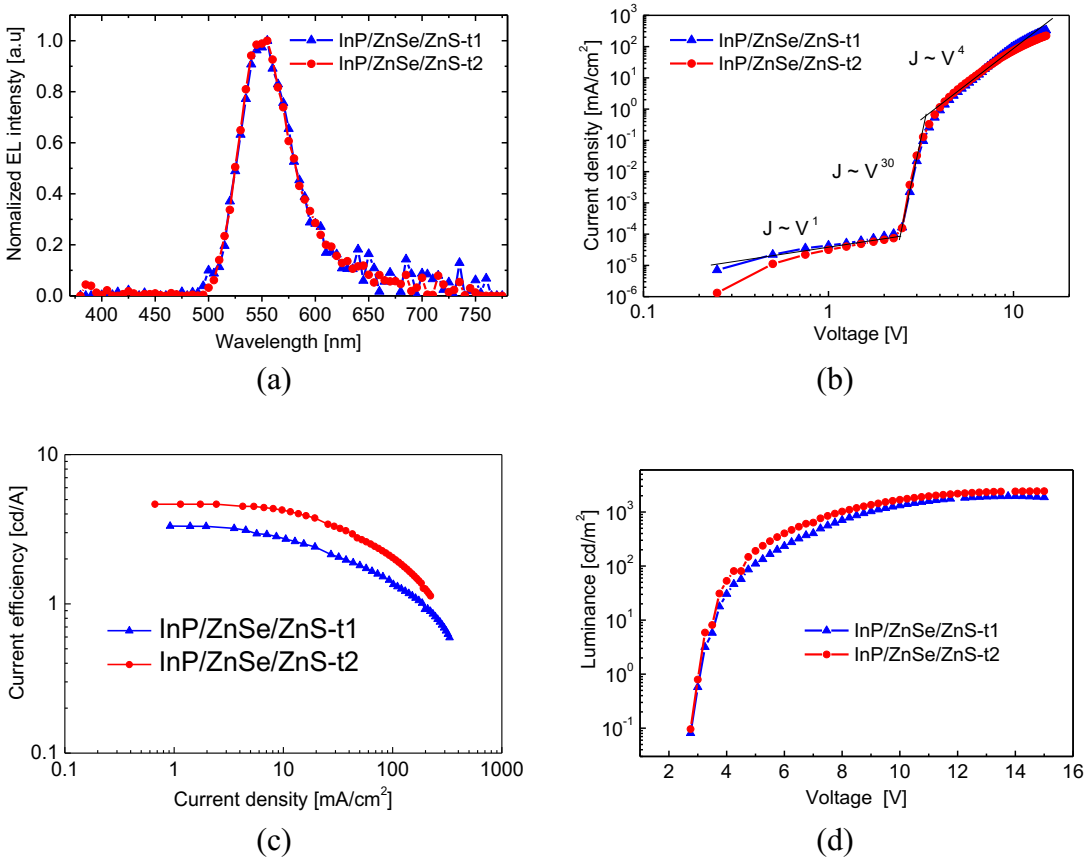

Figure 4.1.3 (a) Normalized EL spectra, (b) current density-voltage, (c) current efficiency-current density and (d) luminance-voltage characteristics of InP/ZnSe/ZnS QLEDs.

The effects of ZnS shell thickness of InP/ZnSe/ZnS QDs on the EL performance of QLEDs were investigated here. Normalized EL spectra, current density-voltage (J-V), current efficiency-current density, luminance-voltage characteristics of both devices are presented in ***Figure 4.1.3***. The peak wavelength of 555 nm and FWHM of 56 nm without any emission from organic layer are observed in the normalized EL spectra for both devices (***Figure 4.1.3a***). However, there is an asymmetric red-shift in EL spectra around 15 nm compared to the peak of PL in QD solution (***Figure 4.1.1a***). It would be originated from the exciton migration to larger QDs in the QD ensemble in the close-packed QD film, the quantum confined Stark effect (QCSE) known as the shift of exciton energy to lower values than band gap energy under electric field, or emission from defect states within the QD band gap [102,103]. While the maximum current efficiency and the luminance reached 3.32 cd/A and 1960 cd/m^2 for the InP QLEDs with thinner ZnS shell, the performance of the device with thicker ZnS shell was enhanced up to 4.65 cd/A and 2430 cd/m^2, respectively. The J-V characteristics of both device in ***Figure 4.1.1b*** show

ohmic conduction up to 2.4 V (J∝ V), trap-limited conduction (J∝ Vn, n>2) up to 3.3 V and pseudo-SCLC (J∝ Vn, n~4) behavior at higher voltage [14,88,104]. J-V curves have the same slope at the trap-limited conduction region above the threshold voltage (V_{th}), which refers to the similar charge injection into the QD (***Figure 4.1.1d***) even though having different thickness of ZnS outer shell. It means the enhancement of current efficiency is not caused by better injection efficiency but by the suppression of quenching mechanism in QDs. J. Jaehoon et al. investigated that the electric field in the QLEDs delocalizes electrons to the shell phase or the surface states because of weak confinement of electrons by lower energy offset between core and shell [35]. The delocalized electrons can cause the non-radiative exciton decay by surface-state recombination. However, the enhancement of potential barrier by the thicker outer shell which provides strong confinement (i.e. exciton localization in QD core) can reduce this luminescence quenching by reducing interaction of excitons with surface charges [35]. On the other hand, W.K. Bae et al. have observed that the thicker shell reduced the rate of Auger decay by exciton delocalization and enhanced the device performance [53]. Here, the exciton delocalization is possible with lower energy offset between the valence and conduction band of the core and shell.

For our InP/ZnSe/ZnS multishell QDs, the outer ZnS shell, which has larger energy offset to InP, provides the strong confinement in InP core, which reduces the luminance quenching efficiently. Consequently, the QDs with thicker ZnS outer shell remain efficiently emissive within our QLEDs and show better performance by the strong confinement and the suppression of luminescence quenching by the surface-state non-radiative recombination [105,106]. A device with much thicker shell (i.e. 4 layers of ZnS) was also fabricated, however, the EL spectrum shows serious emission from poly-TPD because QDs remained the aggregation or void in emission layer, which generates direct leakage path from TPBi to poly-TPD due to the low solubility of QDs (there are still chemistry issues remained and data are not shown here).

Figure 4.1.4a shows the luminance versus operation time graph for the InP-based QLEDs driven with a constant current of 0.84 mA/cm^2. The stability of QLEDs was investigated at low luminance to exclude field-induced luminance quenching [53,80]. The operating time to reach 90% of the initial luminance (LT90) was increased from 55 sec to 123 sec for the thicker shell QDs. This improvement is probably due to the suppressed non-radiative recombination caused by the charged surface defects within QD.

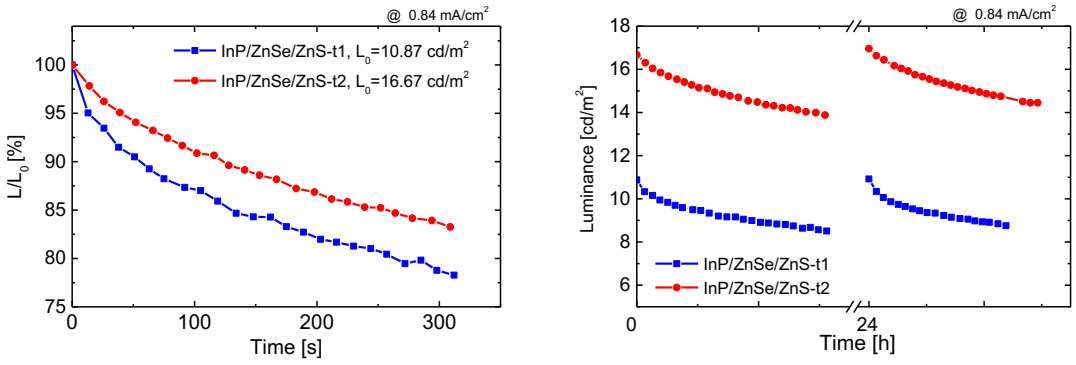

(a) (b)

Figure 4.1.4 (a) Stability data for InP-based QLEDs with different shell thickness, and (b) restored luminance during repeated device stability test after one day. The initial luminance was 10 cd/m^2 for thinner ZnS shell and 17 cd/m^2 for thicker ZnS shell under 0.84 mA/cm^2 of the applied current.

An interesting phenomenon was also observed in repeated lifetime measurements, as shown in the inset of ***Figure 4.1.4b***. The device stability under operation was retested after one day of non-operation, and the initial luminance of both devices was fully recovered. It indicates that the degradation of luminance under low electric field can be explained by QD charging in different energy states. It is known as a critical problem of QLEDs caused by trapped carriers in the QD itself, the surface defects of QDs or the heterostructure of QLEDs [53]. These considerations suggest that thicker ZnS shell suppressed the non-radiative decay caused by the QD charging, which increased the current efficiency and the device stability as well. Previous studies have reported that there is efficiency roll-off at a high current density which is also observed in the ***Figure 4.1.3c*** [80]. I suggest that the efficiency roll-off is not only a problem of field-induced quenching but also one of QD charging because the luminance quenching in our devices was observed even though under the condition of the low electric field, which is also an agreement with the explanation from W.K. Bae et al. [53]. The further fundamental investigation will be needed to understand more how the shell influences the charge behavior in the device. Moreover, there remains the problem of efficiency roll-off influenced by both the strong electric field and the QD charging. However, this issue can be overcome by adopting other technology in the InP-based QLED system such as an Auger-assisted energy up-conversion and a charge neutralization with the oxide nanoparticle-based charge transport layer [107,108].

Applying giant shell QDs in QLEDs

Applying a giant shell of QDs on the QLEDs are very tempting for high performance device since the thick shell has an effect of improving not only the device performance and stability but also PL properties (i.e. QY and stability) [34,106]. Moreover, there are some reports about the positive effects of the giant shell of Cd-based QDs on the device performance by delocalizing hole and electron wave function [46,105]. In our previous development [45], a giant ZnSe/ZnS shell of InP/ZnSe/ZnS QDs also has distinct improvement of stability and QY. However, the device performance with giant shell QD shows quite lower than normal optimized QD structure. ***Figure 4.1.5*** shows the more detailed device results that compare the pristine QD and the giant shell QDs. The details of QD properties and the device performance are also summarized in ***Table 4.2***. The giant shell QD has larger particle size because of thicker both ZnSe and ZnS shell, and higher QY in the solution and film (80% and 52% respectively) because of the efficient surface passivation through thicker shell compared to the pristine QD. Our thick ZnSe/ZnS shell would bring the more delocalization of hole and electron wave function compared to the pristine QD as shown in the suggested scheme from ***Figure 4.1.5d***. Since giant shell could provide the reduced Auger recombination through the exciton delocalization [109], the device performance will be improved by reducing the non-radiative exciton recombination. However, the device with giant shell QDs has lower maximum current efficiency and luminance compared to the pristine QDs as shown in ***Table 4.2***. Since two devices have different EL peak wavelength, EQE is calculated to have a more objective comparison of the thickness effects, regardless the brightness sensitivity of human eye on the wavelength. The EQE of giant shell QD as shown in ***Figure 4.1.5a*** is over 70% lower than pristine QD. The low performance of giant shell can be explained by the observation of J-V characteristic, the purity of EL spectrum and band structure of QLEDs.

Table 4.2 Different parameters according to the giant shell application.

QDs	ZnSe/ ZnS (ML)	PL λ_{max} (nm)	PS (nm)	QY (%)	QY_{film} (%)	V_{th} (V)	Max. EQE (%)	Max. cd/m^2, cd/A
Pristine	1/2	573	4.2±0.9	50	23	~2.3	2.32	2000, 5.6
Giant shell	3/7	554	6.6 ±0.9	80	52	~3	0.67	340, 2.2

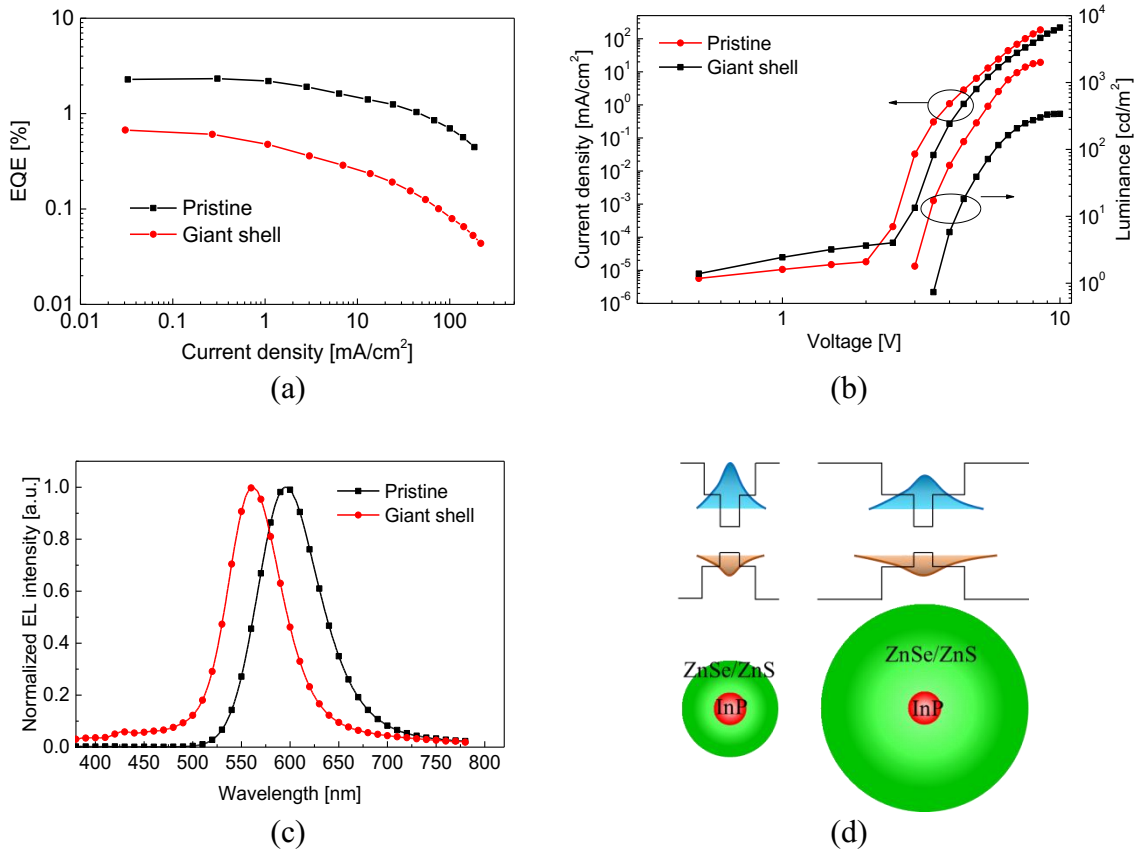

Figure 4.1.5 Conventional device performance with giant shell QDs. (a) EQE-current density, (b) current density-voltage (inset: luminance-voltage), (c) normalized EL spectra @ 6 V and (d) energy level scheme of giant shell QDs. *(YH129, YH130)*

The giant shell shows higher threshold voltage around 3 V compared to the 2.3 V from pristine QD because of giant shell increased the energy barrier for carrier injection into QD. The increased driving voltage at the same current density from giant shell enhanced the field-induced luminance quenching which is also facilitated by more delocalized electron and hole wave function of giant shell QD. Moreover, the giant shell interrupts hole injection into QDs with a higher band offset. The higher hole barrier compared to the electron is attributed to the wide bandgap shell materials as shown in ***Figure 4.1.2b***, which leads to the hole accumulation at poly-TPD/QD interface. On the other hand, the electron injection into LUMO of poly-TPD is facilitated through the thicker ZnSe/ZnS shell because the electrons could be rather transported by CBM of shells than injected into the InP core. Therefore, both influences caused the inevitable poly-TPD parasitic emission shown in ***Figure 4.1.5c*** and the low device efficiency.

4.2 Organic ligands of QDs

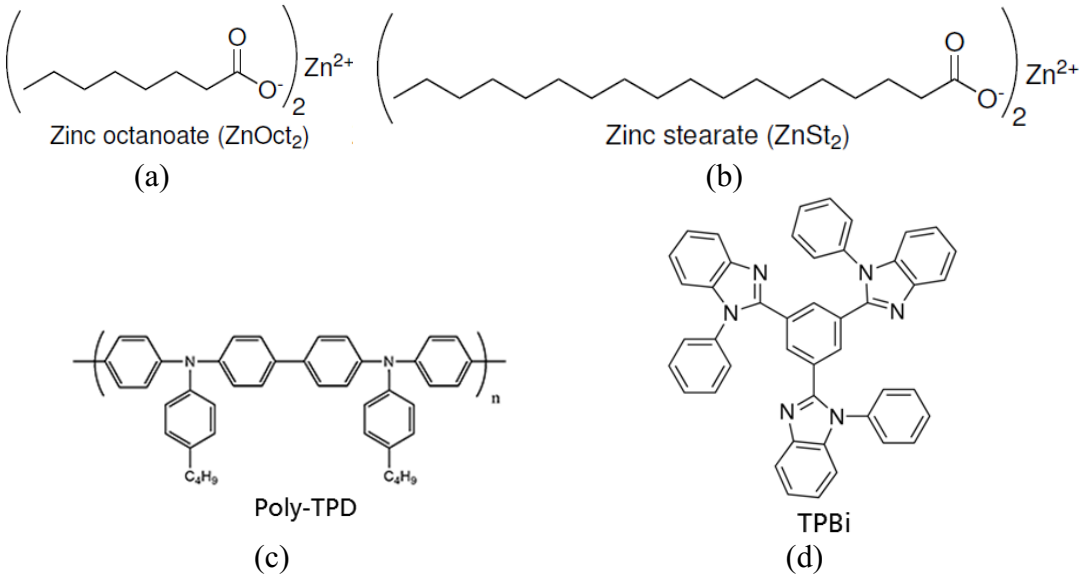

Figure 4.2.1 Chemical structures of (a), (b) zinc precursors with different alkyl chain length of aliphatic ligands, and (c) poly-TPD and TPBi charge transport material.

The surface ligand of QD can differ from the type of zinc precursor used for synthesis [33]. Here, two different zinc precursors (i.e. zinc carboxylates), zinc octanoate and zinc stearate shown in ***Figure 4.2.1a,b***, which have different length of alkyl chain are applied in the QD synthesis, and the effects of ligands on the device performance were investigated. These ligand effects were already compared in previous work regarding EQE and time-resolved PL [45,110], where the octanoate ligands had highest EQE compared to the other ligands including the stearate. However, here I provide a more detailed investigation of the effects of ligands regarding surface morphology and electrical and optical properties in the more optimized QLED structure.

The two different QDs are sophisticatedly designed to have similar QY (~ 50%) and FWHM (62 nm) to reduce the parameter for device application, and there is the only slight difference on maximum PL wavelength (***Table 4.3***). ***Figure 4.2.2a*** shows TGA curves from the synthesized QDs with stearate and octanoate ligands and the residual mass at 600 °C (inorganic core/shell is decomposed at this temperature) is less with octanoate ligands (53% and 78% for stearate and octanoate, respectively). Since octanoate has the shorter alkyl chains, the more remained mass indicates that the QD surface is capped with the shorter ligands (i.e. less mass of total ligands). Moreover, the derivative thermogravimetric (DTG) curves have two peaks at around 330 °C and 440 °C, which indicates the decompose of octanethiol (boiling point 200 °C) and stearate [45] or

octanoate [111], respectively. The octanethiol is used as a sulfur precursor for ZnS outer shell here; therefore, the ligands capped on the QD surface are the both octanethiol and aliphatic chain. According to the DTG peak, the QD synthesized with zinc stearate has more portion of octanethiol compared to the zinc octanoate precursor. Since octanethiol chain length is shorter and the amount on the QD surface is less than that of stearate, the dominant ligands effects would be attributed to the longer stearate ligands. The maximum wavelength of luminescence spectrum in the solution, thin film, and device (i.e. EL) are summarized in ***Table 4.3***. Since the red-shift of luminescence spectrum between the QD solution and QD film is originated from the exciton migration to larger QDs inside of close-packed QD ensemble film due to resonant energy transfer [45,68,112,113], the more closely packed QD film with octanoate ligands shows stronger red-shift of peak wavelength compared to the one measured in solution. The red-shift of QD film measured to 22 nm and 36 nm for the stearate and octanoate, respectively. The shorter ligands remain the QDs more closely packed and enhanced the exciton resonant energy transfer in the film (i.e. interparticle distance is reduced). However, the stronger energy transfer among the QDs in the close-packed film will quench the luminance of QDs by the exciton trapping within reduced interparticle distance (i.e. low internal quantum efficiency) [45].

Figure 4.2.2c,d show the laser scanning confocal microscope images of QDs layer spin-coated on poly-TPD HTL after the filtration. The QD with stearate ligands has a phase separation with poly-TPD during the spin-coating and remains the non-uniform film shown in ***Figure 4.2.2c.*** However, the QD with octanoate ligands shows very uniform surface without any serious phase separation (***Figure 4.2.2d***). The phase separation here may be attributed to the mismatch of chain length between the stearate and poly-TPD (i.e. the QD with stearate would be more nonpolar than poly-TPD).

Table 4.3 Different parameters according to the type of ligands (* red-shift from PL λ_{max} in solution).

QDs	FWHM (nm)	QY (%)	QY_{film} (%)	QD film (nm)	TGA (%)	PL λ_{max} (nm)	PL_{film} λ_{max} (nm)
stearate	62	51.5	14	8	53	548	570(22*)
octanoate	62	50.0	11	11	78	553	588(36*)

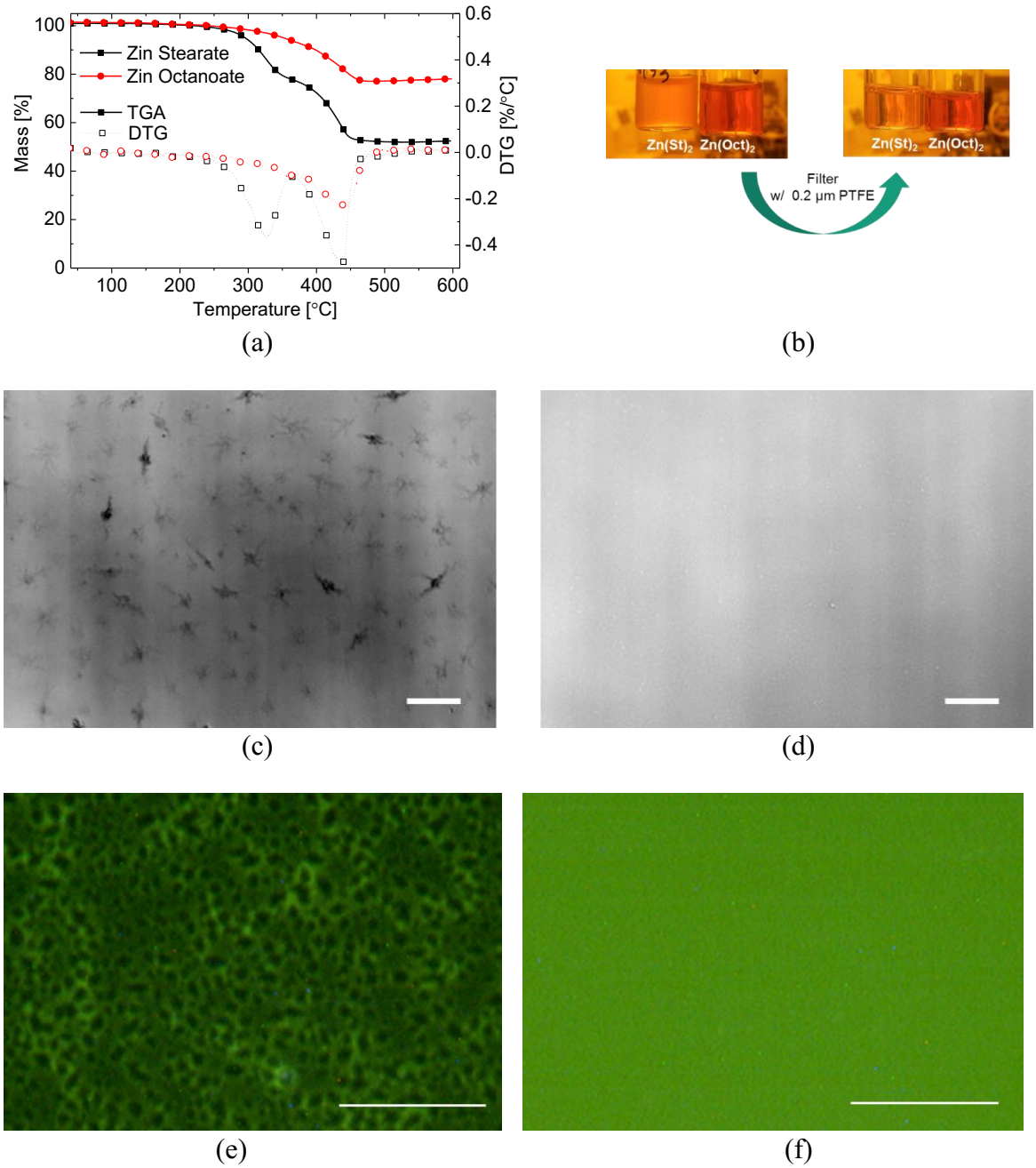

(a) (b)

(c) (d)

(e) (f)

Figure 4.2.2 (a) TGA analysis, (b) different solubility of QDs in hexane, (c),(d) laser scanning confocal microscope images of QD/poly-TPD/SiO_2 film (scale bar: 10 µm, VK-X Keyence) (e) and (f) microscope images of EL (scale bar: 50 µm, Aigo GE 5 [110]).

Moreover, the QDs with octanoate ligands have better solubility in the non-polar solvent such as hexane and nonane because of an impurity of QDs, which is shown in ***Figure 4.2.2b***. Even though the hazy solution with stearate, the solution becomes clear after the filtering. It is expected that the remained zinc stearate precursors in the solution are one of the reasons for the serious phase separation as well. Accordingly, the different film conditions of QD layer attributed to the different ligands lead to the change of EL

uniformity from the pixel. ***Figure 4.2.2e*** with stearate ligands shows a non-uniform EL images but not with ***Figure 4.2.2f*** with octanoate ligands. Even though there is the difference of EL uniformity in micro scale, ***Figure 4.2.3e,f*** show both devices have still saturated green emission from each device. ***Figure 4.2.3*** and ***Table 4.4*** show the device results depending on different QD ligands. Both devices are fabricated with the 3 mg/mL QD solution after filtering, but the QD with octanoate ligands provided slightly thicker layer because of relatively higher inorganic contents of QDs capped with octanoate ligands (***Table 4.3***). The J-V curves in ***Figure 4.2.3a*** show similar threshold voltage (2.5 V) and the current density. However, the current efficiency and luminance are enhanced very effectively with the shorter ligands (***Figure 4.2.3b***). In addition, EQE measured concerning of the different wavelength of two QDs also shows higher value with the octanoate ligands. Maximum EQE recorded to 2.5% and 1.7% for the octanoate and stearate, respectively. The EL spectra shown in ***Figure 4.2.3d*** from both devices also have some differences. The red-shift of EL is stronger with the octanoate sample because of the more close-packed QD film. However, the shifted wavelength is less than that of PL_{film} because the red-shift of EL also depends on the QCSE. Apparently, the QCSE effects suppressed the exciton migration to the adjacent QDs, which could indicate that the luminance self-quenching through the exciton resonant energy transfer in close-packed QD is not a dominant drawback in the QLED. On the other hand, the more close-packed QD film could provide higher probability to generate exciton within the recombination zone (RZ) by higher QD density in the film. Moreover, the EL spectrum from the stearate ligands shows the emission at 425 nm originated from the luminance of poly-TPD hole transport material. This parasitic emission implies that the RZ is shifted more closely to poly-TPD/QD interface followed by the incomplete exciton energy transfer from the poly-TPD to QD, which results in the lower device efficiency. The RZ shift is attributed to the delayed hole transport in QD film by the longer chain length of stearate [114]. Therefore, the transition of RZ strongly supports the enhanced carrier transport and injection in the QD film through shorter capping ligands even though there is no distinct change of J-V curves.

As a result, the enhanced device performance with the octanoate ligands is approved by the improved uniformity of QD layer, the enhanced carrier injection and transport in the QD film, the increased exciton generation probability through more close-packed QD film and the reduced luminance self-quenching through QCSE in the device operation.

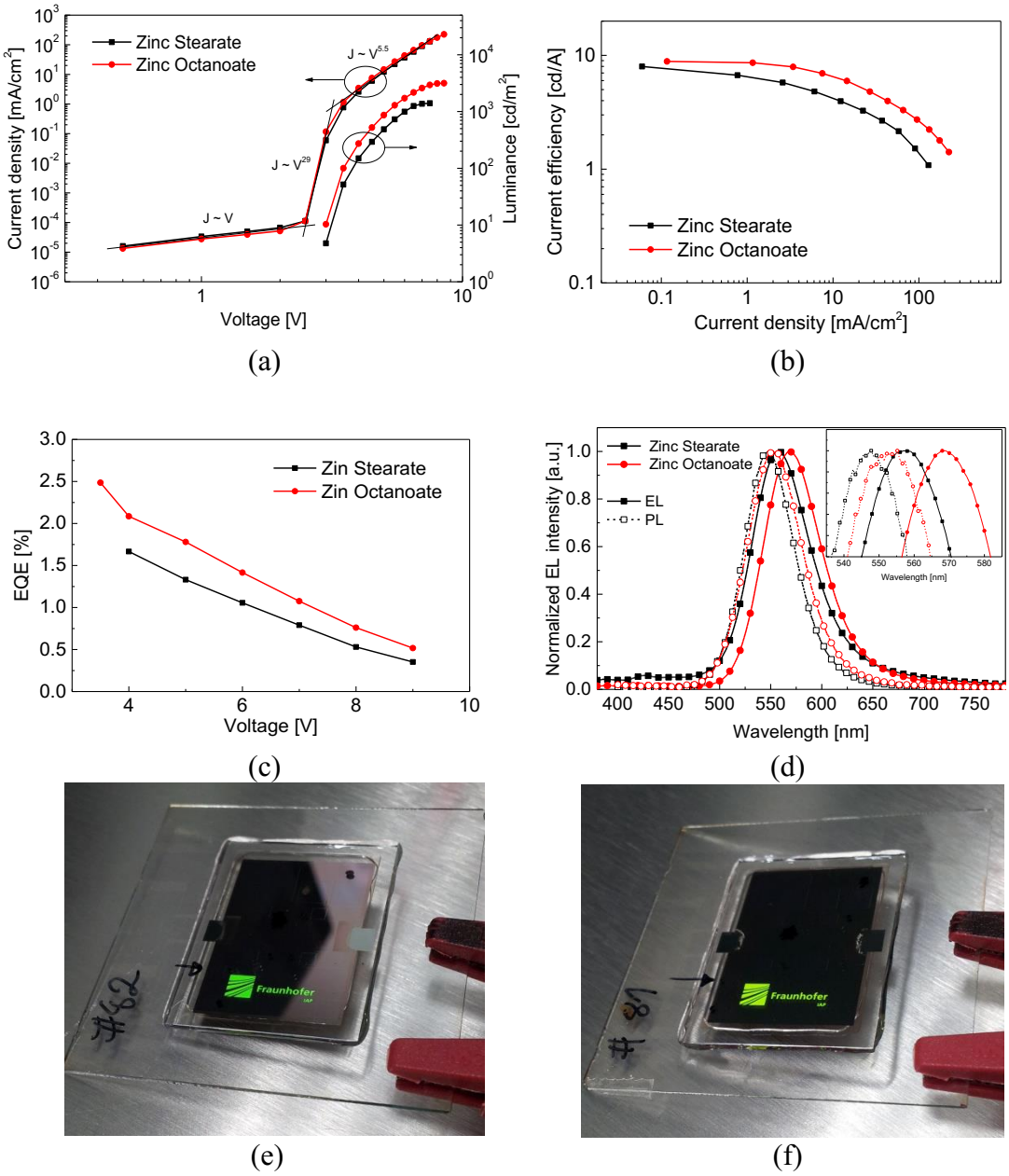

Figure 4.2.3 (a) Current density-voltage (inset: luminance-voltage), (b) current efficiency-luminance, (c) external quantum efficiency-voltage, (d) PL and EL spectra at 10 V and photographs of EL at 4 V for the device with (e) stearate and (f) octanoate. *(YH82, YH81)*

Table 4.4 Summary of device performance of QLEDs with stearate and octanoate ligands (* red-shift from PL λ_{max} in solution).

QDs	EL λ_{max} (nm)	V_{th} (V)	Von (V) @ 10 cd/m^2	Max. EQE (%)	Max. cd/A	Max. cd/m^2
stearate	557(9*)	2.5	3.2	1.7	8.0	1400
octanoate	569(16*)	2.5	3	2.5	8.8	3164

4.3 Summary

The influences of InP/ZnSe/ZnS QD design on the device performance of conventional QLEDs regarding the ZnS shell thickness and the giant shell are investigated in this chapter. I have found that QD charging is responsible for luminance quenching in the device operation, supported by the refreshed luminance in the repeated stability test, indicating the reversible charging effects. However, the EL device with thicker ZnS shell QDs shows better current efficiency and stability because the thicker outer shell suppressed the non-radiative recombination caused by mainly charged defect state of the QDs. Moreover, I strongly suggest that efficiency roll-off under high driving voltage is attributed to the strong electric field as well as the QD charging that results in the serious luminance quenching even under the low electric field in our research. However, the giant shell QD which has higher QY and PL stability shows a negative effect on the device performance because of the increased field-induced luminance quenching through the exciton delocalization and the hindered carrier injection by the wide band gap shell.

Since the organic ligands length of QD is also one important parameter for controlling the charge carrier behavior in QLEDs, the effects of ligands on the device performance with different alkyl chain lengths were investigated. The EQE with the octanoate ligands is enhanced 47% compared to the shorter stearate ligands. Even though the close-packed QD film with shorter ligands could have the self-quenching of luminance by the QD to QD interaction (i.e. exciton resonant energy transfer), it have been found that the self-quenching is not dominant drawback during the operation through the observation of the weaker red-shift of EL spectrum compared to that of PL spectrum from QD film.

In conclusion, the optimizing the QD multishell structure considering the charge injection and the exciton confinement, and the choice of ligands material considering the carrier transport and charge balance in the QLED structure is critical for the developing high efficient QLEDs. With further investigation on optimizing the core/multishell/ligands structure of QDs and charge balance in multilayered device system, the performance of InP-based QLEDs would have more potential to be improved.

Chapter 5

5 Developing high efficient inverted QLEDs

5.1 Drawbacks of conventional QLEDs

Chapter 4 discussed the most promising QD design aspects with well optimized conventional QLED structure consists of mainly organic CTL. Even though the QD design and the device structure were optimized for high efficiency, however, the conventional QLED still has serious efficiency roll-off from the beginning of current density (or voltage) increase. Moreover, the maximum luminance also shows relatively lower (around 3,000 cd/m^2) than that of Cd-based QLEDs (over 10,000 cd/m^2). The main reason of these drawbacks is originated from EL quenching during the device operation by Auger recombination with charged carriers, strong electric field (i.e. field-induced quenching), and device degradation with thermal energy loss in organic CTL or QD/organic interface defects. [34–36,42].

Therefore, it is essential to use other device structure or inorganic charge transport materials to remove these fundamental issues. Inverted QLEDs would provide more wide scope to do these strategies for better stability of device but also the capability to integrate current well-developed OLED backplane technology into the QLED display.

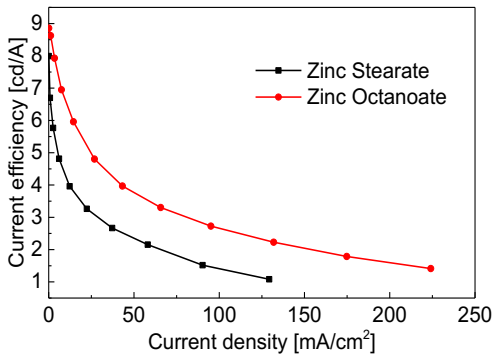

Figure 5.1.1 Efficiency roll-off issue from conventional QLEDs. *(YH82, YH81)*

5.2 Advantages inverted QLED design

InP/ZnSe/ZnS QDs has more potential to develop high-performance QLEDs base on the band alignment in multilayered device structure shown in ***Figure 5.2.1***. Cd-based QDs has a relatively high energy barrier around 2~2.5 eV to inject hole from an ITO anode in conventional structure (***Figure 5.2.1a***). Even though applying the HTL there remains high energy barrier because the selection of materials is limited in a few polymers because of the concerning of orthogonal process with QD solution. Therefore, the inverted structure using inorganic HTL has more feasibility to develop the high performance of Cd-based QLEDs. Even though the adopting various HTL deposited by thermal evaporation, there remains hole injection barrier over 1 eV. On the other hand, the alignment of the band structure of InP/ZnSe/ZnS QDs shown in ***Figure 5.2.1b*** indicates that the injection barrier for hole and electron are relatively lower than that of Cd-based QLEDs, which provides the hole injection barrier below 1 eV in both conventional and inverted structure. The electron injection barriers in the inverted structure also can be easily compensated by applying various inorganic ETL such as ZnO [115], ZrO_2 [20], SnO_2 [116] and TiO_2 [14]. The inverted device structure has several advantages. First of all, it is useful for directly applying QLEDs to the well-developed large size AM OLED technology [54,55,104,117]. A bottom cathode of an inverted device is preferred in AM-OLEDs because the oxide [118] and amorphous silicon (a-Si) [119] TFT used in commercial technology have mostly an n-type characteristic.

Figure 5.2.2 shows the driving concept of the AM-OLED display with n-type TFT in conventional and inverted structure. In the case of n-type TFTs used to drive the conventional OLEDs, the bottom anode of the device is connected to the source line of the n-type TFT. Therefore, the gate voltage (V_{gs}) of n-type TFT is affected by the fluctuations of the OLED driving voltage (V_{diode}), and thus the image quality of the display panel would not be promised. On the other hand, the drain line of the n-type TFT can be connected directly to the bottom cathode in inverted OLED, which makes the gate voltage of n-type TFT lower and independent (i.e. $V_{gate} = V_{gs}$) of the performance of the OLEDs [120]. The inverted device structure is also more favorable for deposition of inorganic ETL by solution processing on the ITO substrate because they sometimes need an annealing process with high temperature to control the electrical properties. Moreover, the inverted device structure broadens the selection of hole transport materials deposited by thermal evaporation [121].

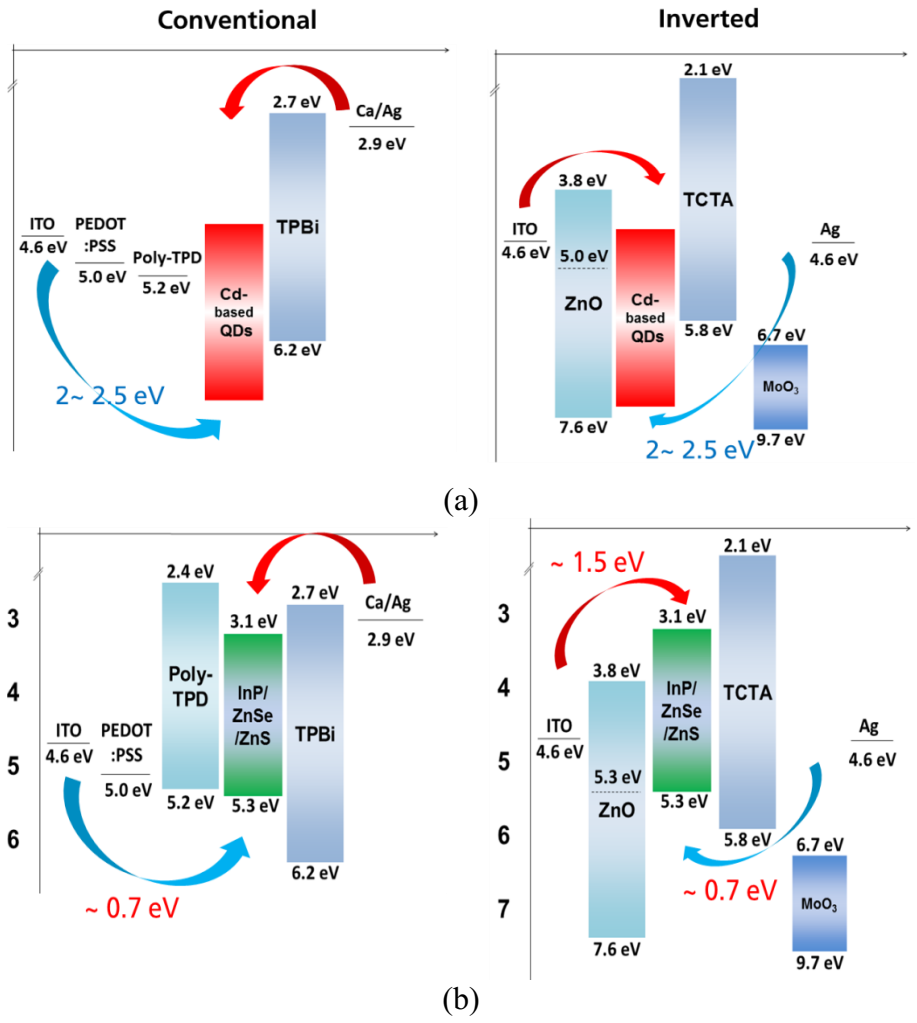

Figure 5.2.1 Band diagram of conventional and inverted QLEDs based on (a) Cd-based QDs and (b) InP-based QDs.

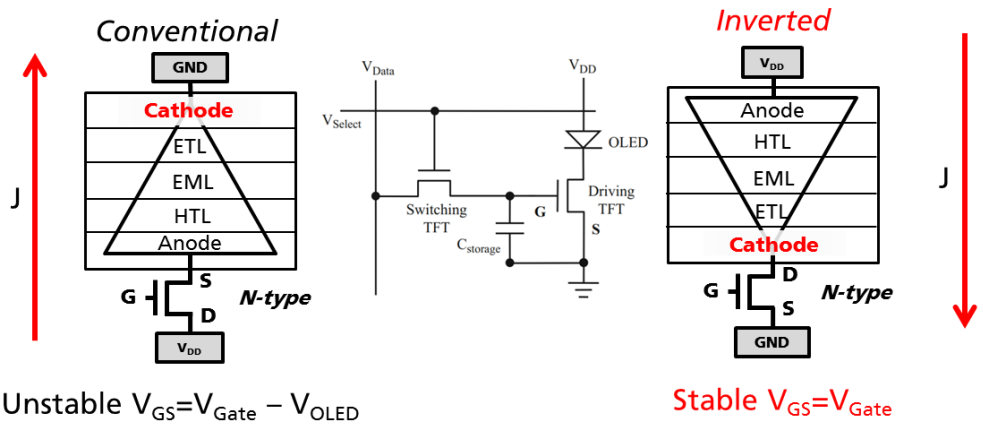

Figure 5.2.2 Schematics show the driving concept of the OLED display with n-type TFT in conventional and inverted structure.

5.3 ITO/QDs interfaces design to control electron injection

5.3.1 Electron injection behavior through the ITO/QD interface condition.

Role of aluminum oxide layer inserted at ITO/QD interface

In order to develop efficient inverted QLEDs, the design of the interface between the cathode (ITO) and QD is quite important because of the 1.6 eV of higher electron injection barriers compared to the holes. Therefore, it is important to understand the electron injection behavior through different ITO/QD interface condition. The insertion of a thin buffer or injection layer at the ITO/QD interface is the simple and effective strategy to control the charge injection. There are variety of interfacial materials to modify the energy level of the ITO, including organic buffer layers, such as copper phthalocyanine (CuPc), polyethyleneimine (PEI), polyethylene oxide (PEO) and poly-allylamine (PAA), and inorganic insulator buffer layer, such as LiF, Al_2O_3, SiO_2, H_fO_x and MoO_3 [122–124]. Among the different strategies, an ultra-thin Al_2O_3 insulating material has an effect of improving the current efficiency and power efficiency of OLEDs [123,125,126]. The several barrier reduction models were suggested to explain the enhanced device performance through the insulating buffer layer [123,125,127].

Here, Al_2O_3 layer fabricated by atomic layer deposition (ALD) at the interface between ITO and QD is applied to improve device efficiency. For the explanation of our results, the barrier reduction model from L. Zhou et al. and S.T. Zhang et al. is adopted [123,125]. They found that the accumulation of hole or electron at the interface of buffer/organic layer is necessary for the electron or hole injection through the buffer layer, which could apply to our QLED device with an Al_2O_3 insulating buffer layer (i.e. hole accumulation at the Al_2O_3/QD interface).

Figure 5.3.1a shows a band diagram of inverted QLEDs with inserted Al_2O_3 layer. In order to have efficient hole injection from the anode, thermally evaporated TCTA HTL, MoO_3 HIL, and Ag anode were chosen for the inverted device structure. ***Figure 5.3.1b*** shows the J-V curves of different devices. With increasing the thickness of Al_2O_3, the driving voltage requested to achieve a certain current density is significantly increased. The threshold voltage also increases as the thickness of Al_2O_3 increases, 2.3 V, 2.6 V, 3.2 V, and 3.5 V for 0.0 nm, 0.4 nm, 0.8 nm and 1.6 nm of Al_2O_3 thickness, respectively. Even though the high driving voltages, the maximum device efficiency interestingly enhanced as the thickness of buffer layer increase to 0.8 nm, while the

performance decreased again with 1.6 nm of the Al_2O_3 layer as shown in ***Figure 5.3.1c.*** Moreover, ***Figure 5.3.1e*** also shows the device with 0.8 nm of Al_2O_3 has highest power efficiency. The parasitic emission at the blue region in EL spectra of the device with an Al_2O_3 buffer layer in ***Figure 5.3.1f*** indicates that the RZ shifted from QD layer to near the QD/TCTA interface, while the device without Al_2O_3 shows clear spectrum without any parasitic emission. The highest intensity of parasitic emission with 0.8 nm of Al_2O_3 measured at 4 V means the largest RZ shift. According to the L. Zhou et al., the electron injection in the device with Al_2O_3 buffer layer can be explained not only the thermionic injection (n_1 in ***Figure 5.3.2a***) but also the quantum tunneling injection (n_{2L} and n_{oxTL} in ***Figure 5.3.2a***) [125]. Electron tunneling probability n_{oxTL} strongly depends on the thickness of oxide layer, while thermionic injection n_{1L} depends on the energy offset between ITO and semiconductor layer. In our device, the n_{1L} could not be enhanced efficiently even though the reduced work function of ITO by the increased Al_2O_3 thickness (***Table 5.1***) because the effects of reduced n_{oxTL} through the thicker Al_2O_3 layer is more dominant.

Table 5.1 Different film and device characteristics depending on the thickness of Al_2O_3. (The values of surface potential are based on the reference [123])

Al_2O_3 thickness (nm)	Surface potential [123] (eV)	V_{th} (V)	Voltage @ 1 cd/m^2	Max. efficiency cd/A	cd/m^2 @ 80 mA/cm^2
0.0	4.7~4.9	2.3	4.3	0.13	100
0.4	4.7	2.6	4.5	0.25	46
0.8	4.5	3.2	5.0	0.47	28
1.6	4.4	3.5	7.3	0.07	30

However, the thermionic injection could increase more efficiently by the stronger band bending of Al_2O_3 buffer layer (i.e. vacuum level shift of oxide layer, ΔeV_{oxH}) and QD layer ($\Delta e\phi_{sH}$) after the driving voltage increase as shown in the scheme of ***Figure 5.3.2b***. The vacuum level shift of oxide layer is facilitated by the increase of the voltage drop across the buffer layer by the efficient hole accumulation at the Al_2O_3/QD interface, which is attributed to the sufficient hole injection into the valence band of QD by our efficient hole transport system in the device (i.e. TCTA/MoO_3/Ag). Therefore, electron injection could be increased by the facilitated both n_{1H} and n_{oxTH}. On the other hand, the current density requested to achieve a certain voltage is still getting lower as the thickness of Al_2O_3 layer increase (***Figure 5.3.1b***), which indicates that the decreasing

rate of n_{oxT} is larger than the increasing rate of thermionic injection n_1. Once again, the increased electron injection has more strong effects on increasing the current efficiency and power efficiency even though the reduced total current density by a thicker insulation layer. Moreover, the shifted RZ recognized by the TCTA emission from the device with Al_2O_3 is another reasonable agreement of the enhanced electron injection by the Al_2O_3 buffer layer.

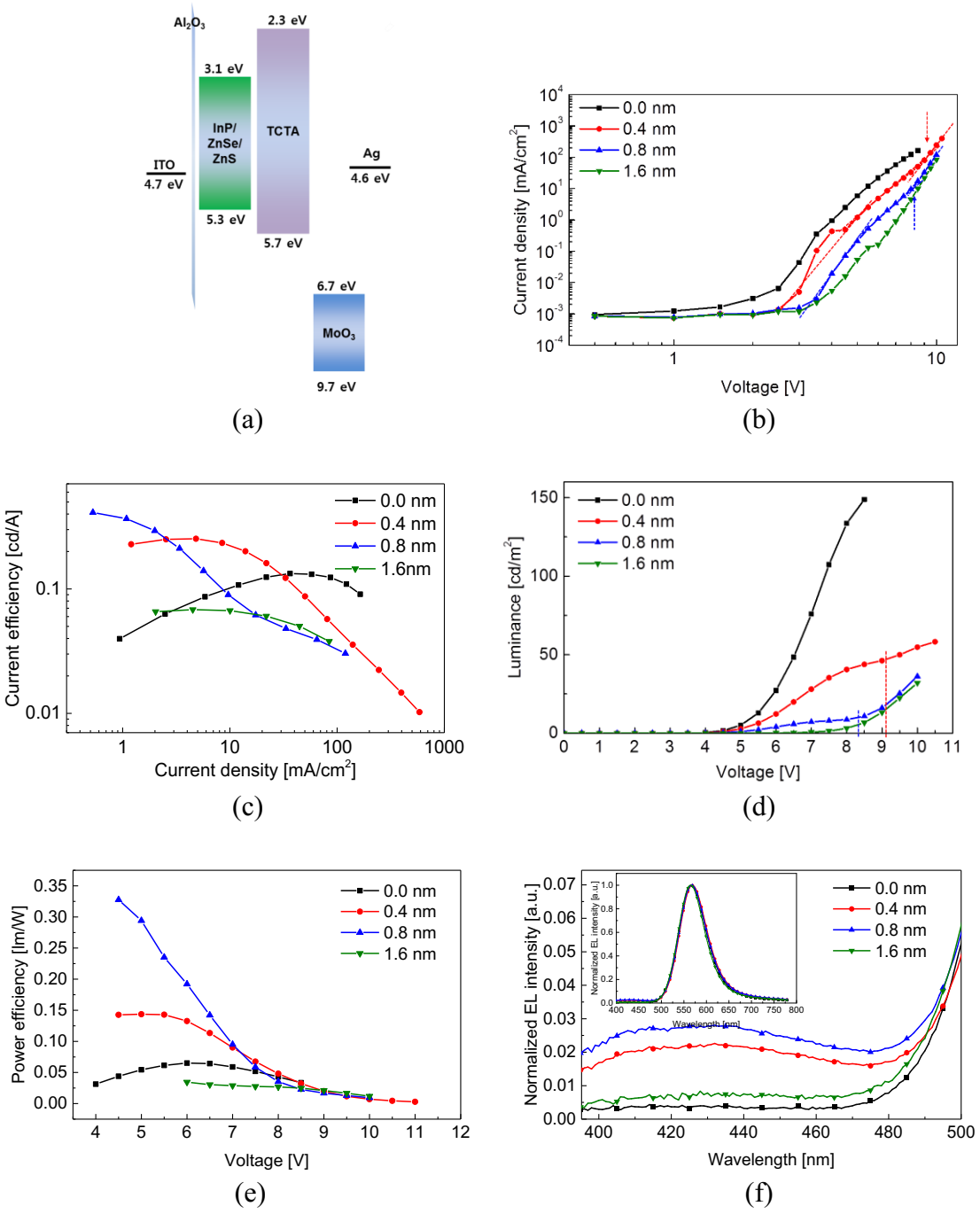

Figure 5.3.1 (a) A band diagram of QLEDs with inserted Al_2O_3 buffer layer, (b) Current density-voltage, (c) current efficiency-current density, (d) luminance-voltage, (e) power efficiency-voltage and (f) EL spectra at 10 V. *(YH197, YH199, YH198, YH196)*

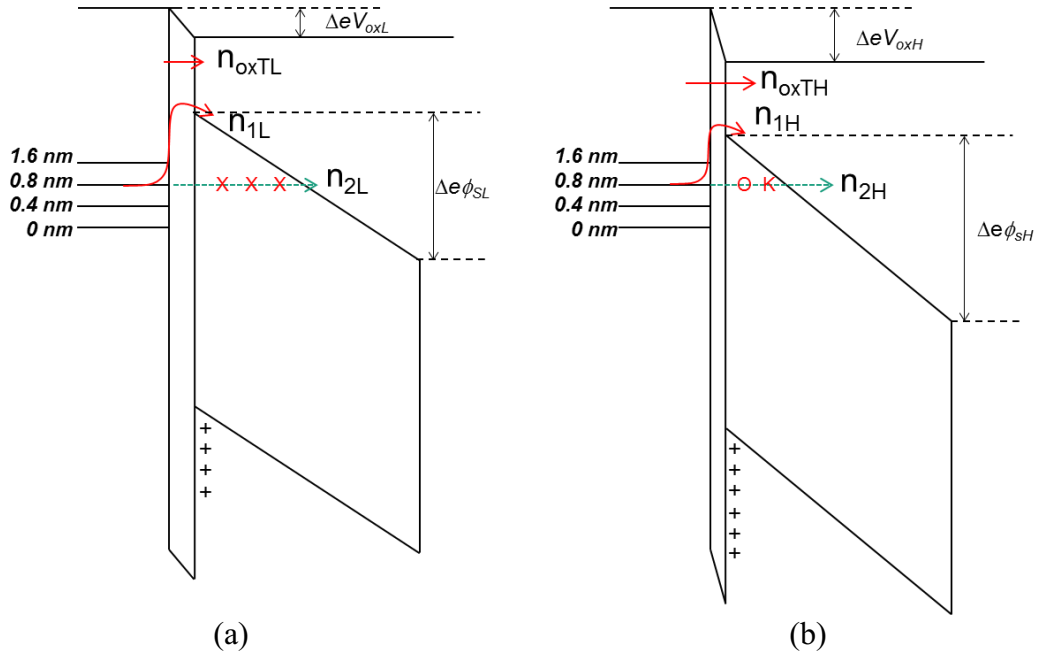

Figure 5.3.2 The schematic of band bending diagram under the relatively (a) low and (b) high electric field.

However, the enhancements of current efficiency are more distinct under the low current density (***Figure 5.3.1c***, < 10 mA/cm^2). These changes can be addressed by the increased parasitic emission in EL spectra through the modification of RZ with the insertion of the Al_2O_3 buffer layer. The increased electron injection into QD by the reduced oxide tunneling barrier under higher current density could induce a severe Auger luminance quenching by the excess of electrons at the RZ [22,53]. Moreover, the luminance quenching becomes more serious problems when the exciton recombines near the QD/TCTA interface or at the TCTA layer because of the non-radiative exciton recombination by the defect states at the interface or the energy loss through the inefficient organic EL. Therefore, the device with 0.8 nm of the Al_2O_3 layer, which has largest parasitic emission, has higher current efficiency drop as the current density increase. The high power efficiency only under low voltage (i.e. below 7.5-9 V) from the devices also corresponds with above explanation.

There is another interesting double diode behavior on J-V-L characteristics in ***Figure 5.3.1b,d***. The luminance and current density of the devices with 0.4 nm and 0.8 nm of the Al_2O_3 buffer layer are increased exponentially again at the 9.1 V and 8.3 V, respectively. As the hole injection increases at the high electric field, more holes can be accumulated at the Al_2O_3/QD interface as shown in ***Figure 5.3.2b***, which will increase the vacuum level shift of oxide layer (ΔeV_{oxH}) by the increasing voltage drop across the

buffer layer. In addition, the strong electric field will enhance the band bending of QD layer ($\Delta e\phi_{sH}$). Both band-bending under the high electric field now enhance the quantum tunneling injection n_{2H}, which increases the current density again by more electron injection into QDs. However, the 0.8 nm of Al_2O_3 could not have efficient quantum tunneling injection n_{2H} because the electron tunneling probability n_{oxT} is still relatively too low. For the device without Al_2O_3, the hole can be easily dissociated to the counter electrode in the absence of buffer layer. Therefore, the double diode behavior cannot be observed from both conditions. Additionally, the reduced plasmon-exciton interaction could also contribute the enhanced current efficiency. The separation of plasmon in the electrode and exciton in the QD by insertion of the buffer layer may suppress the luminance quenching [126,128].

Since the ultra-thin PEI interfacial dipole layer could reduce the work function of ITO just as thin Al_2O_3 layer [122,124], the different concentration of PEI solution for the various thickness was applied in our inverted QLEDs. ***Figure 5.3.3*** shows the current efficiency as a function of luminance characteristics comparing the results from the Al_2O_3 layer. The current efficiencies from the device with PEI increased via the similar mechanism of the Al_2O_3 layer. However, the enhanced value is higher, and the efficiencies are relatively stable as luminance increase than the devices with the Al_2O_3 layer. Since solution processed PEI interfacial layer have lower dielectric constant (i.e. 3.8 [129]) compared to the ALD Al_2O_3 (i.e. 8~9 [130]), the electron tunneling probability (n_{oxT}) in the PEI layer is higher than that of the Al_2O_3 layer. Therefore, the electron injection through PEI is more efficient than Al_2O_3 buffer layer combining the effects of improved thermionic injection with thicker PEI layer (n_1) [131].

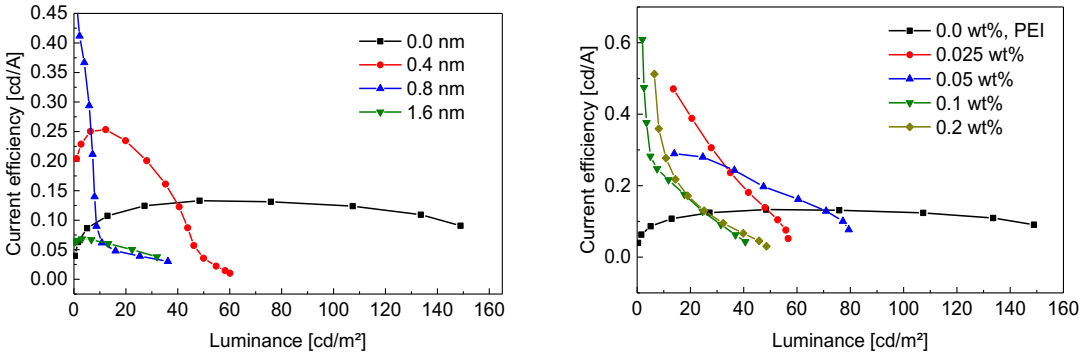

(a) (b)

Figure 5.3.3 Current efficiency-voltage characteristics of the devices with (a) Al_2O_3 and (b) PEI. *(YH197, YH175, YH174, YH173, YH172)*

Electron injection from ITO to QD without any buffer layer

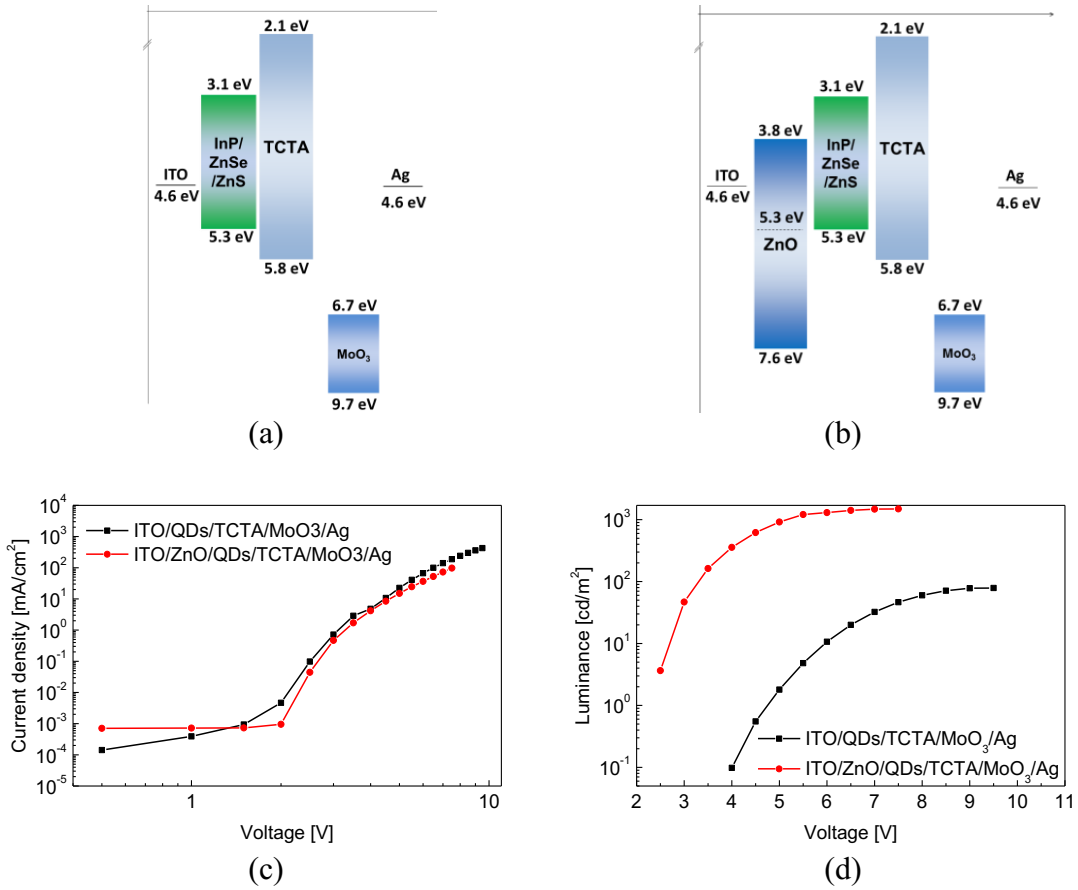

Figure 5.3.4 The band diagram of (a) quasi HOD and (b) bipolar inverted device and their (c) current density-voltage and (d) luminance-voltage characteristics. *(YH180, YH203)*

There is an interesting behavior from the device fabricated without any buffer layer (ITO/QD/TCTA/MoO_3/Ag). This device is basically designed as the hole only device (HOD, ***Figure 5.3.4a***) because 1.6 eV of energy offset between ITO to CBM of QDs would not allow the electron injection. However, ***Figure 5.3.4d*** shows that the EL is observed from 4 V (i.e. turn-on voltage) while the threshold voltage from quasi-HOD is around 2 V. The higher turn-on voltage compared to the threshold voltage indicates the electron injection for the exciton generation and recombination only begins over the 4 V, while the hole injection occurs over the 2 V. On the other hand, the threshold voltage of the bipolar device (***Figure 5.4.3b***) is also around 2 V. According to the observation of the similar threshold voltage from both devices, it can be expected that the threshold voltage is confined by the hole injection barrier into QD layer, not by that of electron injection. In addition, the current density of quasi-HOD is similar to the bipolar inverted device, which also indicates that hole is majority carrier in our inverted device structure. Therefore, the reducing the hole injection barrier would bring the lower threshold voltage

from the device (i.e. low driving voltage) and higher device performance (see the ***Chapter 6.2.2***).

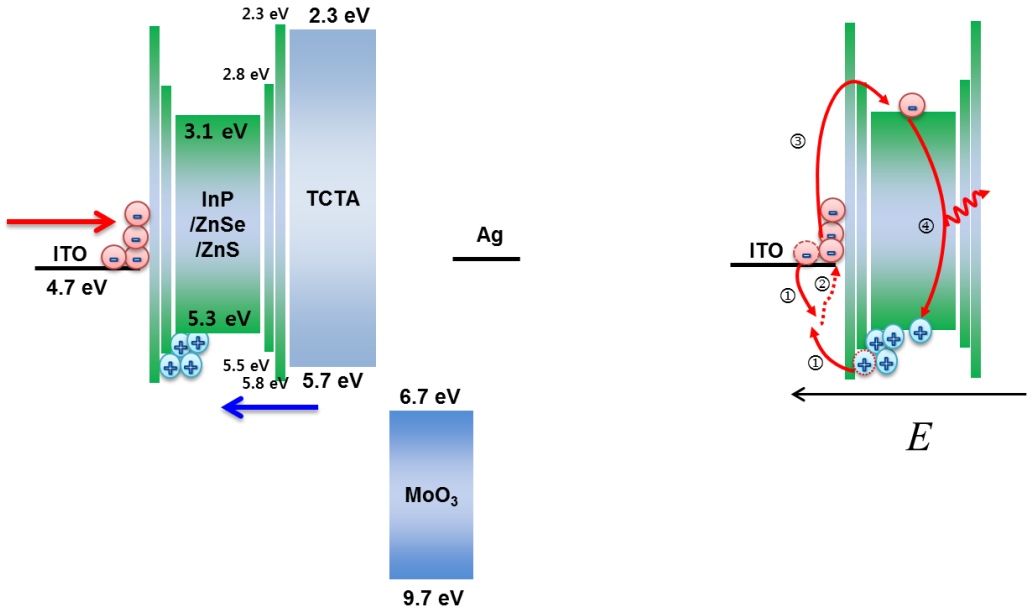

(a) (b)

Figure 5.3.5 (a) Schematic energy level diagram of ITO/QD/TCTA/MoO_3/Ag HOD, and (b) an illustration of the Auger assisted electron injection process at the ITO/QD interface: ① recombination of interfacial exciton, ② resonant energy transfer between from the interfacial exciton to the accumulated electrons, ③ injection of the high energy electron into CBM of QD, and ④ radiative recombination in QD emitter.

Besides the efficient hole injection at low voltage, the possible electron injection over around 4 V is more interesting. The electron injection and the recombination process can be explained based on the Auger-like energy up-conversion process [108]. According to the L. Qian et al., energy up-conversion process can be facilitated in the condition of efficient carrier injection from the electrodes, an accumulation of charge carriers at the interface, and nanoparticle materials for efficient surface interaction [107]. Our system is suitable for the following conditions (***Figure 5.3.5a***). The hole injection into QD is sufficient according to the J-V curves in ***Figure 5.3.4a***, and the injected holes can be accumulated at the edge of the quantum well close to the interface of ITO/QD due to a wide band gap ZnSe/ZnS shell and a localized hole wave function in the InP core. For the electron will be accumulated at the ITO/QD interface by the high offset from ITO to CBM of QD. The Auger assisted energy up-conversion process can also be boosted up by the nanocrystal properties of InP-based QD. Therefore, the possible Auger assisted electron injection process is depicted in the ***Figure 5.3.5b***. The accumulated electrons can recombine with holes accumulated at the QD shell. The recombination energy can be

transferred to the accumulated electrons at the ITO/QD followed by the Auger assisted electron injection into the CBM of QD. Finally, the generated excitons in QD have radiative recombination. However, the injection barrier from ITO to CBM of QD should be reduced by inserting HTL or HTL to develop more efficient inverted QLEDs.

5.3.2 Summary

In conclusion, the efficiency of the inverted device can be enhanced by using the interfacial dipole layer such as Al_2O_3 and PEI between ITO and QD, however, the high driving voltage, the luminance quenching, and the double diode characteristics hinder the developing stable and high performance QLEDs. On the other hand, the efficient hole injection from the TCTA/MoO_3/Ag system is confirmed through the HOD investigation, and the electron injection from the ITO to CBM seems not so difficult somehow through Auger assisted electron injection process even though with the high barrier offset (i.e. 1.6 eV). Therefore, the more stable and efficient device can be realized by applying the proper ETL in the inverted device structure.

5.4 Commercial inorganic ZnO nanoparticles for ETL

5.4.1 Al:ZnO nanoparticle ETL (Nanograde N-10x, PS~15 nm)

This section is based on the modification of a publication in Journal of the Society for Information Display first-authored by the candidate [41].

Recent studies show that organic– inorganic hybrid structures, which has typically the n-type metal oxide as ETL and organic semiconductor as HTL, have better device performance among various types of devices [22]. Commonly, ZnO is used as an electron charge transport layer in the hybrid structures. This n-type semiconducting material offers appealing properties including a wide band gap, high optical transparency, chemical and thermal stability and simple preparation[16,132,133]. Aluminum doped ZnO (Al:ZnO, Nanograde N-10x, 15 nm of mean primary particle size, 2.5 wt% in isopropyl alcohol) nanoparticle layers have been used for controlling the electron transport properties in inverted structures. ZnO nanoparticle provides here easy and low-cost processing, and platforms to control the charge transport properties of ZnO film by the doping concentration of Al [134–136]. Recently, an aliphatic amine interlayer such as PEI and PEIE have been widely applied to enhance electron injection or electron extraction at the interface between the active layer and the cathode. In addition, PEI and PEIE have been deposited on oxide ETL such as ZnO and TiO_2 because they modify the work function via the high interfacial dipole moment of polymer's polar side chains [122,137,138]. The partially protonated amine in the aqueous solution from PEI molecular as shown in ***Figure 5.4.1a*** strongly interacts with the oxygen ions of the ZnO surface and then forms interfacial dipole layer. The interfacial dipole reduces the work function of ZnO layer through the vacuum level shift (Δ in ***Figure 5.4.1b***) [39]. Here, the performance of inverted QLEDs fabricated with synthesized InP/ZnSe/ZnS QDs, commercially available aluminum doped ZnO (Al:ZnO) NP and PEI interfacial layer was investigated.

UV-visible absorption and PL spectrum of InP/ZnSe/ZnS multishell colloidal QDs are shown in ***Figure 5.4.2a***. The multishell QDs exhibit an emission peak at 554 nm which corresponds to a green color with an FWHM of 62 nm. The QY of InP QDs is 50% in solution and 11% in thin films. ***Figure 5.4.2a*** also presents the EL spectra of InP-based inverted QLEDs fabricated with the PEI modified Al:ZnO layer. The normalized EL spectrum of InP/ZnSe/ZnS QLEDs shows green emission at 565 nm which does not

change when the applied voltage increases (***Figure 5.4.2b***). The EL peak of QLEDs is broadened and red shifted by 12 nm when compared to the PL signal in solution. It is a common phenomenon of QLEDs that comes from the ensemble of QDs in the thin film and the quantum confined Stark effect [102,103].

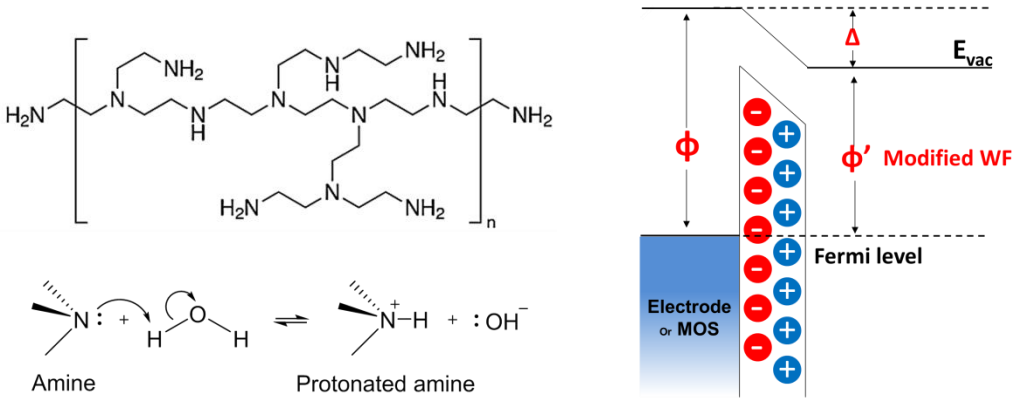

(a) (b)

Figure 5.4.1 (a) The PEI molecular structure (scheme of protonated functional amine) and (b) proposed work function reduction scheme with interface dipole of PEI layer.

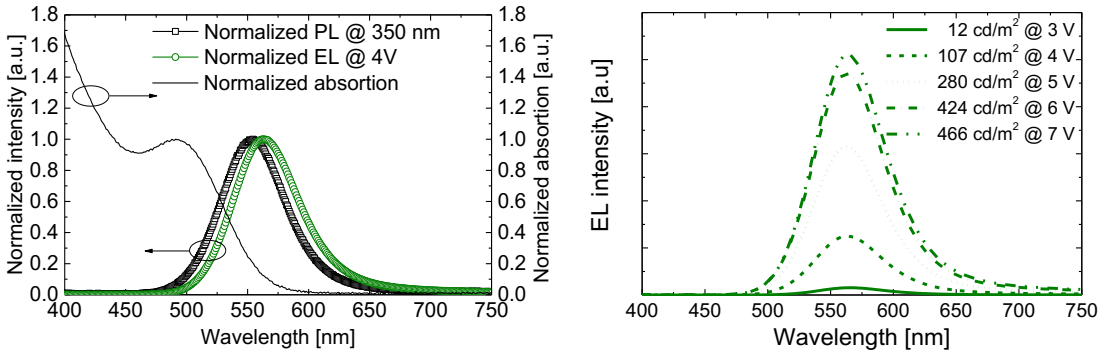

(a) (b)

Figure 5.4.2 (a) UV-vis absorption and PL spectrum of colloidal InP/ZnSe/ZnS QDs are compared with EL spectrum, and (b) the change of EL spectra of inverted QLEDs as a function of the applied bias (device with PEI in the mixture of IPA, ethanol and H_2O (A1)).

Figure 5.4.3 presents a cross-sectional schematic of the InP-based inverted QLEDs and a corresponding energy band diagram. The energy levels of TCTA and MoO_3 are based on the reference [139]. The inverted structure was carefully designed to achieve efficient carrier injection and balance considering energy band alignment and material properties. MoO_3 has excellent hole mobility, high environmental stability, and transparency and it works as an anode buffer which provides an ohmic contact between Ag and TCTA. In order to facilitate the hole transport to the valence-band edge of the

InP/ZnSe/ZnS QDs, TCTA was used. In addition, this material also functions as an electron blocking layer with 2.1 eV of lowest unoccupied molecular orbital (LUMO). Commercially available Al:ZnO NPs were used to reduce the electron injection barrier from ITO to CBM of QDs. However, an energy offset of around 1 eV still remains. The PEI buffer layer was introduced to enhance electron injection from Al:ZnO to the QD layer. The high interfacial dipole moment of the aliphatic amines modified the work function of the Al:ZnO layer. In addition, PEI can be easily prepared under ambient condition from dilute solution in environmentally friendly solvents such as 2-methoxyethanol (2ME), ethanol, isopropanol (IPA) and deionized water [140].

It is investigated how PEI layer on the top of Al:ZnO layer influence the performance of the InP-based inverted QLEDs. As a control device, only Al:ZnO was used as the ETL without the interfacial layer. The performance of the two devices with the PEI interlayer which was deposited from two different solvents, either 2ME or a mixture of IPA, ethanol and H_2O (A1), was compared.

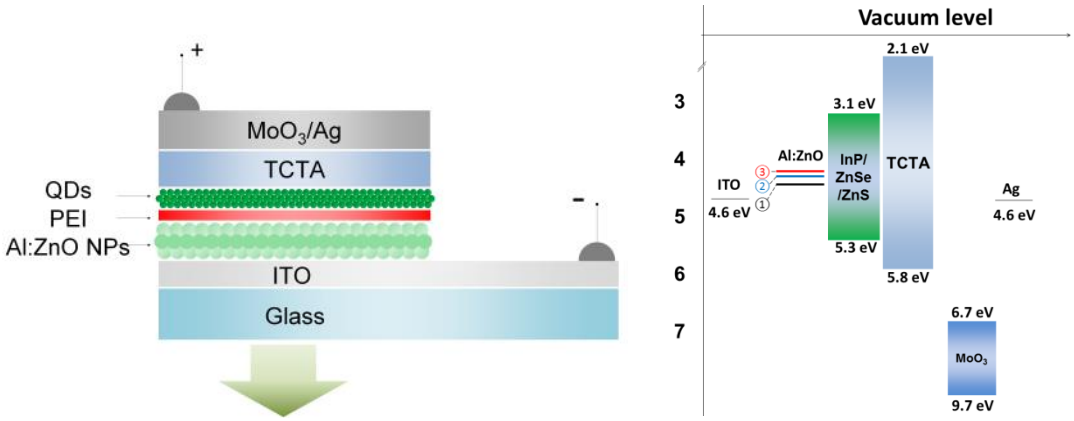

Figure 5.4.3 (a) cross-section schematic and (b) an energy band diagram of inverted QLEDs. (see the ***Appendix B.1*** for film deposition process)

Current density-voltage, current efficiency-current density and luminance-voltage characteristics of the devices are presented in ***Figure 5.4.4***. Turn-on voltage at 1 cd/m^2, maximum current efficiency, and luminance of inverted devices are summarized in ***Table 5.2***. The maximum current efficiency and luminance of the control device with only Al:ZnO layer reached 0.07 cd/A and 221 cd/m^2, respectively. These values were dramatically increased to 3.17 cd/A and 466 cd/m^2, respectively when using the PEI interlayer which was deposited from the alcohol mixture A1. The leakage currents at the ohmic conduction region under 2 V were suppressed by inserting the PEI interlayer which can be seen in the J-V curves in ***Figure 5.4.4b***. The current density of the device

over 5 V can explain more about the PEI thickness effects in ***Figure 5.4.4d***. The current density and J-V slope in J-V curves for the device with Al:ZnO/PEI in A1 were lower than the others. Since PEI layer prepared with Al solvent leads to even thinner QD layer, the higher resistance of the device is originated from the thicker PEI layer (***Table 5.3***). Concerning the solvent which was used to deposit PEI, the alcohol mixture results in the higher current efficiency, luminance and lower leakage current of the devices.

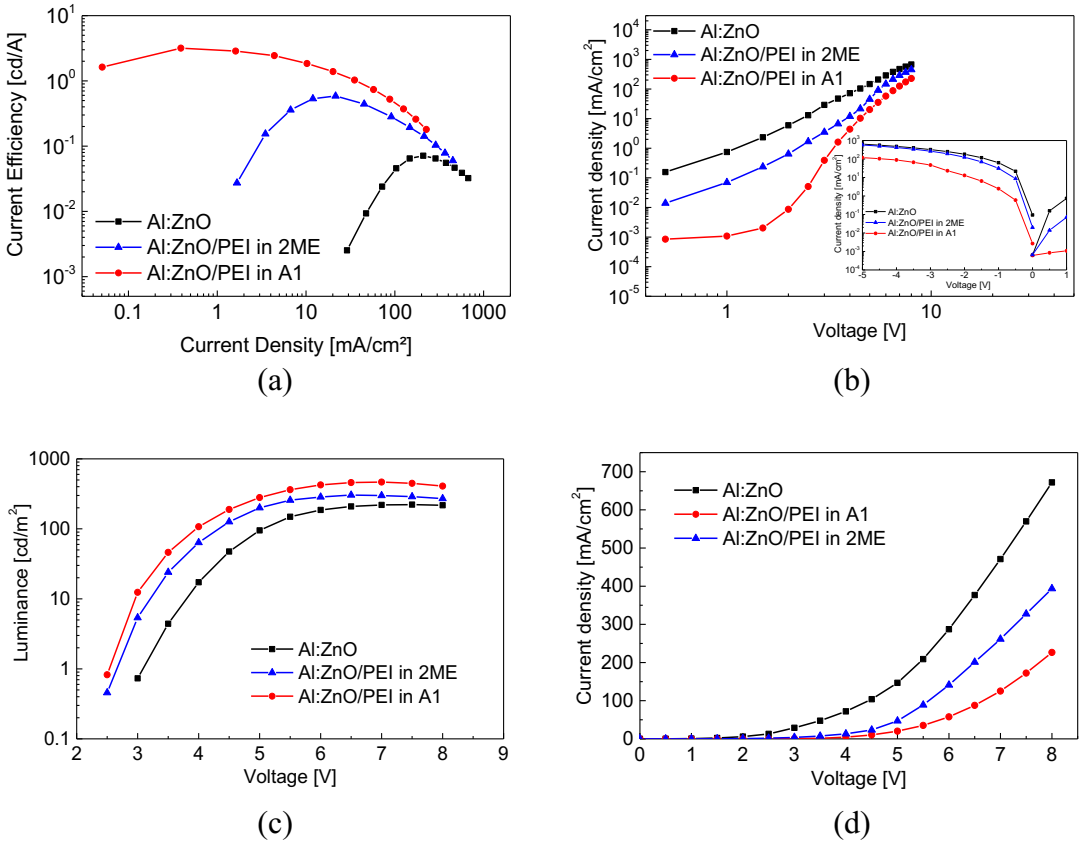

Figure 5.4.4 (a) Current efficiency-current density, (b) current density-voltage (log-log), (c) luminance-voltage and (d) current density-voltage (linear) characteristics of InP/ZnSe/ZnS QLEDs. *(YH136, YH148, YH150)*

Table 5.2 Surface roughness and WF for different thin film layers and the summary of the inverted device performance.

Thin films	Roughness (nm)		IE (eV)	Voltage (V) @ 1 cd/m²	Max. efficiency (cd/A)	Max. luminance (cd/m²)
	R_q	R_{pv}				
ITO	2.37	24.58	4.58	-	-	-
ITO/Al:ZnO ①	6.05	51.12	4.33	3.1	0.07	221
ITO/Al:ZnO/PEI in 2ME ②	5.77	47.40	4.19	2.6	0.59	304
ITO/Al:ZnO/PEI in A1 ③	4.87	41.26	4.10	2.5	3.17	466

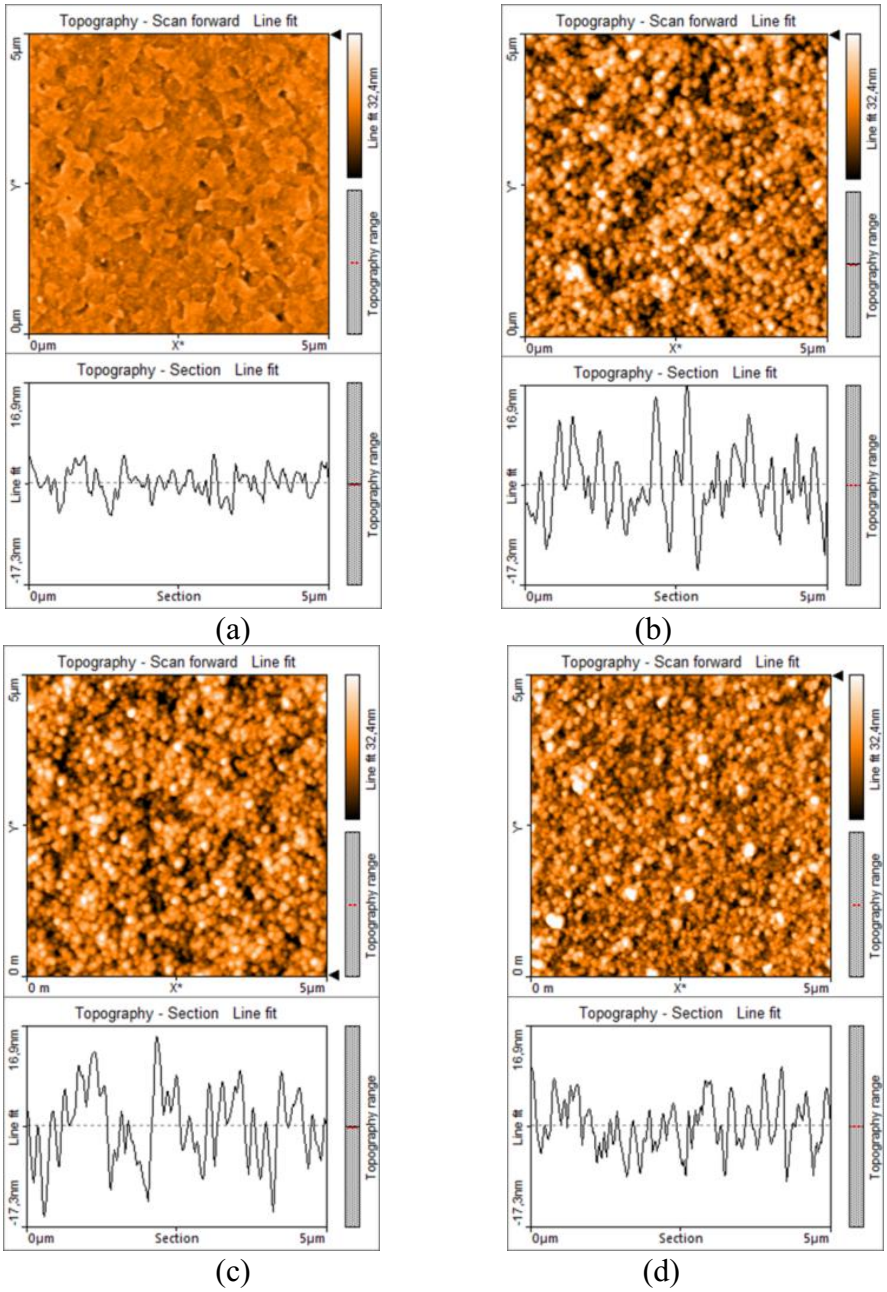

Figure 5.4.5 AFM images of (a) ITO, (b) ITO/Al:ZnO, (c) ITO/Al:ZnO/PEI in 2ME and (d) ITO/Al:ZnO/PEI in A1. (An area of 5 × 5 μm^2 was measured by AFM, and the vertical scales of all the height images are all fitted at 32.4 nm)

Controlled leakage current behavior can be explained by a change in the surface roughness of the Al:ZnO layer as shown in the AFM images from ***Figure 5.4.5***. The ITO substrate used for device fabrication shows a root mean square roughness (R_q) of 2.37 nm and a peak to valley roughness (R_{pv}) of 24.58 nm (***Figure 5.4.5a***). Compared to the ITO substrate, Al:ZnO has higher R_q and R_{pv} roughness of 6.05 nm and 51.12 nm, respectively (***Figure 5.4.5b***). However, the PEI interlayer has an effect on the surface roughness of Al:ZnO layer. The R_q and R_{pv} roughness were calculated to be 5.77 nm and

47.40 nm, respectively, when using 2ME to dissolve PEI (***Figure 5.4.5c***). Furthermore, values of 4.87 nm and 41.26 nm were found when the PEI was deposited from the alcohol mixture A1 (***Figure 5.4.5d***). Based on the AFM measurements, the deep valleys in the Al:ZnO appeared to be filled more, and the surface roughness was also modified to a larger degree with the PEI when deposited from the alcohol mixture A1. Since PEI is an insulating material, it also suppressed the leakage current even though its thickness was roughly around 1 nm.

The estimated IE of the Al:ZnO layer and the PEI modified Al:ZnO layer by PESA shown in the band diagram in ***Figure 5.4.3b*** and ***Table 5.2*** can also explain the enhancement of device performance. The films which were used to measure the IE were prepared in a same way as the devices. The IE of Al:ZnO, Al:ZnO/PEI in 2ME and Al:ZnO/PEI in the alcohol mixture A1 were 4.33 eV, 4.19 eV, and 4.10 eV, respectively. As the PEI was applied on the Al:ZnO, the energy barrier from the ETL to the QDs was reduced from 1.03 eV to 0.8 eV. However, the IE difference between A1 and 2ME is relatively low, only 0.09 eV. The change of IE decreased the turn-on voltage and increased the current efficiency. The energy barriers for electron between HTL to QD can be reduced during operation of the QLEDs by band bending of PEI interfacial layer due to the applied electric field. For the comparison of the two different solvents, the alcohol mixture A1 and 2ME, variations in the thickness of the Al:ZnO film and the QD film (***Table 5.3***) were observed. The thickness of Al:ZnO layer measured after film annealing was around 45 nm. After spin-coating PEI in alcohol mixture, the total thickness of Al:ZnO/PEI was reduced to around 28 nm. It was not observed when spin-coating PEI in 2ME. Electron transport can be facilitated with a thinner Al:ZnO layer in this case. The thickness of the InP-based QDs deposited on the PEI layer with the alcohol mixture A1 and 2ME was around 3 nm and 18 nm, respectively, even though they are deposited with the same condition. According to these thickness differences, it was possible to assume that the PEI layer prepared with alcohol mixture 2ME had better wetting properties to InP-based QD solutions. This different thickness of QDs would change the carrier transport behavior in the device as well (see the ***Chapter 6***). The lower current density of the device with Al:ZnO/PEI in A1 at high applied voltage even though the thinner HTL and QD layer indicates that the thicker PEI layer remained on the Al:ZnO layer.

Consequently, the lower IE, the smoother surface roughness, the thickness reduction of the Al:ZnO ETL layer and QD layer, and the increase of the PEI thickness (it would

disturb the electron injection to QDs, however, here other positive change for better electron transport suppressed the thick PEI effect), controlled by PEI layer deposition from the alcohol mixture A1, improved the charge carrier balance in the multilayer device. However, the device shows low luminance compared to the results from other researches. This low luminance came from the leakage of the device which was still too high. This can be explained by a high current density under the reverse bias as shown in an inset of ***Figure 5.4.4b***. It was measured after the forward bias sweep from 0 V to 10 V. The local electric field concentrated at the high peak or valley area of the Al:ZnO film was suspected to generate short circuits or non-emitting areas in the device by electrochemical degradation of organic materials. The local electric field was getting stronger during the voltage sweep and accelerated the degradation process [141,142]. These current paths generated from the degradation made even higher current density under the reverse bias compared to the forward bias driving. The high roughness of the Al:ZnO layer, which may come from the fast evaporation of IPA during the spin-coating, the 15 nm of particle size and possible particle agglomeration, are the main reasons for the serious leakage current. It is well known that a smooth surface layer, in particular for the deposition of uniform QDs, is quite essential for high performance and stability of QLEDs in both conventional and inverted structures.

Figure 5.4.6a,b show the microscope images of ITO/Al:ZnO/PEI layer and ***Figure 5.4.6c,d*** show EL images from the device fabricated with corresponding layers. ***Figure 5.4.6a*** of Al:ZnO/PEI in A1 layer show radial pattern because the PEI in A1 solvent washed out the Al:ZnO layer and remained non-uniform film during the spin-coating process. Moreover, this different uniformity of PEI layer directly brings the different EL consistency in the pixel area in ***Figure 5.4.6c***. It is expected that the radial pattern could increase the total amount of QD emitter in the pixel area and also could improve the outcoupling efficiency, which could increase the device performance.

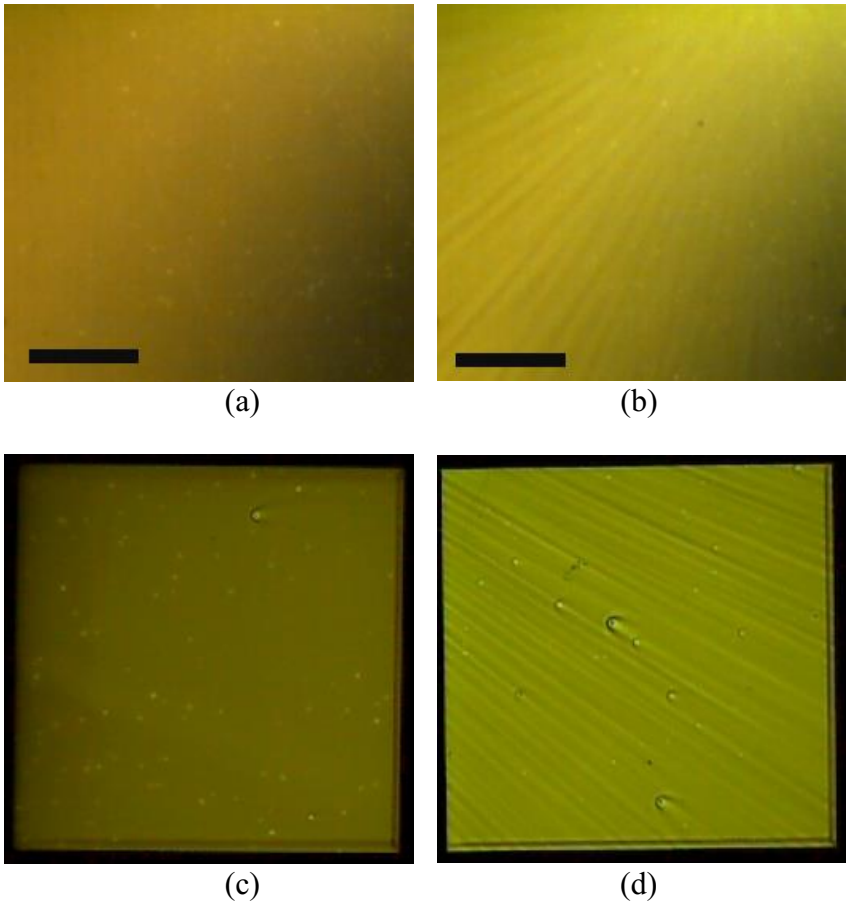

Figure 5.4.6 Microscope images of (a) ITO/Al:ZnO/PEI in 2ME and (b) Al:ZnO/PEI in A1(scale bar: 400 μm), and (c), (d) corresponding EL images captured under 4 V driving with pixel area of 4 mm^2, respectivley.

The change of multilayer thickness

Table 5.3 Thickness of different multilayer. (The thickness was measured Dektak 150 and the values were the average of the 3 ~ 4 points.)

Thin films	Thickness (nm)
ITO/Al:ZnO	45.08
ITO/Al:ZnO/QDs	57.0 (QD: 11.9)
ITO/Al:ZnO/PEI in 2ME	46.1 (PEI: 1.03)
ITO/Al:ZnO/PEI in A1	28.2 (PEI: -)
ITO/Al:ZnO/PEI in 2ME/QDs	64.0 (QD: 17.6)
ITO/Al:ZnO/PEI in A1/QDs	31.3 (QD: 3.03)

According to the measurement of multilayer thickness (***Table 5.3),*** the thickness of PEI layer deposited with 2ME was around 1 nm. It was impossible to measure the thickness of PEI layer deposited with a mixture of IPA, ethanol, and H_2O (A1) because the PEI solution reduced the thickness of Al:ZnO during the spin-coating process.

However, it is assumed that the PEI remained on the surface because the IE of the Al:ZnO layer was changed after the interfacial layer deposition. The thickness of QD layer was lower when it was deposited on the PEI layer using the alcohol mixture A1 because of the surface energy difference between the PEI layers.

Thickness control of Al:ZnO layer for further carrier balance

*Device: ITO/**Al:ZnO**/PEI in A1/QDs/TCTA/Ca/Ag*

In order to investigate the carrier balance of the device with PEI modified Al:ZnO layer, the thickness of Al:ZnO layer controlled by different spin-coating speed (rpm) during the thin film deposition process. ***Figure 5.4.7*** shows device performance according to the thickness change of ETL. The maximum current efficiency, luminance, turn-on voltage and the Al:ZnO film properties are summarized in ***Table*** 5.4. As the rpm increase from 1000 to 4000 rpm, the maximum current efficiency and luminance rose from 1.17 cd/A and 655 cd/m^2 to 3.54 cd/A and 727 cd/m^2, respectively. The surface roughness (R_q and R_{pv}), especially R_{pv}, decreased as the spin-coating rpm increase, which produced the lower leakage current in the ohmic conduction region of J-V curves in the ***Figure 5.4.7b***.

Moreover, the enhanced device performance according to the decreased ETL thickness indicates that the injected electrons into the thin QD emitting layer were relatively lower than injected holes. Therefore, the facilitated electron transport by thinner HTL improved the carrier balance at the emitting layer and led to the higher device performance. The turn-on voltages (at 1 cd/m^2) in the luminance curves as a function of voltage are constant to 2.5 V, which also means the different thickness of HTL changed only the electron transport property. However, the current efficiency drops as luminance increase in ***Figure 5.4.7a*** is more serious with 4000 rpm**,** which corresponds to the stronger efficiency roll-off under the high current driving condition in ***Figure 5.4.7c***. The efficiency roll-off here may be attributed to the exciton dissociation at the higher driving voltage. The Al:ZnO would have not an excellent hole block property at the high driving voltage because the aluminum contents doped in ZnO layer could easily dissociate the exciton (hole) from the QDs to the electrode. This process could be more serious with thinner Al:ZnO layer. The high current density of the device even in the reverse bias sweep has an agreement for the exciton dissociation through the aluminum in Al:ZnO film. Therefore, the higher spin-coating rpm or thicker thickness for the Al:ZnO layer were not promoted for the device stability and high luminance in our

experiment. The EL spectra shown ***Figure 5.4.7d*** are measured under the 4 V of applied voltage, and it shows clear QD emission which is constant even though different ETL condition.

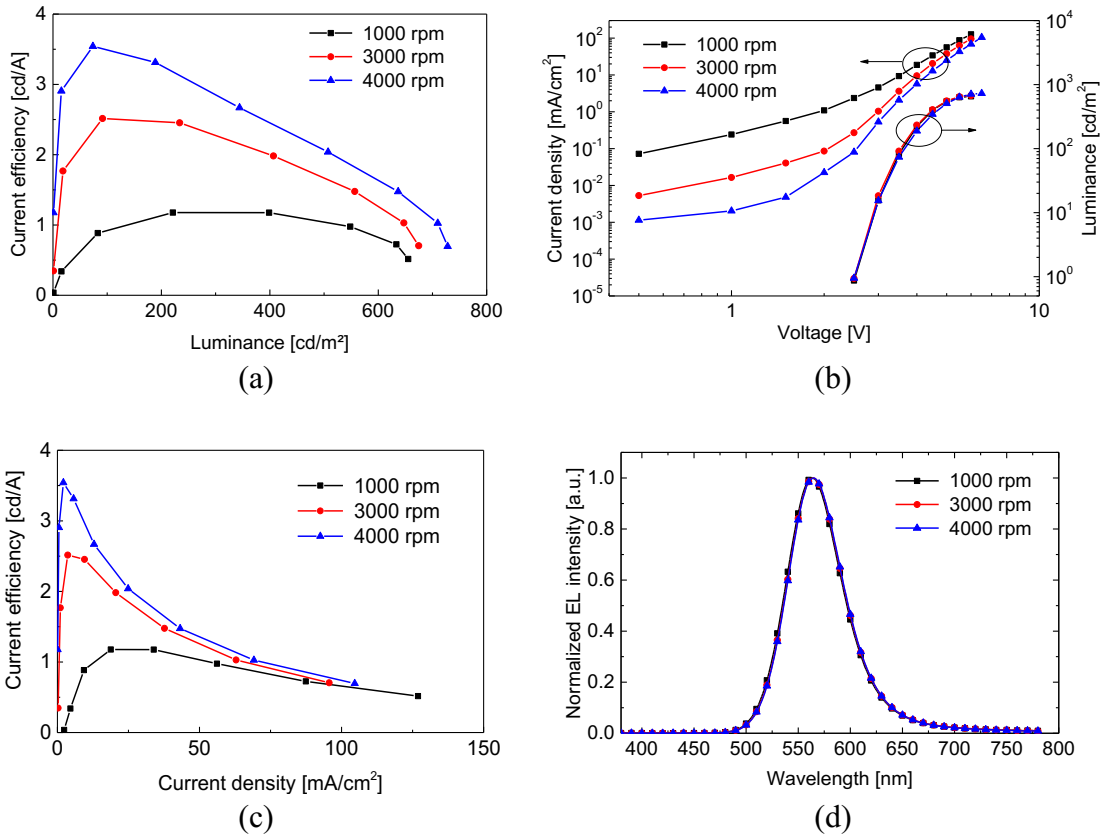

Figure 5.4.7 Device performance according to the change of Al:ZnO thickness. (a) Current efficiency-luminance, (b) current density-voltage (inset: luminance-voltage), (c) current efficiency-current density, and (c) EL spectra at 4 V. *(YH187,YH185, YH184)*

Table 5.4 Film properties from different RPM condition for Al:ZnO layer deposition.

Al:ZnO RPM	Thickness (nm)	Roughness (nm)		Voltage (V) @ 1cd/m^2	Max. efficiency (cd/A)	Max. luminance (cd/m^2)
		R_q	R_{pv}			
1000	62	6.82	74.51	2.5	1.17	655
3000	53	6.42	62.08	2.5	2.51	674
4000	46	6.27	55.82	2.5	3.54	727

5.4.2 ZnO nanoparticle ETL (Aldrich-721077, PS~100 nm)

ZnO nanoparticles solution purchased from Sigma-Aldrich (Aldrich-721077, PS~100 nm, 50 wt% in H_2O) were tested as ETL layer combined with PEI surface modification layer deposited from 0.1 wt% solution in A1 or 2ME solvent. The ZnO solution was diluted with a 50-fold excess of solvent and deposited on top of the cleaned ITO substrate.

The device performance is compared to the Al:ZnO nanoparticles. First of all, the film roughness from Aldrich ZnO was too high compared to the Al:ZnO nanoparticles, which leads to the high leakage current shown in ***Figure 5.4.8b*** and the low current efficiency under low luminance condition (***Figure 5.4.8a***). Here the leakage current value does not correspond to the surface roughness value because too high R_{pv} over 100 nm could bring unexpected leakage current pathway in the device. The thicknesses of the different layer are summarized in ***Table 5.6***.

. Comparing two devices fabricated with Aldrich ZnO nanoparticle, the PEI in 2ME shows higher luminance and efficiency compared to the PEI in A1. Here, the relatively high thickness of QD layer (c.a. 16 nm) from PEI in 2ME would bring the better charge balance by combining the delayed electron transport through thick PEI layer (c.a. 6 nm) under high driving voltage. The PEI is basically insulating material; therefore, such a thick layer would rather disturb the carrier transport even though it reduces the IE (***Table 5.5***). The thin QD layer produced from A1 solvent needs more electron injection into QDs compared to the holes to have better carrier balance (this analysis is based on ***Chapter 6.2 : The influence of QD layer thickness on different charge carrier transfers in the device***). However, the thick PEI layer (c.a. 8 nm) disturbed the electron transport and reduced the device performance by unbalancing the charge carrier in the QD layer. The charge (hole) accumulation originated from carrier unbalance in the QD layer reduced the current flow in the device by increasing the local depletion region. Therefore, the current density from J-V curve with PEI in 2ME (***Figure 5.4.8b***) is higher than PEI in A1. The device with PEI in 2ME also shows low turn-on voltage in ***Figure 5.4.8c*** even though it has thicker QD layer. Therefore, it is expected that the lower driving voltage is attributed to the thinner thickness of PEI layer.

The turn-on voltages with Al:ZnO nanoparticles are relatively high because the IE is higher than the Aldrich ZnO nanoparticles. ***Figure 5.4.8d*** shows the EL spectra from a different device, and they have a different red-shift from the PL spectrum (λ_{peak}: 555 nm) because they have different local electric field applied at the QD layer according to the different carrier charging and total device thickness.

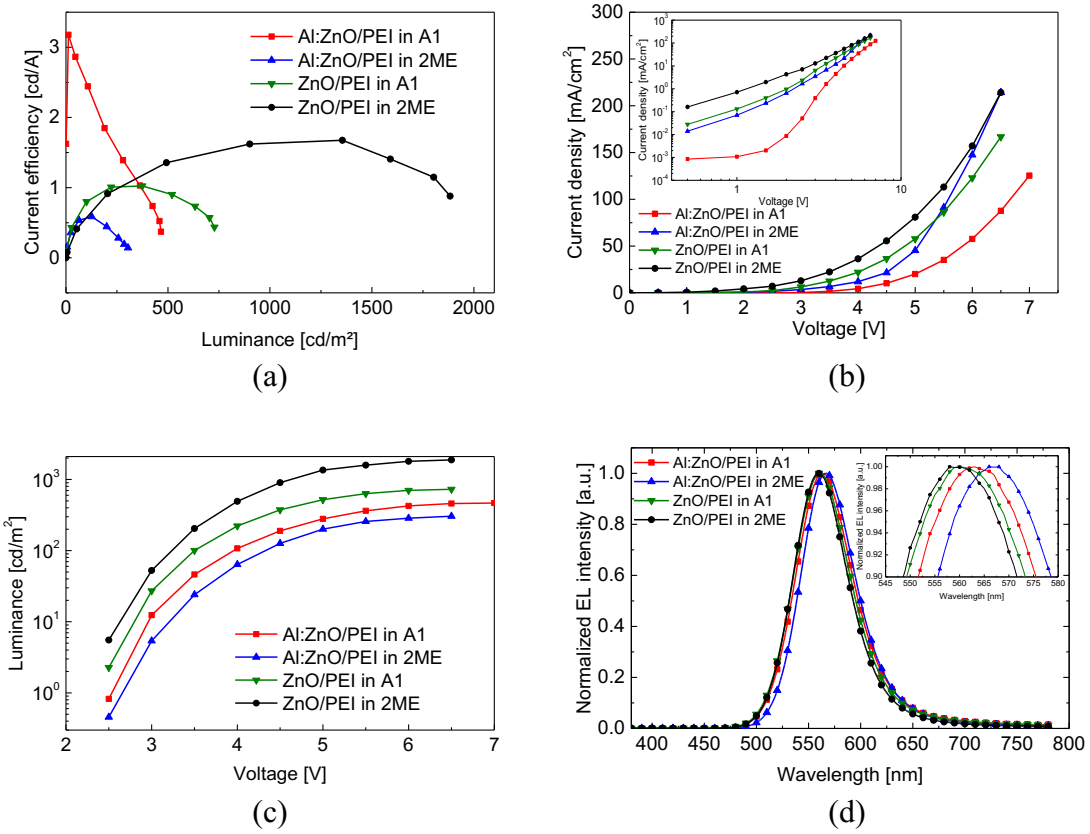

Figure 5.4.8 Device performance with Aldrich ZnO nanoparticles. (a) Current efficiency-luminance, and (b) current density-voltage (inset: logarithm current density-voltage). *(YH149, YH151)*

Table 5.5 Surface roughness and IE for different layers and the summary of device performance.

Thin films	Roughness (nm)		IE (eV)	Max. efficiency (cd/A)	Max. luminance (cd/m^2)
	R_q	R_{pv}			
ITO/ZnO	14.47	134.48	4.26	-	-
ITO/ZnO/PEI in A1	16.21	154.41	4.04	1.03	727
ITO/ZnO/PEI in 2ME	13.86	113.71	4.10	1.67	1883

Table 5.6 Thicknesses of different layers.

Thin films	Thickness (nm)
ITO/ZnO	31.5
ITO/ZnO/PEI in A1	39.6 (PEI: 8.0)
ITO/ZnO/PEI in 2ME	37.4 (PEI: 5.8)
ITO/ZnO/PEI in A1/QDs	42.9 (QD: 3.3)
ITO/ZnO/PEI in 2ME/QDs	54.0 (QD: 16.5)

5.4.3 Summary

Upon applying thin PEI interfacial layers from different solvents between Al:ZnO and InP-based QDs, the maximum current efficiency is increased from 0.07 cd/A to 3.17 cd/A (i.e. over 40 times). The leakage current is substantially suppressed, and the turn-on voltage is also reduced from 3.1 V to 2.5 V. As a result, the current efficiency is dramatically enhanced via controlled carrier balance in the QLEDs because the thin PEI interfacial layers modified the surface roughness, reduced the energy barrier from the CBE of Al:ZnO to the QDs by lowering the IE of the ETL through the interfacial dipole effects, and controlled the thickness of neighboring layers. It is believed that the PEI interfacial layers can be more effective for InP-based inverted QLEDs than Cd-based devices because the former has a higher energy barrier to inject electrons from the ETL to the CBE of QDs when compared to the latter.

With further decrease the thickness of Al:ZnO ETL with PEI modified structure, the efficiency and luminance increase up to 3.54 cd/A to 727 cd/m^2 by increasing the carrier balance with more electron injection into QD layer.

The bigger particles size of the Sigma-Aldrich ZnO nanoparticles leads to the low current efficiency. However, controlled carrier balance through thick QD and thick PEI layer as an insulator bring a higher current efficiency under the entire voltage sweep and a higher current efficiency under low luminance condition.

5.5 Carrier balance control with synthesized ZnO NPs and TAPC HTL

The level of current density at ohmic conduction region and reverse bias region indicate device leakage current which constrains the current efficiency and the luminance, especially under high driving voltage. ***Figure 5.5.1*** shows J-V characteristics of devices fabricated with different interface conditions between ITO and QD layer. In ***Figure 5.5.1a***, the inverted device without other interface materials shows around 10^{-3} mA/cm^2 of current density, however, the leakage current increase around 3~4 orders of magnitude when Al:ZnO layer was applied. This leakage current could be suppressed somehow by adopting PEI layer. Moreover, the EL images of the devices fabricated with Al:ZnO in inverted structure (i.e. ITO/Al:ZnO/QDs...) in ***Figure 5.5.2a*** shows brighter spots which may be originated from the aggregation of QDs or ZnO nanoparticles. However, the images from ***Figure 5.5.2b*** fabricated without any ZnO (i.e. ITO/QDs…) does not show the spots in EL. A device with the conventional structure fabricated with Al:ZnO ETL (i.e. …QDs/Al:ZnO/CaAg) has also these spots in ***Figure 5.5.2c*** and the high leakage current as well in ***Figure 5.5.1b***, but a device with TPBi as ETL shows very uniform EL emissions with lower leakage current. The Al:ZnO nanoparticles have 15 nm of particle size but it has agglomeration in the solution with haze (i.e. milky solution), which results in the high surface roughness especially with the value of R_{pv}. From this observation, it could be addressed that the Al:ZnO nanoparticles lead different current flow through high surface roughness and bring the brighter spots in the devices. Therefore, it is important to have homogeneous ZnO layer to get high performance and stability of QLEDs. Since most of the commercial ZnO nanoparticle dispersions have this problem, here, the clearly dispersed small ZnO nanoparticles were synthesized and applied to the device to have a smooth surface and desirable electronic properties for QLED driving. As J-V curves (***Figure 5.5.1b***) and EL images (***Figure 5.5.2e***) show, the small nanoparticles reduced leakage current effectively and brought the uniform EL as well. This chapter is dedicated to the development of efficient inverted QLED based on the synthesized ZnO nanoparticles.

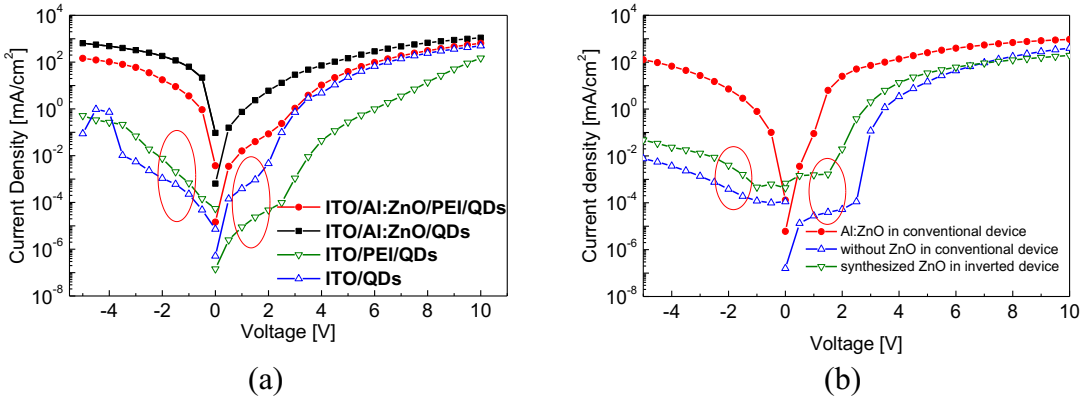

Figure 5.5.1 Current density-voltage characteristics with various device structures. (a) Inverted devices with different ITO/QD interface design, and (b) conventional devices with different QD/cathode interface design (including inverted device fabricated with synthesized ZnO nanoparticles).

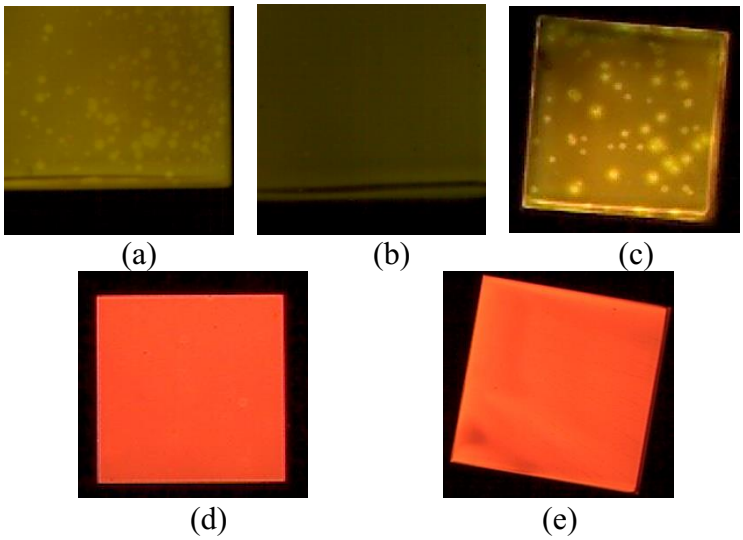

Figure 5.5.2 Electroluminescence pictures from 4 mm^2 of pixels. (a) ITO/Al:ZnO/QDs/TCTA/MoO_3/Ag, (b) ITO/QDs/TCTA/MoO_3/Ag, (c) ITO/PEDOT:PSS/poly-TPD/QDs/Al:ZnO/Ca/Ag, (d) ITO/Synthesized ZnO/QDs/TCTA/MoO_3/Ag and (e) ITO/PEDOT:PSS/poly-TPD/QDs/TPBi/Ca/Ag.

5.5.1 ZnO dispersion for uniform film deposition

Clear ZnO nanoparticle solution was obtained from the sol-gel synthesis method based on the literature [104,143] (***Appendix A.3***). After the washing of ZnO nanoparticles, ZnO precipitations from the centrifuge were dispersed in different alcoholic solvents such as ethanol, 2-methoxyethanol and 1-butanol and so on. However, the particles could not be clearly dispersed in these solvents but remained agglomeration

with the milky solution shown in ***Figure 5.5.3***. Ethanolamine, added during the synthesis to stabilize the particles, could be removed from the nanoparticle surface during the washing steps. Therefore, the particles become agglomerated seriously. It is the common problems with commercial ZnO nanoparticles, and they always do not have clear dispersion, which leads the high surface roughness of thin film. ***Figure 5.5.3b*** shows the AFM images of ZnO film prepared from the butanol solvent. The solution became clear after the filtration, but it had a relatively low concentration which only partially covered ITO layer with 61 nm of high R_{pv} roughness.

(a)

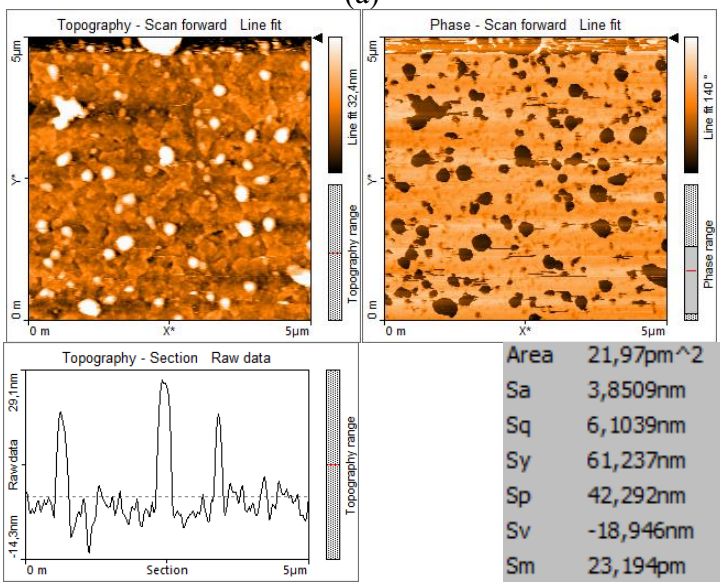

(b)

Figure 5.5.3 (a) Dispersion of ZnO nanoparticles in a different alcoholic solvent and (b) AFM images of thin ZnO thin film prepared from butanol solvent (The ZnO solution was filtered with 0.2 μm PTFE filter and spin-coated on top of cleaned ITO).

Since it is important to have clear ZnO dispersion for homogeneous film, ethanolamine was added more with a volume ratio of 1:0.04 to the milky solution. The ZnO solutions with extra ethanolamine were becoming clear, and the one with butanol became clearly transparent (***Figure 5.5.4b***). Finally, the surface roughness of ZnO film can be modulated by the combination of the solvent and ethanolamine concentration as shown in ***Figure 5.5.4c,d*** and ***Table 5.7***. The solution with ethanol and ethanolamine could deposit the film with high roughness around 146 nm of R_{pv}, but it decreased to

11 nm with butanol and ethanolamine combination. Moreover, the ultra-smooth surface of ZnO layer leads to the homogeneous deposition of QD film on top of it. ***Figure 5.5.4e*** shows the QD film also has a very low surface roughness about 1.1 nm and 12 nm of R_q and R_{pv}, respectively.

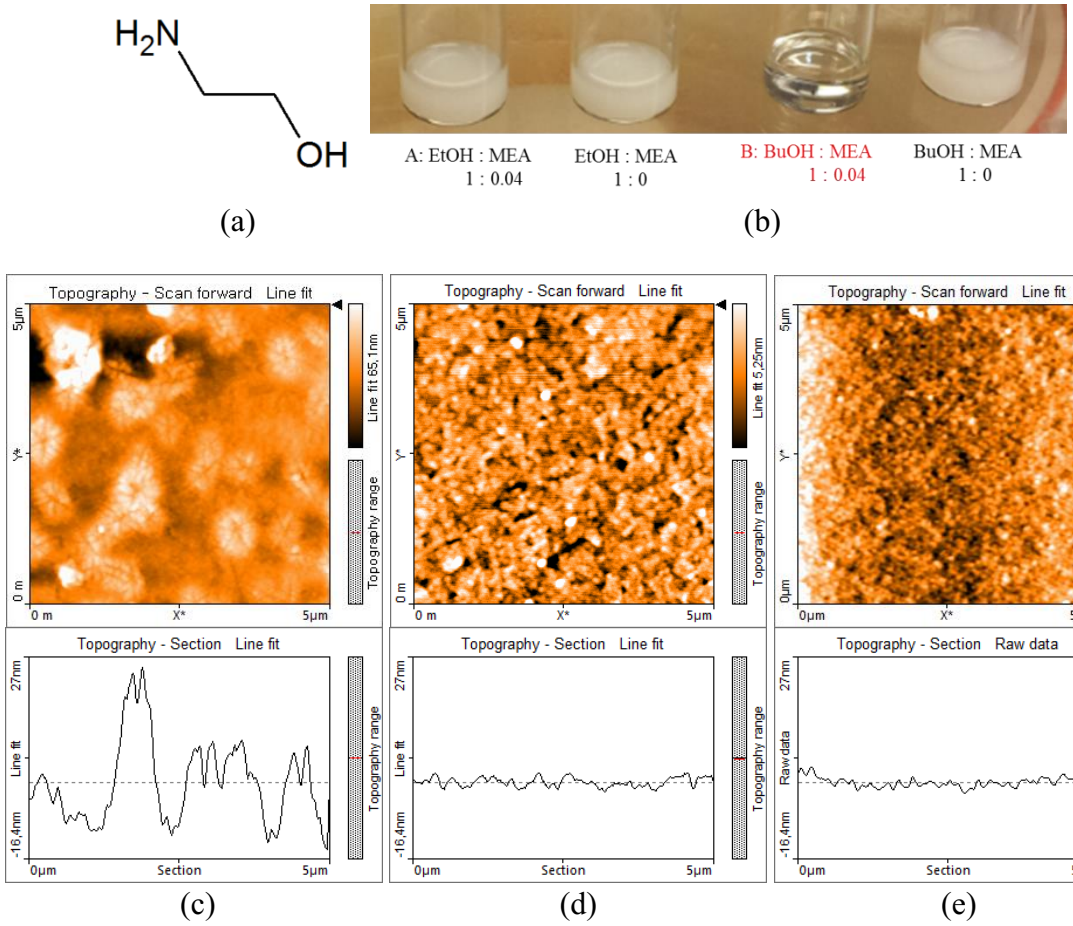

Figure 5.5.4 (a) Chemical structure of ethanolamine (ethanolamine combine the properties of amines and alcohols in one molecule, they exhibit the unique capability from both groups.) and (b) the ZnO solution with extra ethanolamine. The AFM images of ZnO film from the solution of (c) ethanol:ethanolamine = 1:0.04 and (d) butanol:ethanolamine = 1:0.04. (d) The AFM images of QD film deposited on ZnO layer (film deposition: 0.2 µm PTFE filter, 3000 rpm 30 sec, 180 °C 5 min, 10 mg/mL CI938).

Table 5.7 Surface roughness of different ZnO film.

Thin Film	Area (μm^2)	Roughness	
		R_q (nm)	R_{pv} (nm)
ethanol:ethanolamine = 1:0.04	25	12.3	146
butanol:ethanolamine = 1:0.04	25	1.1	11
ITO/ZnO/QDs	25	1.1	12

Figure 5.5.5a shows the normalized absorption spectrum and PL spectrum with an excitation wavelength of 325 nm from the ZnO nanoparticles clearly dispersed in 1-butanol with additional ethanolamine. The ZnO nanoparticles have an absorption peak at 324 nm and broad green emission with 540 nm of peak wavelength. In general, the broad fluorescence of ZnO nanoparticles was attributed to the intrinsic or extrinsic defects in ZnO nanoparticles, which still has controversies on the origin of defect centers [144–147]. However, green emission is quite a common defect emission in ZnO nanostructures.

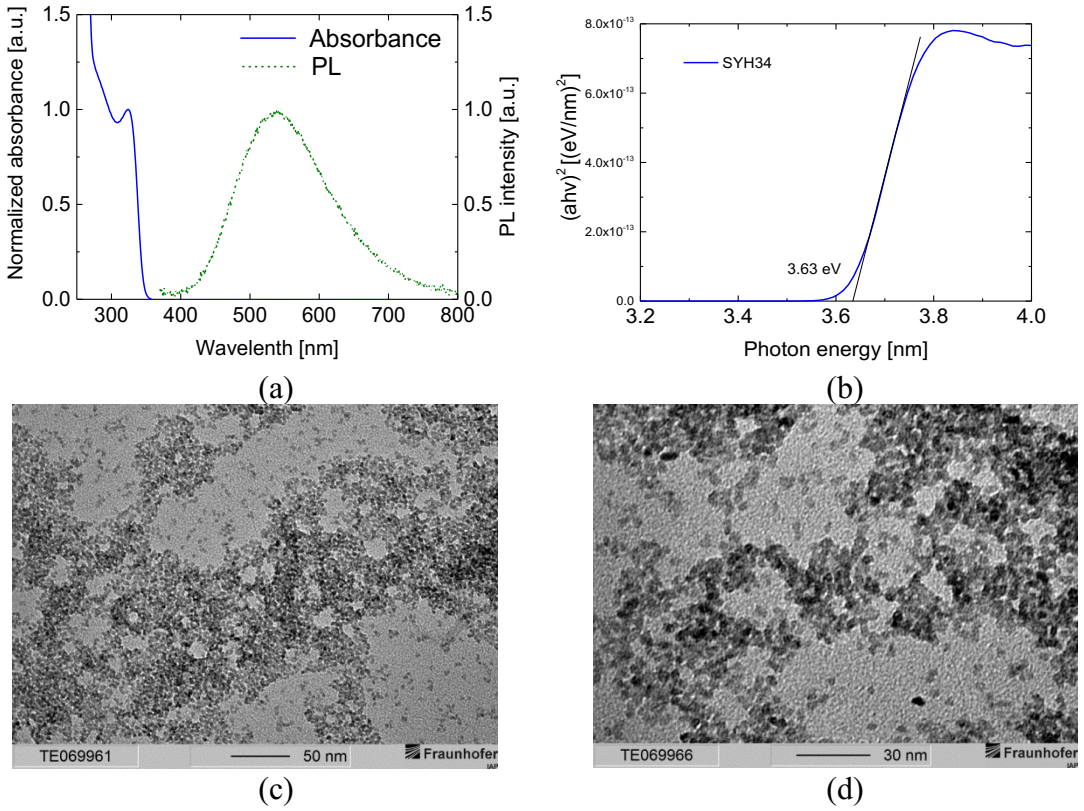

Figure 5.5.5 (a) Normalized UV-vis absorbance and PL spectrum and (b) a Tauc-plot for band gap estimation of ZnO nanoparticles. (c), (d) TEM images of ZnO nanoparticles.

Among the theories for the green band emission, the most widely accepted theory is the recombination of electrons close to the conduction band and deeply trapped holes at mid-gap states; however, it is not a universal explanation for a green emission mechanism. The deep trap levels are attributed to a neutral (V_o), singly charged (V_o^+), doubly charged (V_o^{++}) oxygen vacancy leveled around 1.6 ~ 2 eV lower from the conduction band, shown in ***Figure 5.5.6*** [144,146,148,149]. The Tauc-plot based on the absorption curve was drawn in ***Figure 5.5.5b*** to estimate the ZnO band gap, and it shows around 3.63 eV similar to the reported value. The particles size was measured to

3.8 nm ± 0.3 nm from TEM images (***Figure 5.5.5c,d***) through over 50 particles. TEM images also show the particles have very homogeneous size distribution as well.

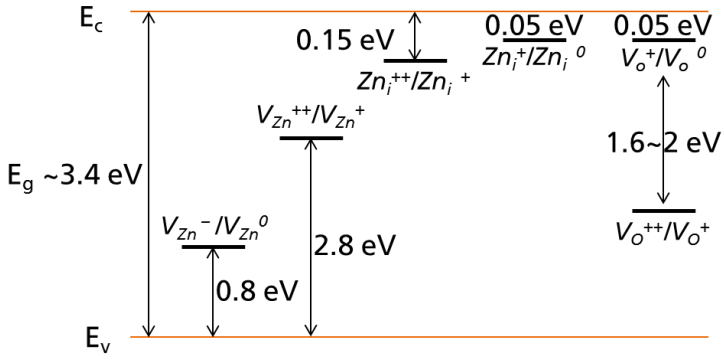

Figure 5.5.6 Energy levels of native defects in ZnO [146]. (V = vacancy, O = oxygen, $^{+}$ indicates positive charge, ^{0} indicates zero charge and $_{i}$ indicates interstitial site)

In ***Figure 5.5.7***, the UV-vis absorbance and Tauc-plots show the comparisons of commercially available and synthesized ZnO particles. Relatively smaller particles size of synthesized ZnO nanoparticles leads lower absorption peak with much larger band gap compared to others. The inset figures in ***Figure 5.5.7a*** shows a completely clear ZnO dispersion without agglomeration and the green illumination under the 312 nm UV exposure.

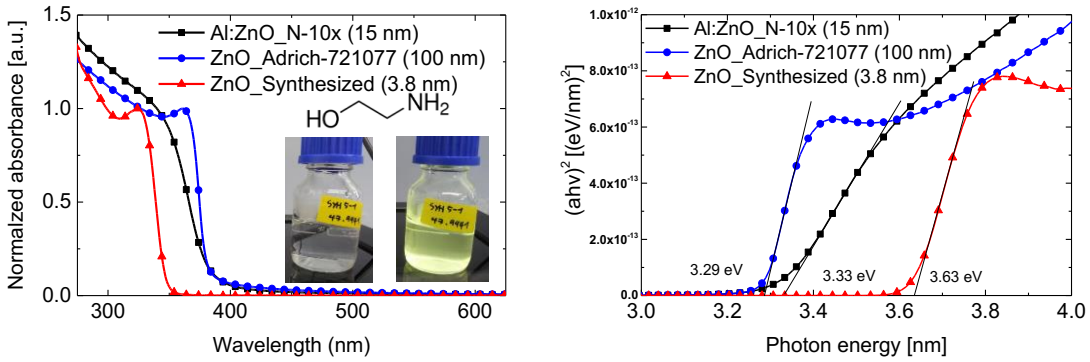

Figure 5.5.7 Normalized UV-vis absorbance and (d) a Tauc-plot for band gap estimation of different ZnO nanoparticle solution.

Table 5.8 shows film thickness and surface roughness difference from these ZnO solutions. R_{pv} effectively reduced to 11 nm by small particle size and good dispersion. Moreover, the film thickness could be reduced more compared to the other ZnO nanoparticles by the small particle size, which would bring the feasibility to control the carrier transport by the ETL thickness.

Table 5.8 Film properties from different ZnO nanoparticles film (deposition: 0.2 μm PTFE filter, 3000 rpm 30 sec, 180 °C 5 min)

Thin Film	ZnO Particle size (nm)	Layer thickness (nm)	Roughness	
			R_q (nm)	R_{pv} (nm)
ITO/ZnO (Aldrich)	100	37	14.47	134.48
ITO/Al:ZnO (Nanograde)	15	45	6.0	51.1
ITO/ZnO (Synthesized)	3.8	15	1.1	11

5.5.2 Efficiency enhancement with multiple spin-coated ZnO NP layer

Interestingly, our ZnO nanoparticles have a feasibility of orthogonal process itself for the layer-by-layer deposition process. Other layer-by-layer processes used to increase the thickness of nanoparticle need buffer layer to protect under layer followed by next coating process [150,151]. However, the stabilized nanoparticle dispersion with ethanolamine provides simple layer-by-layer process without any buffer layer. In the reference, it has been suggested that highly (0 0 2) direction (*c*-axis) oriented ZnO nanoparticle films prepared by the sol-gel and colloidal nanoparticle solution have a feasibility of multilayer system by self-buffer layer process [152,153]. Especially, colloidal nanoparticle solution can be deposited preferentially along the c-axis direction to reduce free surface energy (i.e. (0 0 2) plane of ZnO nanoparticle has the minimum surface free energy), which would make the film more stable against the upcoming solution during the multi spin-coating process [152]. During the annealing process, the diffusion and migration of atoms between the neighboring particles produce coalescence of the adjacent ZnO nanoparticles, which also makes the ZnO film more rigid [152]. Moreover, the annealing process which applied after each spin-coating process makes the particles more coalescence together by removing ethanolamine from the film in our process. The ZnO film was annealed at 180 °C to remove ethanolamine surfactant based on the TGA results of ZnO nanoparticles in ***Figure 5.5.8a***. The mass of ZnO nanoparticles reduced rapidly after 180 °C, and a derivative thermogravimetric (DTG) curve has a peak around 200 °C, which is expected to be originated from the ethanolamine evaporation. Even though ethanolamine has 170 °C of boiling point, it could be removed at relatively higher temperature than a boiling point because it is bonded to the surface of ZnO nanoparticles (i.e. Amine group of ethanolamine could

have covalent bonding with Zn atoms at the surface of ZnO nanoparticle). Additionally, ZnO nanoparticles have a natural affinity to attract and hold some moisture in the air (i.e. hygroscopic) because of highly active surface properties originated from nanostructure with high surface-to-volume ratio. Therefore, the deposited film with commercial ZnO nanoparticles become soft when it is exposed in the air and the film can be easily scratched by steel tweezer. However, the film prepared with our synthesized ZnO nanoparticles is rigid against the scratch even in ambient conditions, which could support more about the rigid film formation from synthesized ZnO nanoparticles.

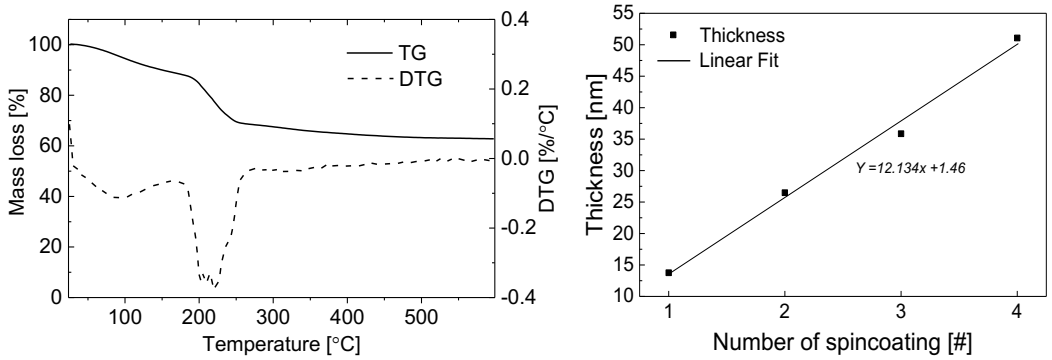

(a) (b)

Figure 5.5.8 (a) TGA and DTG curves from the synthesized ZnO nanoparticles, and (b) thickness of multilayered ZnO nanoparticles as a function of spin-coating number with orthogonal solution process.

Table 5.9 Film properties with different ZnO nanoparticles film (deposition: 0.2 μm PTFE filter, 3000 rpm 30 sec, 180 °C 5 min)

ZnO	Thickness (nm)	Area (μm^2)	Roughness R_q (nm)	Roughness R_{pv} (nm)	Max. efficiency (cd/A)	Max. EQE (%)	Max. luminance (cd/m^2)
2k × 1	14	25	1.17	32.40	5.5	1.8	1360
2k × 2	26	25	1.01	11.04	6.2	1.9	1340
2k × 3	36	25	0.85	13.55	7.8	2.4	1400
2k × 4	51	25	0.71	10.15	10.1	3.1	1500

Table 5.9 and ***Figure 5.5.8b*** show that the ZnO film thickness increased linearly as the number of spin-coating increase. The thickness is increased without damaging under ZnO layer. Moreover, the surface roughness in both R_q and R_{pv} also reduced from 1.17 nm and 32.40 nm to 0.71 nm and 10.15 nm, respectively. The modulated ZnO films were applied in an inverted structure (ITO/ZnO/QDs/TCTA/MoO_3/Ag) QLED depicted in ***Figure 5.5.9a***. The device performance was readily improved in terms of maximum luminance and efficiency, as shown and summarized in ***Figure 5.5.10a,b*** and ***Table 5.9***. The maximum luminance and efficiency were increased from 5.5 cd/A and

1360 cd/m^2 with one-time spin-coated ZnO layer to 10.1 cd/A (EQE: 3.1 %) and 1500 cd/m^2 with four times spin-coated ZnO layer, respectively. Here, 10 mg/mL QD solution was used to deposit around 10 nm emitting layer. The device with multiple QD layers are expected to have more electrons accumulated at the QD/TCTA interface compared to the holes concerning the band alignment (***Figure 5.5.9b***), and electron and hole mobility in the QD layer (explained more in ***Chapter 6***). Therefore, the delayed electron transport by thicker ZnO layer improves the carrier balance at the RZ near the QD/TCTA interface, which leads to the higher current efficiency.

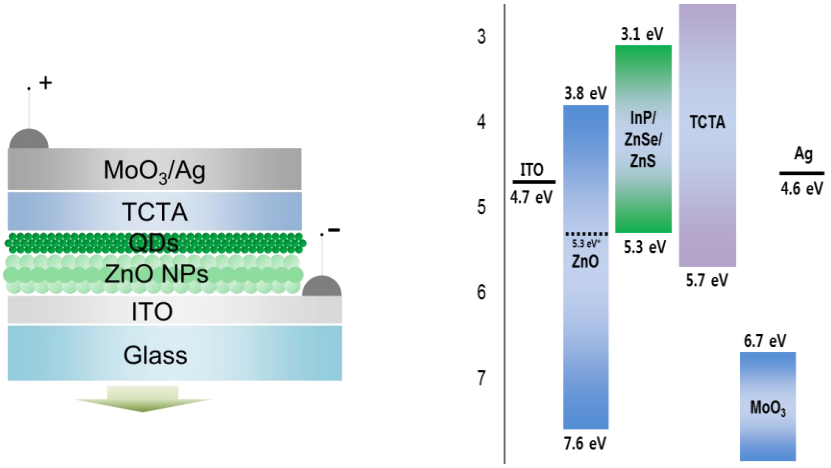

(a) (b)

Figure 5.5.9 (a) A schematic of inverted QLEDs (i.e. ITO/ZnO/QDs/TCTA/MoO_3/Ag) and (b) a corresponding band diagram.

Moreover, as mentioned before, the smoother surface roughness of ZnO film with increasing the number of the spin-coating processes also boosted the performance enhancement because smoother surface roughness makes less interface trap sites between ZnO and QD layer. The J-V curves in a logarithmic scale from ***Figure 5.5.10b*** show all devices have low leakage current around 10^{-3} mA/cm^2. Trap-controlled SCLC region is more or less same along the different thickness of ZnO but only shows a decrease of current density under high driving voltage because of increased resistance by thicker ZnO layer. V_{th} is also constant along the different ETL thickness around 2 V. The EL is observed in all devices between 2 and 2.5 V. These J-V characteristics means ZnO thickness does not change the injection properties but only controll the carrier transport in a multilayer structure. ***Figure 5.5.10c*** shows power efficiencies of all devices. Even though the thicker ZnO layer increases device resistance, the power efficiency from them is even higher because the controlled carrier balance with ZnO thickness efficiently reduced Auger luminance quenching at the RZ.

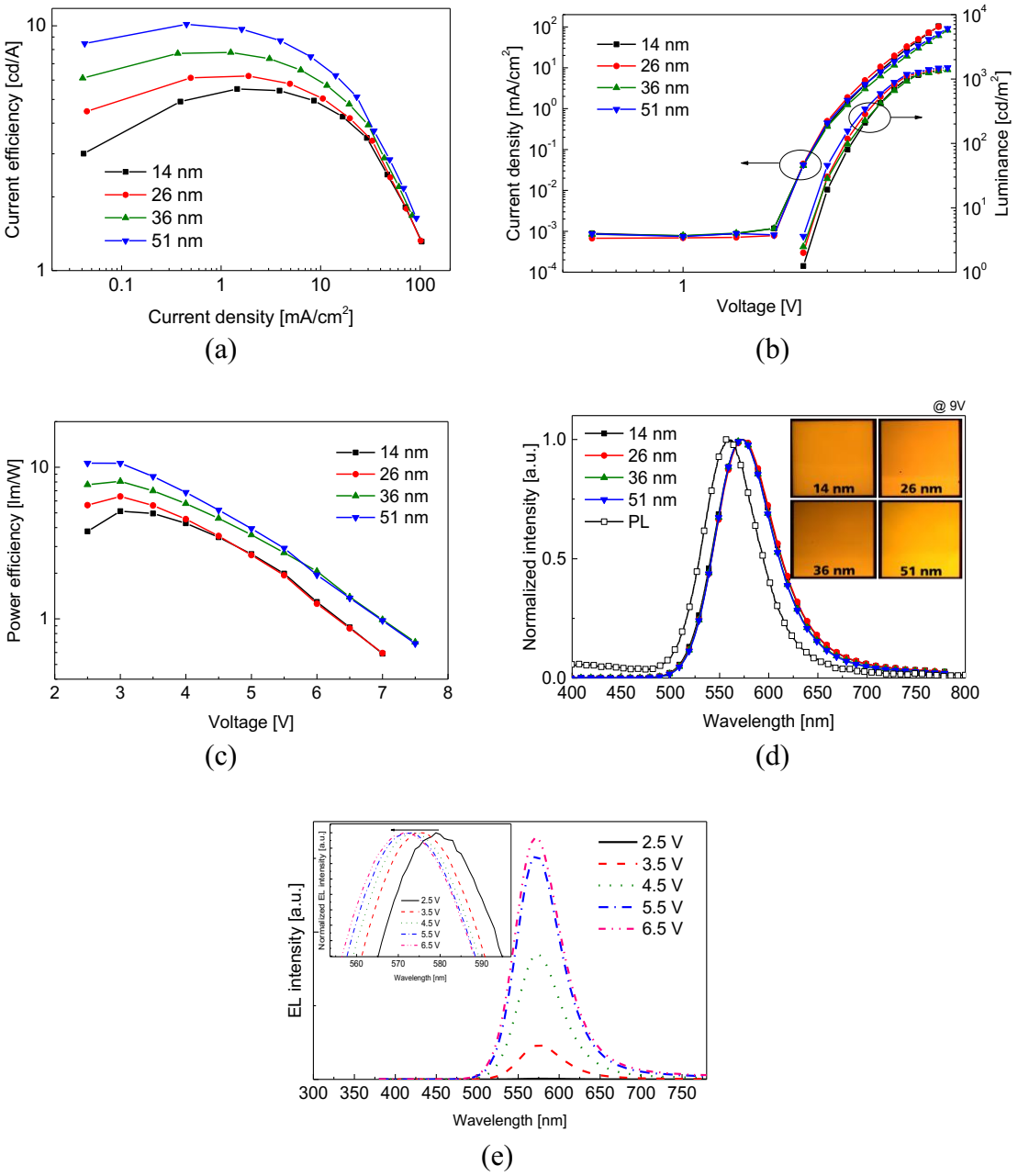

Figure 5.5.10 Device performance according to the thickness of ZnO ETL. (a) Current efficiency-current density, (b) current density-voltage (inset: luminance-voltage), (c) power efficiency-voltage characteristic (d) PL and EL spectra (inset: EL images from 4 mm^2 of pixels driving at 4 V), and (e) EL spectra change as function of driving voltage. *(YH200–YH203)*

Figure 5.5.10d shows EL spectrum is not changed and it has only red-shifted compared to the PL spectrum, and the inset figures show uniform EL emission from 4 mm^2 of the pixel area. ***Figure 5.5.10e*** shows EL spectrum change from the device with 51 nm of ZnO layer as the driving voltage increase from 2.5 V to 6.5 V. There are no serious changes and parasitic emission in the spectrum, which indicates that the

recombination occurred only in the QD emitter, not from the organic layer. However, there is only small blue-shift (< 4 nm) of peak wavelength attributed to the free carrier screening effect in QCSE [154–156]. When carrier density increases in the tilted quantum well by electric filed, suppressed QCSE brings the increase of the effective exciton binding energy by the enhanced wave function confinement, which consequently leads the blue-shifted EL.

Figure 5.5.11a shows current efficiency as a function of luminance curves. Here the maximum efficiency increases about 80 %, but the maximum luminance increase only 10 % comparing the devices with 14 nm and 51 nm of ZnO thickness. This trend also corresponds to more serious efficiency roll-off with thicker ZnO layer, which would indicate that the device with thicker ZnO layer has more serious luminance quenching under the high driving voltage conditions. The luminance quenching under high driving voltage is attributed to the various reasons such as field-induced exciton dissociation in both QD itself and the device structure, a carrier charging (Auger quenching), or a degradation through device defects [157]. However, the main luminance quenching would be expected to come from the charge unbalance or device degradation at the high driving voltage since the ZnO layer, and TCTA layer works well as hole block layer and electron block layer, respectively, QD thickness is constant, and there is the only difference in the ZnO thickness.

The further increase of ZnO nanoparticle thickness investigated in a slightly different device process condition (i.e. QDs from a different batch and different annealing condition for ZnO layer), and the results are shown in ***Figure 5.5.11b***.

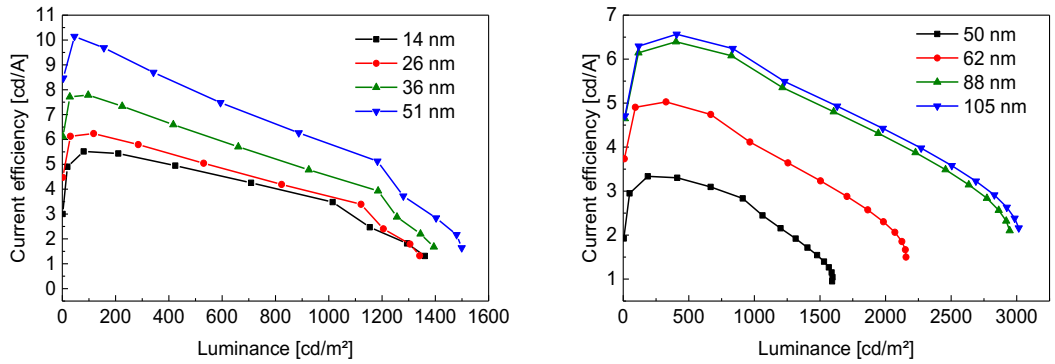

Figure 5.5.11 Current efficiency as a function of luminance characteristic with increasing the thickness of ZnO ETL. (a) 14 nm to 51 nm (ZnO annealing: 180 °C-N_2) and (b) 50 nm to 105 nm (ZnO annealing: 180 °C-Vacuum) for ZnO thickness. *(YH200–YH203,CI914, QY: 60 %), (YH358–YH361, CI938, QY: 52%)*

The luminance and current efficiency increased until 88 nm of ZnO thickness and saturated at 105 nm with the similar increasing ratio. There is 95% increase in current efficiency and 90% for luminance, which indicate that the efficiency roll-off is almost constant to different ZnO thickness in this case. It is suspected that this change is attributed to the vacuum annealing conditions with ZnO nanoparticle layer (more details will be discussed at the end of following ***Chapter 5.5.3***).

5.5.3 Annealing condition of ZnO layer

Since ZnO nanoparticle layer has significant roles regarding device performance in inverted QLEDs, the annealing condition of ZnO nanoparticle layer is investigated. Based on the TGA results, the case of 180 °C annealing under N_2 was chosen as reference annealing condition to evaporate the excess ethanolamine remained in the ZnO film, and 120 °C, which could only remove the solvent (boiling point (BP) of butanol: 117.7 °C), was also compared. In order to examine the effects of annealing atmosphere, the ca. 50 nm of ZnO film annealed in N_2, vacuum, and air with 180 °C for 30 minutes. In this chapter, devices are referred to as X °C – Y, where X is the temperature and Y is the annealing atmosphere.

In order to characterize the ZnO film condition depending on the annealing condition, ionization energy (IE) and surface roughness were measured and summarized in the ***Table 5.10***. In addition, the schematic band diagram illustrating the band bending originated from oxygen absorption and defects conditions according to the annealing condition is shown in ***Figure 5.5.12***, which is based on the explanations from the literature [158–161]. ***Figure 5.5.13a-e*** shows device characteristic, and the maximum efficiency and luminance are summarized in ***Table 5.10***. As shown in ***Figure 5.5.13a,b***, 180 °C-N_2, and 120 °C-N_2 have similar current efficiency trend as a function of luminance, and 180 °C-Vacuum and 180 °C-Air have another similar trend but only with differences in absolute values. The vacuum annealing (180 °C-Vacuum) increase the maximum current efficiency only 4 % but increases the overall current efficiency as increasing current density (i.e. the efficiency after 140 cm/m^2) compared to the others. However, the maximum luminance from 180 °C-Vacuum is increased around 57% compared to the reference. For the 180 °C-Air, both the current efficiency and luminance are decreased around 25% compared to the vacuum annealing sample. For the 120 °C-N_2,

both the current efficiency and luminance are also decreased around 25% compared to the 180 °C annealing condition.

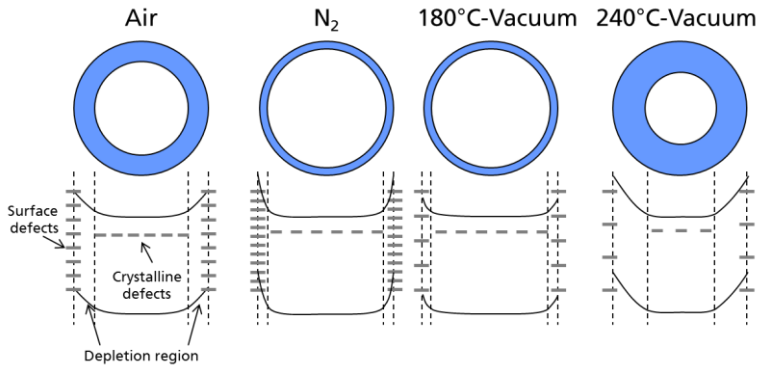

Surface defects: N_2 > Air >> Vacuum
Conductivity: N_2 ≤ Air < Vacuum
Crystalline defects: 180 °C -Vacuum >>240 °C -Vacuum
Conductivity: 180 °C -Vacuum >>240 °C -Vacuum

Figure 5.5.12 A schematic band diagram illustrating the band bending due to oxygen absorption and defects. Air: absorption of oxygen→ non-conducting barrier (broad depletion region) but less surface defects (low band bending at the surface) by the increase of ZnO stoichiometry, N_2: only weak desorption of OH and oxygen remains the more defects states on the surface (strong band bending at the surface), Vacuum: efficient OH and oxygen desorption (weak bending at the surface) → excess of free carriers, weak non-conducting barrier and high conductivity, and 240 °C-Vacuum: efficient desorption of surface and crystalline defects (strong bending at the surface) → low conductivity [158,162].

During the annealing process in both vacuum and N_2, the oxygen which causes non-conductive barrier on the oxide nanoparticle surface and the hydroxyl (OH) group which causes the charge trapping especially electron [163] could be desorbed from the surface of ZnO nanoparticles. This desorption from the nanoparticle surface leads to more free carriers, high mobility, and higher film conductivity by increasing oxygen vacancy (i.e. dominant Zn interstitials). On the other hand, during the air annealing process, the absorption of oxygen on the surface produces the non-conductive barrier or the surface depletion region caused by capturing electrons near the surface, which reduces the conductivity of ZnO film with upward band bending of ZnO nanoparticles [164].

Comparing the N_2 and vacuum condition in our experiments (see the schematic in ***Figure 5.5.12***), the high energy combining with thermal and vacuum condition facilitates desorption of oxygen and OH group more than the N_2 atmosphere. Therefore, the vacuum condition would have fewer surface defects that remain non-conducting barriers, which leads to the higher conductivity of ZnO film with negligible band bending. Since air annealing reduced the defects concentration through the improved ZnO

stoichiometry by the absorption of oxygen, the N_2 annealing would have more defects in the ZnO surface compared to the air annealing condition. Therefore, N_2-annealed ZnO film would have highest defect levels among all the conditions.

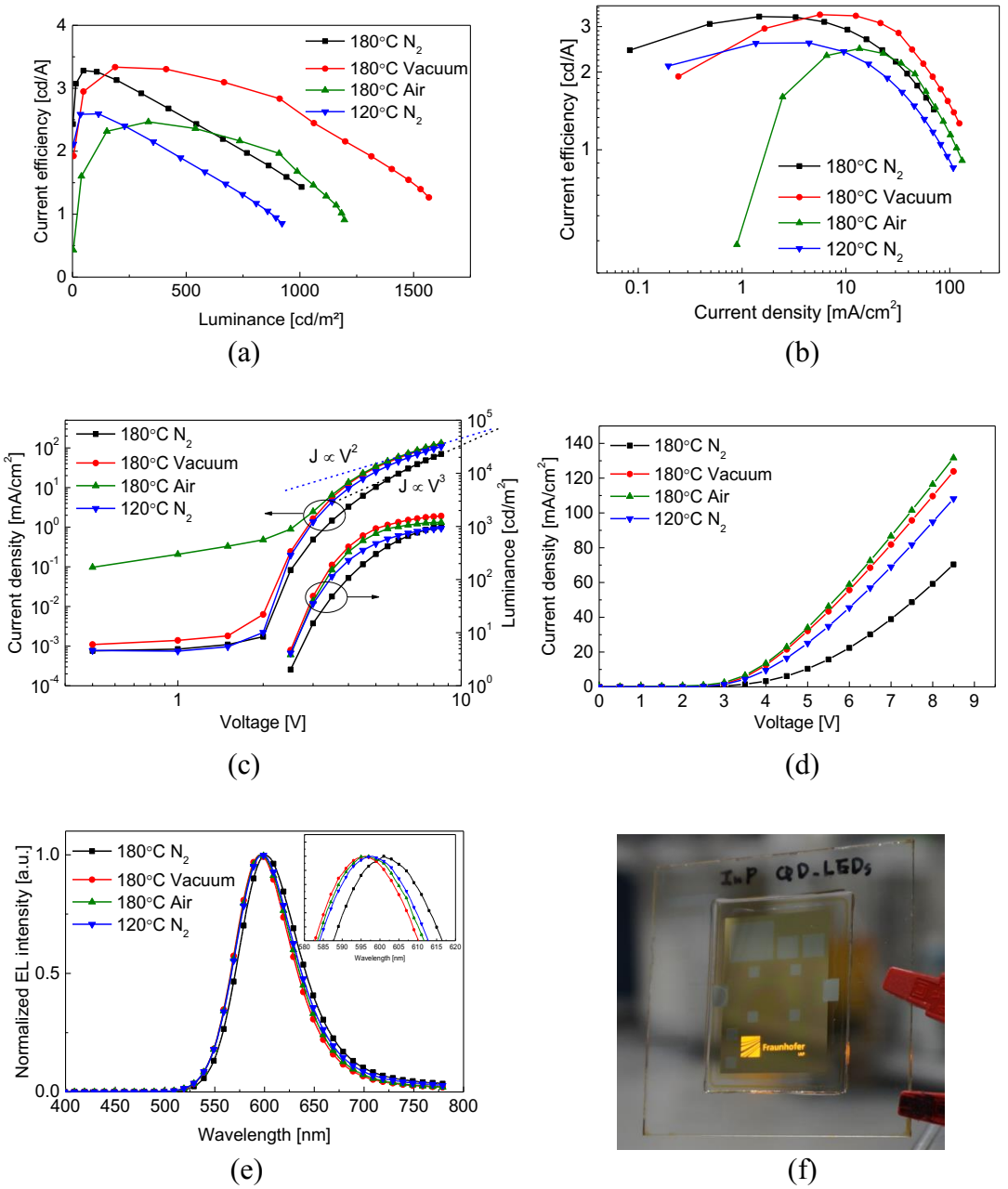

Figure 5.5.13 Device performance according to the annealing condition of ZnO ETL. (a) Current efficiency-luminance, (b) current efficiency-current density, (c) and (d) current density-voltage (inset: luminance-voltage), (e) EL spectra at 4 V and (f) an image of EL from the device driving at 3.5 V. *(YH232-YH235)*

Table 5.10 Film properties from different ZnO annealing conditions and performance summary

ZnO	IE (eV)	Roughness R_q (nm)	Roughness R_{pv} (nm)	Max. efficiency (cd/A)	Max. luminance (cd/m^2)
180 °C-N_2	5.47	1.2	28.5	3.3	1000
180 °C-Vacuum	5.67	1.2	23.3	3.3	1570
180 °C-Air	5.15	1.4	31.9	2.5	1200
120 °C-N_2	5.50	1.4	27.4	2.6	920

The electrical properties of ZnO film with different annealing conditions in our device could be estimated through the J-V curves shown in ***Figure 5.5.13c,d***. First of all, 180 °C-N_2 shows lowest current density along the entire driving voltage and the slope in the linear scale is lower than others (***Figure 5.5.13d***), which indicates the ZnO film has the largest resistance attributed to the more traps. In addition, the slope of 180 °C-N_2 at the high voltage in logarithm scale shows the pseudo-SCLC ($J \propto V^3$) while the other shows trap-free (i.e. most of traps are filled) SCLC ($J \propto V^2$, ***Figure 5.5.13c***). It means there still remained unfilled traps and those are the relatively deep traps compared to the other annealing conditions [95,96].

According to the expectations explained in the literature [161,165], the air annealing would produce the highest resistance of the ZnO film, followed by N_2-annealed and vacuum-annealed samples (i.e. conductivity: Air<N_2<Vacuum). Since the ZnO film was annealed at relatively low temperature compared to the literature (500 °C), however, the conductivity change can be slightly different and weak. In this experiment, 180 °C-N_2 has the lowest conductivity (i.e. $N_2 \leq$ Air < Vacuum) because it remained more defects not only on the film surface but also in the 50 nm of multilayered ZnO film (around 13 monolayers), which leads to high current efficiency under low luminance condition but low current efficiency under high luminance condition compared to 180 °C-Vacuum. Here, the delayed electron transport through the low conductivity of ZnO film could increase the carrier balance under low current density; however, the current efficiency was suppressed with further increase of current density because the remained defects caused the thermal degradation or the luminance quenching.

The 180 °C-Air and 180 °C-Vacuum has similar J-V curves over 4 V, but a very high leakage current is observed from 180 °C-Air at ohmic conduction region. Even though similar J-V curves over 4 V, 180 °C-Air shows lower current efficiency and luminance

over entire voltage because of the high leakage current originated from the high surface roughness of ZnO film.

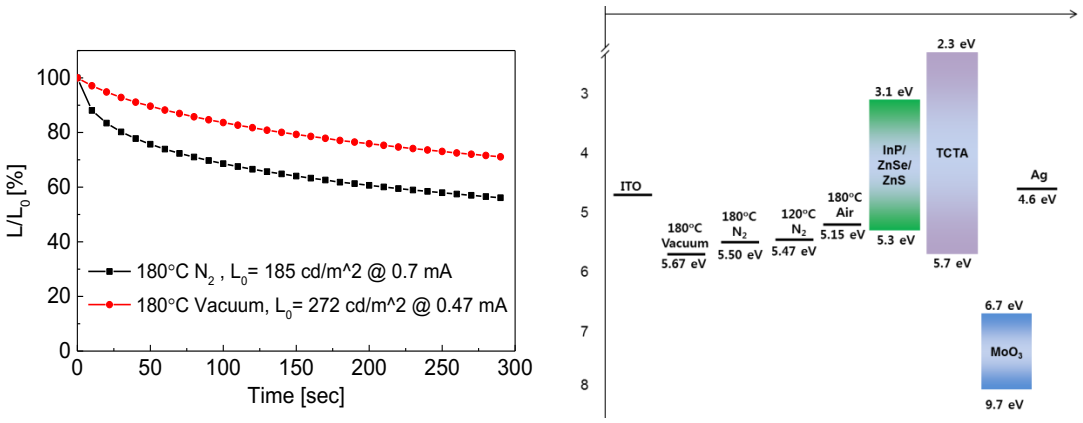

(a) (b)

Figure 5.5.14 (a) Relative luminance as a function of time (short time scale) with 180 °C-N_2 and 180 °C-Vacuum, and (b) band diagram of different devices. *(YH237, YH238; reproduced samples with same annealing conditions)*

For the 120 °C-N_2, the lower annealing temperature could not remove the defects including ethanolamine (i.e. more OH defects could remain), which reduced the device performance compared to the 180 °C-N_2 even though high current density [166]. Presumably effectively delayed electron transport with high ZnO resistance from 120 °C-N_2, a RZ could move from the QD/TCTA interface to the ZnO/QD interface, but not with 180 °C-N_2. (According to the expectation from ***Chapter 6*** , the RZ with thick QD (10 mg/mL) is close to the QD/TCTA interface). The exciton recombination at the ZnO/QD would increase the neutralization effects including the Auger-assisted electron injection into QDs (***Figure 6.1.4***), which could only increase device current density with less charge accumulation. However, even though positive effects with higher current density, 120 °C-N_2 would increase the luminance quenching with lots of defects levels during the radiative exciton recombination process near the ZnO/QD interface.

Figure 5.5.13e shows EL spectra from the devices measured at 4 V, and there is stronger QCSE (i.e. red-shift, < 5 nm) with 180 °C-N_2 compared to other conditions. It is attributed to the enhanced local electric field attributed to the trapped electron charges in the surface defects (OH group) of ZnO nanoparticles [167]. ***Figure 5.5.13f*** shows a photo of QLEDs device operation at 3.5 V (c.a. 200 cd/m^2) under ambient light with a fluorescent lamp. ***Figure 5.5.14a*** shows the lifetime in short time scale (5 min) to examine a charging effect between two devices, 180 °C-N_2, and 180 °C-Vacuum. The

initial luminance from 180 °C-N_2 more rapidly decreases with constant current driving after 5 min to 56 % (180 °C-N_2: 71%). The charges trapped in the defects of ZnO film from the 180 °C-N_2 increased the internal electric field, which leads stronger electric field induced luminance quenching [80]. This result has an agreement with the EL spectra red-shift from 180 °C-N_2.

Thickness increase of vacuum annealed-ZnO nanoparticle layer

Since the annealing atmosphere of ZnO nanoparticle has more effects on the controlling the device defects and stability, the thickness of ZnO film increased more to promote further charge balance by suppressing the electron transport into a QD emitting layer with 180 °C-Vacuum annealing condition. As shown in ***Figure 5.5.15a***, the device maximum efficiency and luminance increased as the thickness increased to 88 nm and saturated with a further increase to 105 nm.

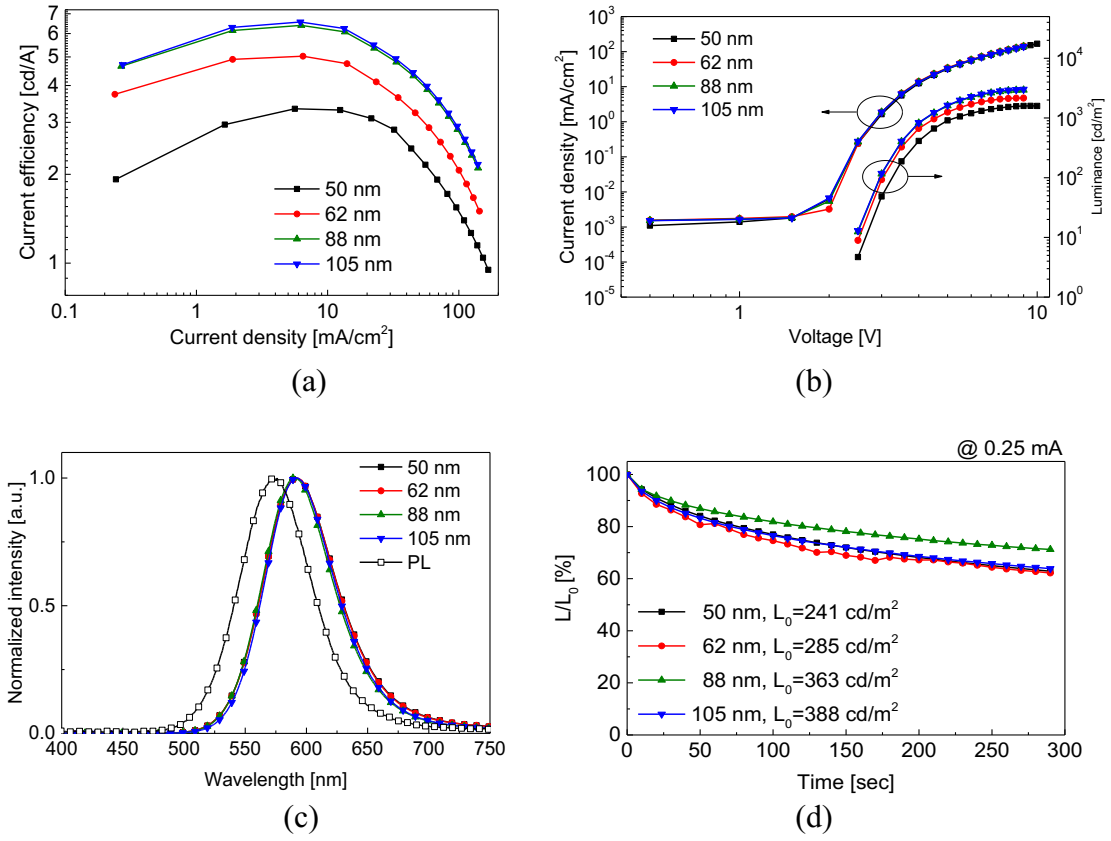

Figure 5.5.15 Device performance according to the thickness of ZnO ETL. (a) current efficiency-current density, (b) current density-voltage (luminance-voltage), (c) EL spectra at 9 V and (d) relative luminance as function of time. *(YH358–YH361)*

The J-V curves, EL spectra and relative luminance decay shown in ***Figure 5.5.15b,c,d*** have only small variation even with different ZnO thickness. As it was

mentioned in ***Figure 5.5.11*** already, the vacuum annealing brought the increase in both efficiency and luminance in the similar ratio as ZnO thickness increase but not with the N_2 annealing (i.e. low increase in luminance).

Moreover, the J-V characteristics shown in ***Figure 5.5.16a*** have distinct differences after turn-on the devices, the slope of J-V keep increasing with 180 °C-N_2 and even higher with thicker ZnO layer. However, the slope is almost constant with 180 °C-Vacuum. The slope in the pseudo-SCLC region is also higher with 180 °C-N_2 from logarithm J-V shown in the inset of ***Figure 5.5.16*** ($J \propto V^{4.4}$ for 180 °C-N_2 and $J \propto V^{2.4}$ for 180 °C-Vacuum). Especially, the high slope in pseudo-SCLC region refers to the shallow trap levels; therefore, the differences are attributed to the less surface defects of ZnO nanoparticles with 180 °C-Vacuum. As a result, the vacuum annealing could efficiently remove the defects level in multilayered ZnO nanoparticle (50-105 nm). Hence, the increase of ZnO film could enhance the current efficiency and luminance with similar ratio compared to the N_2 annealing condition.

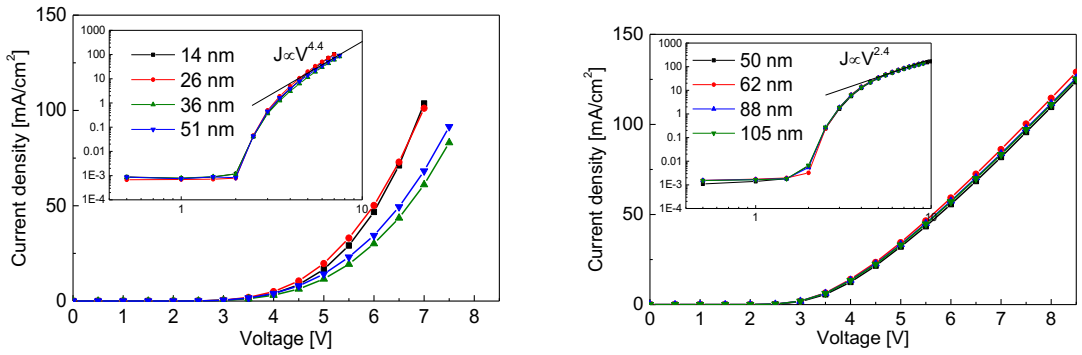

(a) (b)

Figure 5.5.16 Current density as a function of voltage curves with (a) 180 °C-N_2 and (b) 180 °C-Vacuum as increasing the thickness of ZnO ETL.*(YH200–YH203, YH358–YH361)*

Increase temperature for vacuum annealing of ZnO nanoparticle layer

In order to investigate more about the temperature dependent in vacuum annealing condition, 180 °C and 240 °C were compared with 85 nm of ZnO thickness which is higher than previous annealing experiment (~50 nm). 240 °C was chosen because the TGA results show that ZnO starts to decompose at 250 °C. At the same time, 180 °C-N_2 and 180 °C-Air were also repeated. ***Figure 5.5.17a*** shows that 240 °C-Vacuum has lower current efficiency under around 4000 cd/m^2 (at around ~5 V), but it becomes higher as luminance increase. ***Figure 5.5.17b*** shows the J-V curves are more or less similar between 180 °C-Vacuum and 240 °C-Vacuum.

The relative luminance decay curves in ***Figure 5.5.17c*** indicate that 240 °C-Vacuum is more stable, and even there is higher initial luminance increase behavior at the beginning of constant current driving. There is a similar luminance increase in the reference paper, which is depending on the different electron mobility of ZnO nanoparticles [168]; the device with high temperature annealed ZnO nanoparticles has the similar initial luminance increase due to the low electron mobility compared to the low temperature annealed particles. They explained the reduction in the crystalline defects states with higher temperature, not from the surface of the ZnO nanoparticle, can increase the injection barrier and depletion region width at the surface of nanoparticles [162]. In our experimental condition, the high energy combining the vacuum and higher temperature could delay the electron mobility by the same mechanism (***Figure 5.5.12***).

The higher initial luminance increases shown ***Figure 5.5.17c*** are attributed to the neutralization effects at the ZnO/QDs interface including the Auger-assisted electron injection into QDs [104]. This effect is possible due to the shift of RZ near to the interface of ZnO/QDs by the lower conductivity of ZnO layer (more details in ***Figure 6.1.4***). Since the 85 nm of ZnO thickness is enough to delay the electron transport with 180 °C-Vacuum conditions (***Figure 5.5.15***), more strongly delayed electron transport by the lower electron mobility with 240 °C-Vacuum may reduce the current efficiency in the low voltage. However, the efficiency goes higher again because of more efficient neutralization process with more closely located RZ to ZnO/QD interface. One more observation from ***Figure 5.5.17c*** is that the luminance of 180 °C-Vacuum also increases at the beginning, which is not observed with 50 nm of ZnO thickness (***Figure 5.5.14a***) because more efficiently delayed electron transport with thicker ZnO layer also moved the recombination area near to ZnO/QDs interface to have weak neutralization effect.

The 180 °C-N_2 and the 180 °C-Air have much lower performance compared to the 180 °C-Vacuum, and also the difference is higher than the previous experiment setups with 50 nm of ZnO layer (***Figure 5.5.13***) because thick ZnO layer left the relatively high defect density inside of the film, which suppresses the luminance more strongly. Moreover, a further delay of electron transport with a low conductivity of ZnO layer only leads to the unbalance of the carrier at the RZ. In the same way, 180 °C-Air has higher performances than 180 °C-N_2 because of the stronger carrier unbalance by 180 °C-N_2 with the lowest conductivity.

The 180 °C-N_2 still shows red-shift of EL spectrum in ***Figure 5.5.17d*** because the high density of defect states (OH group) is charged and it increases the local electric field that enhances QCSE as explained before. The high density of surface defects also leads to the initial luminance decay (***Figure 5.5.17c)*** even though the possibility of neutralization effects. Namely, the surface defects could disturb the neutralization process between QD and ZnO nanoparticles.

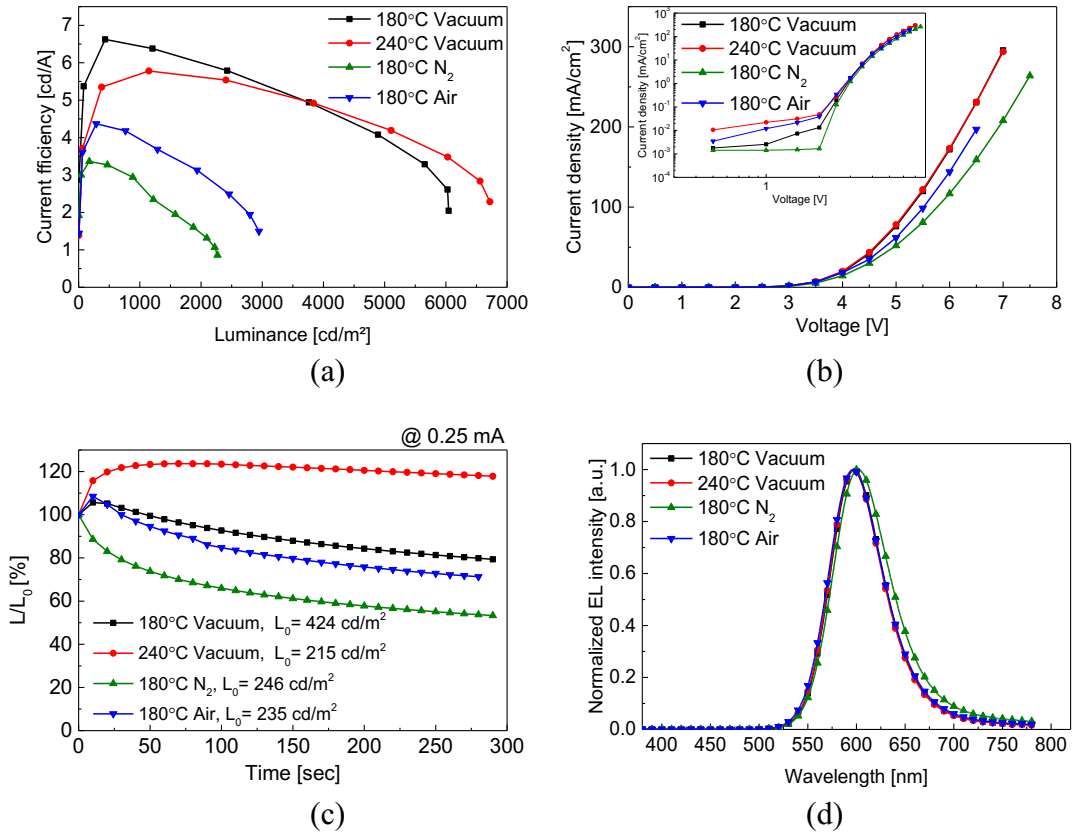

Figure 5.5.17 Different annealing condition for 85 nm of ZnO film. (a) Current efficiency-luminance, (b) current density-voltage, (c) relative luminance as function of time and (d) EL spectra at 5 V. *(YH368–YH371)*

Table 5.11 Film properties from different ZnO annealing conditions and performance summary.

ZnO	IE (eV)	Roughness R_q (nm)	Roughness R_{pv} (nm)	Max. efficiency (cd/A)	Max. luminance (cd/m^2)
180 °C in Vacuum	5.58	1.29	10.91	6.4	6044
240 °C in Vacuum	5.45	1.17	10.38	5.8	6720
180 °C in N_2	5.53	1.12	9.31	3.4	2269
180 °C in Air	5.49	1.27	10.36	4.4	2947

Different annealing conditions of ZnO nanoparticle layer with thin QD layer

At the beginning of this chapter, the annealing condition of ZnO nanoparticle layer was investigated based on the device with 10 mg/mL QD solution and the ZnO thickness of 50 nm. The same annealing condition was compared in the device structure with 3 mg/mL QD solution and the ZnO thickness of 12 nm, which has more efficient carrier balance (see the ***Chapter 6.2***). First of all, while the J-V curves of devices with thick QD layer have the distinct variation according to the annealing condition (***Figure 5.5.13c***), the device with thin QD layer shows quite a similar trend among each other's, shown in ***Figure 5.5.18b***. The reduced variation may be originated from thinner ZnO layer. However, there are more distinct changes in current efficiency-luminance characteristic because annealing conditions effectively changed defects condition of entire relatively thin ZnO layer. There is no opposite trend of performance between the device sets with 12 nm and 50 nm of ZnO thickness by the different QD thickness (reverse trends are observed in ***Chapter 6***) because each case (i.e. thin QD & thin ZnO and thick QD & thin ZnO) has already balanced carrier transport.

As shown in ***Figure 5.5.18a***, 180 °C-N_2 and 180 °C-Vacuum have a similar change in the current efficiency-luminance characteristic compared to the device with thick QD & ZnO layer (***Figure 5.5.13c***). Besides of that here 180 °C-N_2 has more stable current efficiency along the luminance increase compared to the results from ***Figure 5.5.13a*** because the annealing condition removes the defects in the entire thin ZnO layer effectively. As it will be suggested later (***Figure 6.1.3b***), the device with thin QD layer has a neutralization effect at the ZnO/QD interface. Both 180 °C-Air and 180 °C-Vacuum has the initial increase of luminance shown in ***Figure 5.5.18c***, but not with 180 °C-N_2. It is attributed to the surface defects of ZnO nanoparticle from 180 °C-N_2, which may disturb the extraction of accumulated holes to the mid-gap states of ZnO nanoparticles and suppress the neutralization effect at the ZnO/QD interface.

However, there is no distinct red-shift of EL with 180 °C-N_2 in ***Figure 5.5.18d*** because the total amount of trapped charges in the relatively thin ZnO layer was not enough to increase the local electric field. The low performance from 180 °C-Air compared to others is also caused by both the high leakage current and unbalanced charge carrier by delayed electron transport. Since the device with thin QD layer has already efficient hole injection into QD and even hole charging, the electron transport should be increased. However, the non-conducting oxygen barrier formed during oxygen annealing confined the electron transport more than remained OH defects from N_2

annealing because oxygen could penetrate to entire relatively thin ZnO layer, which results in the lower efficiency and luminance (i.e. conductivity: Air < N_2). Therefore, it could be concluded that the surface oxidization layers of ZnO nanoparticle from air annealing are stronger charge barriers than the remained OH surface defects from N_2 annealing.

Once again, here the thickness of ZnO layer is already thin enough to control the carrier balance; therefore, the annealing effect leads to the similar trend to the device with thick QD layer (not reversed). On the other hand, the difference of defect levels causes the changes of luminance stability.

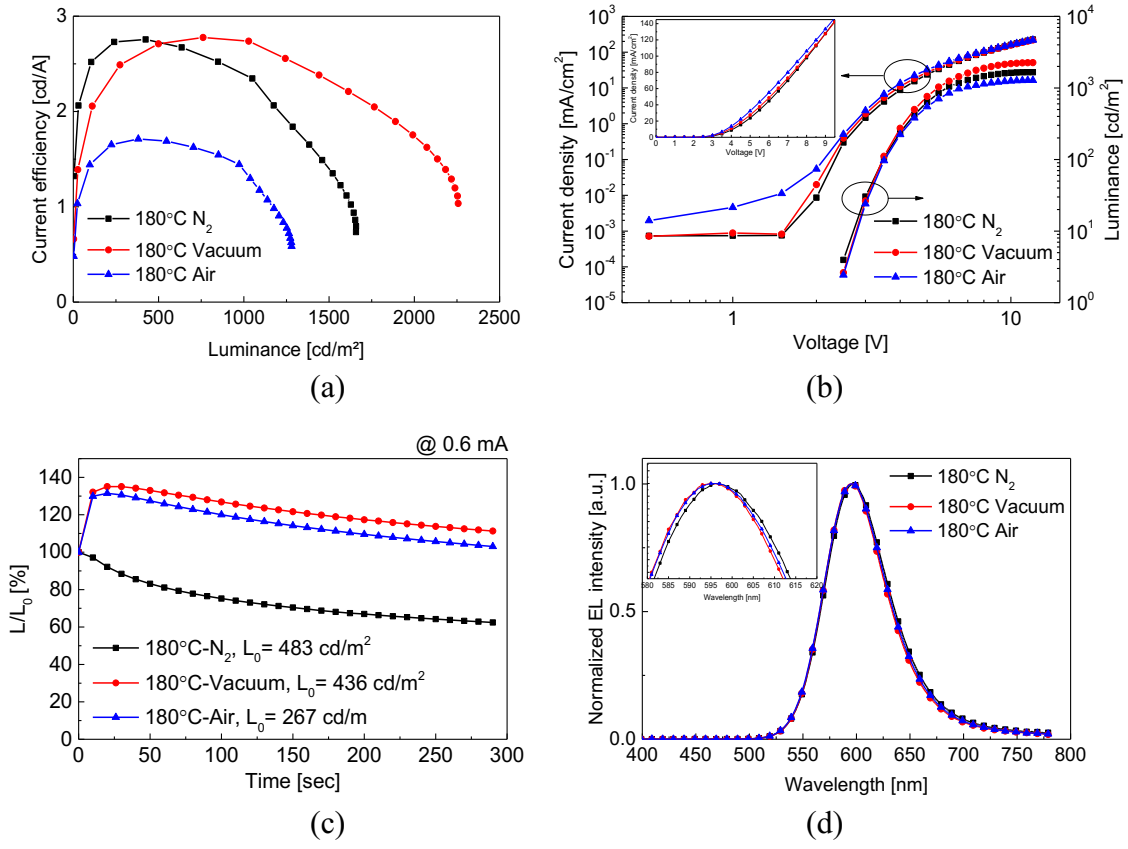

Figure 5.5.18 Different annealing condition for 12 nm of ZnO film (3 mg/mL QD solution). (a) Current efficiency-luminance, (b) current density-voltage (inset: luminance-voltage), (c) relative electroluminescence decay as function of time and (d) EL spectra at 4 V. *(YH265, YH264, YH266)*

5.5.4 PEI interfacial layer for charge balance control

A PEI surface modification layer had an effect to control the performance of the device fabricated with the Al:ZnO nanoparticle (***Chapter 5.4.1***) through the combined

effects of the controlled carrier injection by the reduced work function (i.e. IE), the layer thickness, and the suppressed leakage current of ZnO layer.

Here, the PEI interfacial dipole layer is applied in the inverted QLED incorporated with synthesized ZnO nanoparticles layer to investigate the role of PEI layer. The device structure particularly consists of ca. 15 nm of ZnO ETL and ca. 12 nm of QD emitting layer (i.e. 10 mg/mL QD solution). The PEI layer was deposited from the 0.1 wt% of PEI solution in alcoholic mixture A1. The IE for the pristine ZnO layer and the PEI modified ZnO layer is 5.1 eV and 4.8 eV, respectively (***Table 5.12***). The reduced IE could increase the electron injection from ZnO layer to QD layer. On the other hand, the properties of insulating materials from PEI can be used for charge balance control layer as well [137,169].

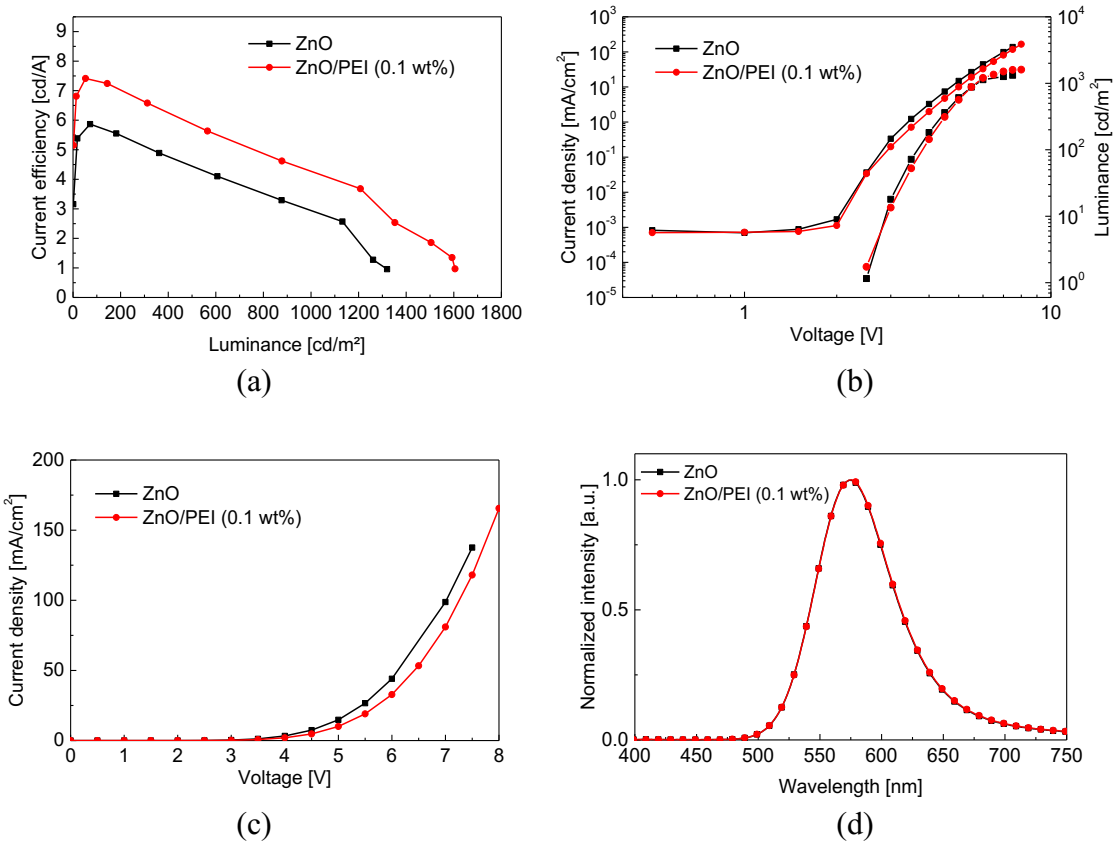

Figure 5.5.19 PEI (0.1 wt%) effects on synthesized ZnO nanoparticle. (a) Current efficiency-luminance, (b) current density-voltage (logarithmic scale, inset: luminance-voltage), (c) current density-voltage (linear scale) and (d) EL spectra at 4 V. (15 nm of ZnO ETL and 12 nm of QD emitting layer) *(YH193, YH195)*

Table 5.12 Summarized device performance according to the PEI layer.

ZnO	Thick. (nm)	IE (eV)	Turn-on @ 1 cd/m^2 (V)	Roughness R_q (nm)	Roughness R_{pv} (nm)	Max. cd/A	Max. cd/m^2
ZnO	~12	5.1	~2.5	0.8	8.7	5.9	1320
ZnO/PEI	~14	4.8	~2.5	0.9	10.0	7.1	1590

Table 5.12 and ***Figure 5.5.19*** show the device characteristics according to the presence of PEI interfacial layer between ZnO and QD interface. The maximum current efficiency and luminance increased around 20% from 5.9 cd/A and 1320 cd/m^2 to 7.1 cd/A and 1590 cd/m^2, respectively, by applying the PEI interlayer. However, the threshold voltage shown in ***Figure 5.5.19b*** are almost constant for both devices, which is unexpected because the reduced IE from 5.06 eV to 4.79 eV by PEI layer should decrease turn-on voltage. In addition, the device with PEI has slightly low current density after the threshold voltage in ***Figure 5.5.19c***. These observations indicate that the device performance in both current efficiency and luminance are enhanced because of the thin PEI interfacial layer (c.a. 2 nm), which has the insulating property, only reduces the electron injection into QDs and then enhances the carrier balance. Since the designed QLEDs which consist of the thick QD layer combined with thin ZnO layer need the less amount of electron at the QD emitter for the carrier balance (see ***Figure 5.5.15***), the delayed electron transport by PEI insulator increases the device performance in this device structure. The EL spectra shown in ***Figure 5.5.19d*** are almost identical to each other because thin PEI layer did not change the local electric field so much.

In order to confirm the effects of PEI as the insulating layer, the higher concentration of PEI layer (i.e. PEI layer was deposited from the 0.4 wt% of PEI solution in 2ME to get much thicker layer) was applied in the same device structure (i.e. 15 nm of ZnO ETL and 12 nm of QD emitting layer). The maximum current efficiency increased around 50% from 5.4 cd/A to 8.11 cd/A. However, the maximum luminance decreased around 87% from 1715 cd/m^2 to 215 cd/m^2 (***Figure 5.5.20***). The threshold voltage and turn-on voltage increased around 0.5 V (***Figure 5.5.20b),*** and the J-V slope (***Figure 5.5.20c)*** increased as well by adopting the higher concentration of PEI solution (i.e. ticker PEI layer). The maximum current efficiency is enhanced under low luminance due to the controlled carrier balance by insulating PEI layer. However, the severe decrease of

current efficiency as luminance increases was observed with the thicker PEI layer because it disturbed the entire current flow in the device.

A red-shift of EL spectrum with the PEI applied device shown in ***Figure 5.5.20d*** supports the insulating property of PEI layer. The stronger internal electric field ($\overrightarrow{E_i}$) applied in the QD layer with the electron accumulation at the ZnO/PEI layer via disturbed electron tunneling injection into the QD by thick PEI layer leads the red-shift (i.e. stronger QCSE) even though the thicker device thickness with applied PEI layer reduced entire applied electric field (i.e. F = V/m) in QD layer at certain voltage, which is illustrated in ***Figure 5.5.21a***.

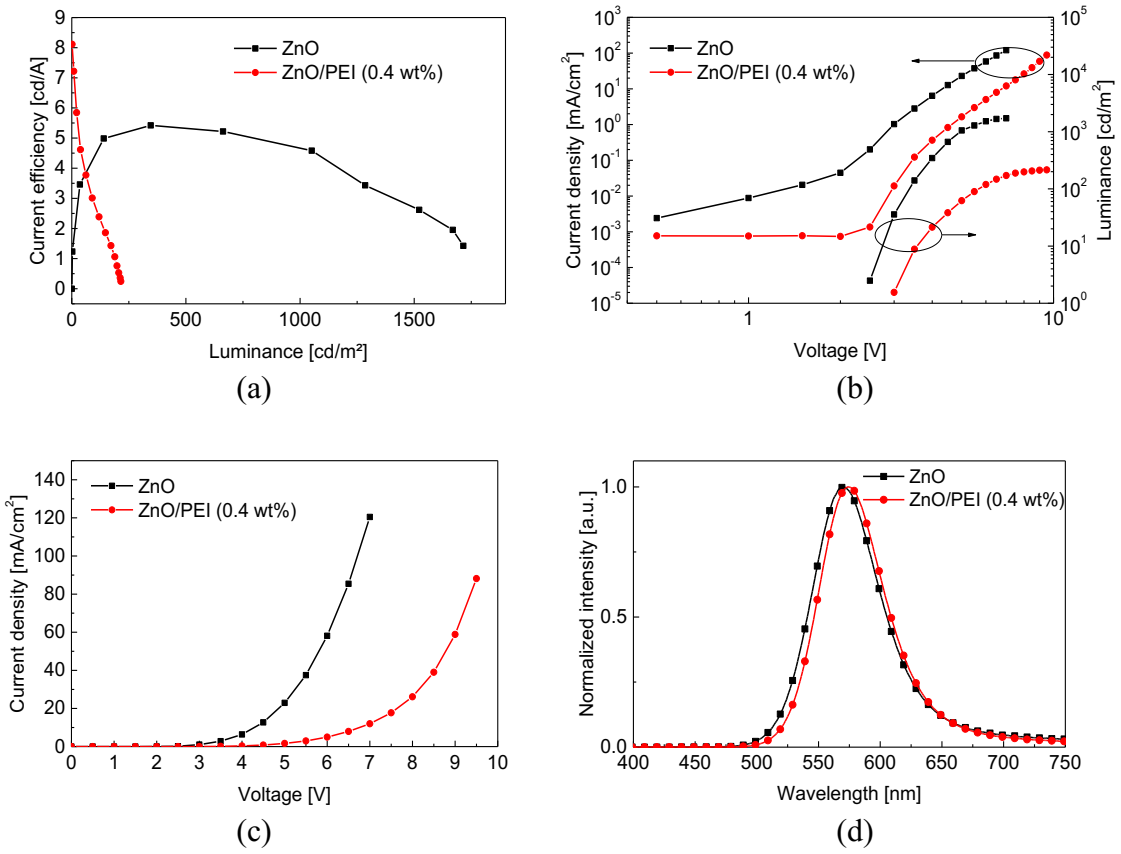

Figure 5.5.20 PEI (0.4 wt%) effects on synthesized ZnO nanoparticle. (a) Current efficiency-luminance, (b) current density-voltage (logarithmic scale, inset: luminance-voltage), (c) current density-voltage (linear scale) and (d) EL spectra at 4 V. *(YH191, YH189)*

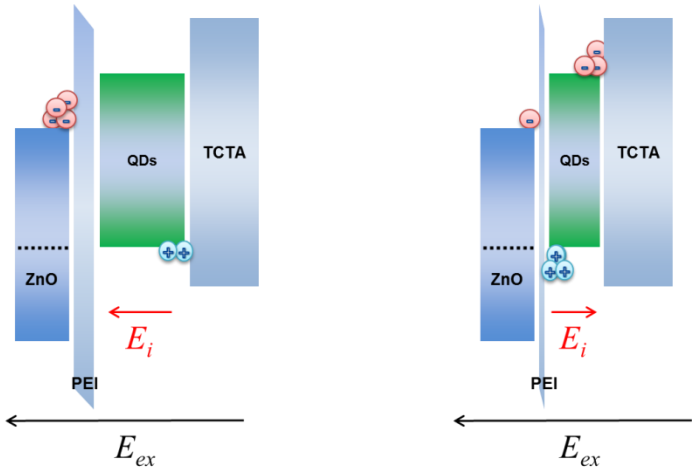

Figure 5.5.21 Schematics of the estimated applied electric field depending on the PEI and QD thickness. (a) A thick PEI and thick QD layer, and (b) a thin PEI combined with the thin QD layer.

Different concentration of PEI interfacial layer was applied in another device structure which consists of ca. 15 nm of ZnO ETL and ca. 3.5 nm of QD emitting layer and their results are shown in ***Figure 5.5.22***. This structure was particularly chosen because the device with thinner QD layer needs more electron injection into QDs for better carrier balance in our inverted QLEDs (i.e. need thinner ZnO layer to enhance the performance; see the ***Chapter 6.2***). Therefore, it was expected that thin PEI layer improves the device performance by reduction of electron injection barrier between ZnO and QD layer with fewer effects of insulating property.

The current density of the devices with 0.05 wt% and 0.1 wt% of PEI solution is higher than a control device (i.e. pristine ZnO layer) as the voltage increases over ca. 3 V, shown in ***Figure 5.5.22a***. In addition, the lower concentration of PEI solution shows higher current density because here the tunneling injection through PEI layer is more dominant than the effects of lower IE with thicker PEI layer (i.e. thicker PEI has lower IE in general [131], see also a similar example with Al_2O_3 in ***Figure 5.3.2***).

On the other hand, the threshold in the J-V curves (***Figure 5.5.22b***) does not decrease with PEI layer but even increased with the device fabricated with 0.2 wt% of PEI solution. These observations could imply that the accumulated electrons at the interface of ZnO/PEI under low applied voltage could be injected into QD layer by more effective tunneling injection through thinner PEI layer with stronger band bending under higher applied voltage.

Even though the PEI modified ZnO layer leads to the higher current density compared to the pristine ZnO layer, the device performance could not be enhanced, shown in ***Figure 5.5.22c***. For the only comparison, the different concentrations of PEI solution (0.05 wt% and 0.1 wt%), the lower concentration of PEI solution (i.e. thinner PEI layer) increased the performance. In contrast, the device with 0.2 wt% of PEI solution shows even higher current efficiency under low luminance condition (< 300 cd/m^2) compared to other devices fabricated with a lower concentration of PEI solution. The increased driving voltage (i.e. higher threshold voltage) through thicker PEI layer could improve carrier injection just after the threshold voltage through the stronger band bending of thicker insulation layer compared to the others. However, the thicker PEI layer accumulates holes more than, the thinner PEI layer at the interface of PEI/QD layer by the less hole extraction into ZnO mid-gap states (see ***Figure 6.1.4*** for ZnO mid-gap states) as the voltage increase further, which results in more severe interrupting on the carrier balance again.

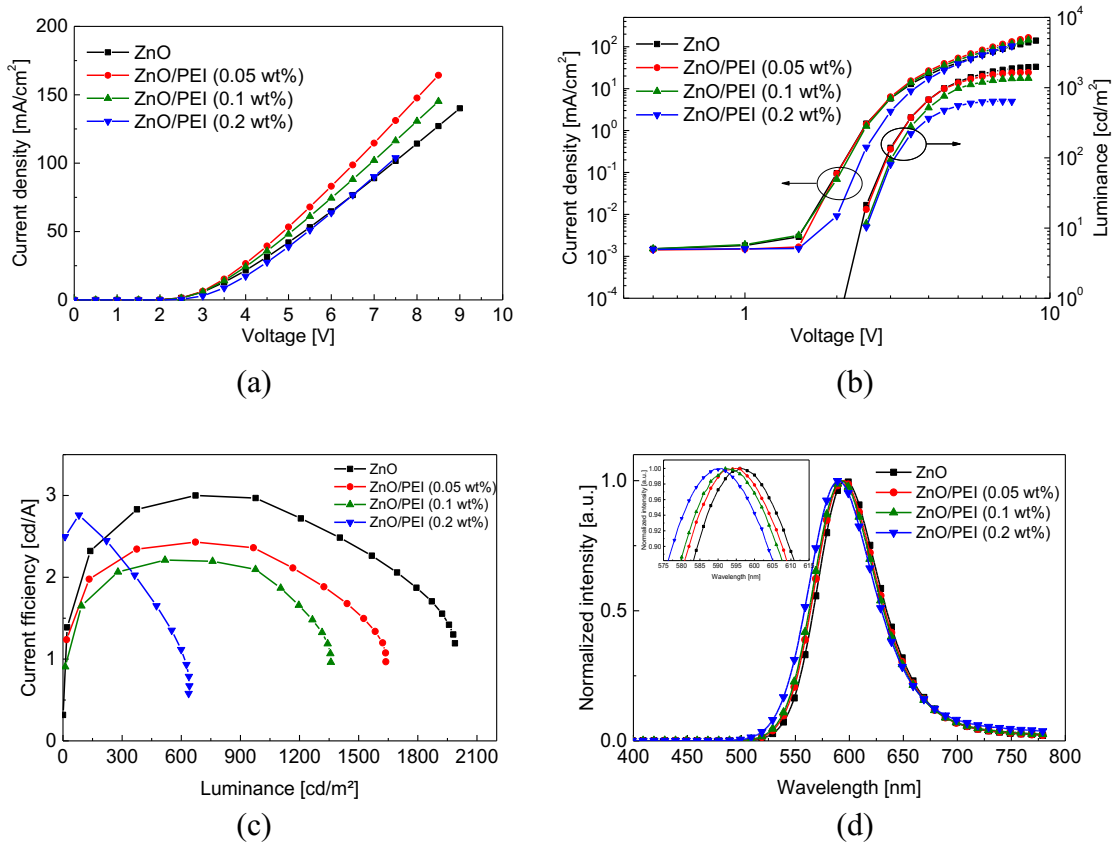

Figure 5.5.22 PEI effects on synthesized ZnO nanoparticle. (a) Current efficiency-luminance, (b) current density-voltage (logarithmic scale, inset: luminance-voltage), (c) current density-voltage (linear scale) and (d) EL spectra at 4 V. *(YH260 –YH263)*

A blue-shift of EL spectrum compared to pristine ZnO layer in ***Figure 5.5.22d*** also support the more hole accumulation at the PEI/QD interface. The blue-shift means QCSE reduced by the suppressed local electric field via adopting PEI layer. It is reverse trend compared to the red-shift with the device with thick QD layer shown in ***Figure 5.5.20d***. In the case of thick QD layer combined with relatively thick PEI layer (***Figure 5.5.21a***), an accumulated electron at the ZnO/PEI interface by thick PEI layer could increase the internal electric field applied to QD layer, which leads to the stronger QCSE (i.e. red-shift). However, in the case of thin QD layer combined with relatively thin PEI layer (***Figure 5.5.21b***), more hole accumulation at the PEI/QD interface by the faster hole transport through thin QD layer could reduce the internal electric field, which decreases QCSE (i.e. blue-shift). The stronger blue-shift with thicker PEI layer in ***Figure 5.5.22d*** can be explained by two effects; a) the weaker applied external electric field in the entire device by the increased total device thickness with thicker PEI layer and b) the weaker QCSE by shielded E-field by more hole accumulation at PEI/QD interface via less hole extraction to the mid-gab state of ZnO layer [156].

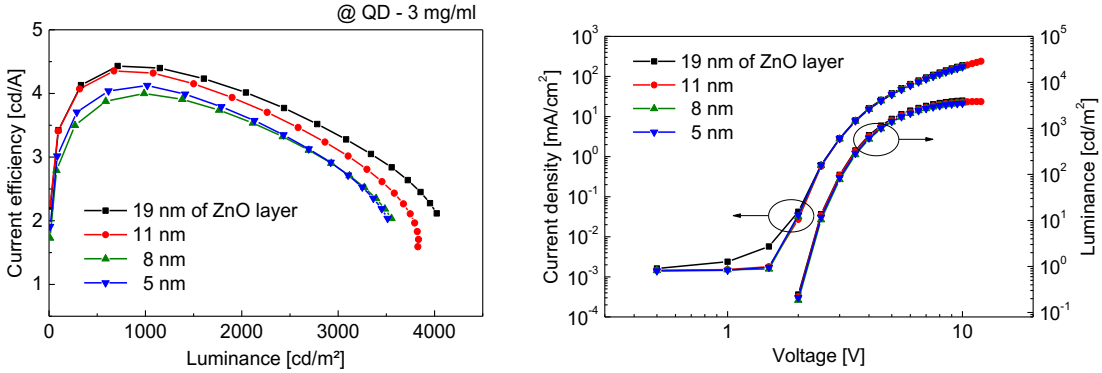

Figure 5.5.23 ZnO thickness effects on QLEDs fabricated with thin QD layer (3 mg/mL). (a) Current efficiency-luminance and (b) current density-voltage (inset: luminance-voltage). The thinner ZnO layer even reduced the performance. Incorporating this result with ***Figure 6.2.1***, c.a. 19 nm is the optimum ZnO thickness for thin QD layer device. *(YH354–YH357)*

Apart from the non-effect on threshold voltage with PEI layer in this investigation, the lower performance of PEI applied devices even with higher current density can only be explained with a carrier unbalance with too much electron injection into QD compared to the control device. Since the control device without PEI layer had already optimized ZnO thickness ca. 19 nm (here used ca. 15 nm) as shown in results of ZnO thickness variation test in ***Figure 5.5.23***, further enhanced electron injection without lowing threshold voltage would disturb the carrier balance at QD layer. In addition, the interrupting a

neutralization effects between QD and mid-gap state of ZnO layer is another reason for lower performance (this will be discussed more in ***Figure 6.2.6***).

As a summary of the effects of PEI layer, the interfacial dipole of PEI layer has some effect of increasing the electron transport but cannot reduce the threshold voltage in our inverted structure. We conclude that our synthesized ZnO has already provided sufficient electron injection through the Auger assisted charge injection mechanism (see the ***Figure 6.1.4***); therefore, PEI could not help to reduce the threshold voltage but only facilitate the control of carrier balance by the insulating property.

5.5.5 Different hole transport layer to compensate the electron charging

Since the different charges are accumulated at the QD emitter in the devices with various QD thickness, a better carrier balance would be accomplished by not only controlled electron transport but also hole transport. As the change of TCTA thickness has minor effects on the device performance in our test, different hole transport materials are considered to control the hole transport properties. ***Figure 5.5.24*** and ***Table 5.13*** show possible candidates and their parameters. Concerning the enhance of device performance, a band alignment with CBM of InP/ZnSe/ZnS QD, a barrier for the electron blocking and hole mobility should be considered. According to the comparison, NPB has a most matched HOMO level. However, the electron block barrier and hole mobility are relatively lower than TCTA and TAPC. TAPC has well matched HOMO level with QD's (i.e. only 0.2 eV difference), 1.1 eV of high energy barrier against electron dissociation and two orders of magnitude higher hole mobility compared to the TCTA. Therefore, here we applied TAPC HTL instead of current TCTA HTL. The molecular structures of TCTA and TAPC are shown in ***Figure 5.5.25***.

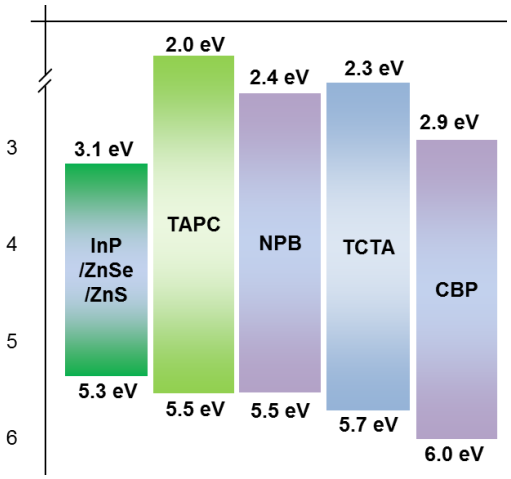

Figure 5.5.24 (a) Band diagram of different hole transport layer compared with QDs.

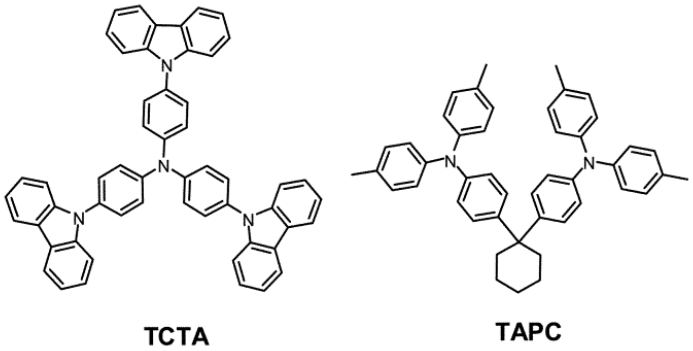

Figure 5.5.25 Molecular structures of TCTA and TAPC hole-transporting materials.

Table 5.13 The value of HOMO, LUMO and hole mobility from different hole transport materials.

HTL	LUMO (eV)	HOMO (eV)	Hole mobility ($cm^2V^{-1}s^{-1}$)
TAPC [170]	2.0	5.5	1×10^{-2}
NPB [104,171]	2.4	5.5	3.3×10^{-7}
TCTA [170]	2.3	5.7	1×10^{-4}
CBP [172]	2.9	6.0	1×10^{-3}

Figure 5.5.26 and ***Table 5.14*** show the device performance depending on the different HTL. As we expected, the device with TAPC shows much higher current efficiency and luminance in ***Figure 5.5.26a***. The maximum current efficiency and luminance were enhanced from 3.8 cd/A and 2160 cd/m^2 to 5.0 cd/A and 2890 cd/m^2, 31% and 25% respectively. The J-V curves in ***Figure 5.5.26b*** show lower threshold voltage from TAPC based device, the value decreased from 2 V to 1.5 V. The lower HOMO of TAPC around 0.2 eV compared to TCTA reduced threshold voltage by more favorable hole injection from the anode, which leads to the low driving voltage (***Figure 5.5.26f***). Maximum power efficiency was also improved 47 % higher (i.e. 3.2 lm/W to 4.7 lm/W, ***Table 5.14***) because the lower driving voltage from TAPC increased it more effectively. The device structure which consists of 70 nm of ZnO layer and 40 nm of TCTA still has more electrons compared to holes in the QD layer (based on the results of ***Figure 5.5.15***). Therefore, increased hole injection into QD by the low hole injection barrier and high hole mobility improved the carrier balance very efficiently. The EL spectrum from TAPC also has smaller red-shift from PL spectrum compared to TCTA (i.e. 22 nm for TAPC, 25 nm for TCTA) because the lower charge accumulation at the ZnO/QD or QD/TAPC interface by better carrier balance decreased the local electric field as well (i.e. suppressed the QCSE). The relative EL decay curves in ***Figure 5.5.26e*** also support

that TAPC device has lower charging effects; the luminance decay from several devices suppressed with TAPC devices. However, the TAPC device still has strong efficiency roll-off like TCTA device in ***Figure 5.5.26c***. Since better charge carrier balance has reduced the device charging, here, the efficiency roll-off is more related to the field induced QD luminance quenching effects (not the exciton dissociation) [80].

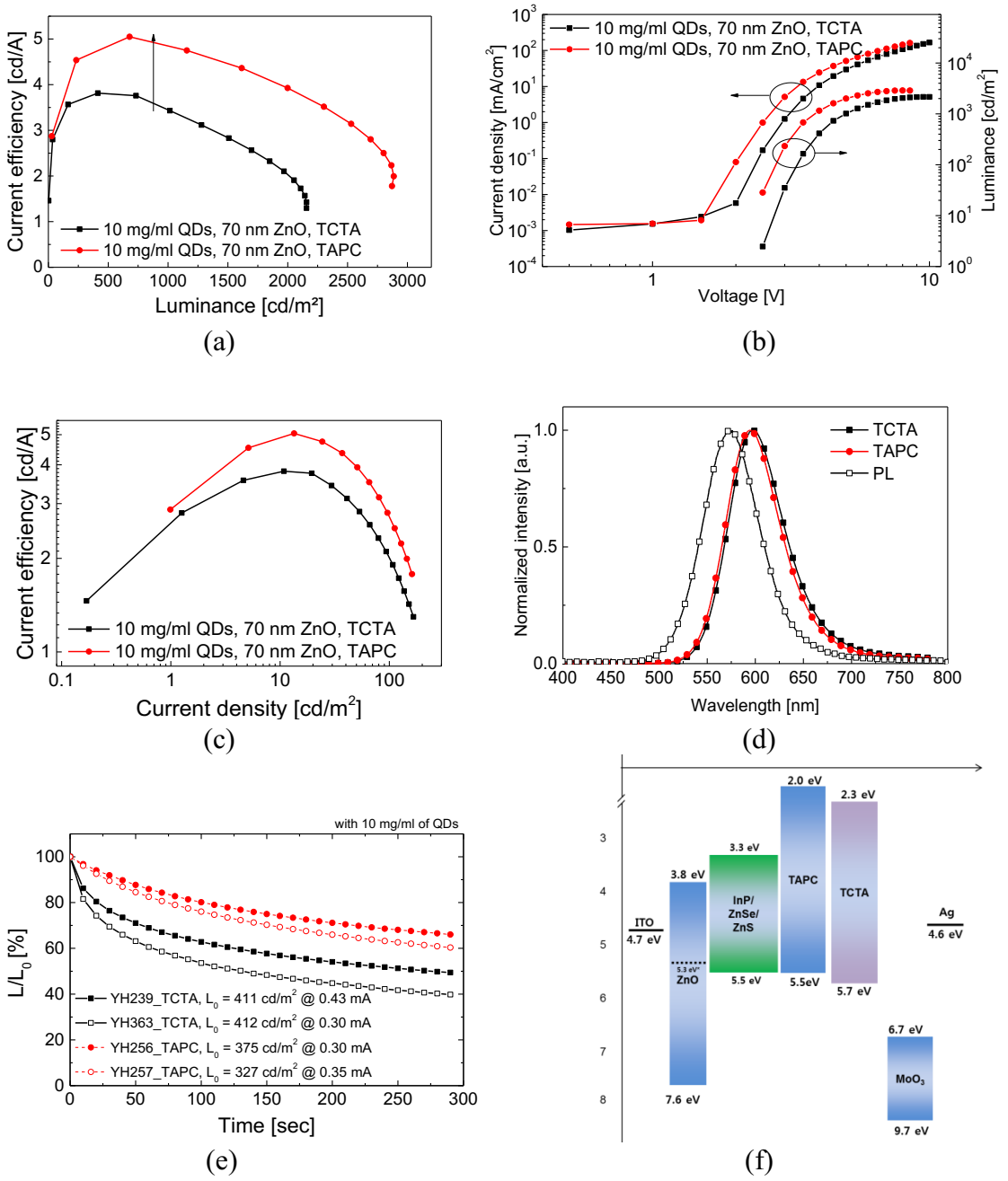

Figure 5.5.26 Device performance with different HTL. (a) Current efficiency – luminance, (b) current density – voltage (logarithmic scale, inset: luminance-voltage), (c) current efficiency – current density, (d) EL spectra at 4 V, (e) relative EL decay curves and (f) a band diagram of inverted QLEDs. *(YH239 YH256, and YH363, YH239, YH257)*

Table 5.14 Summarized device performance according to the different HTL. (absolute value is lower than ***Figure 5.5.15*** because of the low sheet resistance of ITO sub)

HTL	V_{th} (V)	Max. (cd/A)	Max. (lm/W)	Max. (cd/m^2)
TCTA	2	3.8	3.2	2160
TAPC	1.5	5.0	4.7	2890

5.5.6 Summary

The high performance inverted QLEDs are developed using smooth ZnO nanoparticle layer. The clearly dispersed small size (c.a. 8 nm) ZnO nanoparticle solution is prepared by the cooperation with ethanolamine surfactant. The surface roughness of ZnO nanoparticle is controlled by the amount of the ethanolamine in the different solvent condition. Finally, multi spin-coated ZnO nanoparticle layer by orthogonal solvent process provides the dramatic enhancement of device current efficiency and luminance, which is utilized by the ultra-smooth ZnO layer and the controlled electron transport by the thickness and annealing condition of ZnO nanoparticle layer. Here, the reference device with ZnO nanoparticle, which consists of relatively thick QD layer deposited from the 10 mg/mL QD solution in butanol, needs more hole injection or lower electron injection for the better carrier balance at the QD emitter. Therefore, the thicker ZnO nanoparticle layer provides higher device performance. The vacuum condition incorporated with certain temperature for the ZnO layer annealing could remove the surface and crystalline defects as well, which leads to the more stable and efficient device. The insertion of PEI interfacial dipole also improves the device performance because of the delayed electron injection but not the enhanced charge injection in our experiment. The different HTL materials are considered to increase the hole injection into QD for more exciton generation. TAPC HTL, which has lower hole injection barrier and higher hole mobility compared to TCTA, improves the device efficiency and stability by the reduced threshold voltage and enhanced charge balance.

Chapter 6

6 The influence of QD layer thickness on different charge carrier transfers in the device

In order to design high-performance QLEDs using InP-based QDs in the inverted device structure, the charge carrier balance is the most important factor. The organic ligands on the surface of QD provide various opportunities to change their properties and functions by the surface modification for building thin film semiconductor layer. On the other hand, the remaining ligands in the thin film after deposition normally impedes carrier transport between QDs. Therefore, the thickness of the QD layer is a crucial parameter to improve device performance through the function of controlling charge carrier balance in the multilayer system. At the beginning of development of QLEDs, many types of research were focused on developing the technology to deposit monolayers of QDs on top of various carrier transport layer with different techniques like spin-coating, phase separation method or microcontact printing, in order to reduce the drawback caused by remaining ligands in the multilayer QD stacks [13,173–175]. However, a different observation has been reported from other research [117]; the high performance of QLEDs was realized not only from the monolayer of QDs but also from multiple monolayers of QDs. The monolayer QD emitter could be only more advantageous in QLEDs when the excitons generated in the charge transport materials transfer to the QD layer by energy transfer process. However, if the direct charge injection only transfers the charges, the proper thickness of the QD layer is required to have efficient carrier balance in the device structure. Mashford et al. also have investigated the strong dependence of QLED performance on CdSe/CdS emitter thickness regarding the fast charge transfer between QDs and aligned electronic levels of

ZnO nanoparticles [104]. They proposed that the positively charged QD, attributed to the aligned CBM of ZnO nanoparticle and CdSe/CdS QD, rapidly returns to a neutral state by the extraction of holes from the QDs' VBM to mid-gap state on the adjacent ZnO nanoparticles. This process makes the device more stable during the operation, but it gives a low current efficiency of the device. The similar behavior has been observed in our experimental results from the InP/ZnSe/ZnS QD-based inverted device as well. In this chapter, the strong dependence of QD layer thickness on the device performance will be discussed, and the possible device mechanism and model for optimizing the device structure will be suggested to achieve high performance of QLEDs.

6.1 Auger-assisted charge neutralization model

6.1.1 Trade-off according to the concentration of QD solution

Figure 6.1.1 shows the interesting trend in current efficiency as the function of luminance characteristics for the inverted QLEDs with different QD emitter thickness. The device performance shows a strong dependence on the thickness of QD emitting layer. First of all, there is a trade-off between maximum luminance and efficiency according to the change of QD layer thickness. The maximum current efficiency of the device increased from 1.6 cd/A to 2.0 cd/A when the QD layer thickness is increased from approximately 3.5 nm to 10.5 nm (in ***Figure 6.1.1b***). However, the maximum luminance of 1100 cd/m^2 is achieved with 3.5-nm-thick QD, and a fast decrease of luminance was observed with a thicker QD layer. In a ***Figure 6.1.1c***, the luminance is higher with thicker QDs before it reaches around 300 cd/m^2 but the trend changes after this point. The thinner QD shows better luminance and current efficiency over the 20 ~ 30 mA/cm^2 of current density compared to the thicker QD emitter. Multiple monolayers of QDs provide the efficient exciton generation and recombination through the proper charge balance at a RZ, which introduces the higher current efficiency under the low current density. This RZ change in the inverted QLEDs according to the different QD thickness will be discussed in ***Chapter 6.2*** . However, quenching happens in close-packed QD films mainly by two mechanisms: The first is due to an exciton migration to the adjacent QDs or surface defects by the energy transfer [4,176], and due to an Auger recombination quenching process originated from the accumulation of space charges within the QD layer [22]. Moreover, the EL from QDs can be suppressed by high electric-field induced quenching effects as well [80,177]. Therefore, the thicker QD layer

undergoes more severe quenching effects with the higher electric field, which results in the low luminance and current efficiency.

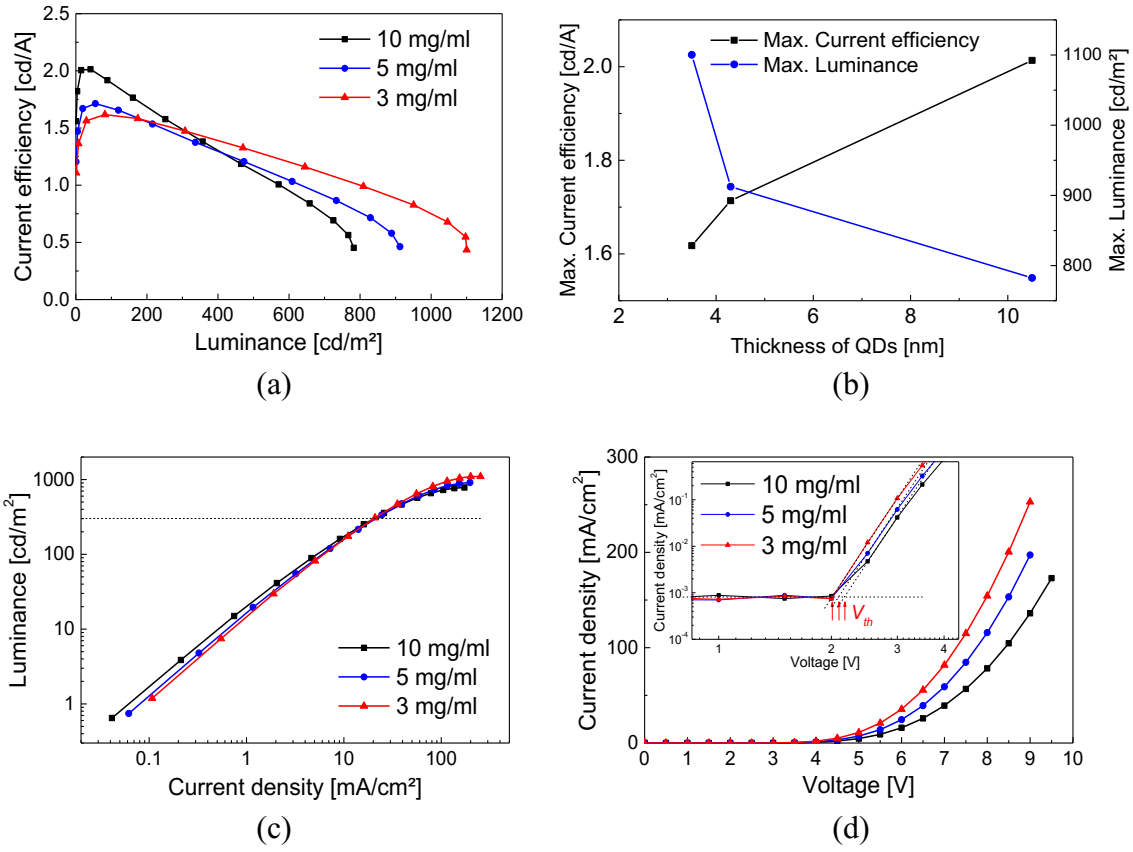

Figure 6.1.1 A trade-off between maximum current efficiency and maximum luminance according to the QD concentration of 3, 5 and 10 mg/mL (correspond to approximately the thickness of 3.5, 4.3, and 10.5 nm, respectively). (a) Current efficiency-luminance, (b) maximum current efficiency as a function of QD thickness, (c) luminance-current density and current density-voltage (inset: V_{th} is 1.98, 2.11, and 2.16 V for 3 , 5, and 10 mg/mL, respectively) *(YH213, YH214, YH215)*

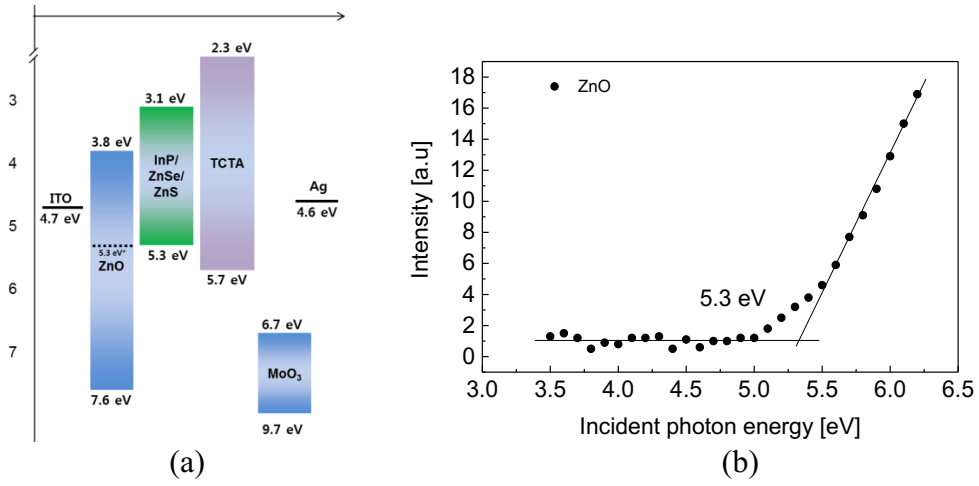

Figure 6.1.2 (a) A band diagram of inverted QLEDs and (b) a measured ionization energy of ZnO nanoparticles through the PESA measurement.

According to the Mashford et al., there is a charge neutralization process between QDs to the adjacent electronic energy levels of ZnO nanoparticles, which enhance the QD emission stability under the device operation [104]. The ZnO nanoparticles, which we synthesized with the method from the same literature, has a similar band gap of 3.63 eV estimated from a Tauc-plot (***Figure 5.5.5b***) and broad green emission with the peak wavelength of 540 nm (***Figure 5.5.5a***). As we discussed before, the broad green emission comes from the recombination between a hole trapped at a mid-gap state and an electron from a donor level near the CBM of ZnO nanoparticles. As our device energy level diagram is depicted in ***Figure 6.1.2a***, there could be similar mechanism occurring in our structure. The band diagram of ZnO is taken from literature [104]. In addition, we measured the ionization energy (IE) of ZnO nanoparticles with photoelectron spectroscopy in the air (AC-2, PESA), shown in ***Figure 6.1.2b***. The measured IE of ZnO was 5.3 eV. This corresponds to the mid-gap state in the ZnO band gap because the low photo-excitation energy (c.a. 3.40 - 6.20 eV) of PESA can only excite the electrons from the mid-gap state of ZnO nanoparticles not from a deep VBM of ZnO (c.a. 7.6 eV). The measured mid-gap energy state of ZnO nanoparticles is similar with the VBM of our InP/ZnSe/ZnS QDs, and the same charge neutralization effects between QDs and ZnO nanoparticles are expected, which will be discussed in details. During the measurement, the efficiency of the device with 3 mg/mL QD solution takes over the one with 10 mg/mL because the luminance from the thicker QD layer is not stable with the self-quenching mechanism as well as, the lower neutralization effects. However, thin QD layer could keep the efficient luminescence through fast charge neutralization with adjacent ZnO NPs. In the charge transfer model from Mashford et al., the ultrafast neutralization process strongly depends on the proximity to ZnO/QD interface. They have found the photo-stability reduces the number of QD monolayer increases because the distance between ZnO and thick QD layer interrupt the neutralization process [104].

As the QD thickness increases in the inset of ***Figure 6.1.1d***, the threshold voltage of the device increases from 1.98 V to 2.16 V. However, the thinner QD layer shows higher current density along the entire driving voltage and the slope of J-V curves at high voltage is lower with thicker QD layer. These J-V curves could explain that thicker QD layer decreases the current density of the device, which results in lower luminance under strong electric field by the reducing exciton generation as well. In addition, the low threshold voltage below the band gap of QDs refers to the efficient Auger-assisted charge injection in our device structure even though there is 0.7 eV of energy barrier from the

CBM of ZnO to QDs (luminance from all devices is observed after the threshold point) [107].

6.1.2 Charge neutralization model accompanying Auger-assisted electron injection

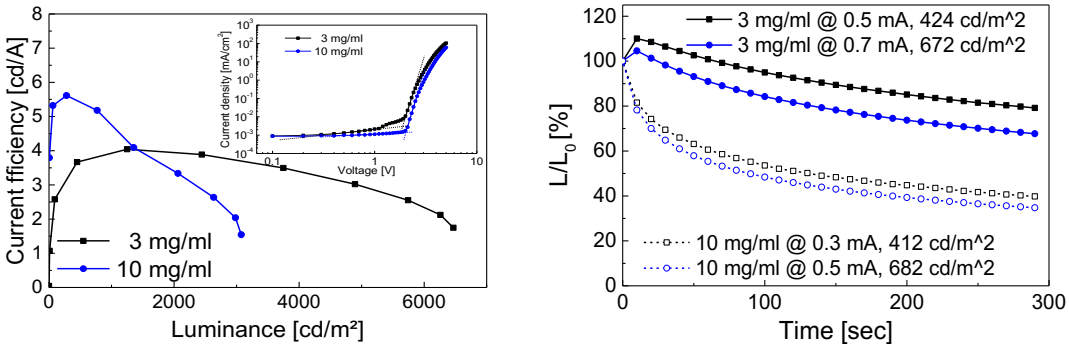

(a) (b)

Figure 6.1.3 (a) Trade-off between maximum current efficiency and maximum luminance and (b) electroluminescence changes as a function of time. (The concentration of 3 and 10 mg/mL are corresponding to the thickness of approximately 3.5 and 10.5 nm, respectively) *(YH362, YH363)*

Figure 6.1.3a shows same trade-off trend caused by the different emitter thickness in a more optimized device structure, in particular with a 21 nm of thin ZnO ETL and a low sheet resistance of ITO. A different charging behavior from these two devices has been observed in the measurement of luminance change along the constant current driving in ***Figure 6.1.3b***. The lifetime test lasted only 5 minutes to see only the effects from the charging which can be refreshed by natural relaxation of the charges or by UV exposure, not from the device degradation. However, it shows significant changes in luminance intensity. Both devices with 3 and 10 mg/mL QD solution were driven under two different initial luminance, around 410 and 670 cd/m^2, to make sure if the difference of initial intensity brings different results. Initially, the device containing a thicker QD layer shows the luminance intensity begins to decrease promptly. However, the device containing thinner QD layer shows the initial luminance intensity increases shortly after the operation followed by the slow decrease compare to the thicker layer. A similar phenomenon has been observed and reported previously in the literature [104]. Mashford et al. reported that the both EL and PL of QDs were more stable in the combination of thinner QD emitter with ZnO nanoparticle layer because of a charge neutralization process. The positively charged QD due to an electron transfer from CBM of QD to that of ZnO can be neutralized by a hole (i.e. positive charge) extraction from VBM of QD to

the energetically aligned mid-gap states of adjacent ZnO nanoparticle. The only difference of our results compared to the reference is that the brightening of luminance is weaker and the increased luminance begins to decrease again in short timescale. In our case, the energy offset between the CBM of ZnO nanoparticles and that of InP/ZnSe/ZnS QDs would bring the lower level of positively charged QDs in the equilibrium state. Moreover, the lower VBM of InP/ZnSe/ZnS QDs than that of CdSe/CdS facilitates the hole injection into QDs, and brings more hole accumulation at the interface of ZnO/QD, which could lessen the effects of neutralization of QD emitter during the operation; the charging behavior is stronger than neutralization process in our devices. Therefore, the brightening of luminance is less than the results from the literature.

A modified model from the reference could explain why the efficiency and luminance of the device with thinner QD layer overtake those from the thicker QD layer at a higher driving current density (***Figure 6.1.4***).

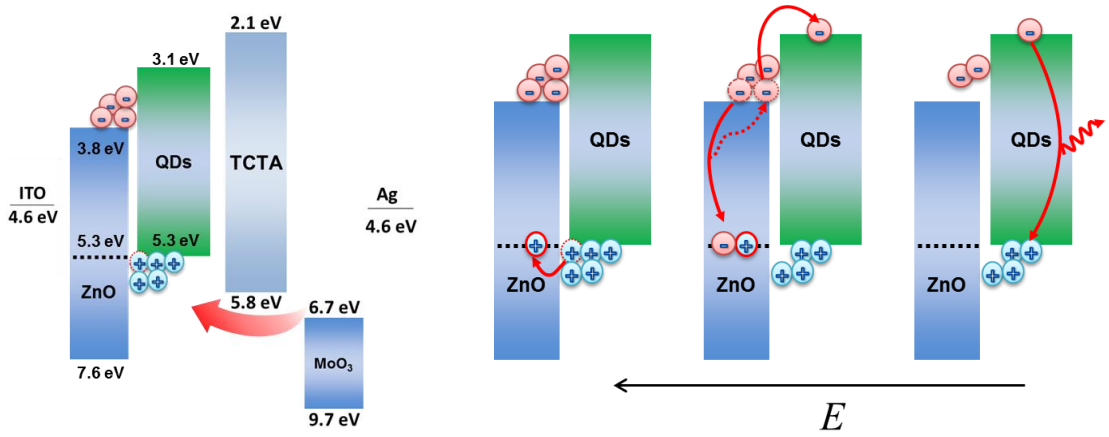

Figure 6.1.4 Illustrated process for neutralization of charged QD and Auger-assisted electron injection through interactions between InP/ZnSe/ZnS QDs and ZnO nanoparticles.

Electrons are accumulated at the CBM of ZnO nanoparticles near the interface with QDs because of the 0.7 eV of the energy barrier to the QDs. Holes are also accumulated more at the VBM of InP/ZnSe/ZnS QDs near the interface of ZnO nanoparticles. However, the accumulated holes could be efficiently extracted to the adjacent mid-gap states of ZnO layer which is well aligned with the VBM of QD layer, and then the extracted hole could recombine with the electron accumulated at the ZnO/QD interface. The energy generated from the recombination transfers to the other electrons at the ZnO/QD interface followed by the electron injection into the CBM of QD, which is the Auger-assisted energy up-conversion process. Moreover, the process of accumulated hole

extraction could be facilitated by the even strong electric field during the operation in the same direction, which would reduce the field-induced quenching problem. Finally, the neutralization of charged QD and Auger-assisted electron injection would remain the QDs in an emissive, less charged state under the high current density operation. Again, the thinner QD layer close to the ZnO would have more stable uncharged state through the explained mechanism, but a thicker QD layer, which has more distance from the ZnO/QD interface, would experience stronger luminance quenching and remain unstable during the operation. Thicker QD layer also needs a high electric field to operate the device, which would cause a more severe field-induced quenching [80]. Even though the hole extraction from QD to ZnO layer is possible in this mechanism, the electron block property against exciton dissociation still works because very low current density (c.a. 1.4 $\times 10^{-4}$ mA/cm^2) is observed when the device is operated in the reverse bias, as shown in ***Figure 6.1.5***.

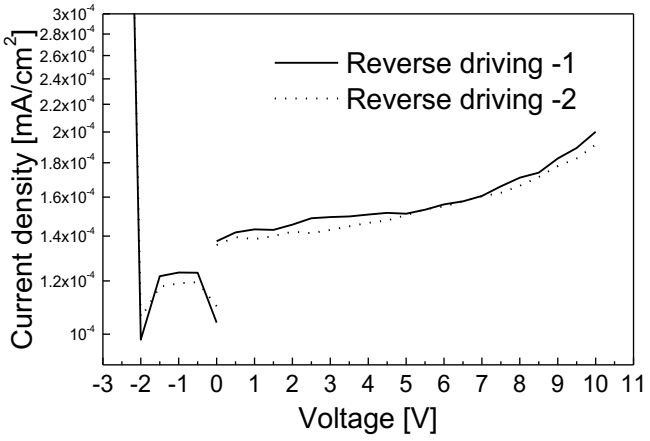

Figure 6.1.5 Current density-voltage characteristic with first reverse bias sweep. *(YH202)*

Interestingly, the conventional QLEDs with different QD thickness show slightly different trends on the device performance as shown in ***Figure 6.1.6***. A trade-off between luminance and efficiency is not observed in ***Figure 6.1.6b***. Moreover, the current efficiency drops immediately as luminance increase in the most of the conventional QLEDs, which is not observed from the inverted QLEDs in our experiments. In the conventional structure, we only used the organic charge transport layer, and then the electron is very easily accumulated at the interface of QD/poly-TPD because of the facilitated electron injection through an only small contact barrier between QD/TPBi interfaces. The accumulated charges at the interface of QD/poly-TPD have no possibility to be neutralized with adjacent organic layers; rather, the charged QD leads to

unstable current efficiency along the driving voltage because the generated excitons in the RZ undergo Auger recombination quenching with the excess holes (i.e. positive charges). This quenching process is severe because the RZ is close to the interface of QD/poly-TPD (***Figure 6.1.6c***), which is indicated by the parasitic emission of poly-TPD at the peak of 425 nm in the EL spectrum of all devices with different QD concentration. Consequently, the current efficiency of all devices begins to decrease seriously by the luminance quenching process from the beginning of the EL of the device.

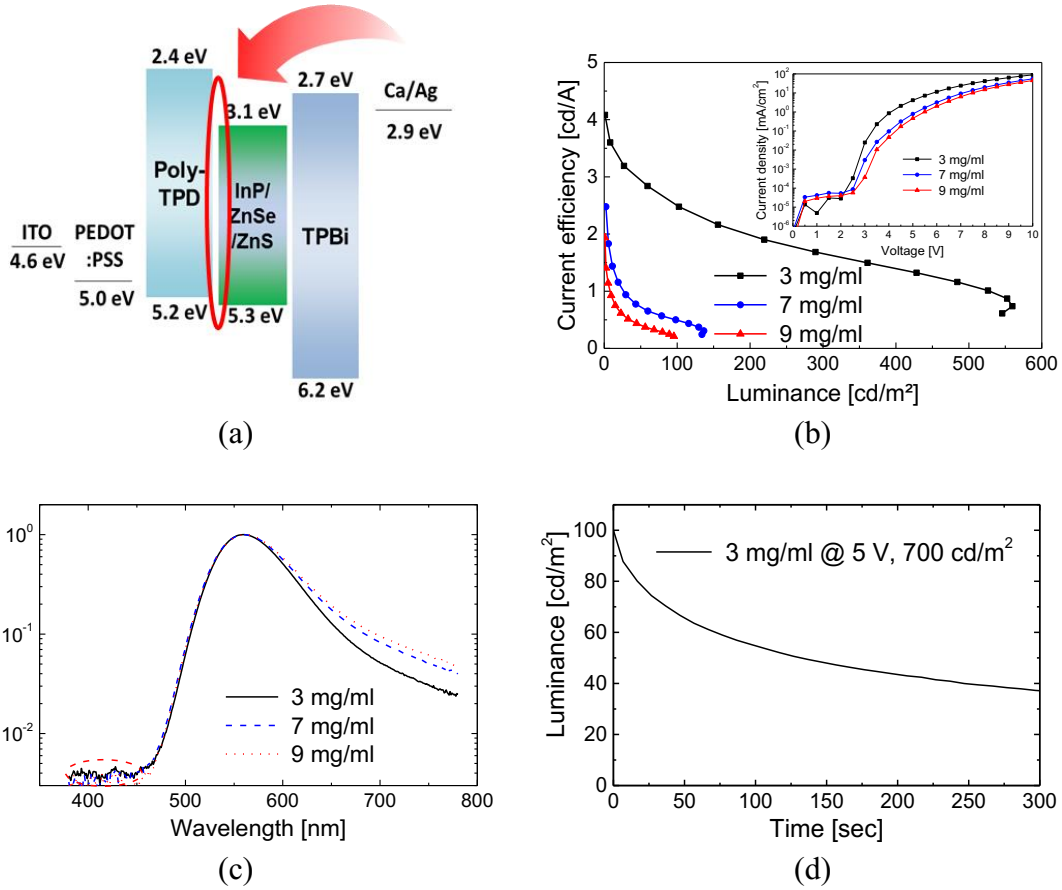

Figure 6.1.6 (a) A band diagram, (b) current efficiency-luminance curves and (c) photoluminescence spectra for the conventional QLEDs with different QD layer conditions. (d) Luminance changes as a function of time, which is measured in the more optimized structure that has maximum current efficiency and luminance of 8.8 cd/A and 3200 cd/m^2, respectively. *(YH37, YH38, YH39, (d) YH81)*

Moreover, the luminance drops from the beginning in the lifetime measurement shown in ***Figure 6.1.6d*** also have the good agreement of no neutralization process in a conventional device with 3 mg/mL QD solution. On the other hand, the thinner QD layer (i.e. lower concentration) increases the performance of the conventional device regarding both luminance and current efficiency by the modulated charge balance. In contrast, the thicker QD layer decreases the exciton generation efficiency because of the charge

unbalance at the RZ near the QD/poly-TPD interface due to the high resistance of the thick emitter layer, which results in the low device performance.

Additionally, the superior efficiency with thicker QD layer at a low luminance region is not observed. It can be addressed by the following hypothesis. The QD layer part which is close to the interface with TPBI has a low probability of generating the excitons because the fast electron injection from the cathode and the low hole mobility of the QD layer still confine the RZ near the QD/poly-TPD interface. Therefore, even thicker QD layer has low exciton recombination efficiency even in the low luminance region. The influence of carrier mobility and thickness of QDs on the RZ will be discussed further in the following chapters.

6.2 Optimization trends according to the thickness of QD layer

6.2.1 Different recombination zone (RZ) model

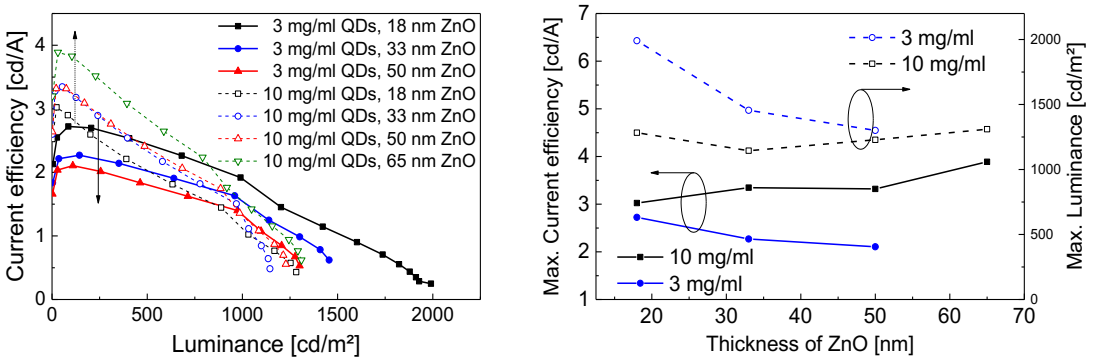

Figure 6.2.1 (a) Current efficiency-luminance curves and (b) maximum current efficiency and luminance as the function of ZnO thickness. *(YH216–YH218, YH220–YH223)*

We have discussed in ***Chapter 6.1.1*** that a different thickness of InP/ZnSe/ZnS QDs leads to a trade-off between luminance and current efficiency in the inverted QLEDs, particularly the ones fabricated with ZnO nanoparticles. Here, the different QD emitter thickness in the inverted QLEDs brings us different carrier balance trends in our experiments. First of all, ZnO thickness was varied to find the better charge balance in the devices with the QD concentration of both 3 and 10 mg/mL. There is a reverse trend according to the increasing thickness of ZnO nanoparticle layer, combining with two different QD layer conditions. ***Figure 6.2.1a*** shows this opposite trend of current efficiency-luminance characteristics. The maximum current efficiency and luminance

point are depicted as a function of the ZnO thickness in ***Figure 6.2.1b*** as well. The maximum luminance and current efficiency decrease as the thickness of ZnO increase for the devices with the 3 mg/mL QD solution, however, the performance increases with the devices with the 10 mg/mL QD solution. According to this reversed trend, first, we could presume that the injected electron amount is less than that of the holes within the RZ when using a thin QD emitter thickness; therefore, the increased number of injected electrons in the QD layer via the reduced ZnO thickness finally enhances the charge balance at the RZ. On the contrary, since thick QD layer has already more electrons than holes in the RZ, the increased ZnO thickness lowers the electron injection and leads to the better charge balance at the RZ. In order to explain this phenomenon more systemically, we hypothesized that the different QD thickness causes a change of RZ region in the inverted device structure. As it is depicted in ***Figure 6.2.2***, the RZ is expected to be located close to the interface of ZnO/QDs or the monolayer of QDs (RZ-A) for the device with thin QD layer, and the interface of QD/HTL for the device with thick QDs (RZ-B).

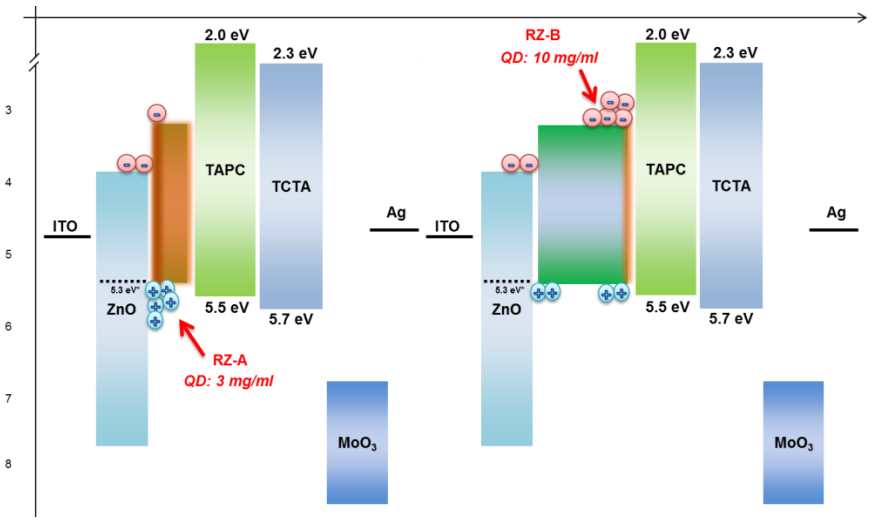

Figure 6.2.2 Band diagrams of inverted QLEDs with the suggested RZ according to the different QD thickness.

The shift of RZ may be originated from the different carrier transport behavior which leads to a different charge accumulation in the thin QD film. Here, the QDs in RZ-A are more positively charged and the QDs in RZ-B are more negatively charged because of the different charge accumulation processes in the device architecture. The electron-only device (EOD, ITO/ZnO/QDs/Ca/Ag) and hole only device (HOD, ITO/QDs/TCTA/MoO_3/Ag) with different thickness of QDs were fabricated to investigate the different carrier transport trends in the QD film. ***Figure 6.2.3c*** shows

the J-V curves from the EOD and HOD. The current density at 2 V, trap-controlled SCLC region, was compared for both single carrier devices with two different QD thickness. The current density increased around 1.5 times with thicker QD layer in the EOD device, but it is increased over 13 times with HOD, which indicates that electron transport is faster than hole transport in the QD film.

Table 6.1 Hall mobility of different bulk materials measured at 300 K.

Bulk	E_g (eV)	E_c (eV)	E_v (eV)	Electron mobility ($cm^2V^{-1}s^{-1}$)	Hole mobility ($cm^2V^{-1}s^{-1}$)
InP	1.35	3.65	5	5400	200
ZnSe	2.7	2.8	5.5	180	5
ZnS	3.6	2.4	6.0	500	30

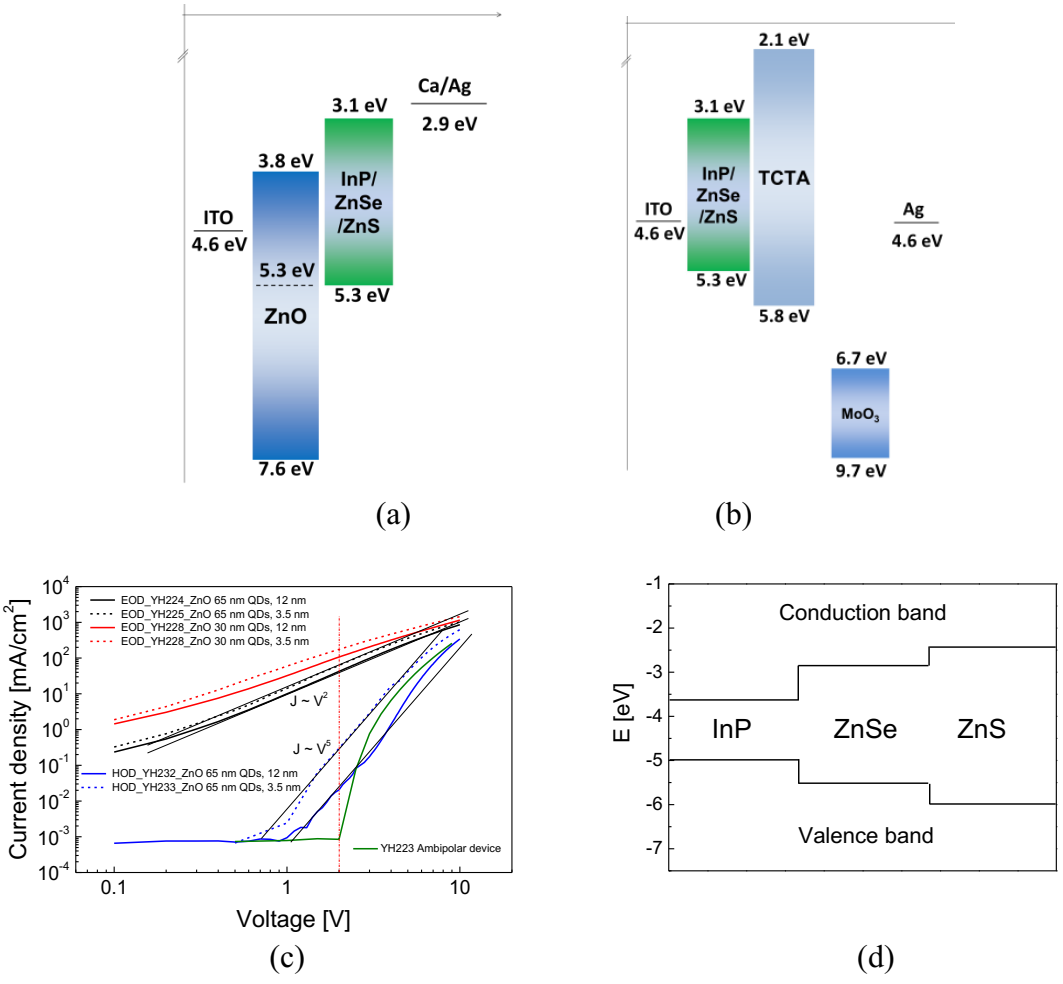

Figure 6.2.3 The band diagram of (a) EOD and (b) HOD, and (c) current density-voltage characteristics from them. (d) A type I heterojunction structure of InP/ZnSe/ZnS QDs [178]. *(YH224, YH225, YH228, YH229, YH223)*

As a type I heterojunction structure of InP/ZnSe/ZnS QDs makes electron more localized in a core compared to the hole, the slower electron transport in QD film is

expected (***Figure 6.2.3d***) [45,178]. However, the bulk mobility of InP, ZnSe, and ZnS in ***Table 6.1*** shows that our results with slow hole transport come from the low hole mobility of the inorganic core/shell materials. It is supposed that the carrier transport between the QD to QD happens with the hopping through the outer ZnS shell, without the experience of strong localization effect in the core. Therefore, the slower hole transport in the QD film is in good agreement. Therefore, the difference between hole and electron mobility in the QD film supports more about the different RZ model according to the change of emitter thickness. When the QD layer thickness is increased, the injected electrons that are faster than holes in QD layer could be accumulated near the QD/HTL interface rather than the ZnO/QD interface. This model also has a strong agreement with the current efficiency and luminance trade-off which is explained in ***Chapter 6.1.1*** . The accumulated holes at the ZnO/QD interface with the thin QDs layer could be efficiently discharged by the extraction to the mid-gap of ZnO nanoparticles (the high luminance at the high voltage). However, the accumulated electrons at QD/HTL interface with the thick QD layer have more chance to have non-radiative Auger recombination (the low luminance at the high voltage) with only the holes in VBM of QDs because the HOMO of HTL blocks electrons.

6.2.2 TAPC HTL effects with the different thickness of QD layer

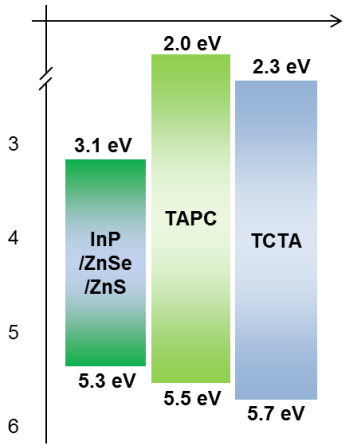

Figure 6.2.4 Band diagram of TAPC and TCTA hole transport layer compared with QDs.

Since the different charges are accumulated at the QD emitter in the devices with various QD thickness, a better carrier balance would be accomplished, not only by controlled electron transport but also by hole transport. As the change of TCTA thickness has minor effects on the device performance in our test, different hole transport materials are considered already in ***Chapter 5.5.5*** to control the hole transport properties.

Figure 6.2.4 and ***Table 6.2*** shows the parameters for TCTA and TAPC again. Concerning the enhance of device performance, the band alignment of QD with CBM of InP/ZnSe/ZnS QDs, the barrier for the electron blocking and the hole mobility should be considered. TAPC has a well-matched HOMO level with QD's and higher hole mobility; 1.1 eV of high energy barrier against electron dissociation and two orders of magnitude higher hole mobility compared to the TCTA.

Table 6.2 The value of HOMO, LUMO and hole mobility from different hole transport materials.

HTL	LUMO (eV)	HOMO (eV)	Hole mobility ($cm^2V^{-1}s^{-1}$)
TAPC [170]	2.0	5.5	1×10^{-2}
TCTA [170]	2.3	5.7	1×10^{-4}

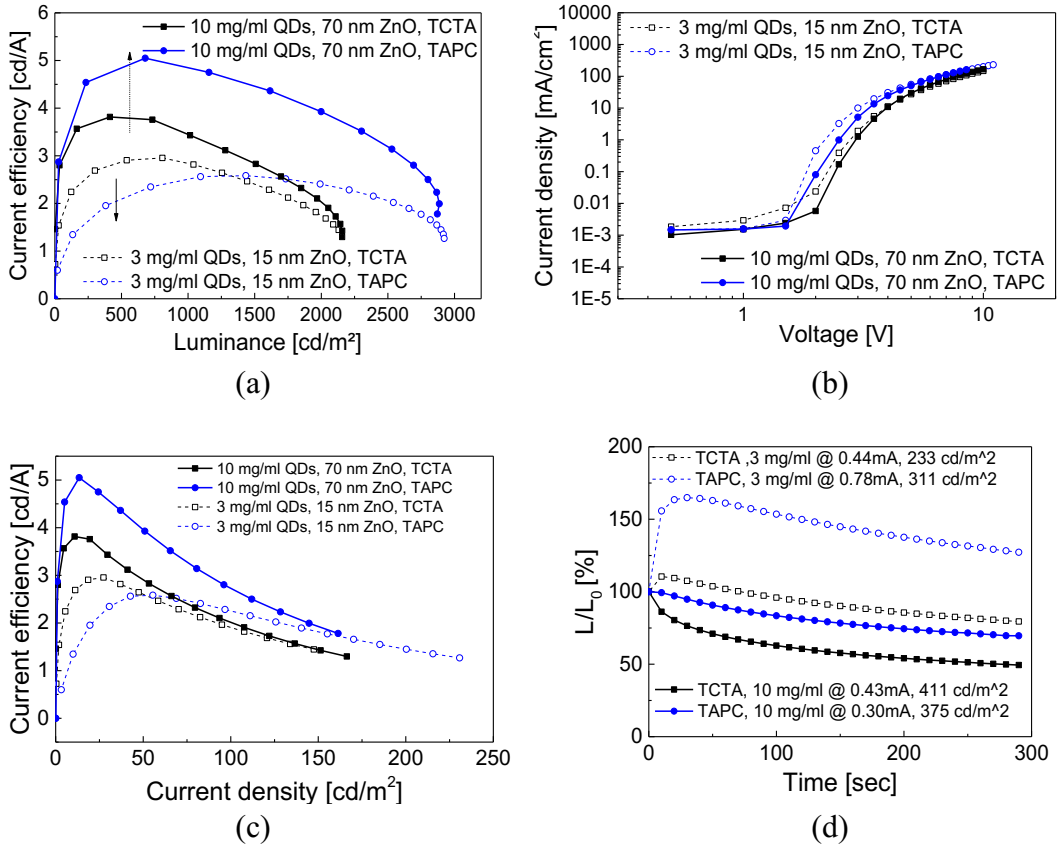

Figure 6.2.5 Compared device performance according to the different HTL, TCTA and TAPC. (a) Current efficiency-luminance, (b) current density-voltage, (c) current efficiency-current density and (d) luminance-time characteristics. *(YH239, YH256, YH252, YH258)*

Figure 6.2.5 shows the performance change after the TAPC is applied in the inverted QLEDs. For the control devices, the ZnO thickness of 15 nm and 70 nm were chosen for

the device with the QD concentration of 3 and 10 mg/mL, respectively. As expected, the performance of devices prepared with the QD concentration of 10 mg/mL and ZnO thickness of 70 nm increased due to the enhanced carrier balance through the increased amount of injected holes at RZ-B by TAPC layer. The maximum current efficiency and luminance increased from 3.8 cd/A and 2157 cd/m^2 to 5.0 cd/A and 2870 cd/m^2, respectively. In contrast, the performance of the device with 3 mg/mL QD solution, which has more positively charged QD at RZ-A, decreased only the maximum current efficiency but increased the luminance as TAPC applied. The maximum current efficiency and luminance changed from 2.95 cd/A and 2130 cd/m^2 to 2.58 cd/A and 2922 cd/m^2, respectively.

The increment of luminance from the device prepared with 3 mg/mL QD solution and TAPC requires a different explanation. ***Figure 6.2.5b*** shows very low threshold voltage of 1.5 V with TAPC device (e.g. 2 V for TCTA), which could be realized by the low HOMO level of TAPC as well as an enhanced Auger-assisted electron injection process by higher hole charge density. Namely, the Auger-assisted charge injection requires a high charge density, and here the enhanced hole transport through TAPC HTL effectively boost this process. Therefore, the low driving voltage effectively suppressed a field-induced quenching effect in the device with 3 mg/mL QD solution, and it increased the luminance and current efficiency at the condition of high current driving (***Figure 6.2.5c***). In addition, a higher energy barrier of 1.1 eV against for electron dissociation under high electric filed compared to the 0.8 eV for TCTA also helps to suppress the quenching effect and increases the device performance.

Figure 6.2.5d shows the results of charging behavior associated with TAPC HTL. The charging effects reduced by applying the TAPC HTL in both devices with the QD concentration of 3 and 10 mg/mL. Surprisingly, there is a stronger brightening effect observed from the device with the thinner QD layer combined with the TCTA. This is in agreement with the charge neutralization effects on ZnO/QD interface during the operation. At the beginning of the operation, holes are more seriously accumulated at the ZnO/QD compared to the TCTA device and maintain the QD more positively charged (i.e. more severe luminance quenching). That is the reason why the initial luminance is restored over 160 % by the neutralization process during the operation, which is more distinct than the TCTA device. On the other hand, the device with 10 mg/mL QD solution and TAPC does not have an increase of the initial luminance because the RZ is

still located away from the ZnO nanoparticle layer, which could not have the neutralization process.

Different charging behavior according to the PEI interfacial dipole layer on TAPC-based QLEDs

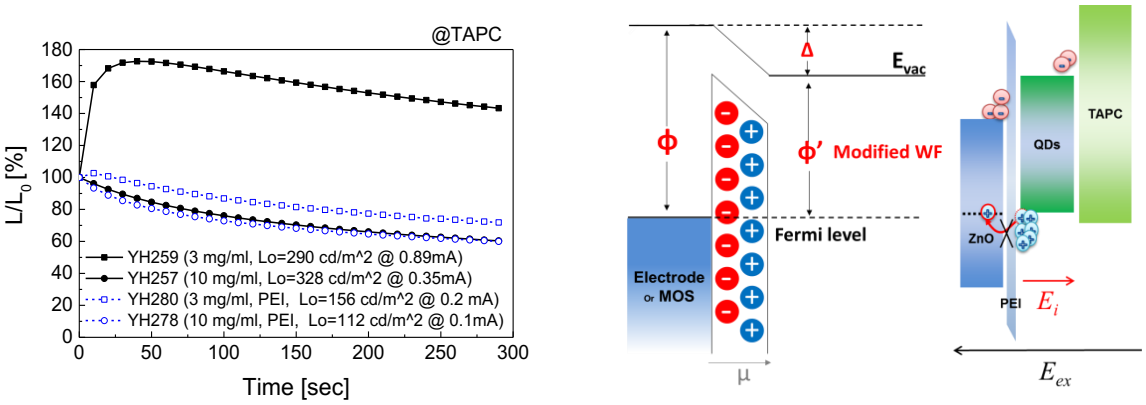

(a) (b)

Figure 6.2.6 (a) Electroluminescence as a function of time and (b) a band diagram of ZnO/PEI/QD layer. *(YH259, YH257, YH280, YH278)*

As we observed through the trends of device charging, the brightening of initial luminance with the device with thin QD layer accounts for the charge neutralization process of accumulated holes at the ZnO/QD interface. ***Figure 6.2.6a*** shows another interesting charging effect from the device with PEI interfacial layer, which strongly supports the process explained above. A very thin layer of PEI used as interfacial dipole was inserted between ZnO ETL and QD layer to increase electron injection efficiency by modifying the work function of ZnO nanoparticles by the vacuum level shift. However, the strong dipole moments from thin PEI layer could interrupt hole extraction from the VBM of QDs to the mid-gap states of ZnO nanoparticles (***Figure 6.2.6b***). As we expected, ***Figure 6.2.6a*** shows the device with thin PEI layer and the 3 mg/mL QD solution shows less luminance increase as a function of time compared to the device without PEI, but clearly not with 10 mg/mL QD solution. Therefore, the charge neutralization process at the ZnO/QD interface with especially thin QD emitter was verified once again through this result. (The absence of charge neutralization effects by applied PEI layer also explains the non-effects of PEI on 3 mg/mL QD solution-based device, ***Figure 5.5.22***)

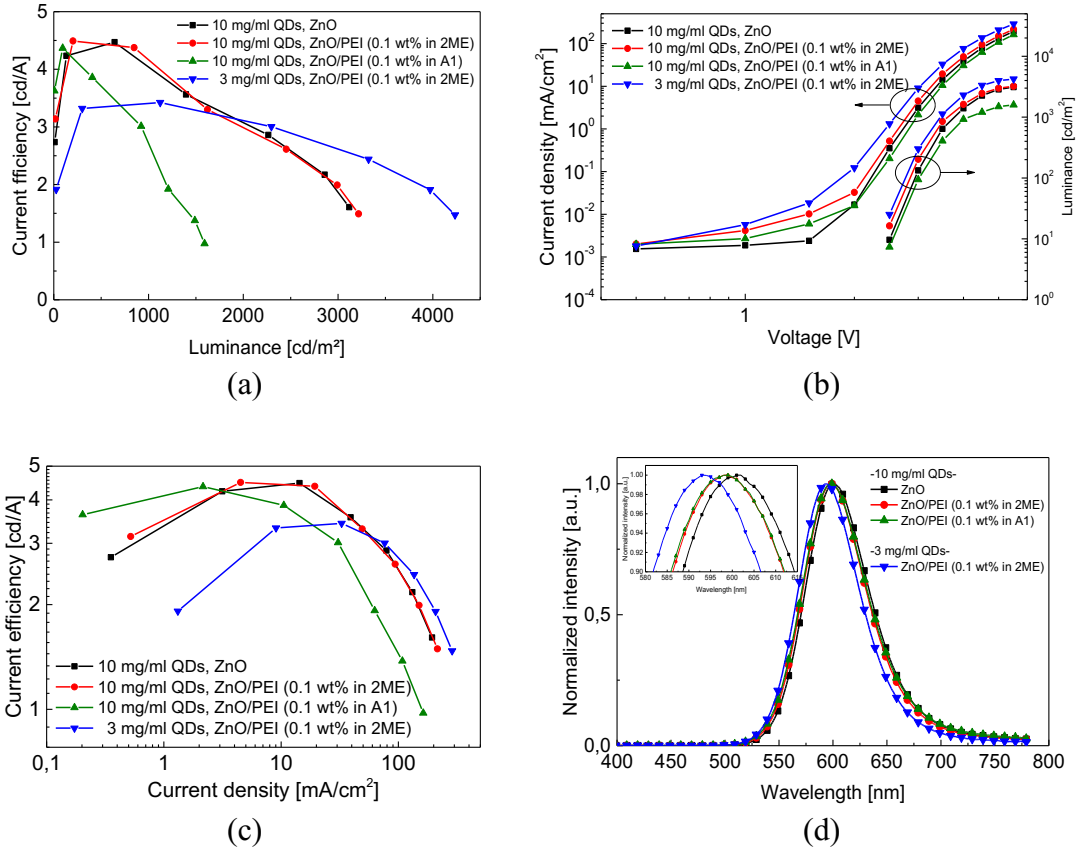

Figure 6.2.7 Compared device performance according to the different thickness of PEI and QD layer. (a) Current efficiency-luminance, (b) current density-voltage, current efficiency-current density and luminance-time characteristics, (c) current efficiency-current density and (d) EL spectra at 4 V. *(YH277–YH280)*

Figure 6.2.7 shows different device performance according to PEI presence combined with the different QD thickness (i.e. the thickness of PEI could not be measured, but it can be addressed by the lower current density of the device with an A1 solvent in ***Figure 6.2.7b***). The addition of a PEI layer has no positive effect on the performance. In addition, the thicker PEI layer deposited with A1 solvent compared to the one with 2ME solvent rather reduces the device performance more in the luminance. Here, the TAPC efficiently enhances the carrier balance by increasing hole injection. Therefore, the delayed electron transport is not necessary for the current device structure (i.e. 75 nm of ZnO delayed electron transport already enough). ***Figure 6.2.7d*** shows the blue-shift of EL spectrum when PEI applied in the device with 10 mg/mL QD solution because the QCSE is reduced by a suppressed local electric field with the PEI layer, as shown in ***Figure 6.2.6b***. Namely, in the case of TAPC applied device, a number of accumulated holes would always be higher than the accumulated electrons at the PEI/QD interface, even with both thick and thin QD layers because the hole injection process was

more efficient than the TCTA based devices. Therefore, the accumulated holes reduced the internal electric filed in most of the case here.

The effects of different ETL thickness on TAPC-based QLEDs

Heretofore, the combination of thin QD layer with thinner ZnO layer and thick QD layer with thicker ZnO layer has an effect of increasing the device performance fabricated with TCTA HTL. We also have found the TAPC HTL has a positive effect on high performance QLEDs by reducing the charging effects with better carrier balance. Different layer thicknesses of ZnO nanoparticles were investigated again to confirm whether the device with TAPC still has an opposite trend depending on the QD thickness. If successful, this would also agree with the suggested RZ model. ***Figure 6.2.8a,b*** shows the similar results to ***Figure 6.2.1a.*** The current efficiency and luminance are increased with thicker ZnO nanoparticles with 10 mg/mL QD solution. However, the change of ETL has stronger effects on brightening the luminance unlike the results with TCTA. As we discussed in ***Figure 6.2.5***, this difference was also attributed to the lower driving voltage of the device with TAPC HTL. The device becomes more stable against the quenching at the even high-electric field. Therefore, it shows more stable efficiency under the high current density, as shown in ***Figure 6.2.8b***. On the other hand, the maximum luminance also increased with thicker ZnO layer with 3 mg/mL QD solution, which is opposite to devices resulting from using TCTA. Here, the accumulated holes at ZnO/QD interface are more likely to extract not only to adjacent mid-gap of ZnO nanoparticles but also to the entire layer of ETL because strong forward bias which applied for electroluminescence could facilitate hole extraction. Therefore, positively charged QD emitter could be effectively neutralized at the high driving voltage and remain the electroluminescence higher. This explanation is supported as well by the stronger luminance increase in the close blue-dot curve shown in ***Figure 6.2.8d.*** An interesting J-V characteristic from the device with 3 mg/mL QD solution also supports the efficient neutralization process with thicker ZnO layer, shown in ***Figure 6.2.8c***. The current density of this device (closed blue-dot curve) is higher (more in the high driving voltage) with 40 nm of ZnO nanoparticles than 15 nm. In general, the thicker charge transport layer reduces the conductivity of device and brings lower current density. However, here a space charge generated from the holes accumulating in the QD layer could be reduced by a neutralization process, which would enhance the charge transport in the device and results in the increase of the current density in the high voltage range.

Figure 6.2.9 shows device capacitance curve as a function of voltage (C-V) measured with the frequency of 1 kHz. In general, the device capacitance increases by the majority charge injection and it rapidly decreases by the minority charge injection followed by the radiative charge recombination [179]. Here, the devices with 3 mg/mL QD solution show only one peak in C-V curves, but the devices with 10 mg/mL QD solution show the second peak as the applied voltage increases. It is expected that the first peak was originated from hole injection in both conditions. However, it is expected the second peak was arisen because of the electron accumulation at the QD/TAPC interface, as the charged QDs with the electrons cannot be neutralized. Therefore, the C-V curves as shown in ***Figure 6.2.9*** can be the other evidence of the Auger-assisted charge neutralization model.

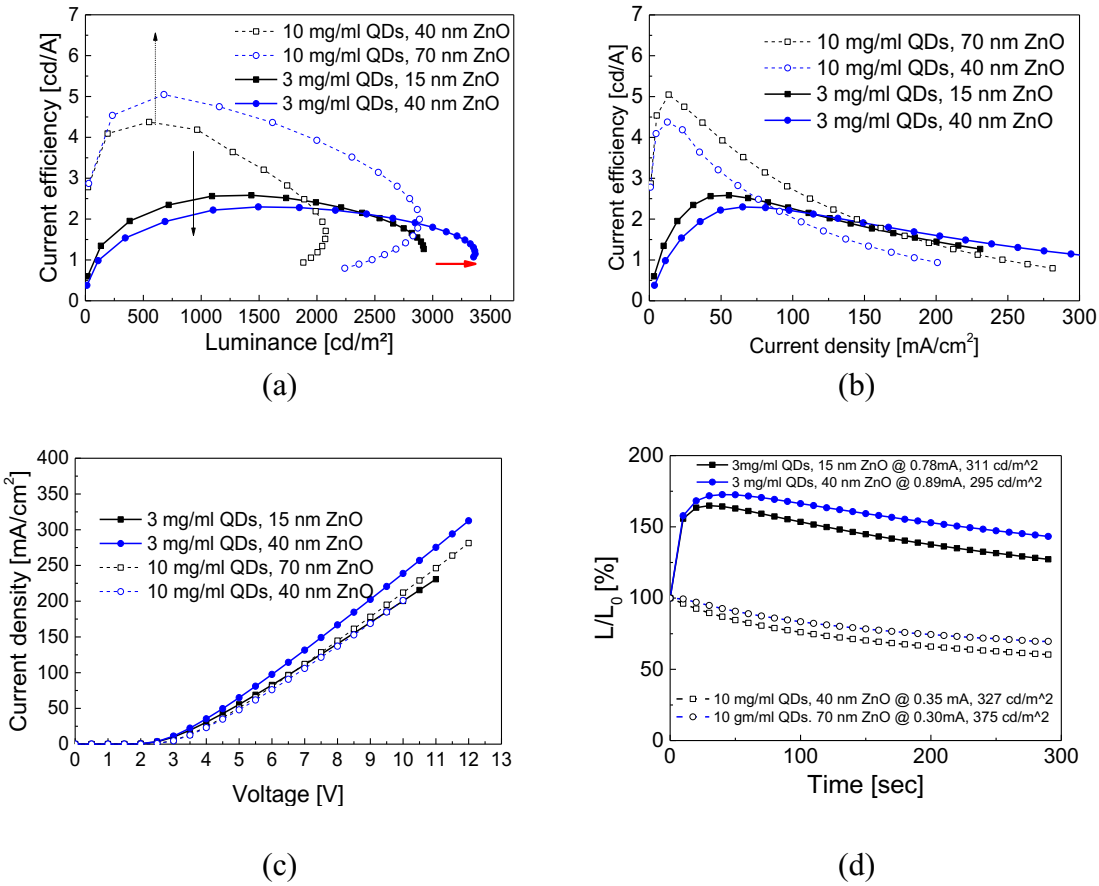

Figure 6.2.8 (a) Current efficiency-luminance, (b) current efficiency-current density, (d) current density-voltage characteristics and (d) electroluminescence decay as a function of time of the devices with different ZnO and QD thickness. *(YH257 YH256 YH258 YH259)*

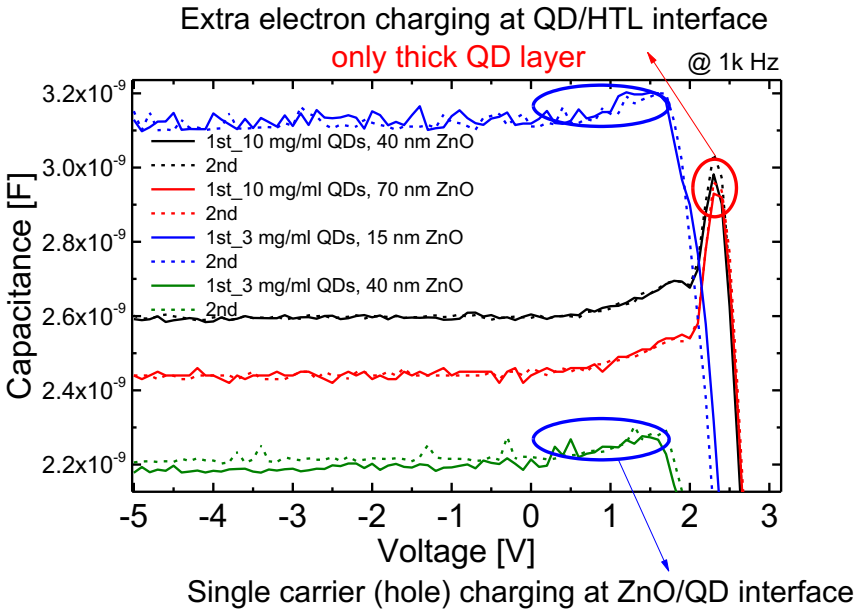

Figure 6.2.9 Capacitance as function of voltage (C-V) characteristic measured with the frequency of 1 kHz. *(YH257 YH256 YH258 YH259)*

Device performance dependent on QD thickness using TAPC as HTL

As discussed earlier in ***Chapter 6.1.1*** , there are trade-off trends according to the different QD concentration in the TCTA-based device. Here, the effects of different QD concentrations in TAPC-based devices are investigated. The inverted device consists of an 88 nm ZnO layer to see the current efficiency as a function of luminance curves, as shown in ***Figure 6.2.10a***, which shows a similar trade-off to ***Figure 6.1.1a***.

Thicker QD layers show higher current efficiency but lower luminance. Thinner QD layers show higher luminance but lower current efficiency. Moreover, thicker QD layers show lower current density in the J-V curve shown in ***Figure 6.2.10b.*** However, the trade-off among the device with 5 and 3 mg/mL is negligible compared to the results of TCTA-based devices. Since TAPC HTL cause the more hole injection into QDs layer (i.e. more hole accumulation near ZnO/QD interface), the RZ should be located near the ZnO/QD interface, which could have lower luminance quenching because of neutralization effects. According to the relative EL decay curves shown in ***Figure 6.2.10c***, the charging effects is reducing when the thickness of QD decreases because the RZ is moving closer to the ZnO/QD interface (i.e. more efficient neutralization effects). The EL spectra in ***Figure 6.2.10d*** shows that there is stronger Stokes shift (i.e. red-shifted EL spectrum compared to the PL spectrum) as the QD layer thickness increases. This red-shift is originated from the exciton migration to larger QDs inside of close-packed QD ensemble film due to resonant energy transfer within the film

[45,68,112,113], which would become larger with the thicker emitting layer. ***Figure 6.2.11*** shows current efficiency curves as a function of current density comparing TAPC and TCTA HTL.

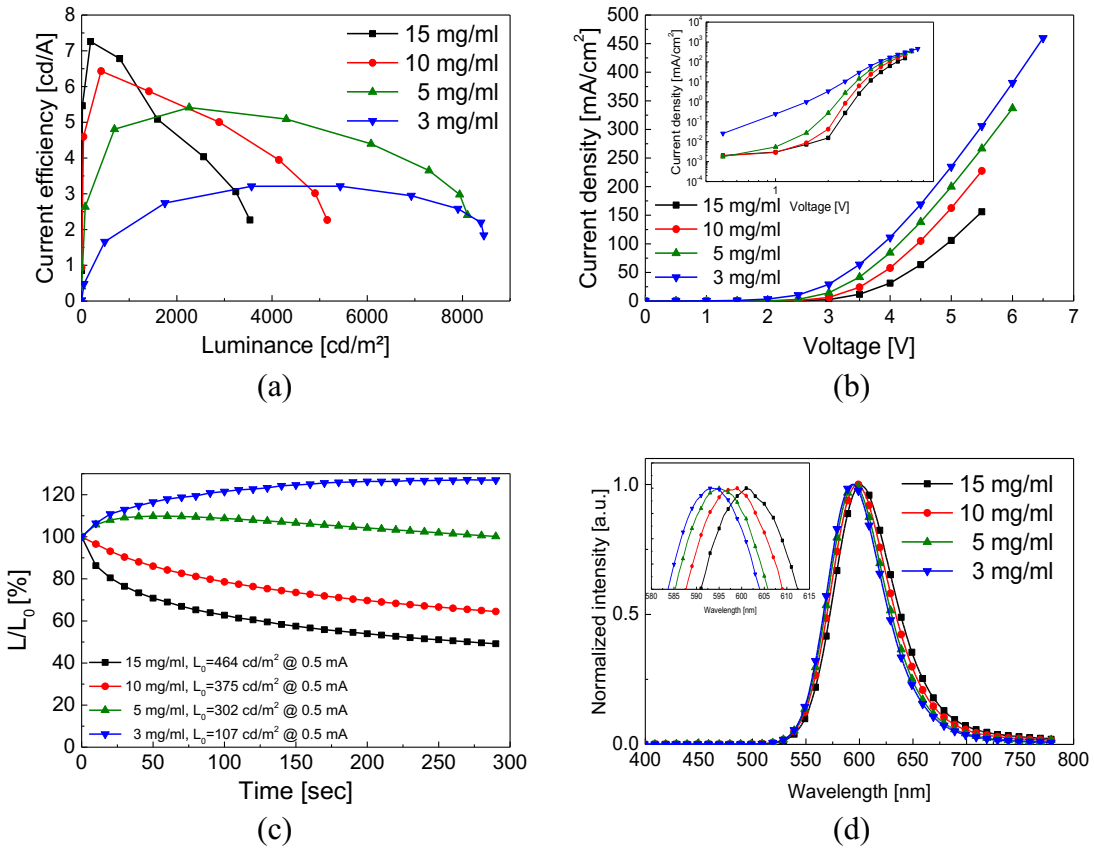

Figure 6.2.10 Device performance according to the different QD concentration. (a) Current efficiency-luminance, (b) current density-voltage (logarithmic scale, inset: luminance-voltage), (c) EL decay as a function of time, and (d) EL spectra at 4 V. *(YH373–YH376)*

Table 6.3 Summarized device performances.

QD (mg/mL)	Turn on @ 1 cd/m^2 (V)	Max. cd/A	Max. EQE (%)	Max. cd/m^2
15	2.2	7.3	3.3	3536
10	2.1	6.4	2.9	5158
5	1.9	5.4	2.5	8106
3	2.0	3.2	1.5	8449

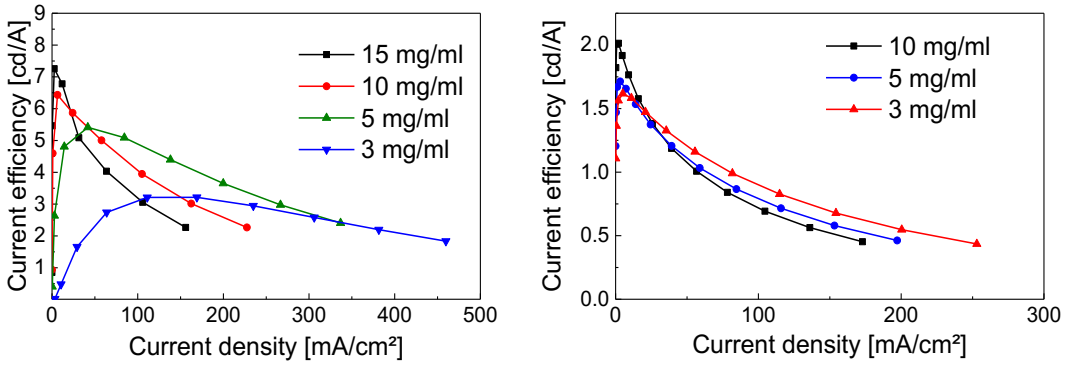

Figure 6.2.11 Current efficiency-current density curves from the device with (a) TAPC and (c) TCTA. *(YH373–YH376, YH213–YH215)*

The TCTA-based inverted devices show a similar efficiency roll-off behavior, which is originated from the luminance quenching by the charging and strong electric field, even though there is a different QD concentration. However, the TAPC-based inverted devices show different efficiency roll-off behavior according to the QD concentration. As the thickness of QD layer decrease, the roll-off of current efficiency is also suppressed because of the efficient charge neutralization effects even in the higher current density conditions. Moreover, the decreased local electric field in QD film with thinner QD layer provokes the suppressed field-induced luminance quenching. The device performances analyzed in this section are summarized in ***Table 6.3***.

EL spectrum shift depending on the QD thickness and applied electric field

Table 6.4 and ***Figure 6.2.12*** show the interesting behavior of the EL spectra, which has an agreement with the different charging behavior according to the QD concentration. As shown in ***Table 6.4,*** the stronger blue-shift of EL spectra is observed under an applied voltage increment from 2 V to 4 V when the QD layer in the devices becomes thinner due to the reduced or shielded electric field (i.e. reduced QCSE) [156]. The applied electric field to the QD films was reduced because the increased hole transport within the QD multilayer because its thinner layer thickness induced more hole accumulation at the interface of ZnO/QD. With this hole accumulation in the valence band of QD, effective bandgap can become larger, which makes stronger blue-shift of EL peak. In addition, the internal electric field ($\overrightarrow{E_i}$), generated to the opposite direction from the applied external electric field ($\overrightarrow{E_{ex}}$) between the two electrodes, also reduces applied E-field in the QD layers. This concept is depicted in ***Figure 6.2.12a*** and it is also

suitable for the explanation of the different spectrum shift displayed in ***Figure 6.2.12b,c and d***. The blue-shift of peak wavelength with the lower concentration of QD solution is more distinct in the inverted device with TAPC (***Figure 6.2.12b***, 6 nm) compared to the device with TCTA (***Figure 6.2.12c,*** 2 nm) and even conventional devices (***Figure 6.2.12d,*** 1 nm). The less hole accumulation at the ZnO/QD or QD/TPBi interface originated from the slower hole injection property of these devices leads to the weaker internal electric field ($\overrightarrow{E_i}$), which consequently suppressed the level of spectrum shift.

Figure 6.2.13 shows another blue-shift of chromaticity coordinates during the EL decay measurement shown in ***Figure 6.2.10c*** for the devices with different QD layer thickness. Even though the small changes of chromaticity coordinate considering the measurement accuracy described in the figure caption, the blue-shift of spectrum indicates another shielded QCSE with thinner QD layers. A red-shift of spectrum was actually expected, as the neutralization process would remove the accumulated holes during the operation (i.e. weaker ($\overrightarrow{E_i}$)). However, hole accumulation was increased during the constant current driving even though with thinner QD layer, which led to the spectrum blue-shift again. Therefore, it could be assumed that the charge accumulation process is still faster than the neutralization process.

Table 6.4 The blue-shift of EL spectrum as increasing the driving voltage *(YH373–YH376)*

Voltage (V)	EL λ_{max} (nm)			
	15 mg/mL	10 mg/mL	5 mg/mL	3 mg/mL
2.0	611	610	612	616
2.5	605	602	599	599
3.0	601	599	595	593
3.5	599	596	593	590
4.0	598	595	592	589
Blue shift (nm)	**13**	15	20	**27**

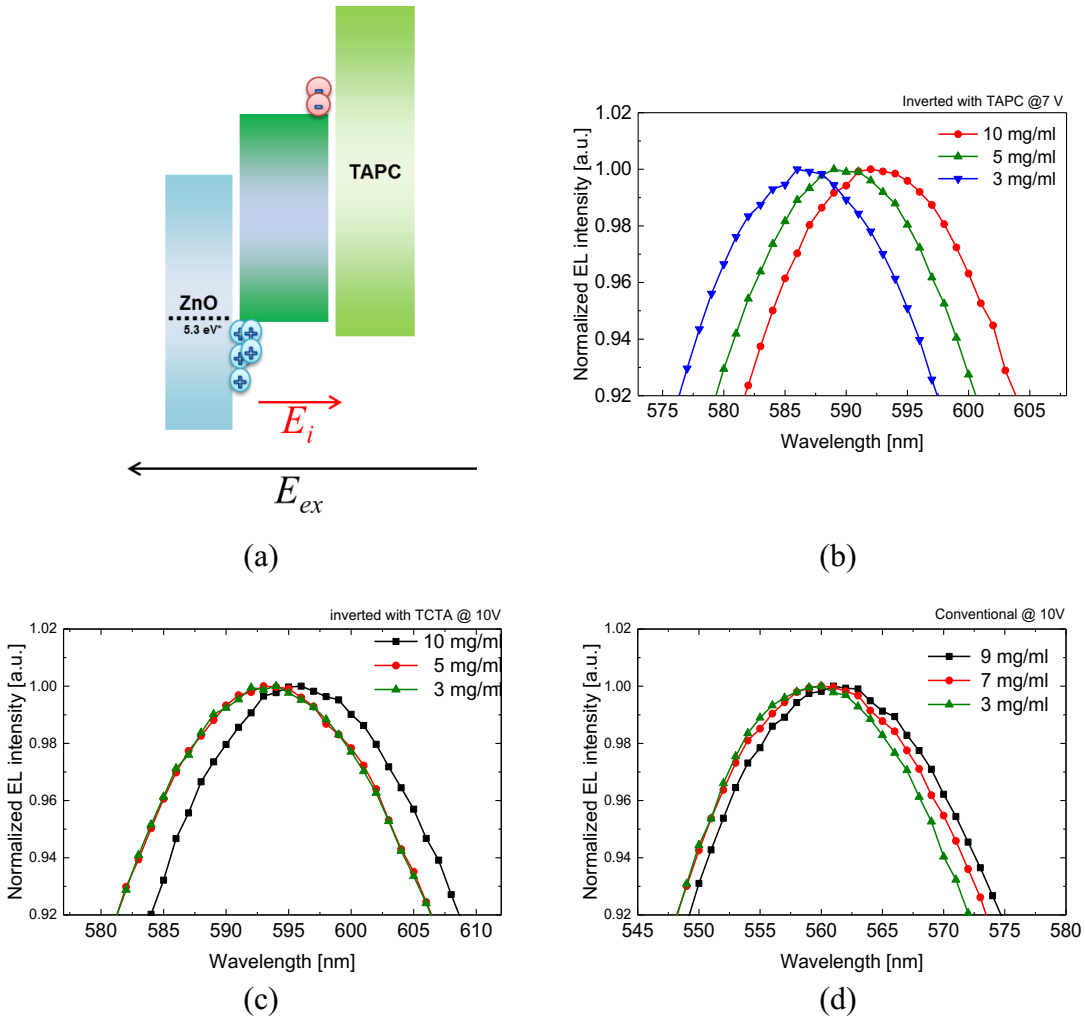

Figure 6.2.12 (a) A schematic of internal electric field induced by hole accumulation at the ZnO/QD interface. EL spectrum shift of different device structure by various QD concentration: (b) Inverted devices with TAPC (*YH374–YH376*, 592 → 586 (6 nm)), (c) inverted device with TCTA (*YH213–YH215*, 595 → 593 (2 nm)) and (d) conventional devices (*YH39–YH37*, 561 → 560 (1 nm)).

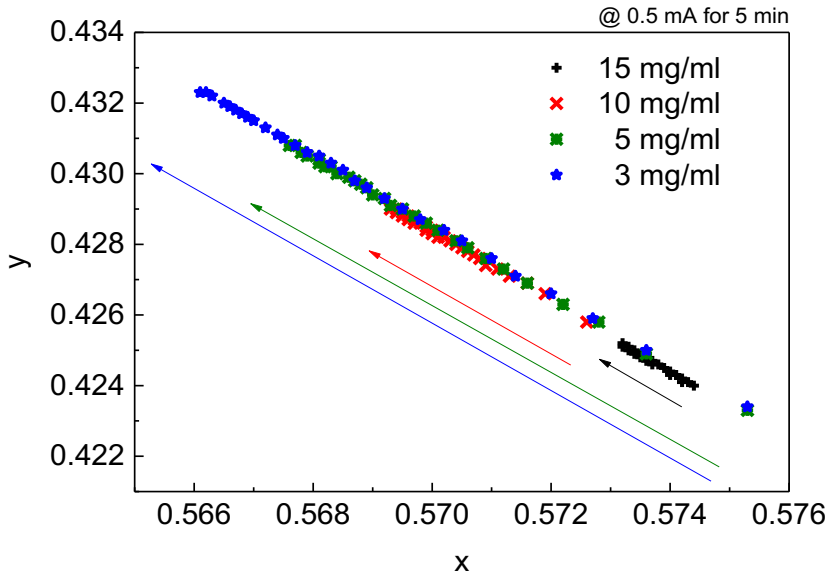

Figure 6.2.13 The CIE (Commission Internationale de l'Eclairage) 1931 chromaticity diagram showing the chromaticity coordinates changes during the EL decay measurement of devices with different QD thickness (Konica-Minolta CS-2000, chromaticity accuracy: x = ±0.0015, y = ±0.001, The temperature of different devices was constant at 21 °C ± 0.1 °C during the entire measurement). (*YH373–YH376*)

6.3 Summary

Since InP/ZnSe/ZnS QDs have a heterojunction structure of type I and are capped with organic ligands, the thickness of the QD layers has a potent effect on device performance and charge carrier balance. First of all, there is a trade-off between maximum luminance and efficiency according to the different thickness of QDs. Maximum current efficiency is higher with thicker QD layers, but maximum luminance is lower compared to thinner QD layers. Second, there are reverse carrier balance trends according to the different QD layer conditions modulating the electron or hole transports properties in the device architecture.

In order to explain the observed results, the model of different RZ positioning dependent on the QD thickness has been suggested. We have found that the hole mobility of InP/ZnSe/ZnS multilayer is slower than electron mobility through the HOD and EOD experiments, which locates the RZ in different positions.

Moreover, the interaction between the InP/ZnSe/ZnS QDs and mid-gap state of ZnO nanoparticles has been explained by the proposed mechanism which is the neutralization process of charged QDs accompanying the Auger-assisted electron injection. The trade-

off and reverse trends are originated from different carrier balance trends depend on different exciton RZ. As a result, thin QD emitters give high and stable luminance at high current driving conditions because the RZ near the ZnO/QDs provides efficient neutralization and Auger-assisted electron injection. On the other hand, thick QD emitters give higher current efficiency because multiple monolayers of QDs provide efficient exciton generation and recombination through the good charge balance at the RZ near the QD/HTL. The suggested models based on the QD thickness will give us the framework to design more efficient InP-based QLEDs.

Chapter 7

7 Conclusions and further directions

Since QLEDs technology arises as the next generation FPDs accompanying excellent device properties accomplished by the saturated and tunable emission color, high brightness and solution processability, the high performance and stable Cd-free QLEDs should be developed for the further commercialization. There has been an intensive investigation on the Cd-based QLEDs to understand the fundamental process, and the device performance is now competitive with the current OLED technology. Even though the lots of researches on Cd-free QLEDs during last five years, the performance, and understanding of the device mechanism are not keeping up with the highly developed Cd-based technology. In this dissertation, highly efficient and bright InP/ZnSe/ZnS QD-based QLEDs are developed through the perspectives of device architecture engineering, and the understanding of fundamental device mechanism, which provides experimental guidelines and theoretical insights for the designing of InP QD-based QLEDs.

7.1 Contributions

The main focuses of this dissertation are including the development of Cd-free QLEDs, enhancing the low performance and stability of Cd-free devices, and the better fundamental understanding of device mechanism.

The results of investigation clearly show the feasibility of the substituting Cd-based QDs with our InP/ZnSe/ZnS multishell QDs. The InP/ZnSe/ZnS multishell QDs are developed concerning the important QD materials design aspects; the effects of ZnS outer shell thickness and the organic ligand chain length were verified through the embedding the synthesized QDs in the conventional device structure. Through the sophisticatedly designed QDs, the maximum EQE and luminance of the conventional

QLEDs reach 2.5 % and 3164 cd/m^2, respectively (***Figure 7.1.1***). The relatively low device luminance and stability of the conventional device are improved through the in-depth of investigation on the inverted QLED architecture with the theoretical models developed through the perspectives of the device optimization process especially related to the thickness of the QD emissive layer. The developed models provide the insight of the location of RZ and the charge neutralization process during device operation and the guidelines for the QLED design and material choice. Through this investigation on the inverted QLEDs, the maximum EQE and luminance of the QLEDs reach 3.3 % and 8449 cd/m^2, respectively, which is promising results compared to other researches on the Cd-free QLEDs (***Figure 7.1.1***). In summary, both experimental device design aspects and theoretical models developed by the optical, electrical, and morphological investigation of QLEDs provide the feasibility of developing Cd-free QLEDs with InP/ZnSe/ZnS multishell QDs. Moreover, the results also give a broad scope to understand the optimization process of the device, a possibility to be applied in the fabrication and characterization of various hybrid optoelectronic devices.

The main contributions of this dissertation can be summarized as follows;

- Feasibility of substituting Cd-based QDs with InP/ZnSe/ZnS multishell QDs

- Promising InP-based QD design aspects for QLEDs; ZnS shell thickness and shorter alkyl chain length of aliphatic ligands

- Design aspects for efficient and stable inverted QLEDs: efficient electron injection via ZnO nanoparticles, the function of PEI interfacial dipole layer, QD layer thickness effects, and charge balance via different HTL materials (TCTA vs. TAPC)

- Developed theoretical models; a RZ shift model with different QD thickness, and an Auger-assisted charge neutralization model considering the ZnO mid-gap energy states and the CBM of InP/ZnSe/ZnS QDs.

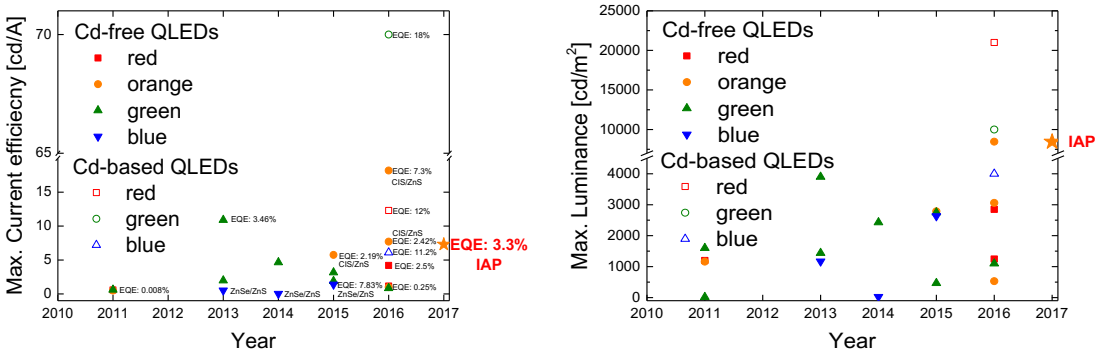

(a) (b)

Figure 7.1.1 The best performance of developed InP/ZnSe/ZnS QLEDs through this dissertation, compared to other Cd-free QLEDs. (a) Maximum current efficiency and (b) luminance.

Key design aspects of InP/ZnSe/ZnS QDs

In ***Chapter 4*** , the key design aspects of InP/ZnSe/ZnS QDs are confirmed, which is outer ZnS shell thickness and ligands chain length, in the well optimized conventional QLEDs structures.

The alloyed core-multishell structure of InP/ZnSe/ZnS QDs provides the delocalization of the exciton through a ZnSe shell, which reduces the serious Auger quenching originated from the QD charging. Moreover, an outer ZnS shell confines the electron and hole wave function again within the ZnSe shell, which minimizes exciton polarization under the applied electric field and improves the passivation of QDs. Therefore, the outer ZnS shell thickness is critical to control the balance between the exciton confinement and sufficient charge injection into the core. In our experiments, the thicker ZnS shell QDs shows better device efficiency and stability due to the suppressed the luminance quenching that is caused by the QD charging. This result is also supported by the enhanced charging behavior measured from the short time scale lifetime measurement under low driving voltage. However, the giant shell QDs limit device performance because of the hindered carrier injection and exciton delocalization even though the high QY and PL stability.

The shorter alkyl chain length of octanoate ligands increases the device EQE 47% compared to the stearate ligands. It has been also suggested that the self-quenching in a more close-packed QD film with the shorter ligands is not a dominant drawback because the device with the octanoate ligands shows the weaker stokes shift (i.e. EL red-shift) compared to the stearate ligands.

Electron injection in inverted QLEDs

The both current efficiency and power efficiency of the inverted QLEDs are enhanced by using interfacial buffer layers such as Al_2O_3 and PEI between ITO and QD layer by the increased electron injection even though reduced total current density with the thicker buffer layer. Moreover, it has been found that an electron injection from ITO to the CBM of QDs seems not so difficult through the Auger assisted electron injection process even though a high energy barrier around 1.6 eV. Consequently, a more stable and efficient device is realized by adopting ZnO nanoparticles as ETL. Commercially available Al:ZnO and ZnO nanoparticles improves the QLEDs performance by the increased electron transport into QD layer facilitated with the high electron mobility. A PEI interfacial layer also dramatically enhances device efficiency with the controlled carrier balance and reduced leakage current.

Surface morphology of ZnO nanoparticle layer

The high roughness of ZnO film leads to the high leakage current of QLEDs. Moreover, the QD layer deposition is strongly dependent on the surface condition of underlayer. The synthesized small ZnO nanoparticles (around 3.8 nm of particle size) clearly dispersed in a solvent with ethanolamine surfactant provide an ultra-smooth oxide transport layer which has 1.1 nm and 11 nm of R_q and R_{pv}, respectively. The surface roughness of ZnO film can be modulated as well by the controlling the concentration of ethanolamine in ZnO solution. In addition, the smooth ZnO layer leads to the smooth roughness of QD film like that of ZnO film, which increased QD/organic HTL interface condition. Our synthesized ZnO nanoparticles also make the multi spin-coating of ZnO layer possible through the orthogonal solvent process, which leads the smoother film as the spin-coating steps increase. Finally, an ultra-smooth interface condition between QD and CTL enhances device efficiency and luminance of the device tremendously through low leakage current and less interface trap states.

Electron and hole carrier balance in multilayer QLEDs

Concerning the parameters governing the EQE of QLEDs, the carrier balance in a multilayer structure is the most important factor to realize a high performance device. In the inverted QLEDs, a ZnO nanoparticle layer provides the effective control of electron transport through the multi spin-coated layer thickness and annealing condition regarding temperature and atmosphere. In ***Chapter 5.5*** , a reference device with the ZnO ETL and

relatively thick QD layer need more hole injections or lower electron injections for the better carrier balance at the QD emitter. Therefore, the increased ZnO layer provides 80% higher maximum efficiency compared to the thin ZnO layer. Vacuum conditions incorporated with a certain temperature for the ZnO layer annealing leads to the more stable and efficient device as well by removing the surface and crystalline defects. To obtain a further increase in the carrier balance, a TAPC HTL which has a lower hole injection barrier and higher hole mobility compared to TCTA is applied. The TAPC layer improves both device efficiency and stability through more efficient exciton generation in the QD emitter and reduces the threshold voltage of the device.

QD thickness dependent QLED optimization process

The thickness of QD layer has the most important effect on the device performance and charge carrier balance because of the heterojunction structure of type I and long insulating organic ligands of InP/ZnSe/ZnS QDs. First, the different thickness of QD layer brings a trade-off between the maximum luminance and efficiency. The maximum efficiency is higher with a thicker QD layer, but the maximum luminance is higher with a thinner QD layer. Seconds, the device with a thin QD layer prefers a thin ZnO layer to increase electron transport. However, a device with thick QD layer rather favors a thick ZnO layer to decrease electron transport into the QDs. This reverse optimization trend is also applicable to the hole transport control. A model for the different positioning of the RZ, which is originated from the slower hole mobility of InP/ZnSe/ZnS QD film compared to the electron mobility, explains distinctly the reverse phenomenon.

ZnO nanoparticle as charge neutralization center

Synthesized ZnO nanoparticles provide efficient electron transport properties that improve the device efficiency and luminance with high electron mobility and robust material stability. Moreover, the neutralization process of charged QDs with the mid-gap states of ZnO nanoparticles is suggested from Cd-based QLEDs, which increases the both initial PL and EL of QLED device as the function of time [104]. The similar behavior is observed in our inverted QLEDs, especially with a relatively thin ZnO and QD layer (i.e. RZ is close to a ZnO/QD interface according to our RZ model). Therefore, it is suggested a modified charge neutralization process model accompanying the Auger-assisted electron injection process, which even can be facilitated by the applied electric field during the device operation. Apparently, the devices with relatively the thick ZnO

and QD layer (i.e. RZ is close to a QD/HTL interface according to our RZ model) do not show the charge neutralization process. In addition, a reduced luminance increase in the lifetime measurement by inserting a PEI interfacial dipole layer between the ZnO and QD layer strongly supports the suggested charge neutralization model.

The high performance of InP/ZnSe/ZnS QD-based QLEDs

As a result, the combination of QD thickness, efficient ZnO nanoparticle ETL, and TAPC HTL brings the maximum EQE of 3.3% (i.e. 7.3 cd/A, 3536 cd/m^2) with a relatively thick QD layer (10 mg/mL), and the maximum luminance of 8449 cd/m^2 (i.e. EQE of 1.56%, 3.2 cd/A) with a relatively thin QD layer (3 mg/mL). The maximum EQE is comparable and the maximum luminance is much higher than the currently reported value with InP-based QLEDs. Considering the both EQE and luminance, the device reaches the EQE of 2.5% and the luminance of 8106 cd/m^2, and their efficiency roll-off is also effectively reduced compared to the device results with the TCTA HTL due to the well-balanced charge carriers and field-assisted charge neutralization process. The EL performance of QLEDs based on the colloidal InP/ZnSe/ZnS QDs will be improved by the further optimization of the device structure and materials design.

7.2 Remained issues and further directions

Although the developments of Cd-free QLEDs in this dissertation would bring a better understanding of the device mechanism and device architecture engineering for high performance QLEDs, there are still several remained issues.

Color saturation for display applications

In this dissertation, the InP/ZnSe/ZnS QDs are designed to understand the device physics but not mainly for the color saturation of display application. Therefore, the color coordinates of developed QLEDs shown in Figure 7.2.1 do not achieve the adobe saturated RGB (sRGB) color gamut even though the pure emission spectrum from QDs without any parasitic emission in the QLEDs. Recently, a BT.2020 (ITU-R Recommendation Broadcasting television 2020, or Rec.2020) standard is recommended to define the various aspects of ultra-high-definition television (UHD TV). Although the Rec. 2020 standard can be realized with red, green and blue laser sources [180], QLEDs also have a potential to achieve it most closely. Therefore, the narrower FWHM of

InP/ZnSe/ZnS QDs, and saturated red, green and blue emission should be developed considering the design aspect for QLEDs.

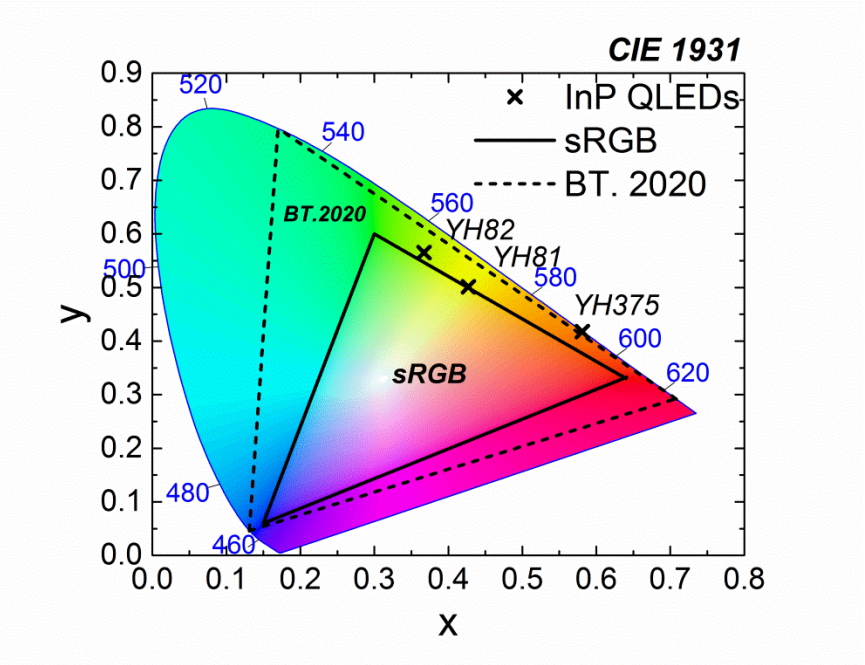

Figure 7.2.1 The CIE (Commission Internationale de l'Eclairage) 1931 chromaticity diagram showing the chromaticity coordinates of developed QLEDs using the InP/ZnSe/ZnS QDs. sRGB and BT.2020 standard triangles are shown in the figure as well.

Device charging and stability

Even though the developed QLEDs device architecture reduces the device efficiency roll-off by the field-assisted charge neutralization effect, the luminance quenching by device charging is still a serious problem for the stability of the InP/ZnSe/ZnS QD-based QLEDs as well as the Cd-based device. ***Figure 7.2.2a*** shows a relatively short lifetime of InP/ZnSe/ZnS QD-based QLEDs. However, the origin of charging in the device is not fully clear yet. Many researchers have been investigated to identify the origin of charge trapping in the QD or QD film through the various measurement technique such as scanning probe microscopy and spectroscopy (STM, STS) [181], and spectro-electrochemistry (SEC) [182]. In addition, capacitance-voltage (C-V) measurement in different frequency and temperature can help to identify the trap density and different trap states in multilayered QLEDs structure [45,179,183,184].

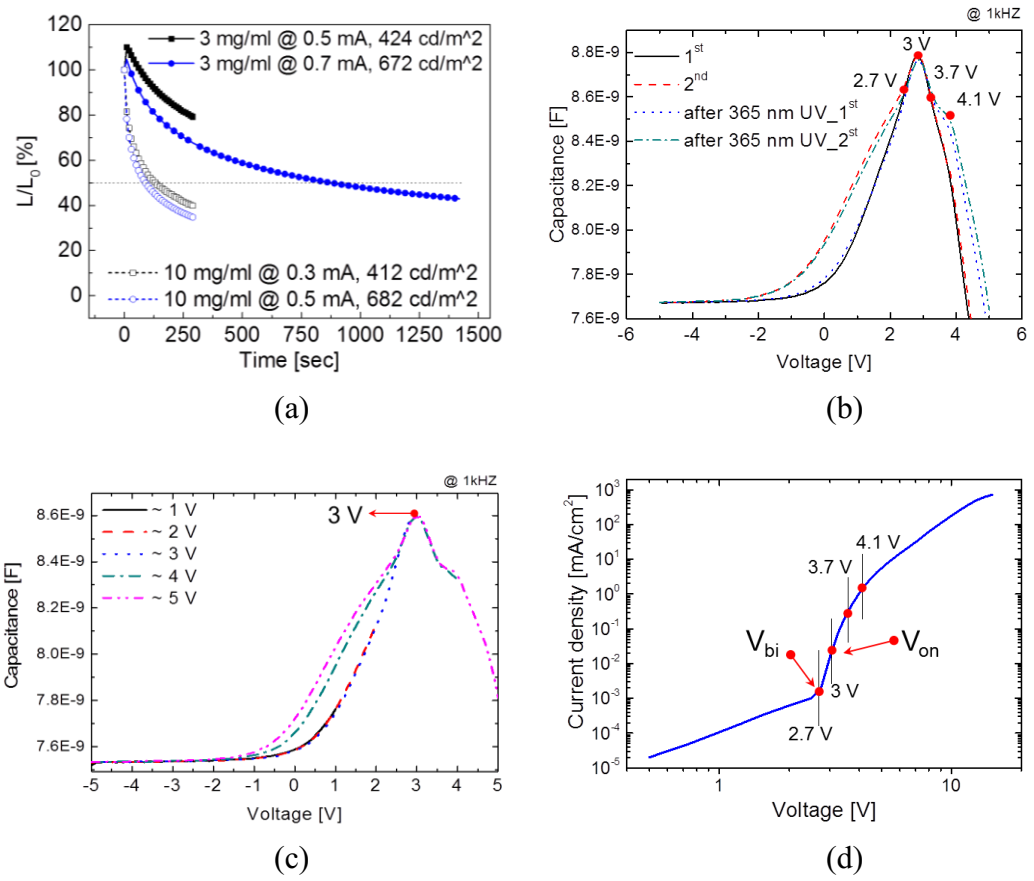

Figure 7.2.2 (a) The lifetime measurement of InP/ZnSe/ZnS QD-based QLEDs *(YH362, YH363)*. C-V measurement with repeated voltage sweep: (b), (c) the increased capacitance is the evidence of device charging and (c) the specific points of J-V curve are directly correlated to the C-V measurement.

The C-V curves shown in ***Figure 7.2.2bc*** are some examples of the charging behavior of QLEDs. They indicate that the capacitance increases after the voltage sweep and it can be refreshed by 365 nm of UV illumination, which means the device is charged after the exciton recombination process, and these charges are not permanent. Moreover, the C-V measurement is directly correlated with J-V characteristics such as a built-in voltage (V_{bi}) and a turn-on voltage (V_{on}) (***Figure 7.2.2d***). Therefore, the more detailed analysis could facilitate the device optimization process more efficiently.

Further directions for other aspects

The device performance of InP/ZnSe/ZnS QD-based QLEDs can have a further increase through various ideas. First of all, the more accurate band alignment between QD and CTL concerning the charge balance would bring the most promising enhancement of device performance. Therefore, the adopting charge control layer such as PMMA[16] and Al_2O_3 [185] layer would bring a more efficient and stable device. Since

the charge accumulation at the RZ causes a serious Auger quenching process, the separation of them by inserting specific materials could lead the more efficient and stable device [172]. In order to reduce the field-induced luminance quenching, QDs can be dispersed in a bipolar organic matrix [74]. A hybrid tandem structure with QDs and organic material can increase the device efficiency and color purity by combining the advantages of OLED and QLEDs [186]. The corporation of phosphorescent organic materials for the efficient exciton generation through FRET in the QD layer would have strong potential considering more developed OLED technology. Regarding the device stability, QLEDs with all inorganic materials would be the ideal target for an air stable device [51]. Besides all other prominent device architecture engineering, the most important future task for commercialization of QLEDs is the developing the patterning process for the QD active layer. Even though a transfer printing technology contributes the high resolution of patterning [19], for scaling up the display size, an inkjet printing technology for not only QD but also other CTL should be more intensively investigated.

Appendix A

Nanoparticle synthesis and properties

A.1. Synthesis of InP/ZnSe/ZnS QDs in Chapter 4.1

InP/ZnSe/ZnS-t1 and InP/ZnSe/ZnS-t2.

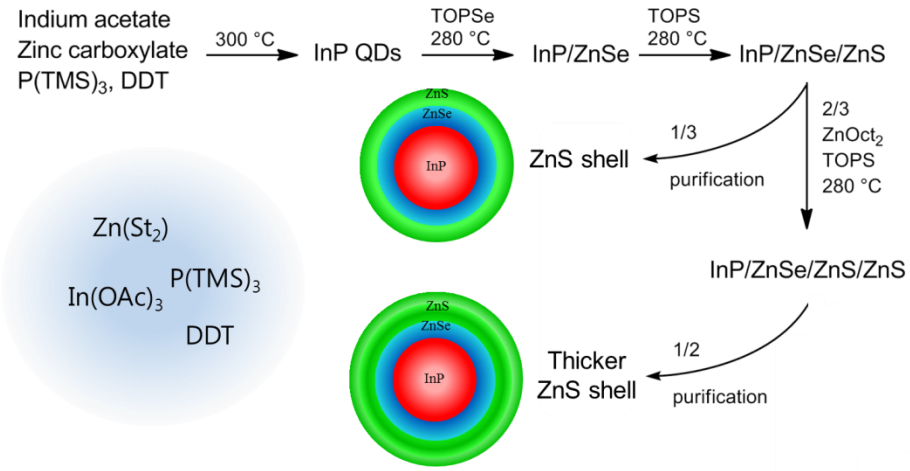

Figure A.1 (a) Synthesis schematic for QD synthesis with different ZnS shell thickness

First, a mixture of indium(III) acetate (1 mmol) and zinc stearate (2 mmol) was heated until a homogeneous solution was obtained, then dodecanethiol (0.5 mmol) and tris(trimethylsilyl) phosphine (1 mmol) were added in the mixture subsequently and heated to 300 °C for 30 min. In order to grow ZnSe shell, trioctylphosphine selenide (0.5 mmol) was added first in the prepared InP core nanoparticles and heated to 280 °C for 10 min. Subsequently, InP/ZnSe nanoparticles were capped with ZnS outer shell in two ways by adding further zinc and sulfur precursor followed by the heating to 280 °C for 10 min. Between the ZnS outer shell growth steps, half the volume of the synthesis solution was subjected to work-up while the other half was further reacted with more

ZnS precursor to get two samples with a different thickness of ZnS outer shell. The raw solutions of multishell QDs were purified several times by acetone-induced precipitation and centrifugation, and the QD powders were dried in the vacuum oven at room temperature and redispersed in nonane for the device fabrication.

A.2. Synthesis of InP/ZnSe/ZnS QDs used in other experiments

Synthesis

For the InP core, indium(III) acetate (10 mmol, 2.92 g) and zinc octanoate (30 mmol, 10.55 g) were weighed into a three-neck flask fitted with a reflux condenser, a rubber septum, and a thermocouple. The mixture was heated under vacuum to 130 °C until a clear yellowish melt was obtained (about 10 min). After cooling to room temperature, the flask was flushed with argon and dodecanethiol (5 mmol, 1.2 mL) was added using a syringe. The mixture was then heated again to 150 °C for 10 min. Subsequently, tris(trimethylsilyl) phosphine (10 mmol, 2.9 mL) was added to the flask at 120 °C. The mixture was heated up to 300 °C within 6 min and kept at this temperature for 30 min. The first exciton absorption maximum at 488 nm corresponds to 4.13 nm particle diameter.

For the ZnSe intermediate shell, tri(n-butyl)phosphine selenide (6.2 mmol, 3.1 mL of a 2 M stock solution in tri(n-butyl)phosphine) was added to the raw solution of InP core nanoparticles at room temperature. The mixture was then heated to 300 °C for 16 min. For the outer ZnS shell, octanethiol (19.5 mmol, 3.4 mL) and zinc octanoate (1.4 mmol, 491 mg) were added to the raw solution of InP/ZnSe core/shell nanoparticles at room temperature. The mixture was again heated to 300 °C for 15 min.

For the stearate ligands capped QDs, the same amount of zinc stearate was used instead of the zinc octanoate.

Purification

QDs were first extracted from the raw solution with n-hexane. The raw solution was transferred to two centrifuge tubes, which were filled up with 40 mL hexane each. The suspension was mixed intimately by ultra-sonication. After centrifugation for 3 min at 4000 rpm, the supernatant was collected in a round flask, and the extraction of the sediment was repeated two more times. The collected supernatants were reduced under vacuum at 45 °C. The resulting oil was then transferred to a centrifuge tube and mixed

with 15 mL of acetone and 20 mL of methanol. After centrifugation for 6 min at 4000 rpm, the supernatant was pipetted off. This precipitation/centrifugation step was repeated with 15 mL acetone and 5 mL methanol. Finally, a fine white residue was washed from the top of the sediment by adding 1 mL acetone and shaking gently.

A.3. Synthesis of ZnO nanoparticles

ZnO nanoparticles were synthesized by the modified sol-gel synthesis procedure from the literature [104,143]. Zinc acetate dihydrate (1.2 g, 5.5 mmol) was dissolved in 2-methoxyethanol (80 ml) at room temperature by a magnetic stirring in a flask. TMAH (1.8 g, 10 mmol) was also dissolved in 2-methoxyethanol (8 mL) in another flask under the same environment. Both solutions were vigorously stirred to have a clear solution. The TMAH solution was added using dropwise method to the zinc acetate solution over 10 min. 2-ethanolamine (1.6 mL) was added to stop the growth and stabilize the particles. The solution was kept for additional 2 min and washed with toluene (176 ml) and hexanes (80 mL). The milky mixture was centrifuged at 4000 rpm for 1 min to precipitate ZnO nanoparticles at the bottom. After centrifugation and removal of the supernatant, the ZnO nanoparticle was redispersed in 1-butanol (22 mL, ~1.4 wt%) and filtered through a syringe filter (0.45 μm PTFE). The dispersion was stored at - 20 °C.

During the synthesis, zinc hydroxide nanoparticles were formed as the first ones (equation A.1), and they were transformed into zinc oxide molecules subsequently (equation A.2) [187].

$$Zn^{2+} + 2OH^{-} \rightarrow Zn(OH)_2 \quad \text{(A.1)}$$

$$Zn(OH)_2 \rightarrow ZnO + H_2O \quad \text{(A.2)}$$

A.4. Properties of synthesized InP/ZnSe/ZnS QDs

Table A.1 InP-based QDs used in this dissertation

QD	Precursor	PL peak	FWHM	QY	QY film	TGA
CI519	$ZnOct_2$	539	52	40.3	-	70.8
CI520	$ZnOct_2$	541	54	41.9	-	72.6
CI741	$ZnSt_2$	544	62	26.´2	9	70
CI892	$ZnOct_2$	555	64	44.9	11	78
CI893	$ZnSt_2$	548	58	36.1	14	52
CI914P1	$ZnOct_2$	561	65	60.8	13.1	67
CI917P2	$ZnOct_2$	573	74	49.9	22.2	79
CI899F	$ZnOct_2$ giant shell	553	59	79.7	51.8	62.5
CI938	$ZnOct_2$	571	71	52	15.6	78

Appendix B

Details of device fabrication

B.1. Film deposition process in Chapter 5.4.1

Al:ZnO NP (Nanograde N-10x, 2wt% in isopropyl alcohol (IPA)) as the ETL, PEI (Fluka analytical, 50% (W/V) in H2O) as the interfacial dipole layer,

Al:ZnO NP (Nanograde N-10x, 2wt% in isopropyl alcohol (IPA)) was spin-coated on cleaned ITO substrates at 3000 rpm for 30 sec followed by drying at 120 °C for 10 min. PEI (Fluka analytical, 50% (W/V) in H_2O) diluted in in 2-methoxyethanol (2ME), or a mixture of IPA, ethanol, and H_2O (A1) was spin-coated at 3000 rpm for 30 sec followed by drying at 120 °C for 10 min.

B.2. List of devices used in this dissertation

Table B.1 List of devices (C: conventional, I: inverted, see the following pages).

Device	Type	ITO (Ω /□)	CIL or CTL	QD	CTL	Top Electrode	Max. EQE (%)	Max. (cd/A)	Max. (cd/m^2)	EL λ_{peak} (nm)
YHK10	C	10~15	CH8000 / Poly-TPD	CI511 (3.8 mg/ml)	TPBi (75 nm)	LiF/Al (0.5 nm/150 nm)	-	3.32	1960	555
YHK11	C	10~15	CH8000 / Poly-TPD	CI520 (3.8 mg/ml)	TPBi (75 nm)	LiF/Al (0.5 nm/150 nm)	-	4.65	2430	555
YH129	C	10~15	CH8000 / Poly-TPD	CI917P2 (6 mg/ml)	TPBi (65 nm)	Ca/Ag (30 nm/150 nm)	2.32	5.6	2000	596
YH130	C	10~15	CH8000 / Poly-TPD	CI899F (6 mg/ml)	TPBi (65 nm)	Ca/Ag (30 nm/150 nm)	0.67	2.2	340	561
YH82	C	10~15	CH8000 / Poly-TPD	CI893 (3 mg/ml)	TPBi (65 nm)	Ca/Ag (30 nm/150 nm)	1.7	8.0	1400	557
YH81	C	10~15	CH8000 / Poly-TPD	CI892 (3 mg/ml)	TPBi (65 nm)	Ca/Ag (30 nm/150 nm)	2.5	8.8	3164	569
YH197	I	10~15	-	CI892 (10 mg/ml)	TCTA (40 nm)	MoO_3/Ag (5 nm/150 nm)	-	0.13	100	568
YH199	I	10~15	Al_2O_3 (0.4 nm)	CI892 (10 mg/ml)	TCTA (40 nm)	MoO_3/Ag (5 nm/150 nm)	-	0.25	46	568
YH198	I	10~15	Al_2O_3 (0.8 nm)	CI892 (10 mg/ml)	TCTA (40 nm)	MoO_3/Ag (5 nm/150 nm)	-	0.47	28	568
YH199	I	10~15	Al_2O_3 (1.6 nm)	CI892 (10 mg/ml)	TCTA (40 nm)	MoO_3/Ag (5 nm/150 nm)	-	0.07	30	568
YH175	I	10~15	PEI (0.025 wt%)	CI892 (10 mg/ml)	TCTA (40 nm)	MoO_3/Ag (5 nm/150 nm)	-	0.47	57	564
YH174	I	10~15	PEI (0.05 wt%)	CI892 (10 mg/ml)	TCTA (40 nm)	MoO_3/Ag (5 nm/150 nm)	-	0.29	80	564
YH173	I	10~15	PEI (0.1 wt%)	CI892 (10 mg/ml)	TCTA (40 nm)	MoO_3/Ag (5 nm/150 nm)	-	0.51	49	564
YH172	I	10~15	PEI (0.2 wt%)	CI892 (10 mg/ml)	TCTA (40 nm)	MoO_3/Ag (5 nm/150 nm)	-	0.61	40	564
YH180	I	10~15	-	CI892 (10 mg/ml)	TCTA (40 nm)	MoO_3/Ag (5 nm/150 nm)	-	0.04	70	564
YH203	I	10~15	ZnO (CI921-2-4, 180 °C-N_2, 51 nm)	CI914 (10 mg/ml)	TCTA (40 nm)	MoO_3/Ag (5 nm/150 nm)	-	10.1	1500	572
YH136	I	10~15	Al:ZnO (45 nm)	CI892 (10 mg/ml)	TCTA (40 nm)	MoO_3/Ag (5 nm/150 nm)	-	0.07	221	571
YH148	I	10~15	Al:ZnO/PEI in 2ME	CI892 (10 mg/ml)	TCTA (40 nm)	MoO_3/Ag (5 nm/150 nm)	-	0.59	304	564
YH150	I	10~15	Al:ZnO/PEI in A1	CI892 (10 mg/ml)	TCTA (40 nm)	MoO_3/Ag (5 nm/150 nm)	-	3.17	466	567

Device	Type	ITO (Ω /□)	CIL or CTL	QD	CTL	Top Electrode	Max. EQE (%)	Max. (cd/A)	Max. (cd/m^2)	EL λ_{peak} (nm)
YH187	I	10~15	Al:ZnO (1k rpm, 62 nm)	CI892 (10 mg/ml)	TCTA (40 nm)	MoO_3/Ag (5 nm/150 nm)	-	1.17	655	564
YH185	I	10~15	Al:ZnO (3k rpm, 53 nm)	CI892 (10 mg/ml)	TCTA (40 nm)	MoO_3/Ag (5 nm/150 nm)	-	2.51	674	564
YH184	I	10~15	Al:ZnO (4k rpm, 46 nm)	CI892 (10 mg/ml)	TCTA (40 nm)	MoO_3/Ag (5 nm/150 nm)	-	3.54	727	564
YH149	I	10~15	Aldrich ZnO (31 nm)/PEI in A1	CI892 (10 mg/ml)	TCTA (40 nm)	MoO_3/Ag (5 nm/150 nm)	-	1.03	727	562
YH151	I	10~15	Aldrich ZnO (31 nm)/PEI in 2ME	CI892 (10 mg/ml)	TCTA (40 nm)	MoO_3/Ag (5 nm/150 nm)	-	1.67	1883	558
YH200	I	10~15	ZnO (CI921-2-4, 180 °C-N_2, 14 nm)	CI914P1 (10 mg/ml)	TCTA (40 nm)	MoO_3/Ag (5 nm/150 nm)	1.8	5.5	1360	574
YH201	I	10~15	ZnO (CI921-2-4, 180 °C-N_2, 26 nm)	CI914P1 (10 mg/ml)	TCTA (40 nm)	MoO_3/Ag (5 nm/150 nm)	1.9	6.2	1340	574
YH202	I	10~15	ZnO (CI921-2-4, 180 °C-N_2, 36 nm)	CI914P1 (10 mg/ml)	TCTA (40 nm)	MoO_3/Ag (5 nm/150 nm)	2.4	7.8	1400	574
YH203	I	10~15	ZnO (CI921-2-4, 180 °C-N_2, 51 nm)	CI914P1 (10 mg/ml)	TCTA (40 nm)	MoO_3/Ag (5 nm/150 nm)	3.1	10.1	1500	574
YH358	I	80	ZnO (SYH35, 2k rpm x 2, 180 °C-Vac, 50 nm)	CI938 (10 mg/ml)	TCTA (40 nm)	MoO_3/Ag (5 nm/150 nm)	-	3.3	1595	592
YH359	I	80	ZnO (SYH35, 2k rpm x 3, 180 °C-Vac, 62 nm)	CI938 (10 mg/ml)	TCTA (40 nm)	MoO_3/Ag (5 nm/150 nm)	-	5.0	2151	592
YH360	I	80	ZnO (SYH35, 2k rpm x 4, 180 °C-Vac, 88 nm)	CI938 (10 mg/ml)	TCTA (40 nm)	MoO_3/Ag (5 nm/150 nm)	-	6.4	2946	592
YH361	I	80	ZnO (SYH35, 2k rpm x 5, 180 °C-Vac, 105 nm)	CI938 (10 mg/ml)	TCTA (40 nm)	MoO_3/Ag (5 nm/150 nm)	-	6.6	3015	592
YH232	I	80	ZnO (SYH5-1, 1k rpm x 4, 180 °C-N_2, 50 nm)	CI938 (10 mg/ml)	TCTA (40 nm)	MoO_3/Ag (5 nm/150 nm)	-	3.3	1000	601
YH233	I	80	ZnO (SYH5-1, 180 °C-Vac, 50 nm)	CI938 (10 mg/ml)	TCTA (40 nm)	MoO_3/Ag (5 nm/150 nm)	-	3.3	1570	596
YH234	I	80	ZnO (SYH5-1, 180 °C-Air, 50 nm)	CI938 (10 mg/ml)	TCTA (40 nm)	MoO_3/Ag (5 nm/150 nm)	-	2.5	1200	567
YH235	I	80	ZnO (SYH5-1, 120 °C-N_2, 50 nm)	CI938 (10 mg/ml)	TCTA (40 nm)	MoO_3/Ag (5 nm/150 nm)	-	2.6	920	598
YH237	I	80	ZnO (SYH4-2, 2k x4, 180 °C-Vac, 56 nm)	CI938 (10 mg/ml)	TCTA (40 nm)	MoO_3/Ag (5 nm/150 nm)	-	3.1	1845	598
YH238	I	80	ZnO (SYH4-2, 2k x4, 180 °C-N_2, 56 nm)	CI938 (10 mg/ml)	TCTA (40 nm)	MoO_3/Ag (5 nm/150 nm)	-	2.0	1004	598

Device	Type	ITO (Ω /□)	CIL or CTL	QD	CTL	Top Electrode	Max. EQE (%)	Max. (cd/A)	Max. (cd/m^2)	EL λ_{peak} (nm)
YH368	I	10~15	ZnO (SYH34, 2k rpm x4, 180 °C-Vac, 85 nm)	CI938 (10 mg/ml)	TCTA (40 nm)	MoO_3/Ag (5 nm/150 nm)	-	6.4	6044	597
YH369	I	10~15	ZnO (SYH34, 2k rpm x4, 240 °C-Vac, 85 nm)	CI938 (10 mg/ml)	TCTA (40 nm)	MoO_3/Ag (5 nm/150 nm)	-	5.8	6720	597
YH370	I	10~15	ZnO (SYH34, 2k rpm x4, 180 °C-N_2, 85 nm)	CI938 (10 mg/ml)	TCTA (40 nm)	MoO_3/Ag (5 nm/150 nm)	-	3.4	2269	602
YH371	I	10~15	ZnO (SYH34, 2k rpm x4, 180 °C-Air, 85 nm)	CI938 (10 mg/ml)	TCTA (40 nm)	MoO_3/Ag (5 nm/150 nm)	-	4.4	2947	597
YH265	I	80	ZnO (SYH8, 2k rpm x1, 180 °C-N2, 12 nm)	CI938 (3 mg/ml)	TCTA (40 nm)	MoO_3/Ag (5 nm/150 nm)	-	2.8	1658	596
YH264	I	80	ZnO (SYH8, 2k rpm x1, 180 °C-Vac, 12 nm)	CI938 (3 mg/ml)	TCTA (40 nm)	MoO_3/Ag (5 nm/150 nm)	-	2.8	2253	596
YH266	I	80	ZnO (SYH8, 2k rpm x1, 180 °C-Air, 12 nm)	CI938 (3 mg/ml)	TCTA (40 nm)	MoO_3/Ag (5 nm/150 nm)	-	1.7	1279	596
YH193	I	10~15	ZnO (CI921-2-4, 2k rpm x1 , 180 °C-N_2, 12 nm)	CI914P1 (10 mg/ml)	TCTA (40 nm)	MoO_3/Ag (5 nm/150 nm)	-	5.9	1320	576
YH195	I	10~15	ZnO (CI921-2-4, 2k rpm x1 , 180 °C-N_2, 12 nm) /PEI 0.1wt% in A1,	CI914P1 (10 mg/ml)	TCTA (40 nm)	MoO_3/Ag (5 nm/150 nm)	-	7.1	1590	576
YH191	I	10~15	ZnO (CI920-1-4, 3k rpm x1 , 180 °C-N_2, 11 nm)	CI892 (10 mg/ml)	TCTA (40 nm)	MoO_3/Ag (5 nm/150 nm)	-	5.4	1715	571
YH189	I	10~15	ZnO (CI920-1-4, 3k rpm x1 , 180 °C-N_2, 11 nm) /PEI 0.1wt% in A1,	CI892 (10 mg/ml)	TCTA (40 nm)	MoO_3/Ag (5 nm/150 nm)	-	8.1	215	574
YH260	I	80	ZnO (SYH8, 180 °C-Vac, 12 nm)	CI938 (3 mg/ml)	TCTA (40 nm)	MoO_3/Ag (5 nm/150 nm)	-	3	1979	596
YH261	I	80	ZnO (SYH8, 180 °C-Vac, 12 nm) /PEI 0.05wt% in A1	CI938 (3 mg/ml)	TCTA (40 nm)	MoO_3/Ag (5 nm/150 nm)	-	2.4	1636	594
YH262	I	80	ZnO (SYH8, 180 °C-Vac, 12 nm) /PEI 0.1wt% in A1	CI938 (3 mg/ml)	TCTA (40 nm)	MoO_3/Ag (5 nm/150 nm)	-	2.2	1358	593
YH263	I	80	ZnO (SYH8, 180 °C-Vac, 12 nm) /PEI 0.2wt% in A1	CI938 (3 mg/ml)	TCTA (40 nm)	MoO_3/Ag (5 nm/150 nm)	-	2.7	638	590
YH354	I	80	ZnO (SYH35, 180 °C-Vac, 19 nm)	CI938 (3 mg/ml)	TCTA (40 nm)	MoO_3/Ag (5 nm/150 nm)	-	4.4	4023	588
YH355	I	80	ZnO (SYH35, 180 °C-Vac, 11 nm)	CI938 (3 mg/ml)	TCTA (40 nm)	MoO_3/Ag (5 nm/150 nm)	-	4.4	3833	588
YH356	I	80	ZnO (SYH35, 180 °C-Vac, 8 nm)	CI938 (3 mg/ml)	TCTA (40 nm)	MoO_3/Ag (5 nm/150 nm)	-	4.1	3553	588
YH357	I	80	ZnO (SYH35, 180 °C-Vac, 5 nm)	CI938 (3 mg/ml)	TCTA (40 nm)	MoO_3/Ag (5 nm/150 nm)	-	4.0	3512	588

Device	Type	ITO (Ω /□)	CIL or CTL	QD	CTL	Top Electrode	Max. EQE (%)	Max. (cd/A)	Max. (cd/m^2)	EL λ_{peak} (nm)
YH239	I	10~15	ZnO (SYH4-2, 2k rpm x5, 180 °C-Vac, 70 nm)	CI938 (10 mg/ml)	TCTA (40 nm)	MoO_3/Ag (5 nm/150 nm)	-	3.8	2160	597
YH256	I	10~15	ZnO (SYH4-2, 2k rpm x5, 180 °C-Vac, 70 nm)	CI938 (10 mg/ml)	TAPC (40 nm)	MoO_3/Ag (5 nm/150 nm)	-	5.0	2890	595
YH363	I	10~15	ZnO (SYH34, 2k rpm x1, 180 °C-Vac, 21 nm)	CI938 (10 mg/ml)	TCTA (40 nm)	MoO_3/Ag (5 nm/150 nm)	-	5.5	3075	591
YH257	I	10~15	ZnO (SYH4-2, 2k rpm x3, 180 °C-Vac, 40 nm)	CI938 (10 mg/ml)	TAPC (40 nm)	MoO_3/Ag (5 nm/150 nm)	-	4.6	2190	595
YH213	I	10~15	ZnO (SYH1-5-1, 2k rpm x3, 180 °C-Vac, 45 nm)	CI938 (10 mg/ml)	TAPC (40 nm)	MoO_3/Ag (5 nm/150 nm)	-	1.6	1100	596
YH214	I	10~15	ZnO (SYH1-5-1, 2k rpm x3, 180 °C-Vac, 45 nm)	CI938 (5 mg/ml)	TAPC (40 nm)	MoO_3/Ag (5 nm/150 nm)	-	1.7	912	593
YH215	I	10~15	ZnO (SYH1-5-1, 2k rpm x3, 180 °C-Vac, 45 nm)	CI938 (3 mg/ml)	TAPC (40 nm)	MoO_3/Ag (5 nm/150 nm)	-	2.0	782	593
YH362	I	10~15	ZnO (SYH34, 2k rpm x1, 180 °C-Vac, 21 nm)	CI938 (3 mg/ml)	TCTA (40 nm)	MoO_3/Ag (5 nm/150 nm)	-	4.1	6467	586
YH363	I	10~15	ZnO (SYH34, 2k rpm x1, 180 °C-Vac, 21 nm)	CI938 (10 mg/ml)	TCTA (40 nm)	MoO_3/Ag (5 nm/150 nm)	-	5.5	3075	591
YH37	C	10~15	CH8000 / Poly-TPD	CI741 (3 mg/ml)	TPBi (65 nm)	Ca/Ag (30 nm/150 nm)	-	4.1	560	560
YH38	C	10~15	CH8000 / Poly-TPD	CI741 (7 mg/ml)	TPBi (65 nm)	Ca/Ag (30 nm/150 nm)	-	2.5	136	560
YH39	C	10~15	CH8000 / Poly-TPD	CI741 (9 mg/ml)	TPBi (65 nm)	Ca/Ag (30 nm/150 nm)	-	1.9	95	560
YH216	I	10~15	ZnO (SYH2-1, 2k rpm x1, 180 °C-N_2, 18 nm)	CI938 (3 mg/ml)	TCTA (40 nm)	MoO_3/Ag (5 nm/150 nm)	-	2.7	1990	595
YH217	I	10~15	ZnO (SYH2-1, 2k rpm x2, 180 °C-N_2, 33 nm)	CI938 (3 mg/ml)	TCTA (40 nm)	MoO_3/Ag (5 nm/150 nm)	-	2.3	1455	595
YH218	I	10~15	ZnO (SYH2-1, 2k rpm x3, 180 °C-N_2, 50 nm)	CI938 (3 mg/ml)	TCTA (40 nm)	MoO_3/Ag (5 nm/150 nm)	-	2.1	1300	595
YH220	I	10~15	ZnO (SYH2-1, 2k rpm x1, 180 °C-N_2, 18 nm)	CI938 (10 mg/ml)	TCTA (40 nm)	MoO_3/Ag (5 nm/150 nm)	-	3.0	1283	596
YH221	I	10~15	ZnO (SYH2-1, 2k rpm x2, 180 °C-N_2, 33 nm)	CI938 (10 mg/ml)	TCTA (40 nm)	MoO_3/Ag (5 nm/150 nm)	-	3.3	1144	597
YH222	I	10~15	ZnO (SYH2-1, 2k rpm x3, 180 °C-N_2, 50 nm)	CI938 (10 mg/ml)	TCTA (40 nm)	MoO_3/Ag (5 nm/150 nm)	-	3.3	1228	599
YH223	I	10~15	ZnO (SYH2-1, 2k rpm x4, 180 °C-N_2, 65 nm)	CI938 (10 mg/ml)	TCTA (40 nm)	MoO_3/Ag (5 nm/150 nm)	-	3.9	1310	601

Device	Type	ITO (Ω /□)	CIL or CTL	QD	CTL	Top Electrode	Max. EQE (%)	Max. (cd/A)	Max. (cd/m2)	EL λpeak (nm)
YH224	EOD	80	ZnO (SYH2-1, 2k rpm x4, 180 °C-N_2, 65 nm)	CI938 (10 mg/ml)	-	Ca/Ag (30 nm/150 nm)	-	-	-	-
YH225	EOD	80	ZnO (SYH2-1, 2k rpm x4, 180 °C-N_2, 65 nm)	CI938 (3 mg/ml)	-	Ca/Ag (30 nm/150 nm)	-	-	-	-
YH228	EOD	80	ZnO (SYH2-1, 2k rpm x2, 180 °C-N_2, 33 nm)	CI938 (10 mg/ml)	-	Ca/Ag (30 nm/150 nm)	-	-	-	-
YH229	EOD	80	ZnO (SYH2-1, 2k rpm x2, 180 °C-N_2, 33 nm)	CI938 (3 mg/ml)	-	Ca/Ag (30 nm/150 nm)	-	-	-	-
YH232	HOD	80	-	CI938 (10 mg/ml)	TCTA (40 nm)	MoO_3/Ag (5 nm/150 nm)	-	-	-	-
YH233	HOD	80	-	CI938 (3 mg/ml)	TCTA (40 nm)	MoO_3/Ag (5 nm/150 nm)	-	-	-	-
YH239	I	80	ZnO (SYH4-2, 2k rpm x5, 180 °C-Vac, 70 nm)	CI938 (10 mg/ml)	TCTA (40 nm)	MoO_3/Ag (5 nm/150 nm)	-	3.8	2160	597
YH256	I	80	ZnO (SYH4-2, 2k rpm x5, 180 °C-Vac, 70 nm)	CI938 (10 mg/ml)	TAPC (40 nm)	MoO_3/Ag (5 nm/150 nm)	-	5.0	2890	595
YH252	I	80	ZnO (SYH4-2, 2k rpm x1, 180 °C-Vac, 15nm)	CI938 (3mg/ml)	TCTA (40 nm)	MoO_3/Ag (5 nm/150 nm)	-	3.0	2130	595
YH258	I	80	ZnO (SYH4-2, 2k rpm x1, 180 °C-Vac, 15nm)	CI938 (3 mg/ml)	TAPC (40 nm)	MoO_3/Ag (5 nm/150 nm)	-	2.9	2916	594
YH259	I	80	ZnO (SYH4-2, 2k rpm x3, 180 °C-Vac, 40 nm)	CI938 (3 mg/ml)	TAPC (40 nm)	MoO_3/Ag (5 nm/150 nm)	-	1.6	3363	594
YH257	I	80	ZnO (SYH4-2, 2k rpm x3, 180 °C-Vac, 40 nm)	CI938 (10 mg/ml)	TAPC (40 nm)	MoO_3/Ag (5 nm/150 nm)	-	4.6	2190	595
YH280	I	10~15	ZnO (SYH9, 2k rpm x5, 180 °C-Vac, 70 nm) /PEI 0.1 wt% in A1	CI938 (3 mg/ml)	TAPC (40 nm)	MoO_3/Ag (5 nm/150 nm)	-	3.4	4293	593
YH278	I	10~15	ZnO (SYH9, 2k rpm x5, 180 °C-Vac, 70 nm) /PEI 0.1 wt% in 2ME	CI938 (10 mg/ml)	TAPC (40 nm)	MoO_3/Ag (5 nm/150 nm)	-	4.6	3216	599
YH277	I	10~15	ZnO (SYH9, 2k rpm x5, 180 °C-Vac, 70 nm)	CI938 (10 mg/ml)	TAPC (40 nm)	MoO_3/Ag (5 nm/150 nm)	-	4.5	3118	602
YH278	I	10~15	ZnO (SYH9, 2k rpm x5, 180 °C-Vac, 70 nm) /PEI 0.1 wt% in 2ME	CI938 (10 mg/ml)	TAPC (40 nm)	MoO_3/Ag (5 nm/150 nm)	-	4.6	3216	599
YH279	I	10~15	ZnO (SYH9, 2k rpm x5, 180 °C-Vac, 70 nm) /PEI 0.1 wt% in A1	CI938 (10 mg/ml)	TAPC (40 nm)	MoO_3/Ag (5 nm/150 nm)	-	4.4	1590	599
YH280	I	10~15	ZnO (SYH9, 2k rpm x5, 180 °C-Vac, 70 nm) /PEI 0.1 wt% in 2ME	CI938 (3 mg/ml)	TAPC (40 nm)	MoO_3/Ag (5 nm/150 nm)	-	3.4	4293	593

Device	Type	ITO (Ω /□)	CIL or CTL	QD	CTL	Top Electrode	Max. EQE (%)	Max. (cd/A)	Max. (cd/m^2)	EL λ_{peak} (nm)
YH257	I	80	ZnO (SYH4-2, 2k rpm x3, 180 °C-Vac, 40 nm)	CI938 (10 mg/ml)	TAPC (40 nm)	MoO_3/Ag (5 nm/150 nm)	-	4.6	2190	595
YH256	I	80	ZnO (SYH4-2, 2k rpm x5, 180 °C-Vac, 70 nm)	CI938 (10 mg/ml)	TAPC (40 nm)	MoO_3/Ag (5 nm/150 nm)	-	5.0	2890	595
YH258	I	80	ZnO (SYH4-2, 2k rpm x1, 180 °C-Vac, 15nm)	CI938 (3 mg/ml)	TAPC (40 nm)	MoO_3/Ag (5 nm/150 nm)	-	2.9	2916	594
YH259	I	80	ZnO (SYH4-2, 2k rpm x3, 180 °C-Vac, 40 nm)	CI938 (3 mg/ml)	TAPC (40 nm)	MoO_3/Ag (5 nm/150 nm)	-	1.6	3363	594
YH373	I	10~15	ZnO (SYH34, 2k rpm x4, 180 °C-Air, 85 nm)	CI938 (15 mg/ml)	TAPC (40 nm)	MoO_3/Ag (5 nm/150 nm)	3.3	7.3	3536	595
YH374	I	10~15	ZnO (SYH34, 2k rpm x4, 180 °C-Air, 85 nm)	CI938 (10 mg/ml)	TAPC (40 nm)	MoO_3/Ag (5 nm/150 nm)	2.9	6.4	5158	593
YH375	I	10~15	ZnO (SYH34, 2k rpm x4, 180 °C-Air, 85 nm)	CI938 (5 mg/ml)	TAPC (40 nm)	MoO_3/Ag (5 nm/150 nm)	2.5	5.4	8106	590
YH376	I	10~15	ZnO (SYH34, 2k rpm x4, 180 °C-Air, 85 nm)	CI938 (3 mg/ml)	TAPC (40 nm)	MoO_3/Ag (5 nm/150 nm)	1.5	3.2	8449	587
YH193	I	10~15	ZnO (CI921-2-4, 2k rpm x1 , 180 °C-N_2, 12 nm)	CI914P1 (10 mg/ml)	TCTA (40 nm)	MoO_3/Ag (5 nm/150 nm)	-	5.9	1320	576
YH194	I	10~15	ZnO (CI921-2-4, 1k rpm x1 , 180 °C-N_2, 18 nm)	CI914P1 (10 mg/ml)	TCTA (40 nm)	MoO_3/Ag (5 nm/150 nm)	-	8.6	1363	576
YH191	I	10~15	ZnO (CI920-1-4, 3k rpm x1 , 180 °C-N_2, 11 nm)	CI892 (10 mg/ml)	TCTA (40 nm)	MoO_3/Ag (5 nm/150 nm)	-	5.4	1715	571
YH192	I	10~15	ITO O_2 plasma /ZnO (CI920-1-4, 3k rpm x1 , 180 °C-N2, 15 nm)	CI892 (10 mg/ml)	TCTA (40 nm)	MoO_3/Ag (5 nm/150 nm)	-	7.3	1517	574
YH225	I	80	ZnO (SYH2-1, 2k rpm x4, 180 °C-N_2, 56 nm)	CI938 (10 mg/ml)	TCTA (40 nm)	MoO_3/Ag (5 nm/150 nm)	-	2.2	1045	599
YH226	I	80	ZnO (SYH3-2, 2k rpm x4, 180 °C-N_2, 56 nm)	CI938 (10 mg/ml)	TCTA (40 nm)	MoO_3/Ag (5 nm/150 nm)	-	2.2	1017	599
YH227	I	80	ZnO (SYH4-2, 2k rpm x4, 180 °C-N_2, 56 nm)	CI938 (10 mg/ml)	TCTA (40 nm)	MoO_3/Ag (5 nm/150 nm)	-	2.2	1030	599

Appendix C

Other parameter controls for device optimization

C.1. Enhance the film thickness with synthesized ZnO nanoparticles

Different spin-coating speeds

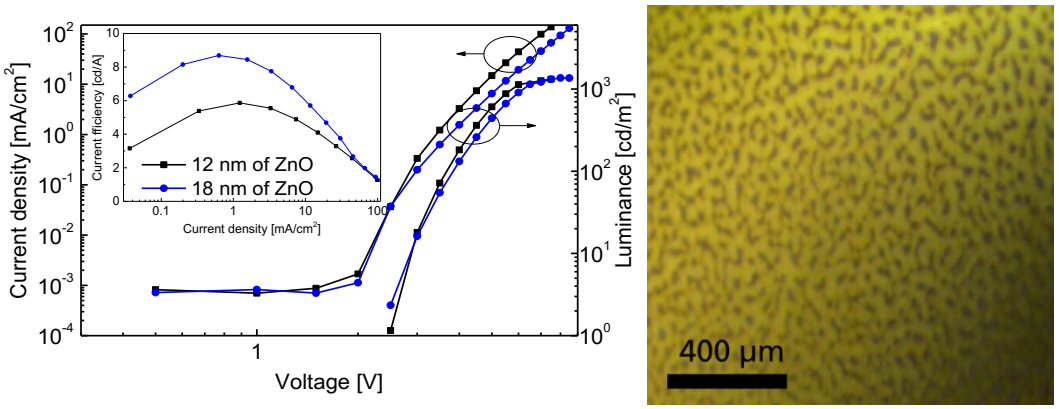

(a) (b)

Figure C.1 (a) Current density – voltage characteristics (inset: current efficiency-current density) of QLEDs and (b) a microscope image of ZnO phase separation. *(YH193, YH194)*

Table C.1 Film properties from different spin-coating RPM of ZnO nanoparticles (deposition: 0.2 µm PTFE filter, 180 °C 5 min in N_2)

Spin coating (rpm)	Thickness (nm)	Area (μm^2)	Roughness	
			R_q (nm)	R_{pv} (nm)
2000	12	25	0.84	8.73
1000	18	25	0.65	6.62

Synthesized ZnO nanoparticles were applied to inverted structure (ITO/ZnO/QDs/ TCTA/MoO_3/Ag). The different RPM for the spin-coating was tested to find better carrier balance with 1.4 wt% of ZnO solution. The device performance was increased with thicker ZnO layer in ***Figure C.1a.*** However, RPM could not modulate the thickness effectively (***Table C.1***). The lower RPM than 1000 normally deposits different thickness over the 5 x 5 cm^2 substrate as well. Therefore, the high concentration of ZnO nanoparticle is desired to increase the film thickness, but the high concentration needs more ethanolamine contents for clear dispersion, which easily brought the phase separation during the spin-coating process like in ***Figure C.1b.***

O_2 plasma treatment for ITO substrate

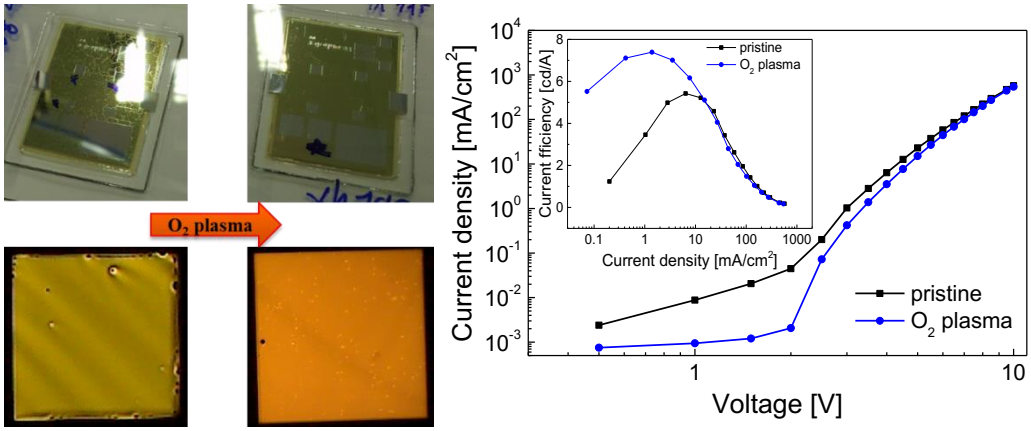

(a) (b)

Figure C.2 (a) The change of uniformity of pixel emission according to the O2 plasma treatment and (b) current density-voltage characteristics (inset: current efficiency-current density) of QLEDs. *(YH191, YH192)*

Table C.2 Film properties of ZnO layer according to the surface treatment.

Thin Film	Thickness (nm)	Area (μm^2)	Roughness R_q (nm)	Roughness R_{pv} (nm)
ITO/ZnO	11	25	0.99	16.0
ITO/O_2 plasma/ZnO	15	25	0.97	8.7

The wetting of ZnO solution on top of the insulation materials from ITO substrate was not enough to make a uniform layer in the pixel area, which is shown in ***Figure C.2a***. O_2 plasma treatment was applied to increase wetting property, and it leads uniform pixel emission and even increased the device performance because of thicker ZnO layer and low leakage current in the device accomplished with low surface roughness (***Table C.2***).

C.2. The effects of ZnO particle size on the device performance

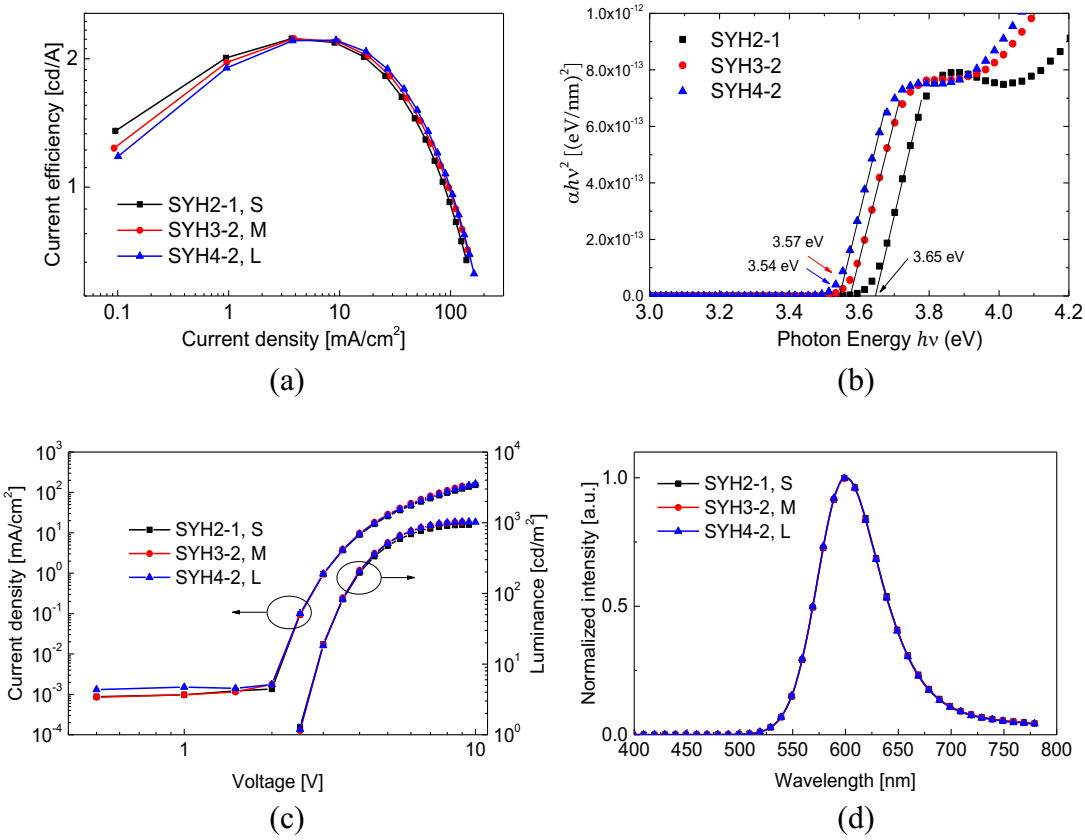

Figure C.3 QLED performances with different ZnO nanoparticle size. (a) Current efficiency – luminance, (b) current density-voltage (inset: luminance-voltage), (c) relative luminance as function of time and (d) EL spectra at 4 V. *(YH225 to YH227)*

The ZnO nanoparticles are synthesized with same process condition; however, there are small changes in the optical band gap, which indicates the different particle size (***Table C.3***). The different size of ZnO nanoparticle has an effect of charging the device performance by changing the carrier balance through the band alignment with QDs and faster electron mobility from smaller particles, according to the reference [115]. However, in our multilayer system, there is the only minimal difference in the device performance because the band gap change is only small within 0.11 eV (***Figure C.3***). Therefore, our synthesized ZnO nanoparticles could provide stable ETL template for QLEDs fabrication.

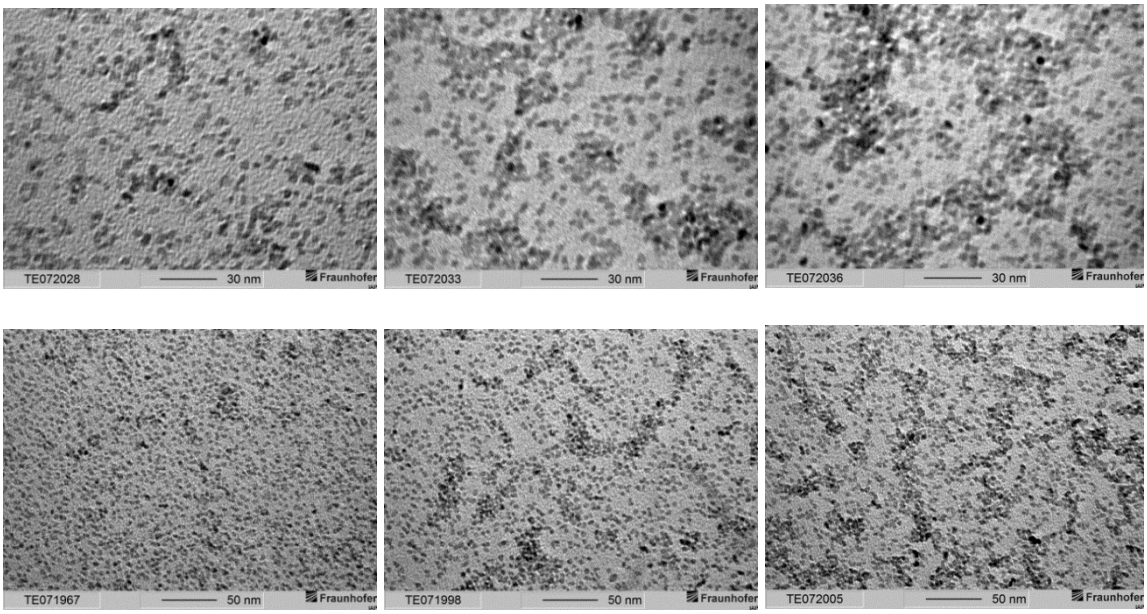

(a) (b) (c)

Figure C.4 TEM images of ZnO nanoparticles with different particle size; relatively (a) small, (b) medium and (c) large particles.

Table C.3 Film properties from different of ZnO nanoparticle size and the device performance with those particles.

ZnO	Band gap (eV)	Thickness (nm)	Roughness		Max. efficiency (cd/A)	Max. luminance (cd/m^2)
			R_q (nm)	R_{pv} (nm)		
SYH2-1_S	3.65	56.42	0.87	7.32	2.23	936
SYH3-2_M	3.57	56.86	0.97	7.43	2.23	1017
SYH4-2_L	3.54	56.78	0.93	7.74	2.21	1020

C.3. Drawback of using PEI layer as the carrier balancing layer

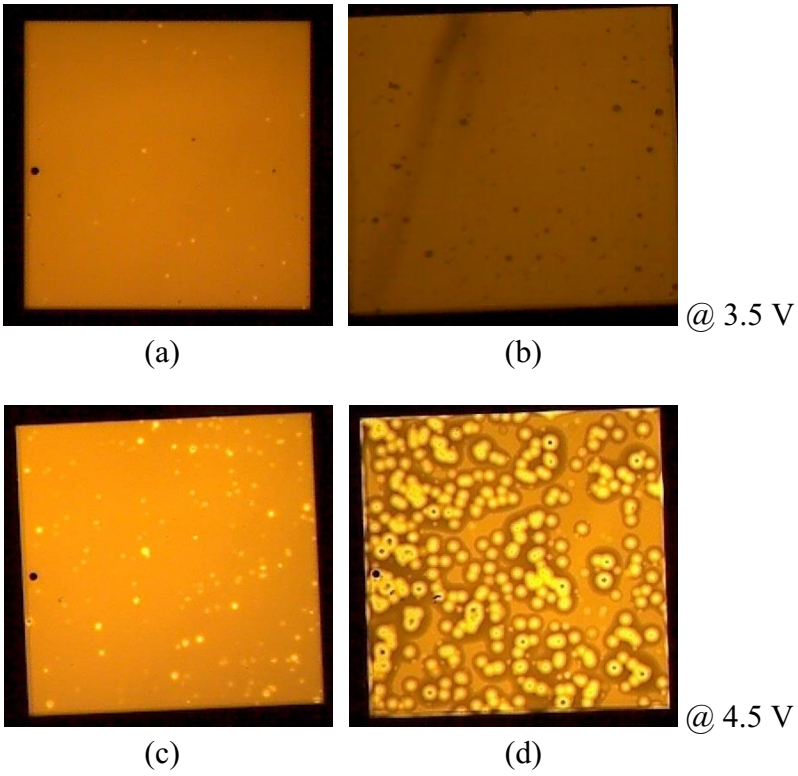

Figure C.5 The degradation of QLEDs according to the PEI layer. The images of a device pixel (4 mm^2) (a) without PEI layer and (b) with PEI layer. (c), (d) The images after 1-day storage.

The PEI layer deposited based on the water (H_2O) based solvent, and the Amine functional group (NH_2) of PEI strongly grabs the H_2O very strongly. The remained H2O in the PEI film would be the origin of device degradation. Therefore, the annealing of PEI layer should be carried on carefully.

Appendix D

Supporting information

D.1. AFM images from *Table 5.9*

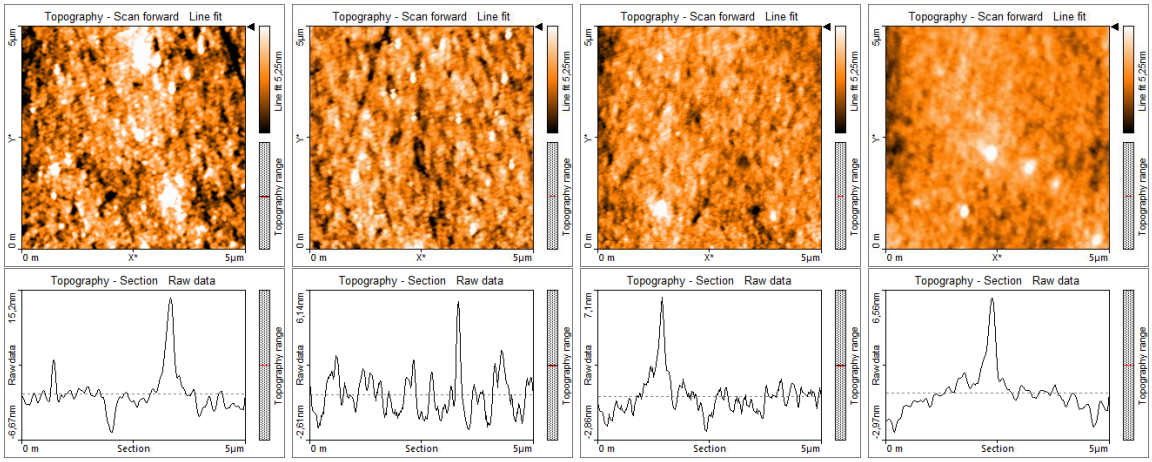

Figure D.1 AFM images of multi spin-coated ZnO nanoparticle layer

D.2. AFM images from *Table 5.5*

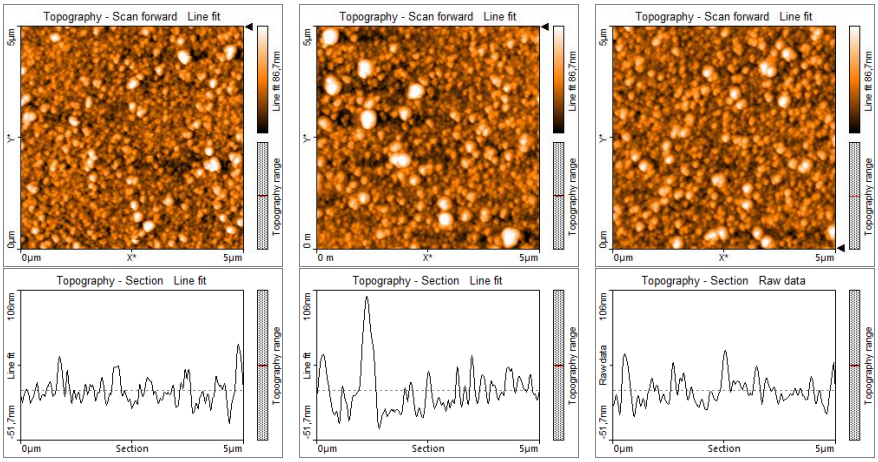

Figure D.2 AFM images of PEI modified ZnO layers.

D.3. AFM images from Table 5.10

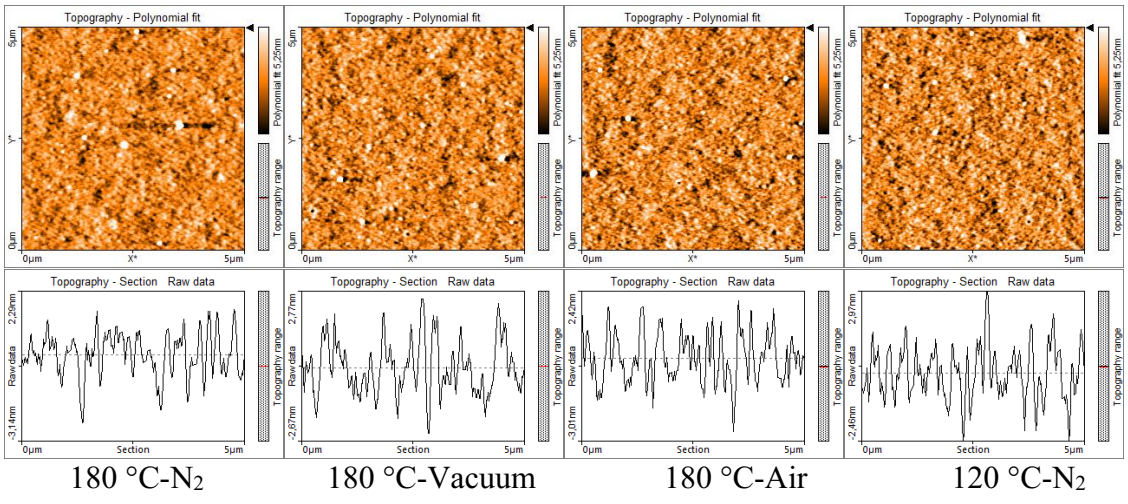

Figure D.3 AFM images of ZnO nanoparticle layer with different annealing conditions

Bibliography

[1] C.W. Tang, S.A. Vanslyke, Organic electroluminescent diodes, Appl. Phys. Lett. 51 (1987) 913–915. doi:10.1063/1.98799.

[2] B. Geffroy, P. le Roy, C. Prat, Organic light-emitting diode (OLED) technology: Materials, devices and display technologies, Polym. Int. 55 (2006) 572–582. doi:10.1002/pi.1974.

[3] Y.R. Cho, H.S. Kim, Y.-J. Yu, M.C. Suh, Highly efficient organic light emitting diodes formed by solution processed red emitters with evaporated blue common layer structure., Sci. Rep. 5 (2015) 15903. doi:10.1038/srep15903.

[4] V. Wood, V. Bulović, Colloidal quantum dot light-emitting devices., Nano Rev. 1 (2010) 1–7. doi:10.3402/nano.v1i0.5202.

[5] P. Reiss, M. Protière, L. Li, Core/Shell semiconductor nanocrystals., Small. 5 (2009) 154–68. doi:10.1002/smll.200800841.

[6] D. Bera, L. Qian, T.-K. Tseng, P.H. Holloway, Quantum Dots and Their Multimodal Applications: A Review, Materials. 3 (2010) 2260–2345. doi:10.3390/ma3042260.

[7] S. Jun, J. Lee, E. Jang, Highly luminescent and photostable quantum dot-silica monolith and its application to light-emitting diodes, ACS Nano. 7 (2013) 1472–1477. doi:10.1021/nn3052428.

[8] U.S. Army RDECOM, CC BY 2.0, Flexible display, (2006). https://www.flickr.com/photos/rdecom/4146880795/.

[9] M. Pesce, CC BY 2.0, Samsung Transparent_OLED Display, (2015). https://www.flickr.com/photos/pestoverde/24182257080/.

[10] J. Turner, CC BY 2.0, The difference of the iPads displays, (2012). https://www.flickr.com/photos/respres/6842257250/sizes/z/in/photostream/.

[11] M. Pesce, CC BY 2.0, Samsung SUHD TVs Showcased at CES 2015, (2015). https://www.flickr.com/photos/pestoverde/16677279979/.

[12] V.L. Colvin, M.C. Schlamp, A.P. Alivisatos, Light-emitting diodes made from cadmium selenide nanocrystals and a semiconducting polymer, Nature. 370 (1994) 354–357. doi:10.1038/370354a0.

[13] S. Coe, W.-K. Woo, M. Bawendi, V. Bulović, V. Bulovic, Electroluminescence from single monolayers of nanocrystals in molecular organic devices, Nat. Lett.

420 (2002) 800–803. doi:10.1038/nature01299.1.

[14] T.-H. Kim, K.-S. Cho, E.K. Lee, S.J. Lee, J. Chae, J.W. Kim, D.H. Kim, J.-Y. Kwon, G. Amaratunga, S.Y. Lee, B.L. Choi, Y. Kuk, J.M. Kim, K. Kim, Full-colour quantum dot displays fabricated by transfer printing, Nat. Photonics. 5 (2011) 176–182. doi:10.1038/nphoton.2011.12.

[15] Y. Yang, Y. Zheng, W. Cao, A. Titov, J. Hyvonen, J.R. Manders, J. Xue, P.H. Holloway, L. Qian, High-efficiency light-emitting devices based on quantum dots with tailored nanostructures, Nat. Photonics. 9 (2015) 1–9. doi:10.1038/nphoton.2015.36.

[16] X. Dai, Z. Zhang, Y. Jin, Y. Niu, H. Cao, X. Liang, L. Chen, J. Wang, X. Peng, Solution-processed, high-performance light-emitting diodes based on quantum dots, Nature. 515 (2014) 96–99. doi:10.1038/nature13829.

[17] J.R. Manders, L. Qian, A. Titov, J. Hyvonen, J. Tokarz-Scott, K.P. Acharya, Y. Yang, W. Cao, Y. Zheng, J. Xue, P.H. Holloway, High efficiency and ultra-wide color gamut quantum dot LEDs for next generation displays, J. Soc. Inf. Disp. 23 (2015) 523–528. doi:10.1002/jsid.393.

[18] B.H. Kim, M.S. Onses, J. Bin Lim, S. Nam, N. Oh, H. Kim, K.J. Yu, J.W. Lee, J.H. Kim, S.K. Kang, C.H. Lee, J.W. Lee, J.H. Shin, N.H. Kim, C. Leal, M. Shim, J.A. Rogers, High-resolution patterns of quantum dots formed by electrohydrodynamic jet printing for light-emitting diodes, Nano Lett. 15 (2015) 969–973. doi:10.1021/nl503779e.

[19] M.K. Choi, J. Yang, K. Kang, D.-H.D.C. Kim, C. Choi, C. Park, S.J. Kim, S.I. Chae, T.-H. Kim, J.H. Kim, T. Hyeon, D.-H.D.C. Kim, Wearable red–green–blue quantum dot light-emitting diode array using high-resolution intaglio transfer printing, Nat. Commun. 6 (2015) 7149. doi:10.1038/ncomms8149.

[20] H.Y. Kim, Y.J. Park, J. Kim, C.J. Han, J. Lee, Y. Kim, T. Greco, C. Ippen, A. Wedel, B.K. Ju, M.S. Oh, Transparent InP Quantum Dot Light-Emitting Diodes with ZrO2 Electron Transport Layer and Indium Zinc Oxide Top Electrode, Adv. Funct. Mater. 26 (2016) 3454–3461. doi:10.1002/adfm.201505549.

[21] A. Wang, H. Shen, S. Zang, Q. Lin, H. Wang, L. Qian, J. Niu, L. Song Li, Bright, efficient, and color-stable violet ZnSe-based quantum dot light-emitting diodes, Nanoscale. (2015). doi:10.1039/C4NR06593J.

[22] Y. Shirasaki, G.J. Supran, M.G. Bawendi, V. Bulović, Emergence of colloidal quantum-dot light-emitting technologies, Nat. Photonics. 7 (2013) 13–23.

doi:10.1038/nphoton.2012.328.

[23] X. Yang, D. Zhao, K.S. Leck, S.T. Tan, Y.X. Tang, J. Zhao, H.V. Demir, X.W. Sun, Full visible range covering InP/ZnS nanocrystals with high photometric performance and their application to white quantum dot light-emitting diodes., Adv. Mater. 24 (2012) 4180–5. doi:10.1002/adma.201104990.

[24] D.P. Puzzo, E.J. Henderson, M.G. Helander, Z. Wang, A. Ozin, Z. Lu, Visible Colloidal Nanocrystal Silicon Light-Emitting Diode, Nano Lett. 11 (2011) 1585–1590. doi:10.1021/nl1044583.

[25] W. Kwon, Y.H. Kim, C.L. Lee, M. Lee, H.C. Choi, T.W. Lee, S.W. Rhee, Electroluminescence from graphene quantum dots prepared by amidative cutting of tattered graphite, Nano Lett. 14 (2014) 1306–1311. doi:10.1021/nl404281h.

[26] W. Ji, P. Jing, W. Xu, X. Yuan, Y. Wang, J. Zhao, A.K. Jen, High color purity ZnSe / ZnS core / shell quantum dot based blue light emitting diodes with an inverted device structure, Appl. Phys. Lett. 103 (2013) 53106. doi:10.1063/1.4817086.

[27] B. Chen, H. Zhong, W. Zhang, Z. Tan, Y. Li, C. Yu, T. Zhai, Y. Bando, S. Yang, B. Zou, Highly emissive and color-tunable CuInS 2-based colloidal semiconductor nanocrystals: Off-stoichiometry effects and improved electroluminescence performance, Adv. Funct. Mater. 22 (2012) 2081–2088. doi:10.1002/adfm.201102496.

[28] J.J.-H. Kim, C.-Y. Han, K.-H. Lee, K.-S. An, W. Song, J.J.-H. Kim, M.S. Oh, Y.R. Do, H. Yang, Performance Improvement of Quantum Dot-Light-Emitting Diodes Enabled by an Alloyed ZnMgO Nanoparticle Electron Transport Layer, Chem. Mater. 27 (2015) 197–204. doi:10.1021/cm503756q.

[29] Z. Liu, K. Zhao, A. Tang, Y. Xie, L. Qian, W. Cao, Y. Yang, Y. Chen, F. Teng, Solution-processed high-efficiency cadmium-free Cu-Zn-In-S-based quantum-dot light-emitting diodes with low turn-on voltage, Org. Electron. Physics, Mater. Appl. 36 (2016) 97–102. doi:10.1016/j.orgel.2016.05.040.

[30] R. Xie, D. Battaglia, X. Peng, Colloidal InP nanocrystals as efficient emitters covering blue to near-infrared, J. Am. Chem. Soc. 129 (2007) 15432–15433. doi:10.1021/ja076363h.

[31] L. Li, P. Reiss, One-pot Synthesis of Highly Luminescent InP/ZnS Nanocrystals without Precursor Injection, J. Am. Chem. Soc. 130 (2008) 11588–11589. doi:10.1021/ja803687e.

[32] S. Xu, J. Ziegler, T. Nann, Rapid synthesis of highly luminescent InP and InP/ZnS nanocrystals, J. Mater. Chem. 18 (2008) 2653. doi:10.1039/b803263g.

[33] S. Tamang, C. Lincheneau, Y. Hermans, S. Jeong, P. Reiss, Chemistry of InP Nanocrystal Syntheses, Chem. Mater. 28 (2016) 2491–2506. doi:10.1021/acs.chemmater.5b05044.

[34] J. Lim, W.K. Bae, D. Lee, M.K. Nam, J. Jung, C. Lee, K. Char, S. Lee, InP@ZnSeS, core@composition gradient shell quantum dots with enhanced stability, Chem. Mater. 23 (2011) 4459–4463. doi:10.1021/cm201550w.

[35] J. Lim, M. Park, W.K. Bae, D. Lee, S. Lee, C. Lee, K. Char, Highly efficient cadmium-free quantum dot light-emitting diodes enabled by the direct formation of excitons within InP@ZnSeS quantum dots, ACS Nano. 7 (2013) 9019–9026. doi:10.1021/nn403594j.

[36] J.-H. Jo, J.-H. Kim, K.-H. Lee, C.-Y. Han, E.-P. Jang, Y.R. Do, H. Yang, High-efficiency red electroluminescent device based on multishelled InP quantum dots, Opt. Lett. 41 (2016) 3984–3987. doi:10.1364/OL.41.003984.

[37] Z. Tan, Y. Zhang, C. Xie, H. Su, J. Liu, C. Zhang, N. Dellas, S.E. Mohney, Y. Wang, J. Wang, J. Xu, Near-band-edge electroluminescence from heavy-metal-free colloidal quantum dots., Adv. Mater. 23 (2011) 3553–8. doi:10.1002/adma.201100719.

[38] Y. Kim, T. Greco, C. Ippen, A. Wedel, M.S. Oh, C.J. Han, J. Kim, Indium Phosphide-Based Colloidal Quantum Dot Light-Emitting Diodes on Flexible Substrate, Nanosci. Nanotechnol. Lett. 5 (2013) 1065–1069. doi:10.1166/nnl.2013.1677.

[39] Y. Kim, C. Ippen, T. Greco, J. Lee, M.S. Oh, C.J. Han, A. Wedel, J. Kim, Increased shell thickness in indium phosphide multishell quantum dots leading to efficiency and stability enhancement in light-emitting diodes, Opt. Mater. Express. 4 (2014) 1436. doi:10.1364/OME.4.001436.

[40] C. Ippen, T. Greco, Y. Kim, J. Kim, M.S. Oh, C.J. Han, A. Wedel, ZnSe/ZnS quantum dots as emitting material in blue QD-LEDs with narrow emission peak and wavelength tunability, Org. Electron. 15 (2014) 126–131. doi:10.1016/j.orgel.2013.11.003.

[41] Y. Kim, C. Ippen, B. Fischer, A. Lange, A. Wedel, Efficiency enhancement of InP-based inverted QD-LEDs by incorporation of a polyethylenimine modified Al:ZnO layer, J. Soc. Inf. Disp. 23 (2015) 377–383. doi:10.1002/jsid.322.

[42] I. Jang, J. Kim, C. Ippen, T. Greco, M.S. Oh, J. Lee, W.K. Kim, A. Wedel, C.J. Han, S.K. Park, Inverted InP quantum dot light-emitting diodes using low-temperature solution-processed metal–oxide as an electron transport layer, Jpn. J. Appl. Phys. 54 (2015) 02BC01. doi:10.7567/JJAP.54.02BC01.

[43] A. Wang, H. Shen, S. Zang, Q. Lin, H. Wang, Q. Lei, J. Niu, L.S. Li, Bright, Efficient, and Color-stable Violet ZnSe-Based Quantum Dots Light-Emitting Diodes, Nanoscale. 21 (2015) 2951–9. doi:10.1039/C4NR06593J.

[44] J.-H. Kim, H. Yang, High-Efficiency Cu–In–S Quantum-Dot-Light-Emitting Device Exceeding 7%, Chem. Mater. 28 (2016) 6329−6335. doi:10.1021/acs.chemmater.6b02669.

[45] C. Ippen, Indium Phosphide and Zinc Selenide Quantum Dots for Light-Emitting Devices : Relationships between Surface Structure and Device Performance, University of Potsdam, 2014.

[46] D. Bozyigit, V. Wood, Challenges and solutions for high-efficiency quantum dot-based LEDs, MRS Bull. 38 (2013) 731–736. doi:10.1557/mrs.2013.180.

[47] C. Ippen, T. Greco, A. Wedel, InP/ZnSe/ZnS: A Novel Multishell System for InP Quantum Dots for Improved Luminescence Efficiency and Its application in a Light-Emitting Device, J. Inf. Disp. 13 (2012) 91–95. doi:10.1080/15980316.2012.683537.

[48] B.S. Mashford, T.-L. Nguyen, G.J. Wilson, P. Mulvaney, All-inorganic quantum-dot light-emitting devices formed via low-cost, wet-chemical processing, J. Mater. Chem. 20 (2010) 167. doi:10.1039/b905256a.

[49] J. Li, Y. Shao, X. Chen, H. Wang, Y. Li, Q. Zhang, All-inorganic quantum-dot light-emitting-diodes with vertical nickel oxide nanosheets as hole transport layer, Prog. Nat. Sci. Mater. Int. 26 (2016) 503–509. doi:10.1016/j.pnsc.2016.09.003.

[50] L. Tang, J. Zhao, X. Zhang, H. Dai, X. Sun, Enhanced electroluminescence of all-inorganic colloidal quantum dot light-emitting diode by optimising the MoO3 intermediate layer, Micro Nano Lett. 9 (2014) 421–424. doi:10.1049/mnl.2014.0079.

[51] V. Wood, M.J. Panzer, J.-M. Caruge, J.E. Halpert, M.G. Bawendi, V. Bulović, Air-stable operation of transparent, colloidal quantum dot based LEDs with a unipolar device architecture, Nano Lett. 10 (2010) 24–9. doi:10.1021/nl902425g.

[52] Y. Shirasaki, G.J. Supran, W. a. Tisdale, V. Bulović, Origin of Efficiency Roll-Off in Colloidal Quantum-Dot Light-Emitting Diodes, Phys. Rev. Lett. 110 (2013)

217403. doi:10.1103/PhysRevLett.110.217403.

[53] W. Bae, Y. Park, J. Lim, D. Lee, Controlling the influence of Auger recombination on the performance of quantum-dot light-emitting, Nat. Commun. 4 (2013) 2661. doi:10.1038/ncomms3661.

[54] H. Lee, I. Park, J. Kwak, D.Y. Yoon, C. Lee, Improvement of electron injection in inverted bottom-emission blue phosphorescent organic light emitting diodes using zinc oxide nanoparticles, Appl. Phys. Lett. 96 (2010) 153306. doi:10.1063/1.3400224.

[55] H.J. Kim, B.D. Chin, Technologies for AMOLED Displays, 2013.

[56] S.I. Pokutny, Exciton States in Semiconductor Quantum Dots in the Modified Effective Mass Approximation, Semiconductors. 41 (2007) 1341–1346. doi:10.1134/S1063782607110097.

[57] L. Brus, Electronic wave functions in semiconductor clusters: experiment and theory, J. Phys. Chem. 90 (1986) 2555–2560. doi:10.1021/j100403a003.

[58] E.O. Chukwuocha, M.C. Onyeaju, T.S.T. Harry, Theoretical Studies on the Effect of Confinement on Quantum Dots Using the Brus Equation, World J. Condens. Matter Phys. 2 (2012) 96–100. doi:10.4236/wjcmp.2012.22017.

[59] T.T. Thao, N.A. Viet, Binding Energy of Exciton in Quantum Dots With the Central-Cell Correction Depending on the Dot Sizes, Commun. Phys. 14 (2004) 95–99.

[60] S. V. Gaponenko, Introduction To Nanophotonics, CAMBRIDGE UNIVERSITY PRESS, 2010.

[61] S.A. Holgate, Understanding Solid State Physics, CRC Press, 2009.

[62] C.A.M. Bonilla, V. V Kouznetsov, " Green " Quantum Dots : Basics , Green Synthesis , and Nanotechnological Applications, in: Green Nanotechnol. - Overv. Furth. Prospect., 2016: pp. 2–20. doi:10.5772/62327.

[63] Y. Masumoto, T. Takagahara, Semiconductor Quantum Dots: Physics, Spectroscopy and Applications, Springer Berlin Heidelberg, Berlin, Heidelberg, 2002. doi:10.1007/978-3-662-05001-9.

[64] C. De Mello Donegá, Nanoparticles: Workhorses of nanoscience, 2014. doi:10.1007/978-3-662-44823-6.

[65] V. LaMer, R. Dinegar, Theory, production and mechanism of formation of monodispersed hydrosols, J. Am. Chem. Soc. 72 (1950) 4847–4854. doi:10.1021/ja01167a001.

[66] T. Nguyen, T. Do, Nanocrystal: Size- and Shape-Controlled Synthesis of Monodisperse Metal Oxide and Mixed Oxide Nanocrystals, InTech, 2011. doi:10.5772/17054.

[67] Z. Wu, S. Yang, W. Wu, Shape control of inorganic nanoparticles from solution, Nanoscale. 8 (2016) 1237–1259. doi:10.1039/C5NR07681A.

[68] G.M. Akselrod, F. Prins, L. V. Poulikakos, E.M.Y. Lee, M.C. Weidman, A.J. Mork, A.P. Willard, V. Bulović, W.A. Tisdale, Subdiffusive exciton transport in quantum dot solids, Nano Lett. 14 (2014) 3556–3562. doi:10.1021/nl501190s.

[69] S. Bhaumik, A.J. Pal, Quantum dot light-emitting diodes in the visible region: Energy level of ligands and their role in controlling interdot spacing and device performance, J. Phys. Chem. C. 117 (2013) 25390–25396. doi:10.1021/jp409937z.

[70] B. Kang, J.-S. Lee, S.-W. Lee, S.-W. Kim, J. Lee, S. Gopalan, J. Park, D. Kwon, J. Bae, H. Kim, S.-W. Kang, Efficient exciton generation in atomic passivated CdSe/ZnS quantum dots light-emitting devices, Sci. Rep. 6 (2016) 34659. doi:10.1038/srep34659.

[71] M. V Kovalenko, M. Scheele, D. V Talapin, Colloidal nanocrystals with molecular metal chalcogenide surface ligands., Science. 324 (2009) 1417–20. doi:10.1126/science.1170524.

[72] Y. Liu, M. Gibbs, J. Puthussery, S. Gaik, R. Ihly, H.W. Hillhouse, M. Law, Dependence of carrier mobility on nanocrystal size and ligand length in PbSe nanocrystal solids., Nano Lett. 10 (2010) 1960–9. doi:10.1021/nl101284k.

[73] S. Wang, S. Yang, C. Yang, Z. Li, J. Wang, W. Ge, Poly(N -vinylcarbazole) (PVK) Photoconductivity Enhancement Induced by Doping with CdS Nanocrystals through Chemical Hybridization, J. Phys. Chem. B. 104 (2000) 11853–11858. doi:10.1021/jp0005064.

[74] W.K. Bae, J. Lim, M. Zorn, J. Kwak, Y.-S. Park, D. Lee, S. Lee, K. Char, R. Zentel, C. Lee, Reduced efficiency roll-off in light-emitting diodes enabled by quantum dot–conducting polymer nanohybrids, J. Mater. Chem. C. 2 (2014) 4974. doi:10.1039/c4tc00232f.

[75] L. Su, X. Zhang, Y. Zhang, A.L. Rogach, Recent Progress in Quantum Dot Based White Light-Emitting Devices, Top. Curr. Chem. 374 (2016) 42. doi:10.1007/s41061-016-0041-3.

[76] A. Khetubol, S. Van Snick, A. Hassinen, E. Fron, Y. Firdaus, L. Pandey, C.C. David, A. Khetubol, S. Van Snick, A. Hassinen, E. Fron, Y. Firdaus, L. Pandey,

C.C. David, K. Duerinckx, W. Dehaen, Z. Hens, Ligand exchange leads to efficient triplet energy transfer to CdSe/ZnS Q-dots in a poly(N-vinylcarbazole) matrix nanocomposite, J. Appl. Phys. 113 (2013) 83507-1–11. doi:10.1063/1.4793266.

[77] A. Efros, M. Rosen, M. Kuno, M. Nirmal, D. Norris, M. Bawendi, Band-edge exciton in quantum dots of semiconductors with a degenerate valence band: Dark and bright exciton states., Phys. Rev. B. Condens. Matter. 54 (1996) 4843–4856. http://www.ncbi.nlm.nih.gov/pubmed/9986445.

[78] G. Gu, D.Z. Garbuzov, P.E. Burrows, S. Venkatesh, S.R. Forrest, High-external-quantum-efficiency organic light-emitting devices, Opt. Lett. 22 (1997) 396–398. doi:10.1364/OL.22.000396.

[79] P.O. Anikeeva, Physical Properties and Design of Light-Emitting Devices Based on Organic Materials and Nanoparticles, MASSACHUSETTS INSTITUTE OF TECHNOLOGY February, 2009.

[80] D. Bozyigit, O. Yarema, V. Wood, Origins of Low Quantum Efficiencies in Quantum Dot LEDs, Adv. Funct. Mater. 23 (2013) 3024–3029. doi:10.1002/adfm.201203191.

[81] W.K. Bae, S. Brovelli, V.I. Klimov, Spectroscopic insights into the performance of quantum dot light-emitting diodes, MRS Bull. 38 (2013) 721–730. doi:10.1557/mrs.2013.182.

[82] P. Anikeeva, C. Madigan, J. Halpert, M. Bawendi, V. Bulović, Electronic and excitonic processes in light-emitting devices based on organic materials and colloidal quantum dots, Phys. Rev. B. 78 (2008) 85434. doi:10.1103/PhysRevB.78.085434.

[83] S. Coe-Sullivan, W.-K. Woo, J.S. Steckel, M. Bawendi, V. Bulović, Tuning the performance of hybrid organic/inorganic quantum dot light-emitting devices, Org. Electron. 4 (2003) 123–130. doi:10.1016/j.orgel.2003.08.016.

[84] J.M. Pietryga, K.K. Zhuravlev, M. Whitehead, V.I. Klimov, R.D. Schaller, Evidence for barrierless auger recombination in PbSe nanocrystals: A pressure-dependent study of transient optical absorption, Phys. Rev. Lett. 101 (2008) 1–4. doi:10.1103/PhysRevLett.101.217401.

[85] H. Huang, A. Dorn, G.P. Nair, V. Bulović, M.G. Bawendi, Bias-induced photoluminescence quenching of single colloidal quantum dots embedded in organic semiconductors., Nano Lett. 7 (2007) 3781–6. doi:10.1021/nl072263y.

[86] E. Güneri, A. Kariper, Optical properties of amorphous CuS thin films deposited chemically at different pH values, J. Alloys Compd. 516 (2012) 20–26. doi:10.1016/j.jallcom.2011.11.054.

[87] J. Tauc, R. Grigorovici, A. Vancu, Optical Properties and Electronic Structure of Amorphous Germanium, Phys. Stat. Sol. 15 (1966) 627–636. doi:10.1016/0025-5408(68)90023-8.

[88] R. a. M. Hikmet, D. V. Talapin, H. Weller, Study of conduction mechanism and electroluminescence in CdSe/ZnS quantum dot composites, J. Appl. Phys. 93 (2003) 3509. doi:10.1063/1.1542940.

[89] S.-J. Park, J.-P. Lee, J.S. Jang, H. Rhu, H. Yu, B.Y. You, C.S. Kim, K.J. Kim, Y.J. Cho, S. Baik, W. Lee, In situ control of oxygen vacancies in TiO2 by atomic layer deposition for resistive switching devices, Nanotechnology. 24 (2013) 295202. doi:10.1088/0957-4484/24/29/295202.

[90] P. Stallinga, Electrical characterization of organic electronic materials and devices, Wiley, 2009.

[91] X. XING, M. ZHANG, Y. CHUNG, L. XIAO, Z. CHEN, B. QU, Q. GONG, Organic electroluminescent materials and devices, Sci. Sin. Phys. Mech. Astron. 43 (2013) 1135. doi:10.1360/132013-249.

[92] B. Phan, C. Jung, T. Choi, J. Lee, Trap-controlled space-charge-limited current conduction in the Cr-doped SrTiO3 thin films deposited by using pulsed laser deposition, J. Korean Phys. Soc. 51 (2007) 664–668. doi:10.3938/jkps.51.664.

[93] D.S. Shang, Q. Wang, L.D. Chen, R. Dong, X.M. Li, W.Q. Zhang, Effect of carrier trapping on the hysteretic current-voltage characteristics in Ag La0.7 Ca0.3 MnO3 Pt heterostructures, Phys. Rev. B - Condens. Matter Mater. Phys. 73 (2006) 245427. doi:10.1103/PhysRevB.73.245427.

[94] L. Znaidi, Sol-gel-deposited ZnO thin films: A review, Mater. Sci. Eng. B Solid-State Mater. Adv. Technol. 174 (2010) 18–30. doi:10.1016/j.mseb.2010.07.001.

[95] J.M.M. Martín, Charge Transport in Organic Semiconductors With Application To Optoelectronic Devices, Universitat Jaume I, 2010.

[96] M.A. Lampert, R.B. Schilling, Current Injection in Solids: The Regional Approximation Method, Semicond. Semimetals. 6 (1970) 1–96. doi:10.1016/S0080-8784(08)62630-7.

[97] J. Kwan Kim, J. Hoon Song, H. Choi, S. Jae Baik, S. Jeong, Space charge limited conduction in ultrathin PbS quantum dot solid diodes, J. Appl. Phys. 115 (2014)

54302. doi:10.1063/1.4863725.

[98] M. Shukla, N. Brahme, R.S. Kher, M.S.K. Khokhar, Elementary approach to calculate quantum efficiency of polymer light emitting diodes, Indian J. Pure Appl. Phys. 49 (2011) 142–145.

[99] X. Ma, Hybrid light emitting diodes based on solution processed polymers, colloidal quantum dots, and colloidal metal nanoparticles, University of Delaware, 2014.

[100] S.R. Forrest, D.D.C. Bradley, M.E. Thompson, Measuring the efficiency of organic light-emitting devices, Adv. Mater. 15 (2003) 1043–1048. doi:10.1002/adma.200302151.

[101] I. Coropceanu, M.G. Bawendi, Core/shell quantum dot based luminescent solar concentrators with reduced reabsorption and enhanced efficiency, Nano Lett. 14 (2014) 4097–4101. doi:10.1021/nl501627e.

[102] L. Yan, J.Y. Zhang, Y. Cui, Y. Qiao, Voltage-dependent electroluminescence from colloidal CdSeZnS quantum dots, Appl. Phys. Lett. 91 (2007) 243114. doi:10.1063/1.2824397.

[103] P. Jing, J. Zheng, Q. Zeng, Y. Zhang, X. Liu, X. Liu, X. Kong, J. Zhao, Shell-dependent electroluminescence from colloidal CdSe quantum dots in multilayer light-emitting diodes, J. Appl. Phys. 105 (2009) 44313. doi:10.1063/1.3079475.

[104] B.S. Mashford, M. Stevenson, Z. Popovic, C. Hamilton, Z. Zhou, C. Breen, J. Steckel, V. Bulovic, M. Bawendi, S. Coe-Sullivan, P.T. Kazlas, High-efficiency quantum-dot light-emitting devices with enhanced charge injection, Nat. Photonics. 7 (2013) 407–412. doi:10.1038/nphoton.2013.70.

[105] B.N. Pal, Y. Ghosh, S. Brovelli, R. Laocharoensuk, V.I. Klimov, J.A. Hollingsworth, H. Htoon, "Giant" CdSe/CdS core/shell nanocrystal quantum dots as efficient electroluminescent materials: Strong influence of shell thickness on light-emitting diode performance, Nano Lett. 12 (2012) 331–336. doi:10.1021/nl203620f.

[106] H. Shen, Q. Lin, H. Wang, L. Qian, Y. Yang, A. Titov, J. Hyvonen, Y. Zheng, L.S. Li, Efficient and bright colloidal quantum dot light-emitting diodes via controlling the shell thickness of quantum dots, ACS Appl. Mater. Interfaces. 5 (2013) 12011–12016. doi:10.1021/am4038068.

[107] L. Qian, Y. Zheng, K.R. Choudhury, D. Bera, F. So, J. Xue, P.H. Holloway, Electroluminescence from light-emitting polymer/ZnO nanoparticle

heterojunctions at sub-bandgap voltages, Nano Today. 5 (2010) 384–389. doi:10.1016/j.nantod.2010.08.010.

[108] H. Zhu, Y. Yang, K. Hyeon-deuk, M. Califano, N. Song, Y. Wang, W. Zhang, O. V Prezhdo, T. Lian, A.H. Zhu, Y. Yang, K. Hyeon-deuk, M. Califano, N. Song, Auger-Assisted Electron Transfer from Photoexcited Semiconductor Quantum Dots, Nano Lett. 14 (2014) 1263–1269. doi:10.1021/nl4041687.

[109] F. García-santamaría, Y. Chen, J. Vela, R.D. Schaller, J. A, V.I. Klimov, Suppressed Auger Recombination in "Giant" Nanocrystals Boosts Optical Gain Performance, October. 9 (2010) 3482–3488. doi:10.1021/nl901681d.Suppressed.

[110] T.L. Greco, Synthese von Halbleiter-Nanopartikeln zur Anwendung in Licht-emittierenden Dioden, University of Potsdam, 2013.

[111] S.A. Maruyama, L.R.S. Kanda, F. Wypych, Isopropyl octanoate synthesis catalyzed by layered zinc n-octanoate, J. Braz. Chem. Soc. 28 (2017) 985–994. doi:10.21577/0103-5053.20160251.

[112] C. Kagan, C. Murray, M. Bawendi, Long-range resonance transfer of electronic excitations in close-packed CdSe quantum-dot solids, Phys. Rev. B. 54 (1996) 8633–8643. doi:10.1103/PhysRevB.54.8633.

[113] M. Achermann, M.A. Petruska, S.A. Crooker, V.I. Klimov, Picosecond Energy Transfer in Quantum Dot Langmuir−Blodgett Nanoassemblies, J. Phys. Chem. B. 107 (2003) 13782–13787. doi:10.1021/jp036497r.

[114] L.F. Santos, G. Gozzi, Conducting Polymer: Ch.7 Electrical Properties of Polymer Light-Emitting Devices, 2016. http://dx.doi.org/10.5772/64358.

[115] J. Pan, J. Chen, Q. Huang, Q. Khan, X. Liu, Z. Tao, Z. Zhang, W. Lei, A. Nathan, Size Tunable ZnO Nanoparticles to Enhance Electron Injection in Solution Processed QLEDs, ACS Photonics. 3 (2016) 215–222. doi:10.1021/acsphotonics.5b00267.

[116] V. Wood, M.J. Panzer, J.E. Halpert, J.M. Caruge, M.G. Bawendi, V. Bulović, Selection of metal oxide charge transport layers for colloidal quantum dot LEDs, ACS Nano. 3 (2009) 3581–3586. doi:10.1021/nn901074r.

[117] L. Qian, Y. Zheng, J. Xue, P.H. Holloway, Stable and efficient quantum-dot light-emitting diodes based on solution-processed multilayer structures, Nat. Photonics. 5 (2011) 543–548. doi:10.1038/nphoton.2011.171.

[118] K. Nomura, H. Ohta, A. Takagi, T. Kamiya, M. Hirano, H. Hosono, Room-temperature fabrication of transparent flexible thin-film transistors using

amorphous oxide semiconductors., Nature. 432 (2004) 488–492. doi:10.1038/nature03090.

[119] P. Servati, S. Prakash, A. Nathan, C. Py, Amorphous silicon driver circuits for organic light-emitting diode displays, J. Vac. Sci. Technol. 20 (2002) 4–9. doi:10.1116/1.1486006.

[120] X. Xu, Q. Cui, S. Chen, S. Li, G. He, X. Guo, Integration of solution processed oxide TFTs with normal structure OLEDS for low-voltage operated top-emitting AMOLEDs, Dig. Tech. Pap. - SID Int. Symp. 44 (2013) 1044–1046. doi:10.1002/j.2168-0159.2013.tb06402.x.

[121] J. Kwak, W.K. Bae, D. Lee, I. Park, J. Lim, M. Park, H. Cho, H. Woo, D.Y. Yoon, K. Char, S. Lee, C. Lee, Bright and efficient full-color colloidal quantum dot light-emitting diodes using an inverted device structure., Nano Lett. 12 (2012) 2362–6. doi:10.1021/nl3003254.

[122] Y. Zhou, C. Fuentes-Hernandez, J. Shim, J. Meyer, A.J. Giordano, H. Li, P. Winget, T. Papadopoulos, H. Cheun, J. Kim, M. Fenoll, A. Dindar, W. Haske, E. Najafabadi, T.M. Khan, H. Sojoudi, S. Barlow, S. Graham, J.-L. Bredas, S.R. Marder, A. Kahn, B. Kippelen, A Universal Method to Produce Low-Work Function Electrodes for Organic Electronics, Science (80-.). 336 (2012) 327–332. doi:10.1126/science.1218829.

[123] L. Zhou, J.Y. Zhuang, S. Tongay, W.M. Su, Z. Cui, Performance improvement of organic light emitting diode with aluminum oxide buffer layer for anode modification, J. Appl. Phys. 114 (2013). doi:10.1063/1.4817239.

[124] H. Kang, S. Hong, J. Lee, K. Lee, Electrostatically self-assembled nonconjugated polyelectrolytes as an ideal interfacial layer for inverted polymer solar cells, Adv. Mater. (2012). doi:10.1002/adma.201200594.

[125] S.T. Zhang, Y.C. Zhou, J.M. Zhao, Y.Q. Zhan, Z.J. Wang, Y. Wu, X.M. Ding, X.Y. Hou, Role of hole playing in improving performance of organic light-emitting devices with an AI2O3 layer inserted at the cathode-organic interface, Appl. Phys. Lett. 89 (2006) 43502. doi:10.1063/1.2220013.

[126] Y. Kurosaka, N. Tada, Y. Ohmori, K. Yoshino, Improvement of electrode/organic layer interfaces by insertion of monolayer-like aluminum oxide film, Jpn. J. Appl. Phys. 37 (1998) L872–L 875.

[127] K. Murata, S. Cinà, N.C. Greenham, Barriers to electron extraction in polymer light-emitting diodes, Appl. Phys. Lett. 79 (2001) 1193–1195.

doi:10.1063/1.1396627.

[128] X. Wu, L. Liu, W.C.H. Choy, T. Yu, P. Cai, Y. Gu, Z. Xie, Y. Zhang, L. Du, Y. Mo, S. Xu, Y. Ma, Substantial performance improvement in inverted polymer light-emitting diodes via surface plasmon resonance induced electrode quenching control, ACS Appl. Mater. Interfaces. 6 (2014) 11001–11006. doi:10.1021/am5033764.

[129] M. Herlem, B. Fahys, G. Herlem, B. Lakard, K. Reybier, A. Trokourey, T. Diaco, S. Zairi, N. Jaffrezic-Renault, Surface modification of p-Si by a polyethylenimine coating: Influence of the surface pre-treatment. Application to a potentiometric transducer as pH sensor, Electrochim. Acta. 47 (2002) 2597–2602. doi:10.1016/S0013-4686(02)00120-2.

[130] M.J. Biercuk, D.J. Monsma, C.M. Marcus, J.S. Backer, R.G. Gordon, Low-temperature atomic-layer-deposition lift-off method for microelectronic and nanoelectronic applications, Appl. Phys. Lett. 83 (2003) 2405–2407. doi:10.1063/1.1612904.

[131] S. Stolz, M. Scherer, E. Mankel, R. Lovrinčić, J. Schinke, W. Kowalsky, W. Jaegermann, U. Lemmer, N. Mechau, G. Hernandez-Sosa, Investigation of solution-processed Ultrathin electron injection layers for organic light-emitting diodes, ACS Appl. Mater. Interfaces. 6 (2014) 6616–6622. doi:10.1021/am500287y.

[132] A. Kolodziejczak-Radzimska, T. Jesionowski, Zinc oxide-from synthesis to application: A review, Materials (Basel). 7 (2014) 2833–2881. doi:10.3390/ma7042833.

[133] D. Luković Golić, G. Branković, M. Počuča Nešić, K. Vojisavljević, A. Rečnik, N. Daneu, S. Bernik, M. Sćepanović, D. Poleti, Z. Branković, Structural characterization of self-assembled ZnO nanoparticles obtained by the sol-gel method from Zn(CH3COO)2·2H2O., Nanotechnology. 22 (2011) 395603. doi:10.1088/0957-4484/22/39/395603.

[134] T. Ameri, N. Li, C.J. Brabec, Highly efficient organic tandem solar cells: a follow up review, Energy Environ. Sci. 6 (2013) 2390–2413. doi:10.1039/c3ee40388b.

[135] H.-M. Kim, A.R. bin Mohd Yusoff, J.-H. Youn, J. Jang, Inverted quantum-dot light emitting diodes with cesium carbonate doped aluminium-zinc-oxide as the cathode buffer layer for high brightness, J. Mater. Chem. C. 1 (2013) 3924–3930. doi:10.1039/c3tc30505h.

[136] D. Guo, K. Sato, S. Hibino, T. Takeuchi, H. Bessho, K. Kato, Low-temperature preparation of transparent conductive Al-doped ZnO thin films by a novel sol–gel method, J. Mater. Sci. 49 (2014) 4722–4734. doi:10.1007/s10853-014-8172-9.

[137] H.H. Kim, S. Park, Y. Yi, D.I. Son, C. Park, D.K. Hwang, W.K. Choi, Inverted quantum dot light emitting diodes using polyethylenimine ethoxylated modified ZnO., Sci. Rep. 5 (2015) 8968. doi:10.1038/srep08968.

[138] S. Höfle, A. Schienle, M. Bruns, U. Lemmer, A. Colsmann, Enhanced electron injection into inverted polymer light-emitting diodes by combined solution-processed zinc oxide/polyethylenimine interlayers, Adv. Mater. 26 (2014) 2750–2754. doi:10.1002/adma.201304666.

[139] J. Meyer, S. Hamwi, M. Kröger, W. Kowalsky, T. Riedl, A. Kahn, Transition metal oxides for organic electronics: Energetics, device physics and applications, Adv. Mater. 24 (2012) 5408–5427. doi:10.1002/adma.201201630.

[140] T.H. Lee, H. Choi, B. Walker, T. Kim, H.-B. Kim, J.Y. Kim, Replacing the metal oxide layer with a polymer surface modifier for high-performance inverted polymer solar cells, RSC Adv. 4 (2014) 4791–4795. doi:10.1039/c3ra46180g.

[141] C.H. Jonda, a B.R. Mayer, U. Stolz, Surface roughness effects and their influence on the degradation of organic light emitting devices, J. Mater. Sci. 35 (2000) 5645–5651. doi:10.1023/A:1004842004640.

[142] K.H.L. and J.R.L. Y. H. Tak, K. B. Kim, H. G. Park, Criteria for ITO (indium–tin-oxide) thin film as the bottom electrode of an organic light emitting diode, Thin Solid Films. 411 (2002) 12–16. doi:10.1016/S0040-6090(02)00165-7.

[143] A. Wood, M. Giersig, M. Hilgendorff, A. Vilas-Campos, L.M. Liz-Marzán, P. Mulvaney, Size Effects in Zno: The Cluster to Quantum Dot Transition, Aust. J. Chem. 56 (2003) 1051–1057. doi:10.1071/CH03120.

[144] A.B. Djurišić, Y.H. Leung, Optical properties of ZnO nanostructures, Small. 2 (2006) 944–961. doi:10.1002/smll.200600134.

[145] H. Zeng, G. Duan, Y. Li, S. Yang, X. Xu, W. Cai, Blue Luminescence of ZnO Nanoparticles Based on Non-Equilibrium Processes: Defect Origins and Emission Controls, Adv. Funct. Mater. 20 (2010) 561–572. doi:10.1002/adfm.200901884.

[146] L. Schmidt-Mende, J.L. MacManus-Driscoll, ZnO - nanostructures, defects, and devices, Mater. Today. 10 (2007) 40–48. doi:10.1016/S1369-7021(07)70078-0.

[147] F.A. Kröger, The Chemistry of Imperfect Crystals, Interscience (Wiley), New York, 1964. doi:10.1126/science.145.3627.40.

[148] A. van Dijken, E.A. Meulenkamp, D. Vanmaekelbergh, A. Meijerink, Influence of Adsorbed Oxygen on the Emission Properties of Nanocrystalline ZnO Particles, J. Phys. Chem. B. 104 (2000) 4355–4360. doi:10.1021/jp993998x.

[149] M.Z. Sahdan, M. Hafiz Mamat, M. Salina, Z. Khusaimi, U.M. Noor, M. Rusop, Heat treatment effects on the surface morphology and optical properties of ZnO nanostructures, Phys. Status Solidi. 7 (2010) 2286–2289. doi:10.1002/pssc.200983722.

[150] M. Eita, A. Usman, A.O. El-Ballouli, E. Alarousu, O.S.M. Bakr, O.F. Mohammed, A layer-by-layer ZnO nanoparticle-PbS quantum dot self-assembly platform for ultrafast interfacial electron injection, Small. 11 (2015) 112–118. doi:10.1002/smll.201400939.

[151] M. Eita, A. El Labban, F. Cruciani, A. Usman, P.M. Beaujuge, O.F. Mohammed, Ambient Layer-by-Layer ZnO Assembly for Highly Efficient Polymer Bulk Heterojunction Solar Cells, Adv. Funct. Mater. 25 (2015) 1558–1564. doi:10.1002/adfm.201402637.

[152] J.A. Alvarado, A. Maldonado, H. Juarez, M. Pacio, Synthesis of colloidal ZnO nanoparticles and deposit of thin films by spin coating technique, J. Nanomater. 2013 (2013). doi:10.1155/2013/903191.

[153] S.S. Shariffudin, M. Salina, S.H. Herman, M. Rusop, Effect of Film Thickness on Structural, Electrical, and Optical Properties of Sol-Gel Deposited Layer-by-layer ZnO Nanoparticles, Trans. Electr. Electron. Mater. 13 (2012) 102–105. doi:10.4313/TEEM.2012.13.2.102.

[154] W. Lv, L. Wang, J. Wang, J. Yu, L. Wang, D. Yang, InGaN quantum dot green light-emitting diodes with negligible blue shift of electroluminescence peak wavelength, Appl. Phys. Express. 7 (1882) 25203.

[155] C. Lu, L. Wang, J. Lu, R. Li, L. Liu, D. Li, N. Liu, L. Li, W. Cao, W. Yang, W. Chen, W. Du, C.T. Lee, X. Hu, Investigation of the electroluminescence spectrum shift of InGaN/GaN multiple quantum well light-emitting diodes under direct and pulsed currents, J. Appl. Phys. 113 (2013). doi:10.1063/1.4772683.

[156] S. Riyopoulos, Electrostatically shielded quantum confined Stark effect inside polar nanostructures, Nanoscale Res. Lett. 4 (2009) 993–1003. doi:10.1007/s11671-009-9347-1.

[157] C. Murawski, K. Leo, M.C. Gather, Efficiency roll-off in organic light-emitting diodes., Adv. Mater. 25 (2013) 6801–27. doi:10.1002/adma.201301603.

[158] M.H. Mamat, M.I. Che Khalin, N.N.H. Nik Mohammad, Z. Khusaimi, N.D. Md Sin, S.S. Shariffudin, M. Mohamed Zahidi, M.R. Mahmood, Effects of annealing environments on the solution-grown, aligned aluminium-doped zinc oxide nanorod-array-based ultraviolet photoconductive sensor, J. Nanomater. 2012 (2012). doi:10.1155/2012/189279.

[159] Y.-S. Ho, Y.-S. Chen, C.-H. Wu, Effect of Annealing Ambient on the Electrical and Optical Properties of Aluminum-Doped ZnO Films Produced via a Sol–Gel Process, J. Electron. Mater. 43 (2014) 2644–2650. doi:10.1007/s11664-014-3114-5.

[160] J.-H. Lee, K.-H. Ko, B.-O. Park, Electrical and optical properties of ZnO transparent conducting films by the sol–gel method, J. Cryst. Growth. 247 (2003) 119–125. doi:10.1016/S0022-0248(02)01907-3.

[161] W. Tang, D.C. Cameron, Aluminum-doped zinc oxide transparent conductors deposited by the sol-gel process, Thin Solid Films. 238 (1994) 83–87. doi:10.1016/0040-6090(94)90653-X.

[162] A.J. Morfa, N. Kirkwood, M. Karg, T.B. Singh, P. Mulvaney, Effect of defects on the behavior of ZnO nanoparticle FETs, J. Phys. Chem. C. 115 (2011) 8312–8315. doi:10.1021/jp200208k.

[163] C. Gi Choi, B.-S. Bae, Effects of Hydroxyl Groups in Gate Dielectrics on the Hysteresis of Organic Thin Film Transistors, Electrochem. Solid-State Lett. 10 (2007) H347–H350. doi:10.1149/1.2779946.

[164] D. Wang, N. Reynolds, Photoluminescence of Zinc Oxide Nanowires: The Effect of Surface Band Bending, ISRN Condens. Matter Phys. 2012 (2012) 1–6. doi:10.5402/2012/950354.

[165] M.R. Alfaro Cruz, N. Hernandez-Como, I. Mejia, G. Ortega-Zarzosa, G.-A. Martínez-Castañón, M.A. Quevedo-Lopez, Impact of the annealing atmosphere in the electrical and optical properties of ZnO thin films, J. Sol-Gel Sci. Technol. 79 (2016) 184–189. doi:10.1007/s10971-016-4035-y.

[166] X. Yang, E. Mutlugun, C. Dang, K. Dev, Y. Gao, S.T. Tan, X.W. Sun, H.V. Demir, Highly flexible, electrically driven, top-emitting, quantum dot light-emitting stickers, ACS Nano. 8 (2014) 8224–8231. doi:10.1021/nn502588k.

[167] N. Strekal, A. Medzvedz, S. Maskevich, O. Kulakovich, A. Orlova, A. Fedorov, A. Baranov, Influence of polar environment on CdSe/ZnS nanocrystals: Stark effect modelling, in: Physics, Chem. Appl. Nanostructures, World Scientific, 2011: p.

192.

[168] N. Kirkwood, B. Singh, P. Mulvaney, Enhancing Quantum Dot LED Efficiency by Tuning Electron Mobility in the ZnO Electron Transport Layer, Adv. Mater. Interfaces. 3 (2016) 1600868. doi:10.1002/admi.201600868.

[169] S. Zairi, K. Reybier, N. Jaffrezic-Renault, C. Martelet, B. Fahys, Enhanced ionodetection by using polyethyleneimine as an insulator material, Mater. Sci. Eng. C. 21 (2002) 35–41. doi:10.1016/S0928-4931(02)00066-8.

[170] F.-S. Juang, L.-A. Hong, S.-H. Wang, Y.-S. Tsai, M.-H. Gao, Y. Chi, H.-P. Shieh, J.-S. Hsu, Power Efficiency Improvement of White Phosphorescent Organic Light-Emitting Diode with Thin Double-Emitting Layers and Hole-Trapping Mechanism, Jpn. J. Appl. Phys. 50 (2011) 04DK04. doi:10.1143/JJAP.50.04DK04.

[171] M. Ramar, S.S. Rawat, R. Srivastava, S.K. Dhawan, C.K. Suman, Impact Of Cross Linking Chain Of N,N'-bis(napthalen-|-y|)-N,N'-bis(phenyl)-benzidine On Temperature dependent Transport Properties, Adv. Mater. Lett. 7 (2016) 783–789. doi:10.5185/amlett.2016.6305.

[172] W. Ji, Y. Tian, Q. Zeng, S. Qu, Efficient Quantum Dot Light Emitting Diodes by Controlling the Carrier Accumulation and Exciton Formation, ACS Appl. Mater. Interfaces. 6 (2014) 14001–14007. doi:10.1021/am5033567.

[173] H. Bourvon, S. Le Calvez, H. Kanaan, S. Meunier-Della-Gatta, C. Philippot, P. Reiss, Langmuir-Schaeffer monolayers of colloidal nanocrystals for cost-efficient quantum dot light-emitting diodes, Adv. Mater. 24 (2012) 4414–4418. doi:10.1002/adma.201200981.

[174] J. Lim, W.K. Bae, J. Kwak, S. Lee, C. Lee, K. Char, Perspective on synthesis, device structures, and printing processes for quantum dot displays, Opt. Mater. Express. 2 (2012) 594–628. doi:10.1364/OME.2.000594.

[175] L. Kim, P.O. Anikeeva, S. a Coe-Sullivan, J.S. Steckel, M.G. Bawendi, V. Bulović, Contact printing of quantum dot light-emitting devices, Nano Lett. 8 (2008) 4513–4517. doi:10.1021/nl8025218.

[176] T.F. Chang, A. Maria, P.W. Cyr, V. Sukhovatkin, L. Levina, E.H. Sargent, High near-infrared photoluminescence quantum efficiency from PbS nanocrystals in polymer films, Synth. Met. 148 (2005) 257–261. doi:10.1016/j.synthmet.2004.10.003.

[177] D. Bozyigit, V. Wood, Y. Shirasaki, V. Bulovic, Study of field driven electroluminescence in colloidal quantum dot solids, J. Appl. Phys. 111 (2012)

113701. doi:10.1063/1.4720377.

[178] K. Kim, H. Lee, J. Ahn, S. Jeong, Highly luminescing multi-shell semiconductor nanocrystals InP/ZnSe/ZnS, Appl. Phys. Lett. 101 (2012) 10–14. doi:10.1063/1.4745844.

[179] V. Shrotriya, Y. Yang, Capacitance-voltage characterization of polymer light-emitting diodes, J. Appl. Phys. 97 (2005) 54504. doi:10.1063/1.1857053.

[180] R. Zhu, Z. Luo, H. Chen, Y. Dong, S.-T. Wu, Realizing Rec 2020 color gamut with quantum dot displays, Opt. Express. 23 (2015) 23680. doi:10.1364/OE.23.023680.

[181] I. Swart, P. Liljeroth, D. Vanmaekelbergh, Scanning probe microscopy and spectroscopy of colloidal semiconductor nanocrystals and assembled structures, Chem. Rev. 116 (2016) 11181–11219. doi:10.1021/acs.chemrev.5b00678.

[182] S.C. Boehme, H. Wang, L.D.A. Siebbeles, D. Vanmaekelbergh, A.J. Houtepen, Electrochemical Charging of CdSe Quantum Dot Films: Dependence on Void Size and Counterion Proximity, ACS Nano. 7 (2013) 2500–2508. doi:10.1021/nn3058455.

[183] J. Choung, J.G. Lee, J.B. Choi, I.S. Oh, S.J. Cho, J.Y. Yoon, H.J. Song, Y.H. Lee, C.H. Lee, W.J. Kim, Y.W. Song, J.H. Lee, S.C. Kim, Study of Space Charges in Hole Transfer Layer of OLED Devices using Impedance Spectroscopy and Transient Electroluminescence, SID Dig. (2011) 825–828.

[184] J. Bisquert, G. Garcia-Belmonte, Á. Pitarch, H.J. Bolink, Negative capacitance caused by electron injection through interfacial states in organic light-emitting diodes, Chem. Phys. Lett. 422 (2006) 184–191. doi:10.1016/j.cplett.2006.02.060.

[185] H. Zhang, N. Sui, X. Chi, Y. Wang, Q. Liu, H. Zhang, W. Ji, Ultra-Stable Quantum-Dot Light Emitting Diodes by Suppression of Leakage Current and Exciton Quenching Processes, ACS Appl. Mater. Interfaces. 8 (2016) 31385−31391. doi:10.1021/acsami.6b09246.

[186] H. Zhang, Y. Feng, S. Chen, Improved Efficiency and Enhanced Color Quality of Light-Emitting Diodes with Quantum Dot and Organic Hybrid Tandem Structure, ACS Appl. Mater. Interfaces. 8 (2016) 26982−26988. doi:10.1021/acsami.6b07303.

[187] M. Fiedot, O. Rac, P.S. Woźniak, I. Karbownik, H. Teterycz, Polymer – surfactant interactions and their influence on zinc oxide nanoparticles morphology, in: Manuf. Nanostructures, One Central Press (OCP), 2014: pp. 108–128.

Publications

Parts of this dissertation have been published in the following publications.

- **Y. Kim**, C. Ippen, B. Fischer, A. Lange, A. Wedel, Efficiency enhancement of InP-based inverted QD-LEDs by incorporation of a polyethylenimine modified Al:ZnO layer, J. Soc. Inf. Disp. 23 (2015) 377–383. doi:10.1002/jsid.322.

- **Y. Kim**, C. Ippen, T. Greco, J. Lee, M.S. Oh, C.J. Han, C.J. Han, A. Wedel and J. Kim, Increased shell thickness in indium phosphide multishell quantum dots leading to efficiency and stability enhancement in light-emitting diodes, Opt. Mater. Express. 4 (2014) 1436. doi:10.1364/OME.4.001436.

During my Ph.D. study the following contributions have also been made.

Journal

- **Y. Kim**, B. Heyne, A. Abouserie, C. Pries, C. Ippen, C. Günter, A. Wedel, Y. Kim, B. Heyne, A. Abouserie, C. Pries, C. Ippen, G. Christina, CuS nanoplates from ionic liquid precursors — Application in organic photovoltaic cells, J. Chem. Phys. 148 (2018) 193818. doi:10.1063/1.4991622.
- H.Y. Kim, Y.J. Park, J. Kim, C.J. Han, J. Lee, **Y. Kim**, T. Greco, C. Ippen, A. Wedel, B.K. Ju, M.S. Oh, Transparent InP Quantum Dot Light-Emitting Diodes with ZrO2 Electron Transport Layer and Indium Zinc Oxide Top Electrode, Adv. Funct. Mater. 26 (2016) 3454–3461. doi:10.1002/adfm.201505549.
- C. Ippen, T. Greco, **Y. Kim**, C. Pries, J. Kim, M.S. Oh, C.J. Han, A. Wedel, Color tuning of indium phosphide quantum dots for cadmium-free quantum dot light-emitting devices with high efficiency and color saturation, J. Soc. Inf. Disp. 23 (2015) 285–293. doi:10.1002/jsid.308.
- S. Lim, **Y. Kim**, J. Lee, C.J. Han, J. Kang, J. Kim, Investigation of Colloidal PbS Quantum Dot-Based Solar Cells with Near Infrared Emission, J. Nanosci. Nanotechnol. 14 (2014) 9346–9350. doi:10.1166/jnn.2014.10138.

Conference

- A Wedel, **Y. Kim**, B. Heyne and A. Geßner, From the Synthesis of High-Quality InP-based Quantum Dots to the Development of Efficient QD Light-Emitting

Diodes, SID Symposium Digest of Technical Papers_accepted number 4.2, Los Angeles, California, USA, May 2018, Oral)

- **Y. Kim**, B. Heyne, A. Geßner, Y. Park, M. Kang, S. Ahn, B. Lee, and A. Wedel, Efficient InP-based Quantum Dot Light Emitting Diodes utilizing a Crosslinkable Hole Transport Layer, SID Symposium Digest of Technical Papers_ accepted number p.110, (Los Angeles, California, USA, May 2018, Poster)
- **Y. Kim**, A. Geßner and A Wedel, High Performance Indium Phosphide Quantum Dot LEDs utilizing an inverted Device Structure, LOPEC Scientific Conference (Munich, Germany, 2018, Oral)
- **Y. Kim**, B. Heyne, B. Fischer, S. Kreißl, A. Geßner, C.J Han, M.S Oh, B Yoo and A Wedel, Design of high-performance InP quantum dot light-emitting diodes, SID-ME Fall Meeting (EuroDisplay, Berlin, Germany, 2017, Oral)
- C. Boeffel, **Y. Kim**, U. Koepke, G. Tobias, T. Riedl, Processing of Metal Oxide Nanoparticle Inks for OPV and OLED Applications by a Novel new Synthesis Route, LOPEC Technical Poster Session (Munich, Germany, 2017, Poster)
- **Y. Kim**, B. Heyne, C. Pries, B. Fischer, S. Kreißl and A. Wedel, Design of high-performance InP/ZnSe/ZnS quantum dot-based light-emitting diodes, SID-ME Fall Meeting (Berlin, Germany, 2016, Oral)
- **Y. Kim**, B. Heyne, A. Abouseriea, C. Pries, A. Taubert and A. Wedel, Metal Chalcogenide Semiconductor Nanostructures for Hybrid Solar Cell Application, International conference on ionic liquids (Potsdam, Germany, 2016, Oral)
- **Y. Kim**, C. Ippen and A. Wedel, Efficiency Enhancement of InP-Based Inverted QD-LEDs by Polyethylenimine-Modified Al:ZnO Layer, SID Symposium Digest of Technical Papers 46, p.44 (EuroDisplay, Ghent, Belgium, 2015, Oral)
- J. Kim, I. Jang, C. Ippen, **Y. Kim**, W. K. Kim, A. Wedel, S. K. Park, C. J. Han, Study of Interfacial Treatment on the Metal-Oxide Electron Transport Layer in the InP Quantum Dot Light-Emitting Diodes, SID Symposium Digest of Technical Papers 46, p.85 (EuroDisplay, Ghent, Belgium, 2015, Oral)
- M.S. Oh, C. J. Han, B. Yoo, J. Lee, H. Y. Kim, Y. J. Park, B. K. Joo, **Y. Kim** and A. Wedel, Ecofriendly Quantum Dot Light-Emitting Diode With Inorganic Charge Transport Layer, SID Symposium Digest of Technical Papers 46, p.10 (EuroDisplay, Ghent, Belgium, 2015, Oral)